ASME
SETTING THE STANDARD

Transactions of the ASME, Journal of Fluids Engineering
(ISSN 0098-2202) is published monthly by
The American Society of Mechanical Engineers,
Three Park Avenue, New York, NY 10016.
Periodicals postage paid at New York, NY
and additional mailing offices.
POSTMASTER: Send address changes to Transactions of the
ASME, Journal of Fluids Engineering, c/o THE AMERICAN
SOCIETY OF MECHANICAL ENGINEERS,
22 Law Drive, Box 2300, Fairfield, NJ 07007-2300.
CHANGES OF ADDRESS must be received at Society
headquarters seven weeks before they are to be effective.
Please send old label and new address.

Journal of Fluids Engineering

Published Monthly by ASME

VOLUME 129 • NUMBER 10 • OCTOBER 2007

TECHNICAL PAPERS

(Contents continued on inside back cover)

This journal is printed on acid-free paper, which exceeds the ANSI Z39.48-1992 specification for permanence of paper and library materials. ♾™
♻ 85% recycled content, including 10% post-consumer fibers.

The ASME Journal of Fluids Engineering is abstracted and indexed in the following:

Applied Science & Technology Index, Chemical Abstracts, Chemical Engineering and Biotechnology Abstracts (Electronic equivalent of Process and Chemical Engineering), Civil Engineering Abstracts, Computer & Information Systems Abstracts, Corrosion Abstracts, Current Contents, Ei EncompassLit, Electronics & Communications Abstracts, Engineered Materials Abstracts, Engineering Index, Environmental Engineering Abstracts, Environmental Science and Pollution Management, Excerpta Medica, Fluidex, Index to Scientific Reviews, INSPEC, International Building Services Abstracts, Mechanical & Transportation Engineering Abstracts, Mechanical Engineering Abstracts, METADEX (The electronic equivalent of Metals Abstracts and Alloys Index), Petroleum Abstracts, Process and Chemical Engineering, Referativnyi Zhurnal, Science Citation Index, SciSearch (The electronic equivalent of Science Citation Index), Shock and Vibration Digest, Solid State and Superconductivity Abstracts, Theoretical Chemical Engineering

A General Strategy to Extend Turbulence Models to Rough Surfaces: Application to Smith's *k-L* Model

B. Aupoix
ONERA/DMAE/TMP,
Centre d'Études et de Recherches de Toulouse,
B.P. 74025, 2 Avenue Édouard Belin,
31055 Toulouse Cedex 4, France
e-mail: bertrand.aupoix@onera.fr

A general procedure to extend turbulence models to account for wall roughness, in the framework of the equivalent sand grain approach, is proposed. It is based on the prescription of the turbulent quantities at the wall to reproduce the shift of the logarithmic profile and hence provide the right increase in wall friction. This approach was previously applied to Spalart and Allmaras one equation (1992, "A One-Equation Turbulence Model for Aerodynamic. Flows," 30th Aerospace Sciences Meeting and Exhibit, Reno, NV, AIAA paper No. 92-0439; 1994, ibid, Rech. Aerosp. ***1****, pp. 5–21). Here, the strategy is detailed and applied to Smith's two-equation k-L model (1995, "Prediction of Hypersonic Shock Wave Turbulent Boundary Layer Interactions With The k-l Two Equaton Turbulence Model," 33rd Aerospace Sciences Meeting and Exhibit, Reno, NV, Paper No. 95-0232). The final model form is given. The so-modified Spalart and Allmaras and Smith models were tested on a large variety of test cases, covering a wide range of roughness and boundary layer Reynolds numbers and compared with other models. These tests confirm the validity of the approach to extend any turbulence model to account for wall roughness. They also point out the deficiency of some models to cope with small roughness levels as well as the drawbacks of present correlations to estimate the equivalent sand grain roughness.* [DOI: 10.1115/1.2776960]

Keywords: skin friction, turbulence modeling, wall roughness

1 Introduction

Rough walls are encountered in a wide variety of applications. The first interests were mainly focused on ship hulls, surface roughness being due not only to poor surface state but also to seaweeds or shells, or on pressure drop in pipes, due to pipe casting and manufacturing processes. Modern applications can also be related to surface ablation due to hard working conditions, such as those encountered on high pressure turbine blades, in rocket nozzles, or on entry missile nosetips.

These examples correspond to distributed roughness; i.e., a large surface, compared to the boundary layer thickness, is covered by roughness elements the size of which in any direction is small compared with the boundary layer thickness. Therefore, in the boundary layer, some distance above the roughness elements, the flow statistics no longer depend on the exact location with respect to the roughness elements.

1.1 Roughness Effects. Flows over rough surfaces were investigated since the 19th century, but the first main work, which still constitutes a reference, is due to Nikuradse [1]. He investigated a water flow inside a pipe, roughened with calibrated sand grains following a very careful procedure. He so evidenced three regimes according to the roughness height in wall variables

$$h_s^+ = \frac{\rho u_\tau h_s}{\mu} \tag{1}$$

where $u_\tau = \sqrt{\tau_w/\rho}$ is the friction velocity based on the skin friction τ_w and the sand grain height h_s, as

- $h_s^+ < 3.5$: The flow is not affected by the wall roughness. This is the hydraulically smooth regime.
- $3.5 < h_s^+ < 68$: The roughness influence increases with the Reynolds number; the flow around the roughness is not fully viscous. This is the transition regime.
- $68 < h_s^+$: The roughness effect becomes independent of the roughness size; viscous effects are negligible. This is the completely rough regime.

Another key result of Nikuradse's works deals with the velocity profile. Over a rough surface, Nikuradse checked that the logarithmic region still exists, but the logarithmic region and the wake are shifted down. This is shown in Fig. 1, which compares the velocity profiles in wall variables for boundary layers over a smooth and a rough wall. Over a rough wall, the inner region makes no sense as it is within the roughness elements. A mean velocity profile makes sense only some distance above the roughness elements. Only the logarithmic region and the wake can be plotted, provided the Reynolds number is high enough. Nikuradse related the shift Δu^+ to the reduced roughness height h_s^+ as

$$\Delta u^+ = \frac{1}{\kappa} \ln h_s^+ + C - B \quad \kappa = 0.40 \quad C = 5.5 \tag{2}$$

with

$$\begin{aligned} 1 < h_s^+ < 3.5 \quad & B = 5.5 + \frac{1}{\kappa} \ln h_s^+ \\ 3.5 < h_s^+ < 7 \quad & B = 6.59 + 1.52 \ln h_s^+ \\ 7 < h_s^+ < 14 \quad & B = 9.58 \\ 14 < h_s^+ < 68 \quad & B = 11.5 - 0.7 \ln h_s^+ \\ 68 < h_s^+ \quad & B = 8.48 \end{aligned} \tag{3}$$

Contributed by the Fluids Engineering Division of ASME for publication in the JOURNAL OF FLUIDS ENGINEERING. Manuscript received June 26, 2006; final manuscript received April 27, 2007. Review conducted by Ye Zhou.

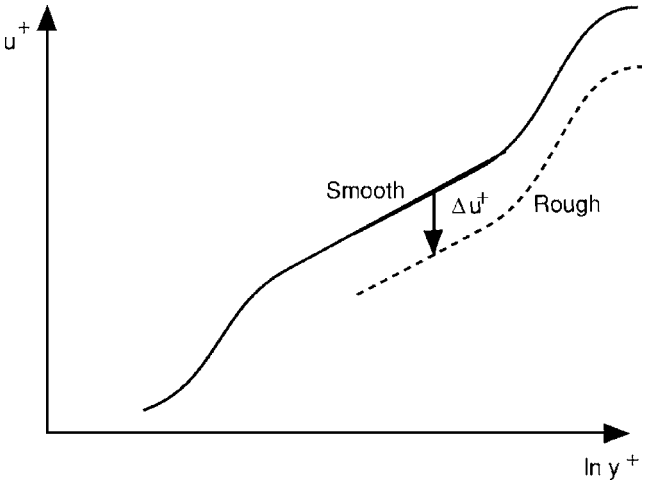

Fig. 1 Velocity profiles over smooth and rough walls plotted in wall variables

1.2 Rough Wall Modeling. In the framework of industrial design, i.e., relying on industrial software, three approaches can be considered to predict the flow over rough surfaces (see, e.g., Patel [2]).

- On the edge of the above assumptions, for well identified roughness patterns, the solution of the averaged Navier–Stokes equations can be performed on the real surface, accounting for the exact shape of the surface roughness (see, e.g., Reijasse et al. [3]).
- The "discrete element approach" accounts for the roughness by extra terms in the flow equations, which represent the flow blockage due to the roughness elements and the drag and heat flux on roughness elements. Several derivations of the complete set of equations were proposed, e.g., by Coleman et al. [4] or Aupoix [5]. Simplified formulations were also put forward.
- The "equivalent sand grain approach" proceeds in two steps. First, following Schlichting [6], it links the real roughness to a reference roughness that provides the same increase in wall friction. The reference experiments are, of course, Nikuradse's experiments so that the equivalent sand grain in Nikuradse's experiment is sought for. The height of the equivalent sand grain is deduced from the real roughness shape with the help of empirical correlations, usually the correlation proposed by Dirling Jr. [7] and Grabow and White [8].

The roughness effect is then mimicked by increasing the turbulent eddy viscosity in the wall region to obtain higher skin friction and wall heat flux levels. Here, again, two kinds of model can be considered.

- Models in which the eddy viscosity is null at the boundary. The roughness correction then mainly acts through a reduction of the turbulence damping in the wall region. van Driest [9] and Krogstad [10] proposed such extensions for the mixing length model. Chen and Patel [11] and Durbin et al. [12] applied this approach to two-layer k-ε models, which reduce to one equation models in the wall region, Wilcox [13] to his k-ω model, and Zhang et al. [14] to a k-ε model.
- Models in which the eddy viscosity is finite at the boundary. Rotta [15] and Blanchard [16] proposed such extensions for the mixing length model. Blanchard also applied this strategy to a k-ε model. This is also the route chosen by Aupoix and Spalart [17] in their two extensions of Spalart and Allmaras' one-equation model [18,19].

Drag increase over rough surfaces is mainly through pressure forces on the roughness elements, while heat transfer increase is mainly due to surface increase so that the heat transfer is less enhanced by roughness elements than the drag (Dipprey and Sabersky [20]). The discrete element approach treats the dynamical and thermal aspects in different ways and is able to cope with this difference. In the equivalent sand grain approach, only the turbulence model is altered so that the real physics is not represented. The drag increase is represented via the turbulence model, i.e., via an increase of momentum transfer toward the wall. The momentum and heat transfer toward the wall are increased in a similar manner. Hence, the heat transfer increase is usually overestimated (see, e.g., Aupoix and Spalart [17]).

The key advantage of the equivalent sand grain approach is that it uses the same set of equations as for the flow over a smooth wall. In the most correct derivations of the discrete element approach, the advection and diffusion fluxes are modified to account for the blockage due to roughness elements, and source terms are added. This means that the implementation of the discrete element approach in a general purpose Navier–Stokes solver requires drastic changes to the code.

The drawback of the equivalent sand grain approach is that it heavily relies on correlations to determine the equivalent sand grain, the accuracy of which is questionable.

Therefore, the equivalent sand grain approach remains the only approach applicable in industrial practices. Nevertheless, while two-equation models are now popular in the industry, only Wilcox's k-ω model and some k-ε models can account for wall roughness using the equivalent sand grain approach. In this framework, the present paper presents a general strategy, in the sense that it can be applied to any turbulence model, to extend it to rough surfaces. This technique was already applied but is here completely described in Sec. 2. As an example, Sec. 3 details its application to Smith's k-L turbulence model. Section 4 gives some validation examples.

2 Modeling Strategy

As shown in Fig. 1, the roughness shifts the logarithmic region and the wake without modifying them. In other words, the roughness mainly affects the inner region. Although this has been controversial, the wake region feels the wall roughness only through the change in the friction velocity u_τ.

As the equivalent sand grain approach is unable to finely reproduce the roughness effect, the only reasonable requirement is a good reproduction of the wall friction increase due to roughness. The wall friction coefficient C_f is directly related to the reduced velocity at the outer edge of the boundary layer since

$$u_e^+ = \frac{u_e}{u_\tau} = \sqrt{\frac{2}{C_f}} \tag{4}$$

Therefore, the reproduction of the wall friction only requires the right shift Δu^+ of the logarithmic region.

This can be easily achieved by introducing a shift in the wall distance d_0 such that, respectively noting s and r as the solutions over smooth and rough surfaces, these solutions are linked by

$$\frac{\partial u_r^+}{\partial y^+}(y^+) = \frac{\partial u_s^+}{\partial y^+}(y^+ + d_0^+) \tag{5}$$

The integration of the above relation directly gives the velocity shift

$$\Delta u^+ = u_s^+(d_0^+) \tag{6}$$

so that d_0^+ is linked to the reduced roughness height h_s^+ with the help of Eqs. (2) and (3).

As in the wall region, the momentum equation can be reduced to

$$(\mu + \mu_t)\frac{\partial u}{\partial y} = \tau_w \tag{7}$$

Equation (5) is fulfilled if

$$\mu_{t_r}^+(y^+) = \mu_{ts}^+(y^+ + d_0^+) \tag{8}$$

i.e., if all turbulent quantities (e.g., L^+) satisfy the same relation

$$L_r^+(y^+) = L_s^+(y^+ + d_0^+) \tag{9}$$

This is obtained by imposing as wall condition for each transported turbulent quantity its value at a distance d_0 over a smooth surface. If the wall distance y appears in the turbulence model, which is the case for Spalart and Allmaras' model or Smith's model to be considered below, it has to be changed everywhere in the model equations into $y+d_0$.

This is roughly the procedure which was already applied by Aupoix and Spalart [17] in the ONERA extension of the Spalart and Allmaras one-equation model to rough surfaces.

The limitations of the proposed strategy deserve to be pointed out.

- It is designed only to finely reproduce the increase in skin friction due to wall roughness through a correct shift of the logarithmic region. The validity of the approach at very low Reynolds numbers is therefore questionable and surely model dependent.
- It is exact only for zero pressure gradient flows. For boundary layers submitted to pressure gradients, the right side of Eq. (7) is $\tau_w+(dp/dx)y$, which introduces a difference $(dp/dx)d_0$, but this difference remains small compared to the wall friction. Moreover, very few is presently known about the combined effects of roughness and pressure gradient.
- A referee pointed out that another quantity that deserves to be looked at is the mass flow within the roughness elements, i.e., the blockage due to roughness. This could be important for internal flows but cannot be addressed with so crude a representation of the roughness effects.
- If the wall distance appears in the model, the present strategy leads to a reevaluation of the wall distance as $y+d_0$. The distance shift d_0 is a priori unknown so that convergence on d_0 is required. Our experience in a Navier–Stokes solver is that only several evaluations of d_0 are required as convergence on the distance shift is quick, but this also imposes one either to link each point in the flow field to a point on a surface where the distance shift d_0 is evaluated or to change boundary conditions in the routine used to compute the wall distance.

3 Application to Smith's *k-L* Model

3.1 Basic Model. Smith [21] initially developed a *k-kL* model in which the turbulence length scale kL is derived from an integral of two-point correlations. As $kL \approx y^3$ in the wall region, Smith [22] rewrote this model as a *k-L* model. Transport equations for the turbulent kinetic energy $q^2=2k$ and the turbulent length scale L read

$$\rho\frac{Dq^2}{Dt} = 2P_k - 2\frac{\rho q^3}{B_1 L} - 2\mu\ \underline{\text{grad}}\ q \cdot \underline{\text{grad}}\ q + \text{div}[(\mu + S_q\mu_t)\underline{\text{grad}}\ q^2] \tag{10}$$

$$\rho\frac{DL}{Dt} = (2-E_2)\frac{\rho q}{B_1}\left[1 - \left(\frac{L}{\kappa d}\right)^2\right] - S_q\frac{\mu_t}{L}\left(\frac{L}{\kappa d}\right)^2 \underline{\text{grad}}\ L \cdot \underline{\text{grad}}\ L + \rho L\ \text{div}\underline{U} + \frac{2S_q\mu_t}{q^2}\ \underline{\text{grad}}\ L \cdot \underline{\text{grad}}\ q^2 + \text{div}[(\mu + S_q\mu_t)\underline{\text{grad}}\ L] \tag{11}$$

where d is the distance to the nearest wall and $P_k = -\underline{u}' \otimes \underline{u}' : \underline{\underline{\text{grad}}}\ \underline{u}$ is the turbulent kinetic energy production rate. Model coefficients are

$$B_1 = 18.0 \quad E_2 = 1.2 \quad S_q = 0.7 \quad \kappa = 0.41$$

and the eddy viscosity reads

$$\mu_t = \mu\chi\Phi$$

with

$$\chi = \frac{\rho q L}{\mu B_1^{1/3}} \quad \Phi = \left(\frac{C_1^4 f_1 + C_2^2\chi^2 + \chi^4}{C_1^4 + C_2^2\chi^2 + \chi^4}\right)^{1/4} \quad f_1 = \exp\left[-50\left(\frac{L}{\kappa d}\right)^2\right]$$

$$C_1 = 25.5 \quad C_2 = 2$$

This model is very stable as $L \propto y$ in the wall region and gives fair predictions. Its drawback is that it is slightly sensitive to external levels of L, as pointed out by Prasad and Hassan [23] and analyzed by Ferrey and Aupoix [24]. Smith [25] proposed a revised version, with a shear stress (SST) limiter, to improve the prediction of flows close to separation. Both model versions are available in the ONERA Navier–Stokes solver elsA and are widely used because of their good numerical properties and fair predictions.

3.2 Extension to Rough Walls

3.2.1 Strategy to Account for Wall Roughness. The strategy to account for wall roughness is the one presented in Sec. 2. The roughness correction can be simply derived from the knowledge of the one-dimensional solution in the wall region. A given roughness height h_s^+ is related to a velocity shift Δu^+ by relations (2) and (3). From the one-dimensional solution in the wall region, the values of d_0^+, $q^{2+}(d_0^+)$, and $L^+(d_0^+)$ can be derived. Some analytical solutions will first be considered.

3.2.2 Model Behavior for Weakly Rough Surfaces. For weakly rough surfaces, the velocity shift Δu^+ is small so that it corresponds to a shift of the reference surface in the linear region close to the wall. Therefore, from Eqs. (2) and (3), the velocity shift reads

$$\Delta u^+ = d_0^+ = \frac{1}{\kappa}\ln h_s^+ + 5.5 - (6.59 + 1.52\ln h_s^+) = 0.92\ln h_s^+ - 1.09 \tag{12}$$

Of course, this relation gives negative values of the velocity shift and the wall displacement for values of h_s^+ smaller than 3.5. It can be applied only for larger values, i.e., not in the hydraulically smooth regime. The final form is thus

$$d_0^+ = \max(0; 0.92\ln h_s^+ - 1.09) \tag{13}$$

A close inspection of the length scale profile shows that the model solution is $L=\kappa y$ in most of the wall region but slightly departs from it very close to the wall where $L \approx 0.507y$. Therefore, the limiting behavior reads

$$L^+ = 0.507 d_0^+ = \max(0; 0.466\ln h_s^+ - 0.553) \tag{14}$$

At last, in the wall region, the turbulent kinetic energy behaves as $0.093y_0^{+2}$ so that

$$q^{2+} = 0.093 d_0^{+2} \tag{15}$$

3.2.3 Model Behavior for Very Rough Surfaces. For very rough surfaces, the velocity shift corresponds to a point in the logarithmic region for the flow over a smooth surface. The velocity shift then reads

$$\Delta u^+ = \frac{1}{\kappa}\ln d_0^+ + C = \frac{1}{\kappa}\ln h_s^+ + C - 8.48 \tag{16}$$

so that

$$d_0^+ = h_s^+ \exp(-8.48\kappa) = 0.0309 h_s^+ \tag{17}$$

Then

$$L^+ = \kappa y^+ = 0.0127 h_s^+ \tag{18}$$

and

$$q^{2+} = \frac{1}{2a_1} = 6.66 \tag{19}$$

It must be pointed out that this limiting behavior is somewhat academic as the logarithmic region starts above $y^+=50$ so that these behaviors hold for $h_s^+ > 1600$, i.e., very large roughness levels.

3.2.4 General Case. Although the roughness correction for the two limiting cases of weakly and very rough surfaces can be derived analytically from the model equations, the roughness correction for most realistic cases first requires us to determine numerically the *k-L* model solution over a smooth surface. For that purpose, the model equations together with the momentum equation are rewritten in wall variables, noted $^+$, i.e., making them dimensionless with the viscosity and the friction velocity; advection terms are neglected so that the equation set reduces to

$$1 = \frac{\partial u^+}{\partial y^+} - \langle u'v' \rangle^+ = (1+\nu_t^+)\frac{\partial u^+}{\partial y^+} \tag{20}$$

$$\nu_t^+ = \chi \Phi \tag{21}$$

$$0 = -2\overline{u'v'}^+ \frac{\partial u^+}{\partial y^+} - 2\frac{q^{+3}}{B_1 L^+} - 2\left(\frac{\partial q^+}{\partial y^+}\right)^2 + \frac{\partial}{\partial y^+}\left[(1+S_q\nu_t^+)\frac{\partial q^{+2}}{\partial y^+}\right] \tag{22}$$

$$0 = (2-E_2)\frac{q^+}{B_1}\left[1-\left(\frac{L^+}{\kappa y^+}\right)^2\right] - S_q\frac{\nu_t^+}{L^+}\left(\frac{L^+}{\kappa d^+}\right)^2\left(\frac{\partial L^+}{\partial y^+}\right)^2 + \frac{2S_q\nu_t^+}{q^{+2}}\frac{\partial L^+}{\partial y^+}\frac{\partial q^{+2}}{\partial y^+} + \frac{\partial}{\partial y^+}\left[(1+S_q\nu_t^+)\frac{\partial L^+}{\partial y^+}\right] \tag{23}$$

The above set of equations is solved to obtain the velocity, turbulent kinetic energy, and length scale profiles in the wall region on a smooth surface. A very fine grid is used to achieve grid independent solutions. From that, the corrections $d_0^+(h_s^+)$, $L_0^+(h_s^+)$, and $q_0^{+2}(h_s^+)$ can be determined. They were fitted as

$$d_0^+ = \max(0;0.92\ln h_s^+ - 1.09 - 0.0309 h_s^+)\exp\left(-\frac{-h_s^+}{70}\right) + \max(0;2.93\ln h_s^+ - 7.33)\exp\left(-\frac{-h_s^+}{880}\right) + 0.0309 h_s^+ \tag{24}$$

$$L_0^+ = [0.507\max(0;0.92\ln h_s^+ - 1.09) - 0.0127 h_s^+]\exp\left(-\frac{-h_s^+}{70}\right) + \max(0;1.67\ln h_s^+ - 4.25)\exp\left(-\frac{-h_s^+}{920}\right) + 0.0127 h_s^+ \tag{25}$$

$$q_0^{+2} = \max(q_1;10q_1^{1.73})\min\left\{1;\min\left[\left(\frac{h_s^+}{45}\right)^{-0.5};\max\left\{\left(\frac{h_s^+}{60}\right)\right\}^{-0.66};0.666 q_1^{-1.73}\right]\right\} \tag{26}$$

where

$$q_1 = 0.093[\max(0;0.932\ln h_s^+ - 1.09)]^2$$

The above formulas of course, fulfill the two limiting behaviors previously evidenced. The numerical solution and the above fits only slightly depart for h_s^+ about 10.

4 Validation

Model validation was performed using ONERA's two-dimensional boundary layer code CLIC2 (Aupoix [26]). An automatic grid adaptation procedure ensures grid converged results. Some transient can be observed at the beginning of the computations due to the initial boundary layer profile generation from a locally self-similar solution.

A set of experiments had to be selected. Attention was first paid to the skin friction measurement accuracy and to the availability of several measurement stations to document boundary layer evolution. Academic, well defined, roughness elements as well as random ones, covering a wide range in Reynolds numbers based as well on the roughness h_s^+ as on the boundary layer momentum thickness R_θ, were retained. At last, pressure gradient effects were addressed. As the poor ability of the equivalent sand grain approach to predict heat transfer was already pointed out above, only dynamical aspects will be considered here.

For each experiment, a smooth wall calculation is presented to evidence the friction increase due to the roughness. The predictions of the presently modified *k-L* model are compared with those of the following models

- The ONERA modification of the Spalart and Allmaras model (Aupoix and Spalart [17]) which was derived using the same strategy
- Wilcox's correction of the *k-ω* model, here applied to Menter [27] base line (BSL) model to get rid of any influence of small freestream turbulence levels (in Wilcox's correction, only the level of the specific dissipation ω is changed at the wall)
- Krogstad's [10] correction of the mixing length model in which the wall damping function is altered
- Rotta's [15] correction of the mixing length model in which the wall distance is shifted to have a nonzero turbulence level at the wall

These models were selected to give samples of popular models. No two-layer model was retained as they are not well suited for use in general Navier–Stokes solvers. The two mixing length models are no longer really used but are significant examples of roughness modeling practices. The Boeing extension of Spalart and Allmaras' model was not retained, the reader is referred to Aupoix and Spalart [17] to check that the differences between the predictions of the two extensions of Spalart and Allmaras' model are minor.

4.1 Mississippi State University Experiments

4.1.1 Presentation. Various experiments of flow over geometrical roughness elements were performed at the Mississippi State University (MSU). Scaggs et al. [28] and Taylor et al. [29] investigated the flow in a pipe. Roughness elements were hemispheres or cones, arranged on a staggered grid, with only one roughness size or alternate rows of two roughness heights. Hosni et al. [30–32] studied boundary layer development over the same type of roughness elements in a low speed wind tunnel specifi-

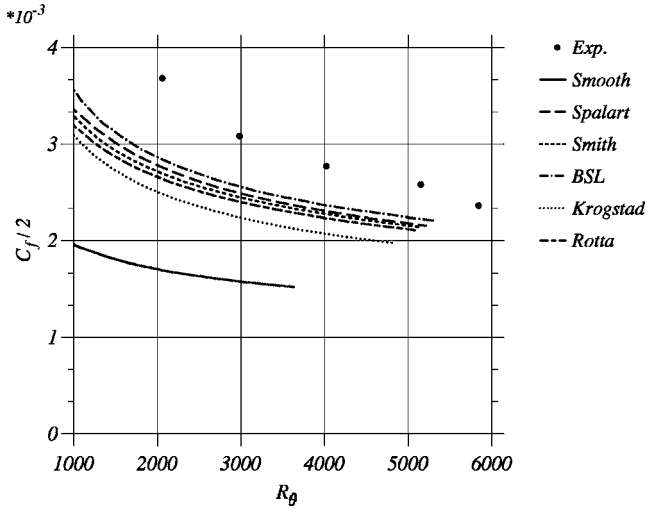

Fig. 2 MSU experiments, hemispherical roughness elements, spacing/diameter ratio of 2, external velocity of 12 m s^{-1}, predictions of the skin friction coefficient versus momentum thickness Reynolds number

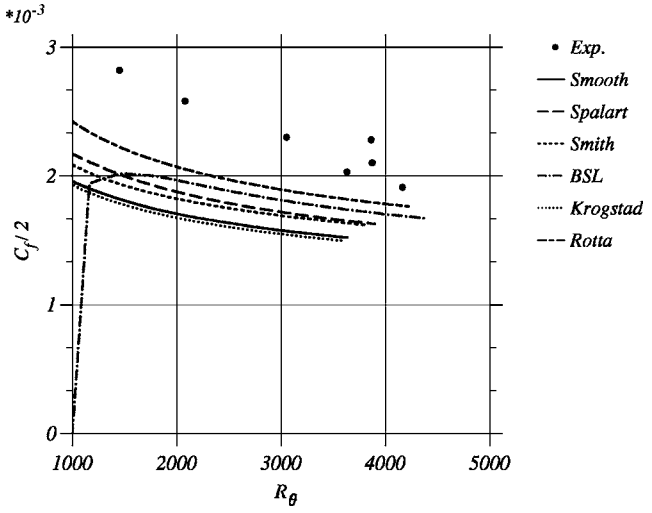

Fig. 3 MSU experiments, hemispherical roughness elements, spacing/diameter ratio of 4, external velocity of 12 m s^{-1}, predictions of the skin friction coefficient versus momentum thickness Reynolds number

cally designed to also measure heat transfer. At last, Chakroun [33] and Chakroun and Taylor [34] investigated the joint effects of roughness and acceleration but only measured heat transfer.

Hosni et al. data for zero pressure gradient flows are used here. Only hemispheres of 0.635 mm radius are considered, as little information is available for the cone experiments. Among the available experiments, two spacings of twice and four times the base diameter and two velocities of 12 m s^{-1} and 58 m s^{-1} are chosen as they allow us to investigate a significant range in Reynolds number R_θ and flow regime h_s^+. The equivalent sand grain roughness was obtained with Dirling, Jr.'s [7] correlation; they are 1.1 mm and 0.29 mm, respectively, for spacings of twice and four times the base diameter.

Skin friction was deduced from the Reynolds shear stress $\langle u'v' \rangle$ above the roughness elements, corrected via a momentum balance. It was checked at ONERA that these skin friction levels are in good agreement with estimates from the von Kármán equation.

The Reynolds number based on the momentum thickness R_θ ranges between 1000 and 6000 for the 12 m s^{-1} experiment and between 5000 and 30,000 for the 58 m s^{-1} experiment.

However, the initial boundary layers are poorly documented. We are not even sure that the boundary layer is turbulent at the beginning of the rough plate for the 12 m s^{-1} experiments. All computations were started with a small value of the Reynolds number based on the momentum thickness R_θ=500. To get rid of the influence of the initial data, skin friction predictions are plotted versus the Reynolds number R_θ.

4.1.2 External Velocity of 12 m s^{-1}*: Spacing/Diameter Ratio of 2*. With hemispheres spaced twice their diameter and an external velocity of 12 m s^{-1}, the reduced equivalent sand grain roughness h_s^+ is about 45, i.e., a transition regime.

The roughness effect is significant; the experimental skin friction is about twice that on a smooth wall. All models underestimate this increase, as shown in Fig. 2. Smith's and Spalart and Allmaras' models give very close predictions, as expected, Spalart and Allmaras' model being slightly higher. Wilcox's model gives a higher friction level. Rotta's and Krogstad's models predict lower skin friction levels.

4.1.3 External Velocity of 12 m s^{-1}*: Spacing/Diameter Ratio of 4*. When the spacing is increased, the surface is less rough so that the reduced equivalent sand grain roughness is about 10, i.e., a transition regime. The experimental skin friction is about 50% higher than on a smooth wall.

Rotta's model here predicts the highest friction level; then, Wilcox's model the next highest. Spalart and Allmaras' and Smith's models again give similar results, while Krogstad's model is unable to cope with so small a roughness and gives a "smooth" prediction, as shown in Fig. 3.

4.1.4 External Velocity of 58 m s^{-1}*: Spacing/Diameter Ratio of 2*. When the velocity is increased, the reduced sand grain roughness rises to about 220, i.e., a fully rough regime.

The roughness effect is important; the friction is more than doubled compared to the smooth case, as shown in Fig. 4. All models nearly give the same prediction, in fair agreement with experiments. Smith's and Wilcox's models give the highest skin

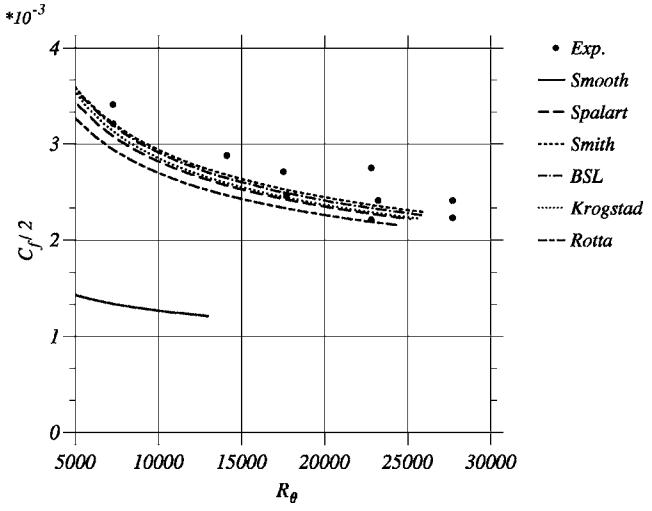

Fig. 4 MSU experiments, hemispherical roughness elements, spacing/diameter ratio of 2, external velocity of 58 m s^{-1}, predictions of the skin friction coefficient versus momentum thickness Reynolds number

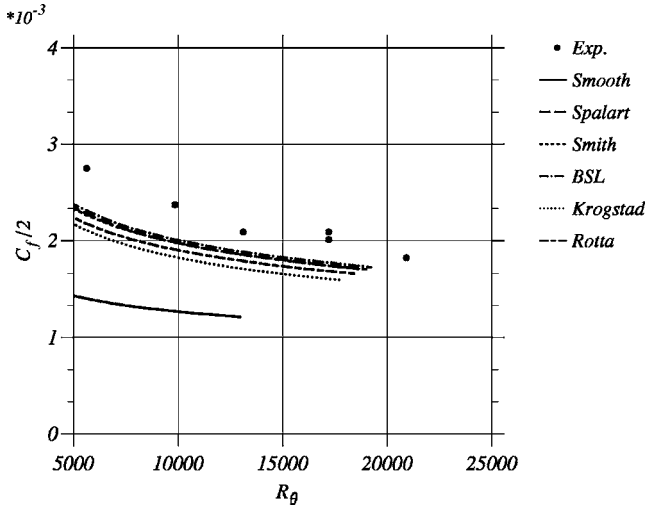

Fig. 5 MSU experiments, hemispherical roughness elements, spacing/diameter ratio of 4, external velocity of 58 m s^{-1}, predictions of the skin friction coefficient versus momentum thickness Reynolds number

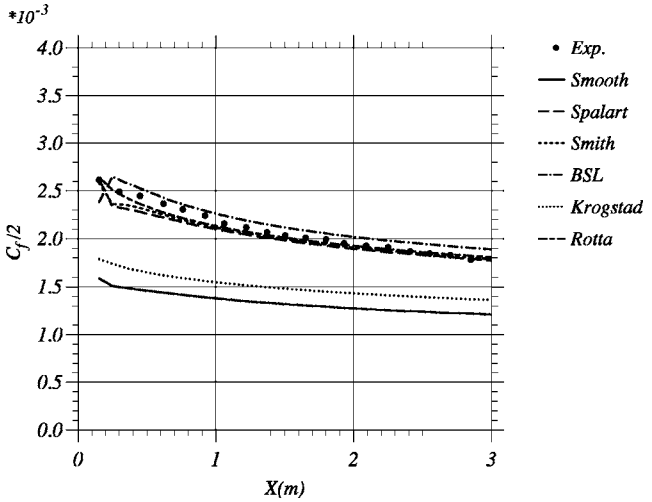

Fig. 6 Acharya et al. experiments, SRS1 surface, predictions of the skin friction coefficient

friction levels, Spalart and Allmaras' and Krogstad's models slightly lower levels, and Rotta's model the lowest.

4.1.5 External Velocity of 58 m s^{-1}*: Spacing/Diameter Ratio of 4*. With the same flow velocity but doubling the spacing between roughness elements, the reduced sand grain roughness is now about 50, similar to the first test case, still in the transition regime. The experimental skin friction is again nearly twice that on a smooth wall.

The agreement with experimental data is fair, but models still underpredict the skin friction. As shown in Fig. 5, the model ranking is similar to the first test case. Wilcox's model still predicts the highest skin friction level, Spalart and Allmaras' and Smith's models again give identical results, while Rotta's model is slightly below and Krogstad's model predicts lower skin friction levels.

All models give rather satisfactory predictions for both 58 m s^{-1} experiments and underestimate more significantly the wall friction for the 12 m s^{-1} one. This suggests that the equivalent sand grain roughness is underestimated by the correlation and may, moreover, depend on the roughness Reynolds number.

4.2 Acharya et al. Experiments

4.2.1 Presentation. At the Brown Bowery Research Center, Acharya et al. [35] performed various experiments on rough plates. Two plates were sand blasted to obtain different roughness shapes and heights. Two plates were designed to mimic the surface roughness of a water pump blade. For that purpose, the plates were first covered with ball spheres; then, spaces between the spheres were filled with silicium carbide and finally covered with lacquer. This technology was developed by trial and error to reproduce realistic surface shapes, concerning as well height distributions as slope distributions. These plates were labeled SRS for simulated rough surface. A SRS1 plate was covered with acrylic paint to make it smoother. The averaged roughness R_a is 93 μm and the average slope 6 deg. A SRS2 plate had an averaged roughness R_a of 113 μm and an average slope of 10 deg. At last, a grid was also investigated. Only plates SRS1 and SRS2, which are closer to applications, will be considered here.

Statistics of roughness are given in the publication. The equivalent sand grain roughness was determined from Tarada's work [36]. The SRS1 surface has a roughness height of 0.345 mm and an equivalent sand grain roughness of 0.524 mm. The SRS2 surface has a roughness height of 0.399 mm and an equivalent sand grain roughness of 1.064 mm.

Although various velocity speeds were investigated, results are available only for a velocity of 19 m s^{-1}, which will be the investigated case. The Reynolds number R_θ ranges between 2000 and 10,000.

The wall friction was measured using a floating element balance coated with the same rough surface. It must be mentioned that shape factor values are noisy as they were computed from the displacement and momentum thickness, extracted from a small figure in the article.

4.2.2 SRS1 Surface. This case corresponds to a reduced equivalent sand grain roughness height h_s^+ about 25, i.e., a transition regime.

Predictions of the skin friction coefficient and of the shape factor are plotted in Figs. 6 and 7. The skin friction is increased by about 50%. All models reproduce this increase fairly well, but now Spalart and Allmaras', Smith's, and Rotta's models predict nearly identical results, in fair agreement with experiments while Wilcox's model yields slightly larger levels and Krogstad's model again underpredicts the skin friction increase.

The differences on the shape factor are not similar, Rotta's and Wilcox's models giving the highest values, Smith's and Spalart

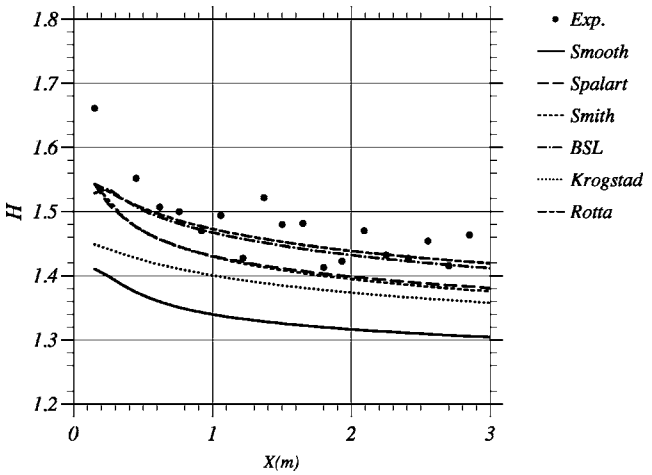

Fig. 7 Acharya et al. experiments, SRS1 surface, predictions of the shape factor

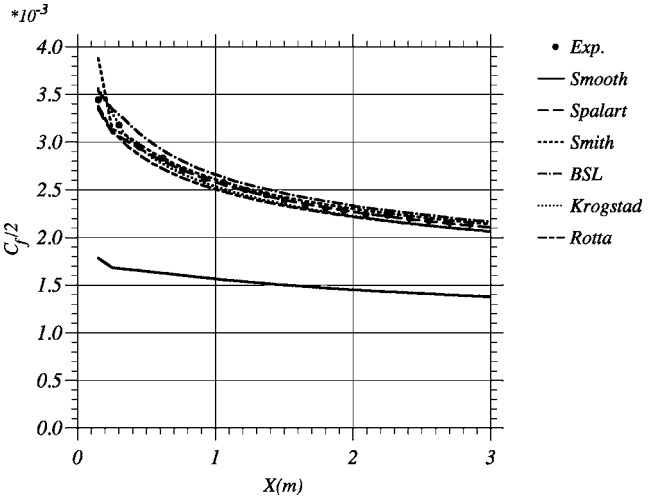

Fig. 8 Acharya et al. experiments, SRS2 surface, predictions of the skin friction coefficient

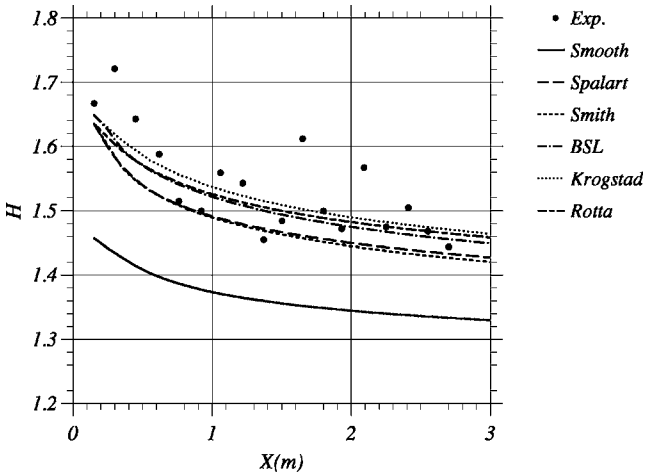

Fig. 9 Acharya et al. experiments, SRS2 surface, predictions of the shape factor

and Allmaras' models identical and lower values, and Krogstad's model, of course, the lowest value. It must be recalled that for self-similar boundary layers

$$H = \frac{1}{1 - G\sqrt{C_f/2}} \tag{27}$$

where G is constant for a zero pressure gradient boundary layer ($G \approx 6$) so that an increase of the skin friction coefficient leads to an increase of the shape factor. Different rankings on the skin friction and shape factor levels must be blamed on the turbulence model itself, which provides the value of G.

It must, however, be pointed out that differences in the shape factor values between experiments and computations may also reflect differences in the near wall region where the definition of the wall distance and, hence, the integration to compute integral thicknesses is questionable.

4.2.3 SRS2 Surface. This surface is rougher than the previous one. The reduced equivalent sand grain roughness h_s^+ is about 70, i.e., the border between the transition and fully rough regimes.

Although the reduced sand grain roughness is moderate, the skin friction increases by more than 60%. All models nearly predict the same skin friction, as shown in Fig. 8, in excellent agreement with experiments. Here, again, Wilcox's model gives slightly larger values, followed by Spalart and Allmaras' model, then by Smith's model; Krogstad's and Rotta's models predict the lowest levels. The shape factor evolution is also well reproduced, as shown in Fig. 9. The highest levels are obtained with Krogstad's and Rotta's models, a little above Wilcox's model, while Spalart and Allmaras' and Smith's models yield the lowest levels. Here, again, the influence of the turbulence model is retrieved, with the use of the mixing length model leading to higher shape factor values.

4.3 Blanchard's Experiments

4.3.1 Presentation. At ONERA, Blanchard [16] used sand paper or grids to generate rough surfaces. Only sand paper experiments, where the surface is closer to applications, are considered here.

Two surfaces, one with an average roughness height of 0.425 mm and the other one of 0.58 mm, are considered. For the first surface, an experiment without pressure gradient, for an external velocity of 45 m s^{-1}, and an experiment with decelerated flow are available. For the second surface, only a zero pressure gradient experiment is available. The Reynolds number R_θ ranges between 3000 and 10,000.

Velocity profiles were measured with hot wires. Skin friction was deduced from the velocity profiles, checked with turbulent stress measurements above the roughness elements and the balance of the von Kármán equation. Boundary layer integral thicknesses are tabulated in the thesis. Boundary layer profiles are available for the last experiment.

Blanchard gave some information about the roughness elements and proposed to model them as cones, with a base diameter to height ratio of 4/3. The roughness spacing L/h is estimated to be about 2.3. Finally, Blanchard proposed the sand grain roughness height to be half the average roughness height, which is not consistent with Dirling Jr.'s correlation using the above geometrical description. This value was used in all calculations.

4.3.2 0.425 mm *High Roughness: Zero Pressure Gradient Flow*. For this experiment, the reduced equivalent sand grain roughness h_s^+ is about 150, i.e., a fully rough regime.

Predictions of the skin friction coefficient and of the shape factor are plotted in Figs. 10 and 11. The roughness effect is important as the skin friction level doubles. Wilcox's, Smith's, and Krogstad's models predict the highest friction levels, in fair agreement with experiments, while Spalart and Allmaras' and Rotta's

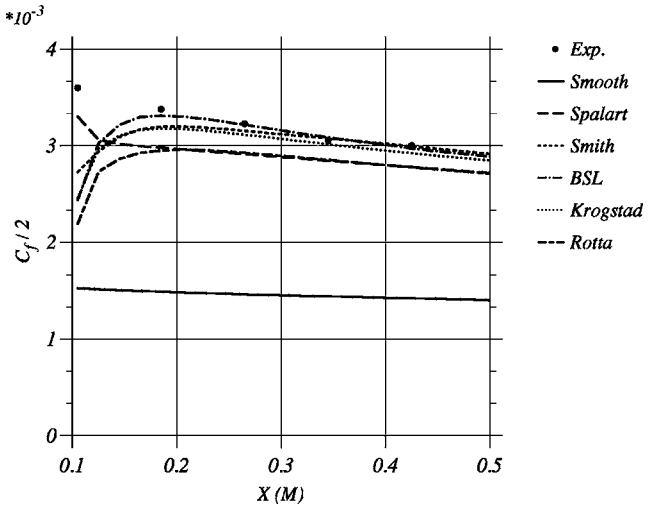

Fig. 10 Blanchard's experiments, roughness height of 0.425 mm, zero pressure gradient flow, predictions of the skin friction coefficient

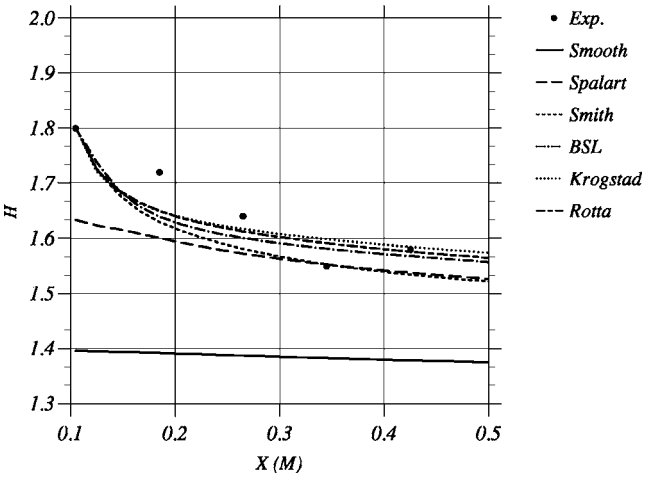

Fig. 11 Blanchard's experiments, roughness height of 0.425 mm, zero pressure gradient flow, predictions of the shape factor

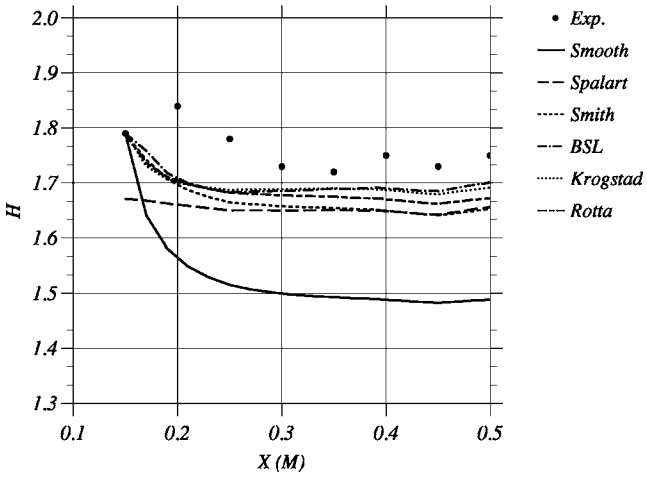

Fig. 13 Blanchard's experiments, roughness height of 0.425 mm, positive pressure gradient flow, predictions of the shape factor

models give slightly lower levels.

The shape factor increase is well reproduced by all models, the ranking being similar to the one obtained for the SRS2 surface.

4.3.3 0.425 mm *High Roughness: Positive Pressure Gradient Flow*. The roughness is the same as the previous one. Thanks to the flow deceleration, the h_s^+ level decreases, but the flow remains in the fully rough regime.

Predictions of the skin friction coefficient and of the shape factor are plotted in Figs. 12 and 13. Here, again, Smith's and Wilcox's models give the highest friction levels, in fair agreement with experiments. Krogstad's model is fair but decreases too quickly. Spalart and Allmaras' and Rotta's models give close predictions and slightly underestimate the friction level.

The same differences as the previous ones are observed on the shape factor, Smith's and Spalart and Allmaras' model giving similar results while Wilcox's, Krogstad's, and Rotta's models yielding higher values.

4.4 0.58 mm High Roughness: Zero Pressure Gradient Flow. For bigger roughness elements, the reduced sand grain height h_s^+ is about 200, still a fully rough regime, comparable to the third MSU experiment.

Predictions of the skin friction coefficient and of the shape factor are plotted in Figs. 14 and 15. The skin friction more than doubles. Wilcox's, Smith's, and Krogstad's models are in fair agreement with experiment; Spalart and Allmaras' and Rotta's models give lower friction levels.

Here, again, the agreement with the experimental shape factor is satisfactory, Wilcox's, Rotta's, and Krogstad's models giving similar levels while Smith's and Spalart and Allmaras' models slightly lower levels.

Velocity profiles at the last station are plotted in Fig. 16. Only the transport equation models are plotted for the sake of clarity. Nearly no differences can be observed between the three models; small differences can be observed with the mixing length models. The key difference between rough and smooth surfaces is due to the change in skin friction level since the velocity profile is self-similar in such an experiment without pressure gradient so that the velocity profile can be expressed as

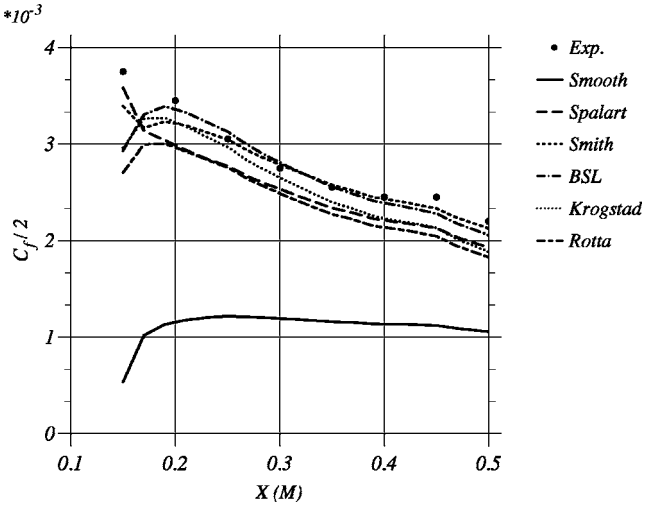

Fig. 12 Blanchard's experiments, roughness height of 0.425 mm, positive pressure gradient flow, predictions of the skin friction coefficient

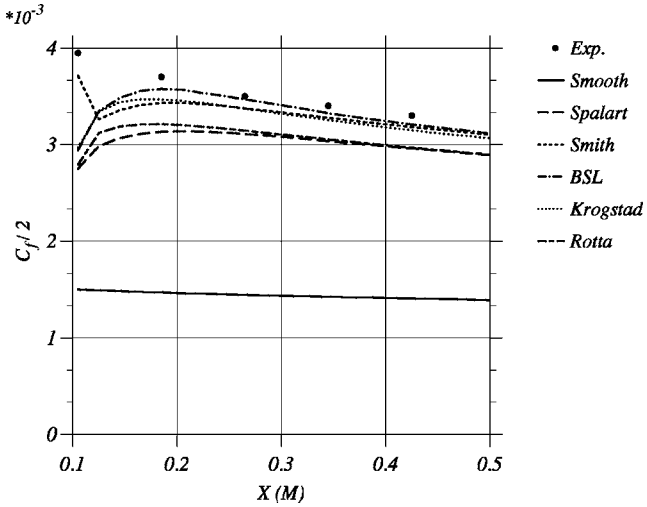

Fig. 14 Blanchard's experiments, roughness height of 0.58 mm, zero pressure gradient flow, predictions of the skin friction coefficient

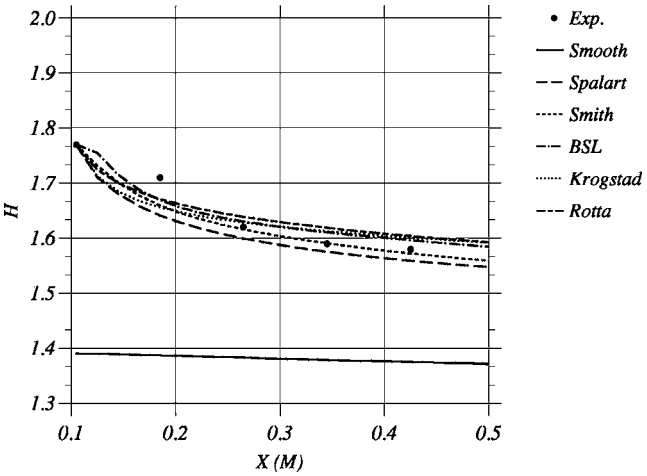

Fig. 15 Blanchard's experiments, roughness height of 0.58 mm, zero pressure gradient flow, predictions of the shape factor

$$\frac{u_e - u}{u_\tau} = f\left(\frac{y}{\delta}\right)$$

Hence, the agreement between model predictions and experimental data is good, except very close to the wall where results are more sensitive to slight differences in the definition of the wall distance between experiments and computations.

5 Conclusion

A general procedure was proposed to extend any turbulence model to account for wall roughness by forcing the model to reproduce the shift in the logarithmic region. This procedure was applied to Smith's *k-L* and Spalart and Allmaras' one-equation models.

Models were compared over a wide range of roughness and boundary layer Reynolds numbers. For all cases, Spalart and Allmaras' and Smith's model extensions give nearly identical predictions, which supports the logics of the proposed procedure. Application to an adverse pressure gradient test case tends to validate the procedure in the presence of pressure gradients. This is confirmed by comparison with new experimental results obtained at ONERA (to be published soon).

For small roughness elements, Krogstad's model is unable to correctly predict the roughness influence. This is a drawback of reproducing roughness effects only by altering the model damping functions. Over rougher walls ($h_s^+ \geqslant 50$), all the tested models give similar predictions as all were at least educated to reproduce the completely rough regime.

The agreement with experiments is generally fair, except for the MSU experiments in the transition regime. For these test cases, the equivalent sand grain roughness determined from Dirling Jr.'s correlation is not consistent with the experimental skin friction increase. This shows the need for more efficient correlations to determine the equivalent sand grain roughness as Dirling Jr.'s correlation heavily relies on academic roughness as the one used in the MSU experiment but fails to predict it correctly.

The model ranking, concerning skin friction levels, depends on the reduced sand grain roughness h_s^+, not on the boundary layer Reynolds number R_θ. This is not surprising as the roughness effect mainly affects the inner region of the boundary layer. Wilcox's model generally yields larger skin friction values.

Finally, it must be mentioned that the present extension of Smith's *k-L* model was implemented and validated in ONERA Navier–Stokes solver elsA.

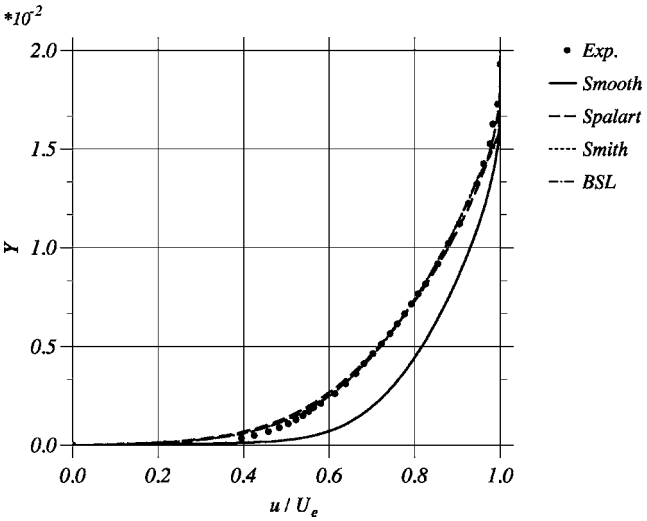

Fig. 16 Blanchard's experiments, roughness height of 0.58 mm, zero pressure gradient flow, predictions of the velocity profile

Acknowledgment

This work was partly supported by the research project "Unsteady Transitional Flows in Axial Turbomachines" funded by the European Commission under Contract No. G4RD-CT-2001-00628.

Nomenclature

Latin Alphabet

- C_f = skin friction coefficient
- d_0 = shift in wall distance
- h = roughness element height
- h_s = equivalent sand grain height
- k = turbulent kinetic energy
- L = turbulence length scale
- q = turbulent velocity scale ($q^2 = 2k$)
- u = longitudinal velocity component
- u_τ = friction velocity
- y = wall normal coordinate

Greek Alphabet

- Δu^+ = shift of the logarithmic region due to wall roughness
- ε = turbulent kinetic energy dissipation rate
- κ = von Kármán constant
- μ = viscosity
- μ_t = turbulent viscosity
- ρ = density
- τ_w = skin friction

Symbols

- $+$ = value in wall units
- e = value at the outer edge of the boundary layer
- r = value over a rough surface
- s = value over a smooth surface

References

[1] Nikuradse, J., 1933, "Strömungsgesetze in rauhen Rohren," VDI-Forschungsheft, Technical Report, No. 361.

[2] Patel, V. C., 1988, "Perspective: Flow at High Reynolds Number and Over Rough Surfaces—Achilles Heel of CFD," ASME J. Fluids Eng., **120**, pp. 434–444.

[3] Reijasse, P., Oswald, J., Aupoix, B., and Steinfeld, P., 1998, "Expert Evaluation of Ariane 502 Roll Causes," *Third European Symposium on Aerothermo-*

dynamics for Space Vehicles, Noordwijk, The Netherlands.
[4] Coleman, H. W., Hodge, B. K., and Taylor, R. P., 1983, "Generalized Roughness Effects on Turbulent Boundary Layer Heat Transfer—A Discrete Element Predictive Approach for Turbulent Flow over Rough Surfaces," Air Force Armament Laboratory, Mississippi State University, Report No. AFATL-TR-83-90.
[5] Aupoix, B., 1994, "Modelling of Boundary Layers Over Rough Surfaces," *Advances in Turbulence V*, R. Benzi, ed., Kluwer Academic Press, Sienna, pp. 16–20.
[6] Schlichting, H., 1936, "Experimentelle Untersuchungen zum Rauhigkeitsproblem," Ing.-Arch., **7**(1), pp. 1–34.
[7] Dirling, R. B., Jr., 1973, "A Method for Computing Rough Wall Heat Transfer Rates on Reentry Nosetips," *AIAA Eigth Thermophysics Conference*, Palm Springs, CA AIAA Paper No. 73–763.
[8] Grabow, R. M., and White, C. O., 1975, "Surface Roughness Effects on Nosetip Ablation Characteristics," AIAA J., **13**(5), pp. 605–609.
[9] van Driest, E. R., 1956, "On Turbulent Flow Near a Wall," J. Aeronaut. Sci., **23**(11), pp. 1007–1011.
[10] Krogstad, P. Å., 1991, "Modification of the van Driest Damping Function to Include the Effects of Surface Roughness," AIAA J., **29**(6), pp. 888–894.
[11] Chen, H. C., and Patel, V. C., 1988, "Near-Wall Turbulence Models for Complex Flows Including Separation," AIAA J., **26**(6), pp. 641–648.
[12] Durbin, P. A., Medic, G., Seo, J. M., Eaton, J. K., and Song, S., 2001, "Rough Wall Modification of Two-Layer k-ε," ASME J. Fluids Eng., **123**, pp. 16–21.
[13] Wilcox, D. C., 1988, "Reassessment of the Scale-Determining Equation for Advanced Turbulence Models," AIAA J., **26**(11), pp. 1299–1310.
[14] Zhang, H., Faghri, M., and White, J. K., 1996, "A New Low-Reynolds Number k-ε Model for Turbulent Flow Over Smooth and Rough Surfaces," ASME J. Fluids Eng., **118**, pp. 255–259.
[15] Rotta, J., 1962, "Turbulent Boundary Layers in Incompressible Flows," Prog. Aeronaut. Sci., **2**, pp. 73–82.
[16] Blanchard, A., 1977, "Analyse Expérimentale et Théorique de la Structure de la Turbulence d'une Couche Limite sur Paroi Rugueuse," Ph.D. thesis, Université de Poitiers U.E.R.-E.N.S.M.A.
[17] Aupoix, B., and Spalart, P. R., 2003, "Extensions of the Spalart–Allmaras Turbulence Model to Account for Wall Roughness," Int. J. Heat Fluid Flow, **24**, pp. 454–462.
[18] Spalart, P. R., and Allmaras, S. R., 1992, "A One-Equation Turbulence Model for Aerodynamic Flows," *30th Aerospace Sciences Meeting and Exhibit*, Reno, NV, AIAA Paper No. 92–0439.
[19] Spalart, P. R., and Allmaras, S. R., 1994, "A One-Equation Turbulence Model for Aerodynamic Flows," Rech. Aerosp., **1**, pp. 5–21.
[20] Dipprey, D. F., and Sabersky, R. H., 1963, "Heat and Momentum Transfer in Smooth and Rough Tubes at Various Prandtl Numbers," Int. J. Heat Mass Transfer, **6**, pp. 329–353.
[21] Smith, B. R., 1990, "The k-kl Turbulence Model and Wall Layer Model for Compressible Flows," *21st Fluid and Plasma Dynamics Conference*, Seattle, WA, AIAA Paper No. 90–1483.
[22] Smith, B. R., 1995, "Prediction of Hypersonic Shock Wave Turbulent Boundary Layer Interactions with the k-l Two Equation Turbulence Model," *33rd Aerospace Sciences Meeting and Exhibit*, Reno, NV, AIAA Paper No. 95–0232.
[23] Prasad, R. O. S., and Hassan, H. A., 1998, "An Evaluation of the Two-Equation k-l Model for Simple Shear Flows," *36th Aerospace Science Meeting and Exhibit*, Reno, NV, AIAA Paper No. 98–0321.
[24] Ferrey, P., and Aupoix, B., 2006, "Behaviour of Turbulence Models Near a Turbulent/Non-Turbulent Interface," Int. J. Heat Fluid Flow, **27**(5), pp. 831–837.
[25] Smith, B. R., 1997, "A Non-Equilibrium Turbulent Viscosity Function for the k-l Two Equation Turbulence Model," *28th AIAA Fluid Dynamics Conference, Fourth Shear Flow Control Conference*, Snowmass Village, CO, AIAA Paper No. 97–1959.
[26] Aupoix, B., 1999, "Couches Limites Bidimensionnelles Compressibles. Descriptif et Mode d'Emploi du Code CLIC 2," DMAE, ONERA, Final Report No. R. F. 1/5620.02-1/5620.05.
[27] Menter, F. R., 1994, "Two-Equation Eddy-Viscosity Turbulence Models for Engineering Applications," AIAA J., **32**(8), pp. 1598–1605.
[28] Scaggs, W. F., Taylor, R. P., and Coleman, H. W., 1988, "Measurement and Prediction of Rough Wall Effects on Friction Factor: Uniform Roughness Results," ASME J. Fluids Eng., **110**, pp. 385–391.
[29] Taylor, R. P., Coleman, H. W., and Hodge, B. K., 1985, "Prediction of Turbulent Rough-Wall Skin Friction Using a Discrete Element Approach," ASME J. Fluids Eng., **107**, pp. 251–257.
[30] Hosni, M. H., Coleman, H. W., and Taylor, R. P., 1989, "Measurements and Calculation of Surface Roughness Effects on Turbulent Flow and Heat Transfer," Thermal and Fluid Dynamics Laboratory, Mechanical and Nuclear Engineering Department, Mississippi State University, Technical Report No. TFD-89-1.
[31] Hosni, M. H., Coleman, H. W., and Taylor, R. P., 1991, "Measurements and Calculations of Rough-Wall Heat Transfer in the Turbulent Boundary Layer," Int. J. Heat Mass Transfer **34**(4/5), pp. 1067–1082.
[32] Hosni, M. H., Coleman, H. W., Gardner, J. W., and Taylor, R. P., 1993, "Roughness Element Shape Effects on Heat Transfer and Skin Friction in Rough-Wall Turbulent Boundary Layer," Int. J. Heat Mass Transfer, **36**(1), pp. 147–153.
[33] Chakroun, W., 1992, "Experimental Investigation of the Effects of Acceleration on Flow and Heat Transfer in the Turbulent Rough-Wall Boundary Layer," Ph.D. thesis, Mississippi State University.
[34] Chakroum, W., and Taylor, R. P., 1993, "Heat Transfer and Fluid Dynamics Measurements in Accelerated Rough-Wall Boundary Layer," *ASME International Gas Turbine and Aeroengine Congress and Exposition*, Cincinnati, OH.
[35] Acharya, M., Bornstein, J., and Escudier, M. P., 1986, "Turbulent Boundary Layers on Rough Surfaces," Exp. Fluids, **4**(1), pp. 33–47.
[36] Tarada, F. H. A., 1987, "Heat Transfer to Rough Turbine Blading," Ph.D. thesis, University of Sussex.

Friction Factor Directly From Transitional Roughness in a Turbulent Pipe Flow

Noor Afzal
Department of Mechanical Engineering,
Aligarh University,
Aligarh 202002, India
e-mail: noor.afzal@yahoo.com

The friction factor data from transitional rough test pipes, from the measurements of Sletfjerding and Gudmundsson (2003, "Friction Factor Directly From Roughness Measurements," J. Energy Resour. Technol. ***125****, pp. 126–130), have been analyzed in terms of directly measurable roughness parameters, R_a the arithmetic mean roughness, R_Z the mean peak to valley heights roughness, R_q the root mean square (rms) roughness, and R_q/H rms textured roughness (H, the Hurst exponent is a texture parameter), in addition to h the equivalent sand grain roughness. The proposed friction factor λ, in terms of new scaling parameter, viz., the roughness Reynolds number $\mathrm{Re}_\phi=\mathrm{Re}/\phi$ (where ϕ is a nondimensional roughness scale), is a universal relation for all kinds of surface roughness. This means that Prandtl's smooth pipe friction factor relation would suffice provided that the traditional Reynolds number Re is replaced by the roughness Reynolds number Re_ϕ. This universality is very well supported by the extensive rough pipe data of Sletfjerding and Gudmundsson, Shockling's (2005, "Turbulence Flow in Rough Pipe," MS thesis, Princeton University) machined honed pipe surface roughness data, and Nikuradse's (1933, Laws of Flow in Rough Pipe, VDI, Forchungsheft No. 361) sand grain roughness data. The predictions for the roughness function ΔU_+, and the roughness scale ϕ for inflectional roughness compare very well with the data of the above mentioned researchers. When surface roughness is present, there is no universality of scaling of the friction factor λ with respect to the traditional Reynolds number Re, and different expressions are needed for various types of roughnesses, as suggested, for example, with inflectional roughness, monotonic roughness, etc. In traditional variables, the proposed friction factor prediction for inflectional roughness in the pipes, is supported very well by the experimental data of Sletfjerding and Gudmundsson, Shockling, and Nikuradse. In the present work, the predictions of friction factor as implicit relations, as well as approximate explicit relations, have also been proposed for various roughness scales.*
[DOI: 10.1115/1.2776961]

Keywords: friction factor, turbulent flow, wall roughness, universal relations, pressure drop, natural gas

1 Introduction

In fully developed turbulent flow in a smooth pipe, the friction factor λ is the function of Reynolds number Re, where $\mathrm{Re}=U_b d/\nu$ and

$$\lambda = -\frac{dp}{dx}\frac{2d}{\rho U_b^2} = \frac{8\tau_w}{\rho U_b^2} = 8\left(\frac{u_\tau}{U_b}\right)^2 \tag{1}$$

Here, U_b is the velocity averaged over the pipe cross-sectional area, $\delta=a$ is the pipe radius, $d=2a$ is the pipe diameter, ν is the kinematic viscosity, τ_w is the wall shear stress, ρ is the fluid density, dp/dx is the pressure drop per unit length, and $u_\tau=\sqrt{\tau_w/\rho}$ is the friction velocity. The Reynolds number $\mathrm{Re}=U_b d/\nu$ based on average velocity U_b and pipe diameter d is the characteristic parameter of the flow.

The wall roughness in turbulent flow is often a dominating effect in the friction factor. In offshore gas pipelines, for example, where the Reynolds number is of the order of 10^7, the wall roughness contributes the most to the pipeline pressure drop. In such pipelines, it is a common practice to apply a coating on pipe walls to reduce wall roughness and thus the pressure drop. Similarly, in flow past merchant ships where the viscous drag dominates the resistance, the wall roughness also significantly increases the drag. The friction factor for transitional rough pipes has been proposed from various sources [1–8]. The sand grain-type inflectional roughness friction factor data were presented by Nikuradse [1]. For monotonic (Colebrook) roughness, the implicit friction factor expression was proposed by Colebrook [2], which has been extensively considered in the literature. Barr [5] proposed explicit approximate expression for monotonic roughness of Colebrook [2] (see also Refs. [6,7]). Alternate, approximate expressions for friction factor were also proposed by Sletfjerding [3], Sletfjerding and Gudmundsson [4], and Haaland [8], but the inflectional-type roughness data were not satisfactorily described, which is also a subject of present work. Moreover, these relations are based on Karman constant of about $k=0.4$ from smooth pipe data (Ref. [9]), but recent proposal $k=0.432$ (Ref. [10]) from superpipe is also considered here.

Warburton [11] measured the peak to valley roughness height R_Z, for prediction of the friction factor due to roughness of a graphite surface. Sletfjerding [3] and Sletfjerding and Gudmundsson [4] measured the surface roughness in the pipe using a profilometer (Perthometer SP3), having a stylus radius of 5 mm (immediately after the flow tests measured the profile). The roughness profiles were measured at the bottom of the pipe along the axial direction. The standard roughness parameters such as R_a the arithmetic mean roughness, R_Z the mean peak to valley height roughness, R_q the root mean square (rms), and H the Hurst exponent (a

Contributed by the Fluids Engineering Division of ASME for publication in the JOURNAL OF FLUIDS ENGINEERING. Manuscript received June 25, 2006; final manuscript received May 16, 2007. Review conducted by Ugo Piomelli

texture parameter) based on various tested pipes are tabulated in Table 1 of Ref. [4]. The roughness parameters are mean values of hundred samples. In the table, the coated pipes are listed according to increasing bead size of the coating. The roughness parameters generally increase with increasing bead size. The slope of the power spectral density (PSD) function (the Hurst exponent) is a measure of the rate of change of the mean square value of the profile roughness and is essentially a texture measure. The Hurst exponent H may be combined with the rms-roughness parameter R_q to form a roughness measure R_q/H=HT roughness (containing both a height measure and a texture measure). The experimental data of Sletfjerding [3] and Sletfjerding and Gudmundsson [4] do not include data in the transition region between smooth and rough flows. Further experimental work is needed to verify the behavior of the friction factor in the transition region at high Reynolds numbers. Nevertheless, departure of their data from the fully rough pipe relationship may throw some light on inflectional roughness, Colebrook monotonic roughness, or any other type of roughness.

The present work deals with alternative new transitional roughness scales, such as the nondimensional roughness scale ϕ (which is associated with the roughness function ΔU_+ of Clauser [12] and Hama [13]), transitional roughness inner variable $\zeta=Z_+/\phi$, roughness friction Reynolds number $R_\phi=R_\tau/\phi$, and roughness Reynolds number $\mathrm{Re}_\phi=\mathrm{Re}/\phi$ (Ref. [14]). The predictions of velocity profile and friction factor are universal, explicitly independent of transitional pipe roughness. For inflectional-type roughness, the prediction of roughness function ΔU_+ and roughness scale ϕ compare well with the data. The friction factor in traditional variables proposed for inflectional-type roughness is not a universal relation, which compares with the entire data very well. The transitional pipe roughness data of Sletfjerding [3] and Sletfjerding and Gudmundsson [4] with respect to alternate roughness parameters R_a, R_Z, R_q, and R_q/H have been correlated with h, which is the equivalent sand grain roughness of Nikuradse [1]. The friction factor based on the alternate roughness parameters R_a, R_q, R_Z, and R_q/H has been proposed for transitional roughness in pipes.

2 Transitional Roughness in Pipes

The roughness function ΔU_+ is a useful descriptor of the surface roughness effects on mean velocity distribution above the sublayer in the inner region. It is a physical representation of the roughness dominated shift in the velocity profile of the smooth wall law. For $\Delta U_+>0$, the shift is downward due to increase of drag and for $\Delta U_+<0$, the shift is upward due to reduction of the drag on the rough surface. Clauser [12] and Hama [13] introduced the term roughness function ΔU_+ as an additional term to the smooth wall log law, for the description of the transitional rough wall region. This also remains valid for the power law (or any other law) that describes the velocity profile (Ref. [14]). The overall description of turbulent flows is in terms of two length scales of the inner and outer layers. Based on dimensional analysis, the inner region and outer wake region scales are considered.

The traditional velocity distribution and skin friction logarithmic laws on a transitional rough wall are the sum of the roughness function ΔU_+ and the smooth wall log law (Refs. [15–17])

$$\frac{u}{u_\tau}=\frac{1}{k}\ln Z_+ + B - \Delta U_+ + DW(Y) \tag{2}$$

$$\frac{U_c}{u_\tau}=\frac{1}{k}\ln R_\tau + B - \Delta U_+ + D \tag{3}$$

where $Z_+=Zu_\tau/\nu$ is the wall variable, $Y=Z/\delta$ is the outer variable, and ΔU_+ is the roughness function. Here, u is the axial velocity at a distance y from the pipe surface of radius $\delta=a$. The function $W(Y)$ is the Coles wake function with the boundary conditions $W(0)=0$ and $W(1)=1$. The normal coordinate is $Z=y+\epsilon_r$, where ϵ_r is the origin of the normal coordinate on the rough surface, caused by irregular protrusions of the hydraulic roughness of height h. It is a particular level between the protrusion peaks and valleys, which automatically satisfies the constraints $0<\epsilon_r<h$ and $\epsilon_r=0$ for a fully smooth surface. Further, $R_\tau=u_\tau\delta/\nu$ is the roughness Reynolds number, $u_\tau=\sqrt{\tau_w/\rho}$ is the friction velocity, U_c is the velocity at pipe centerline, k is the Karman constant, B is the additive term in the log law for smooth surface, and D is the additive term in the outer velocity defect log law. In terms of fully rough wall variable δ/h, the skin friction law (3) becomes

$$\frac{U_c}{u_\tau}=\frac{1}{k}\ln\left(\frac{\delta}{h}\right)+B_T+D \tag{4}$$

and the roughness function is given by the relation

$$\Delta U_+=\frac{1}{k}\ln h_+ + B - B_T \tag{5}$$

Here, $B_T=B_T(h_+)$ is the additive term in transitional rough surface log law of the wall and for fully rough surfaces, $B_T=B_F$ is a constant.

At this stage, we introduce here new variable ζ for the transitional rough wall variable and three parameters R_ϕ the roughness friction Reynolds number and Re_ϕ, the roughness Reynolds number defined as

$$\zeta=\frac{Z_+}{\phi}\quad R_\phi=\frac{R_\tau}{\phi}\quad \mathrm{Re}_\phi=\frac{\mathrm{Re}}{\phi} \tag{6}$$

where roughness scale ϕ is connected to the roughness function ΔU_+ as

$$\phi=\exp(k\Delta U_+)\quad \Delta U_+=\frac{1}{k}\ln\phi \tag{7}$$

From the relations (6) and (7), the velocity profile log law (2) and skin friction log law (3) become

$$\frac{u}{u_\tau}=\frac{1}{k}\ln\zeta + B + DW(Y) \tag{8}$$

$$\frac{U_c}{u_\tau}=\frac{1}{k}\ln R_\phi + B + D \tag{9}$$

which are the universal relations for all types of surface roughness. The integration of composite wall-wake velocity profile (8) yields the sectional average velocity U_b and the friction factors (3) in the light of relations (6) and (7) become

$$\sqrt{\frac{8}{\lambda}}=\frac{1}{k}\ln\left(\mathrm{Re}_\phi\sqrt{\frac{\lambda}{32}}\right)+B+D-D_b \tag{10}$$

$$\sqrt{\frac{8}{\lambda}}=\frac{1}{k}\ln\left\{\frac{\delta}{h}\exp[k(B_T-B)]\right\}+B+D-D_b \tag{11}$$

where

$$U_b=U_c-u_\tau D_b\quad D_b=\frac{3}{2k}+\frac{\Pi}{k}\left[W(1)-2\int_0^1(1-Y)W(Y)dY\right] \tag{12}$$

The power law velocity profile and the power law friction factor, as a function of the frictional Reynolds number R_τ, as well as the roughness friction Reynolds number Re_ϕ, may also now be considered. These relations for transitional wall roughness are obtained from addition of the roughness function ΔU_+ and the smooth wall power law relations as

$$\frac{u}{u_\tau}=C_pZ_+^\gamma+E\Omega(Y)-\Delta U_+ \tag{13}$$

$$\frac{U_c}{u_\tau} = C_p R_\tau^\gamma + E - \Delta U_+ \tag{14}$$

where γ is the power index and C_p is the power law prefactor for fully smooth surfaces (Refs. [14,18]). The function $\Omega(Y)$ is the power law wake function with the boundary conditions $\Omega(0)=0$ and $\Omega(1)=1$. The power law velocity profile and power law friction factor for a transitional rough surface proposed by Afzal et al. [14] are universal relations, explicitly independent of transitional pipe roughness, stated below, viz.,

$$\frac{u}{u_\tau} = A_p \zeta^\alpha + E\Omega(Y) \tag{15}$$

$$\frac{U_c}{u_\tau} = A_p R_\phi^\alpha + E \tag{16}$$

It may be pointed out that based on the roughness scale (7), the power law velocity profile (13) and power law friction factor (14) do not yield the proposed universal power laws (15) and (16), but the traditional velocity profile log law (2) and friction factor log law (3) do yield the proposed universal log laws (8) and (9). The envelope of power law friction factor (16) with $A_p = a/\alpha + b$ yields [14]

$$\alpha = \frac{\Gamma}{\ln R_\phi} \tag{17a}$$

$$A_p = \left(\frac{\Gamma}{k\alpha} + B\right)\exp(-\Gamma) \tag{17b}$$

$$\Gamma = \left(1 + \frac{kB}{\ln R_\phi}\right)^{-1} \tag{17c}$$

where power index $\alpha = \alpha(R_\phi)$ and prefactor $A_p = A_p(R_\phi)$ are universal relations, explicitly independent of transitional surface roughness. Further, the envelope of the skin friction power law (16) also gives the skin friction log law [14] as follows:

$$\frac{U_c}{u_\tau} = k^{-1} \ln R_\phi + B + E \tag{18}$$

where

$$k^{-1} = \frac{a}{\Gamma}\exp(\Gamma) \tag{19a}$$

$$B = b\exp(\Gamma) \tag{19b}$$

Here, the constants k and B, from power law theory, depend on Γ, which in turn depends on the Reynolds number. For large Reynolds numbers $R_\phi \to \infty$ the function $\Gamma \to 1$ and k and B relations (19*a*) and (19*b*) become universal constants independent of Reynolds number, and the power law theory becomes equivalent to log law theory.

The power law velocity profile (15) may be integrated over the entire cross section (say, a pipe of radius δ) to obtain the bulk averaged velocity

$$\frac{U_b}{u_\tau} = 2\int_0^\delta (1-Y)u_+ dY = R_\phi^\alpha \frac{2A_p}{(1+\alpha)(2+\alpha)} + E_b \tag{20}$$

where

$$E_b = 2E\int_0^1 (1-Y)\Omega(Y)dY \tag{21}$$

The friction factor power law equation (20) may also be expressed as

$$\lambda = 8\left[\frac{2A_p}{(1+\alpha)(2+\alpha)}R_\phi^\alpha + E_b\right]^{-2} \tag{22}$$

In fully developed turbulent pipe flow, the outer wake is weak ($E_b \approx 0$) and the expression (22) is simplified as

$$\lambda = 8\left[\frac{2^{\alpha-1}}{A_p}(1+\alpha)(2+\alpha)\mathrm{Re}_\phi^{-\alpha}\right]^{2/(1+\alpha)} \tag{23}$$

where $n = 2\alpha/(1+\alpha)$ is the friction factor power law index. For fully smooth pipe, $\phi = 1$ and $\mathrm{Re}_\phi = \mathrm{Re}$ and fully rough flows, $\phi = h_+$ and $\mathrm{Re}_\phi = \delta/h$, and in transitional pipe roughness, $\mathrm{Re} \leqslant \mathrm{Re}_\phi \leqslant \delta/h$. Further, for specific value $\alpha = 1/7$ or $n = 1/4$, the power law friction factor (23) for transitional rough pipes becomes

$$\lambda = \frac{0.3164}{\mathrm{Re}_\phi^{1/4}} \tag{24}$$

where numerical constant 0.3164 is adopted from Blasius (see Ref. [19]) power law for fully smooth pipes valid in a domain $3 \times 10^3 < \Re_\phi < 2 \times 10^5$. The power law friction factor is not further considered here and the literature on power law relations is described elsewhere [14].

The friction factor log laws (10) for transitional roughness in pipes, based on Prandtl's [2] choice of the constants for fully smooth pipe data of Nikuradse [20] over the Reynolds number range $3.1 \times 10^3 < \mathrm{Re} < 3.2 \times 10^6$, are given below:

$$\frac{1}{\sqrt{\lambda}} = 2\log_{10}(\mathrm{Re}\sqrt{\lambda}) - 0.8 - \Delta U_+ \tag{25a}$$

$$\frac{1}{\sqrt{\lambda}} = 2\log_{10}(\mathrm{Re}_\phi\sqrt{\lambda}) - 0.8 \tag{25b}$$

where, in particular, $A = [k\sqrt{8}\log_{10}(e)]^{-1} = 2$. For Reynolds numbers greater than about 10^6, the Princeton's superpipe data of McKeon [10] lie a little above this line for smooth pipe flow. Based on the proposal of McKeon [10], for smooth pipe constants, the alternate correlation for transitional pipe roughness becomes

$$\frac{1}{\sqrt{\lambda}} = 1.93\log_{10}(\mathrm{Re}\sqrt{\lambda}) - 0.537 - \Delta U_+ \tag{26a}$$

$$\frac{1}{\sqrt{\lambda}} = 1.93\log_{10}(\mathrm{Re}_\phi\sqrt{\lambda}) - 0.537 \tag{26b}$$

It may be pointed out that the three layer theory (with mesolayer) by Afzal [21] proposed the friction factor, which for transitional rough pipes becomes

$$\frac{1}{\sqrt{\lambda}} = A\log_{10}(\mathrm{Re}\sqrt{\lambda}) + b_1 - \Delta U_+ \quad \frac{1}{\sqrt{\lambda}} = A\log_{10}(\mathrm{Re}_\phi\sqrt{\lambda}) + b_1 \tag{27}$$

$$A = \frac{1}{\sqrt{32}\log_{10} e}(A_i + A_o) \approx 3 \tag{28}$$

where $A_o = 1/k = 2.5$ and $A_i = 5$ are, respectively, the slopes of the log law velocity profile in the mesolayer at its two asymptotic ends, and which matches with inner and outer layers (see also Ref. [22]). If $A_i = A_0 = 1/k$, the mesolayer becomes trivial where friction factor equations (27) and (28) yield two layer theory friction factor equation (10). The implication of this mesolayer on higher order low Reynolds number effects is also analyzed later in this work.

Roughness Function. It has been pointed out by Bendrict [17] (see also Ref. [23]) that one of the amazing fortuitous happenings in engineering, and a tribute to Colebrook's [2] insight is the simple addition of two limiting expressions associated with the log terms in the friction factors for fully smooth and fully rough

pipes that predict a transitional friction factor increasing monotonically with h_+. The roughness scale ϕ for the Colebrook [2] commercial pipe roughness corresponds to $\phi=1+\chi h_+$, with $\chi=\exp[k(B-B_F)]=0.306$, $B=5.5$, and $B_F=8.5$, giving the well known friction factor plot of Moody [24]. Other values of χ were also proposed by Yen [25] for open channel flows, and Grigson [26] for different types of finish on hull surfaces of ships. Grigson [26] also represented the roughness scale by a power series $\phi=1+\Sigma_{n=1}^{m} b_n h_+^n$, and the coefficients b_n were fitted to the data. Sletfjerding [3], Sletfjerding and Gudmundsson [4], and Haaland [8] also modified the Colebrook friction factor relation.

The inflectional roughness data of Nikuradse [1] have been analyzed by Loselevich and Pilipenko (see Ref. [27]) to suggest a correlation. In the present work, dealing with inflectional roughness in pipes, a simple expression for the roughness scale ϕ is proposed by introducing an exponential function $\exp(-j/h_+)$ in the Colebrook [4] relation, viz., $\phi=1+\chi h_+$ and $\chi=\exp[k(B-B_F)]$ to yield

$$\phi = 1 + \chi h_+ \exp\left(-\frac{j}{h_+}\right) \tag{29a}$$

$$\Delta U_+ = \frac{1}{k} \ln \phi \tag{29b}$$

where $j=0$ corresponds to the Colebrook monotonic commercial roughness and $j\neq 0$ is a free parameter. The relation (29) for the roughness scale ϕ, for $j\neq 0$, has a point of inflection at the origin $h_+=0$. Further, the exponential function in the relation (18) approaches unity for $h_+\to\infty$ and zero for $h_+\to 0$, which, respectively, maintain the traditional friction factor relations of Nikuradse [1] for fully rough pipes and for that of Prandtl [9] for fully smooth pipes. For inflectional type roughness, the choice $j=11$ has been obtained by curve fitting the data of Sletfjerding [3], Nikuradse [1], Shockling [28], and Shockling et al. [29]. The alternate roughness parameters R_a, R_Z, R_q, and R_q/H have been measured for test pipes by Sletfjerding [3] and the data are described in Table 1 by Sletfjerding [3] and Sletfjerding and Gudmundsson [4], but they proposed no correlations with h, the equivalent sand grain roughness [1].

The friction factor (10) for inflectional roughness may be expressed in traditional variables by using the roughness function (29) in terms of the Reynolds number $\mathrm{Re}=U_b d/\nu$ and becomes

$$\sqrt{\frac{8}{\lambda}} = -\frac{1}{k} \ln\left\{ \exp[-k(B+D+D_b)]\left[\frac{1}{\mathrm{Re}}\sqrt{\frac{32}{\lambda}} + \chi \frac{h}{\delta} \exp\left(-\frac{j}{\mathrm{Re}}\sqrt{\frac{32}{\lambda}}\frac{\delta}{h}\right)\right]\right\} \tag{30}$$

In terms of the rough wall parameter δ/h, the friction factor Eq. (11) may also be expressed as

$$\frac{1}{\sqrt{\lambda}} = \frac{1}{k\sqrt{8}} \ln\left(\frac{\delta}{h}\right) + b_T \tag{31}$$

$$b_T = \frac{1}{\sqrt{8}}(B_T + D - D_b) \tag{32}$$

$$B_T = B - \frac{1}{k} \ln\left[\frac{1}{h_+} + \chi \exp\left(-\frac{j}{h_+}\right)\right] \tag{33}$$

The friction factor equation (25) from roughness function (29) or Eq. (30), based on smooth pipe constants of Prandtl [9], becomes

$$\frac{1}{\sqrt{\lambda}} = -2 \log_{10}\left[\frac{2.51}{\mathrm{Re}\sqrt{\lambda}} + \frac{h}{3.7\delta} \exp\left(-j\frac{5.66}{\mathrm{Re}\sqrt{\lambda}}\frac{\delta}{h}\right)\right] \tag{34}$$

Based on smooth pipe constants from McKeon [10] and relation (26) or (30), the friction factor becomes

$$\frac{1}{\sqrt{\lambda}} = -1.93 \log_{10}\left[\frac{1.90}{\mathrm{Re}\sqrt{\lambda}} + \frac{h}{3.7\delta} \exp\left(-j\frac{5.66}{\mathrm{Re}\sqrt{\lambda}}\frac{\delta}{h}\right)\right] \tag{35}$$

The explicit approximate relation for the friction factor (34) becomes

$$\frac{1}{\sqrt{\lambda}} = -2 \log_{10}\left[\frac{5.74}{\mathrm{Re}^{0.9}} + \frac{h}{3.7\delta} \exp\left(-j\frac{12.91}{\mathrm{Re}^{0.9}}\frac{\delta}{h}\right)\right] \tag{36}$$

and the friction factor (35) becomes

$$\frac{1}{\sqrt{\lambda}} = -1.932 \log_{10}\left[\frac{4.22}{\mathrm{Re}^{0.9}} + \frac{h}{3.7\delta} \exp\left(-j\frac{9.50}{\mathrm{Re}^{0.9}}\frac{\delta}{h}\right)\right] \tag{37}$$

The above relations with $j=11$ fit well with the inflectional roughness data. For monotonic roughness ($j=0$) Eq. (34) yields the Colebrook [2] friction factor relation and the explicit approximate equation (36) yields the friction factor proposed by Barr [5], Churchill [6], and Swamee and Jain [7]. Furthermore, for fully smooth pipes, the explicit approximate friction factor equation (36) yields [2]

$$\frac{1}{\sqrt{\lambda}} = -2 \log_{10}\left(\frac{5.74}{\mathrm{Re}^{0.9}}\right) \tag{38}$$

which describe the data for $5\times 10^3 \leqslant \mathrm{Re} \leqslant 10^8$ and the explicit approximate friction factor equation (37) yields [3]

$$\frac{1}{\sqrt{\lambda}} = -1.932 \log_{10}\left(\frac{4.22}{\mathrm{Re}^{0.9}}\right) \tag{39}$$

The above equations (38) and (39) would be used in Table 1, while dealing with explicit approximate friction factor relations for various types of transitional roughness.

3 Second Order Effects

The Reynolds equations of mean momentum in a turbulent flow are open equations containing the unknown Reynolds stress tensor. In dealing with open equations for turbulent motion, without any closure models based on eddy viscosity, mixing length, $k-\epsilon$, etc., it is not easy to access the higher order effects. The extension of Izakson–Millikan argument for moderately large Reynolds numbers requires the order of knowledge of the higher order effect (Ref. [30]). Furthermore, for lower Reynolds numbers, it is not known to what order the Izakson [31] and Millikan [32] argument is valid. For fully developed turbulent flow in a pipe or channel, the higher order effect of order ϵ was postulated by Afzal [30]. Later, from the mesolayer theory, it was postulated by Afzal [21,22] that the higher order effect is of order $\sqrt{\epsilon}$. The analysis of higher order effects in a fully developed turbulent pipe flow, following Refs. [21,22,28], gives the friction factor as follows:

$$\frac{1}{\sqrt{\lambda}} = -(A + A_{1/2}\sqrt{\epsilon} + A_1\epsilon + \cdots)\log \epsilon + C + C_{1/2}\sqrt{\epsilon} + C_1\epsilon + \cdots \tag{40}$$

$$\epsilon^{-1} = \mathrm{Re}_\phi \sqrt{\lambda} \quad R_\phi = \frac{\mathrm{Re}}{\phi} \tag{41}$$

As an engineering approximation, the slope of the log law may be considered to be independent of the Reynolds number (Refs. [30,33,34]) implying $A_{1/2}=A_1=0$, and thus the friction factor becomes

$$\frac{1}{\sqrt{\lambda}} = A \log(\mathrm{Re}_\phi\sqrt{\lambda}) + C + \frac{C_{1/2}}{(\mathrm{Re}_\phi\sqrt{\lambda})^{1/2}} + \frac{C_1}{\mathrm{Re}_\phi\sqrt{\lambda}} + \cdots \tag{42}$$

Afzal [30] regarded that the second order effects are of order ϵ, which implies $C_{1/2}=0$, whereupon the friction factor becomes

Table 1 Roughness scale and friction factor in fully rough and transitional rough pipes

Scale	Friction factor for fully rough pipes	Friction factor for transitional rough pipes implicit and approximate explicit expressions	
R_q	$\frac{1}{\sqrt{\lambda}}=-2\log_{10}\left(\frac{R_q}{0.7\delta}\right)$	$\frac{1}{\sqrt{\lambda}}=-2\log_{10}\left[\frac{2.51}{\mathrm{Re}\sqrt{\lambda}}+\frac{R_q}{0.7\delta}\exp\left(-j\frac{1.062}{\mathrm{Re}\sqrt{\lambda}}\frac{\delta}{R_q}\right)\right]$	1a
		$\frac{1}{\sqrt{\lambda}}=-2\log_{10}\left[\frac{5.74}{\mathrm{Re}^{0.9}}+\frac{R_q}{0.7\delta}\exp\left(-j\frac{2.58}{\mathrm{Re}^{0.9}}\frac{\delta}{R_q}\right)\right]$	1b*
R_Z	$\frac{1}{\sqrt{\lambda}}=-2\log_{10}\left(\frac{R_Z}{3\delta}\right)$	$\frac{1}{\sqrt{\lambda}}=-2\log_{10}\left[\frac{2.51}{\mathrm{Re}\sqrt{\lambda}}+\frac{R_Z}{3\delta}\exp\left(-j\frac{4.55}{\mathrm{Re}\sqrt{\lambda}}\frac{\delta}{R_Z}\right)\right]$	2a
		$\frac{1}{\sqrt{\lambda}}=-2\log_{10}\left[\frac{5.74}{\mathrm{Re}^{0.9}}+\frac{R_Z}{3\delta}\exp\left(-j\frac{10.41}{\mathrm{Re}^{0.9}}\frac{\delta}{R_Z}\right)\right]$	2b*
R_a	$\frac{1}{\sqrt{\lambda}}=-2\log_{10}\left(\frac{R_a}{0.57\delta}\right)$	$\frac{1}{\sqrt{\lambda}}=-2\log_{10}\left[\frac{2.51}{\mathrm{Re}\sqrt{\lambda}}+\frac{R_a}{0.57\delta}\exp\left(-j\frac{0.754}{\mathrm{Re}\sqrt{\lambda}}\frac{\delta}{R_a}\right)\right]$	3a
		$\frac{1}{\sqrt{\lambda}}=-2\log_{10}\left[\frac{5.74}{\mathrm{Re}^{0.9}}+\frac{R_a}{0.57\delta}\exp\left(-j\frac{1.724}{\mathrm{Re}^{0.9}}\frac{\delta}{R_a}\right)\right]$	3b*
R_q/H	$\frac{1}{\sqrt{\lambda}}=-2\log_{10}\left(\frac{R_q/H}{0.5\delta}\right)$	$\frac{1}{\sqrt{\lambda}}=-2\log_{10}\left[\frac{2.51}{\mathrm{Re}\sqrt{\lambda}}+\frac{R_q/H}{0.5\delta}\exp\left(-j\frac{0.754}{\mathrm{Re}\sqrt{\lambda}}\frac{\delta}{R_q/H}\right)\right]$	4a
		$\frac{1}{\sqrt{\lambda}}=-2\log_{10}\left[\frac{5.74}{\mathrm{Re}^{0.9}}+\frac{R_q/H}{0.5\delta}\exp\left(-j\frac{1.724}{\mathrm{Re}^{0.9}}\frac{\delta}{R_q/H}\right)\right]$	4b*
h	$\frac{1}{\sqrt{\lambda}}=-2\log_{10}\left(\frac{h}{3.7D}\right)$	$\frac{1}{\sqrt{\lambda}}=-2\log_{10}\left[\frac{2.51}{\mathrm{Re}\sqrt{\lambda}}+\frac{h}{3.7\delta}\exp\left(-j\frac{5.66}{\mathrm{Re}\sqrt{\lambda}}\frac{\delta}{h}\right)\right]$	5a
		$\frac{1}{\sqrt{\lambda}}=-2\log_{10}\left[\frac{5.74}{\mathrm{Re}^{0.9}}+\frac{h}{3.7\delta}\exp\left(-j\frac{12.91}{\mathrm{Re}^{0.9}}\frac{\delta}{h}\right)\right]$	5b*
h	$\frac{1}{\sqrt{\lambda}}=-1.93\log_{10}\left(\frac{h}{3.7D}\right)$	$\frac{1}{\sqrt{\lambda}}=-1.93\log_{10}\left[\frac{1.90}{\mathrm{Re}\sqrt{\lambda}}+\frac{h}{3.7\delta}\exp\left(-j\frac{5.66}{\mathrm{Re}\sqrt{\lambda}}\frac{\delta}{h}\right)\right]$	6a
		$\frac{1}{\sqrt{\lambda}}=-1.93\log_{10}\left[\frac{4.22}{\mathrm{Re}^{0.9}}+\frac{h}{3.7\delta}\exp\left(-j\frac{9.50}{\mathrm{Re}^{0.9}}\frac{\delta}{h}\right)\right]$	6b*

* Explicit friction factor equations (1b)–(5b) with $A=2$ are based on approximate fully smooth pipe equation (38) and friction factor equation (6b) with $A=1.93$ in Eq. (39).
R_q=root mean square (rms) roughness
R_Z=mean peak to valley height roughness
R_a=arithmetic mean roughness
R_q/H=height-texture (HT) roughness
h=equivalent sand grain roughness

$$\frac{1}{\sqrt{\lambda}}=A\log(\mathrm{Re}_\phi\sqrt{\lambda})+C+\frac{C_1}{\mathrm{Re}_\phi\sqrt{\lambda}} \tag{43}$$

Afzal and Yajnik [34] estimated the friction factor for fully smooth pipes ($\phi=1$ or $\Delta U_+=0$) as

$$\frac{1}{\sqrt{C_f}}=4\log(\mathrm{Re}\sqrt{C_f})-0.93+\frac{150}{\mathrm{Re}\sqrt{C_f}} \tag{44a}$$

$$\frac{1}{\sqrt{\lambda}}=2\log(\mathrm{Re}\sqrt{\lambda})-1.06+\frac{150}{\mathrm{Re}\sqrt{\lambda}} \tag{44b}$$

where $C_f=\lambda/4$. These relations may be compared with earlier work on smooth pipes given below:

(Zagarola and Smits [35]) $$\frac{1}{\sqrt{\lambda}}=1.869\log(\mathrm{Re}\sqrt{\lambda})-0.241-233(\mathrm{Re}\sqrt{\lambda})^{-0.9} \tag{45}$$

(McKeon etal. [36]) $$\frac{1}{\sqrt{\lambda}}=1.92\log(\mathrm{Re}\sqrt{\lambda})-0.475-7.04(\mathrm{Re}\sqrt{\lambda})^{-0.55} \tag{46}$$

Here, the second order low Reynolds number effects were attributed to viscous effects [35,36] and data from the average of the difference between log law velocity and Spalding [37] empirically velocity profile were fitted with Reynolds number power index −0.9 [35] and later −0.55 [36]. These authors neither made any link between the nature of their curve fit with Reynolds number

power index −0.9 or −0.55 and nor associated it with the physics of turbulent motion. Moreover, the comparison of friction factors (45) and (46), with experimental data, were not explicitly shown in their work.

The Karman constans from fully smooth pipe data considered as $k=0.4$ ($A=2$) by Prandtl [9], $k=0.42$ ($A=1.93$) by McKeon [10], and $k=0.432$ ($A=1.89$) by Zagarola and Smits [35]. The transitional rough pipe data of Sletfjerding [3] for inflectional roughness P2-P8, Shockling [28] machine honed surface roughness, Nikuradse [1] sand grain roughness, and Blasius-type 1/4 power law for transitional roughness given by Eq. (24), along with fully smooth pipe data of McKeon [10], Oregon's data (McKeon et al. [38]), and data of Patel and Head [33], have been analyzed in Sec. 4 leading to the following results given in advance. If second order effect is of order ϵ, then the friction factor law (43) for $A=2$ and $A=1.93$, respectively, becomes

$$\frac{1}{\sqrt{\lambda}} = 2\log(\mathrm{Re}_\phi\sqrt{\lambda}) - 0.88 + 75(\mathrm{Re}_\phi\sqrt{\lambda})^{-1} + O[(\mathrm{Re}_\phi\sqrt{\lambda})^{-2}] \tag{47}$$

$$\frac{1}{\sqrt{\lambda}} = 1.93\log(\mathrm{Re}_\phi\sqrt{\lambda}) - 0.537 - 85(\mathrm{Re}_\phi\sqrt{\lambda})^{-1} + O[(\mathrm{Re}_\phi\sqrt{\lambda})^{-2}] \tag{48}$$

If the second order effects are of order $\sqrt{\epsilon}$, then the friction factor law (42), for $A=2$ and $A=1.93$, respectively, becomes

$$\frac{1}{\sqrt{\lambda}} = 2\log(\mathrm{Re}_\phi\sqrt{\lambda}) - 0.88 + 2.2(\mathrm{Re}_\phi\sqrt{\lambda})^{-1/2} + O[(\mathrm{Re}_\phi\sqrt{\lambda})^{-1}] \tag{49}$$

$$\frac{1}{\sqrt{\lambda}} = 1.93\log(\mathrm{Re}_\phi\sqrt{\lambda}) - 0.537 - 3.8(\mathrm{Re}_\phi\sqrt{\lambda})^{-1/2} + O[(\mathrm{Re}_\phi\sqrt{\lambda})^{-1}] \tag{50}$$

Equations (47) and (49) for $A=2$ and Eqs. (48) and (50) for $A=1.93$ from the same data show the sign change in the order of magnitude of the second order low Reynolds number effects. Clearly, a more judicious criterion for choice of universal numerical value for the Karman constant k or $A=[k\sqrt{8}\log_{10}(e)]^{-1}$ is also needed for the estimation of the second order low Reynolds number effects.

In Eqs. (49) and (50) to the lowest order, the mesolayer is trivial and its implications on higher order effects have been investigated. If the mesolayer is a substantive or distinguished layer, then from three layer theory, the friction factor equations (27) and (28) where $A_i=5$ and $A_o=2.5$ and $A\approx 3$, have been investigated in two cases where second order effects are of order $(\mathrm{Re}_\phi\sqrt{\lambda})^{-1}$ and $(\mathrm{Re}_\phi\sqrt{\lambda})^{-1/2}$. The present predictions, respectively, yield

$$\frac{1}{\sqrt{\lambda}} = 3\log(\mathrm{Re}_\phi\sqrt{\lambda}) - 4.2 + 325(\mathrm{Re}_\phi\sqrt{\lambda})^{-1} + O[(\mathrm{Re}_\phi\sqrt{\lambda})^{-2}] \tag{51}$$

$$\frac{1}{\sqrt{\lambda}} = 3\log(\mathrm{Re}_\phi\sqrt{\lambda}) - 5 + 33.4(\mathrm{Re}_\phi\sqrt{\lambda})^{-1/2} + O[(\mathrm{Re}_\phi\sqrt{\lambda})^{-1}] \tag{52}$$

where the numerical value of second order effect shows that Eq. (52) is more appropriate.

4 Results and Discussion

The roughness function ΔU_+, and the roughness scale ϕ deduced from the data of Sletfjerding [3] for the roughness parameters $a/h=402$ (P7), 519 (P6), 845 (P5), 976 (P8), 1201 (P4), 2720 (P3), 3280 (P2), and 68160 (P1) are shown in Figs. 1(*a*) and 1(*b*). Shockling [28] machine honed surface roughness data for $a/h=7190$ and Nikuradse [1] sand grain roughness data for $a/h=507$ are also shown in these figures. The seven data sets of Sletfjerding [3] for $a/h=402$ (P7), 519 (P6), 845 (P5), 976 (P8), 1201 (P4), 2720 (P3), and 3280 (P2) and the data of Shockling [28] for $a/h=7091$ show inflectional-type roughness, analogous to Nikuradse [1] sand grain roughness. In the roughness function ΔU_+ and roughness scale ϕ predictions (29*a*) and (29*b*) for inflectional roughness, the free constant $j\neq 0$ was estimated as $j=11$ from fit to inflectional roughness data of Sletfjerding [3] and Shockling [28]. With $\Delta U^+=k^{-1}\ln\phi$, the author proposed ϕ and h predictions (29) for inflectional roughness with $j=11$ and these functions were used for estimation of friction factor in traditional variables from our universal friction factor variables. Sletfjerding [3] data $a/h=68{,}160$ (P1) is also shown in the same figures where the roughness function ΔU_+ and roughness scale ϕ show monotonic roughness. The predictions[29] with $j=0$ corresponding to Colebrook [2] monotonic roughness compare very well with the data.

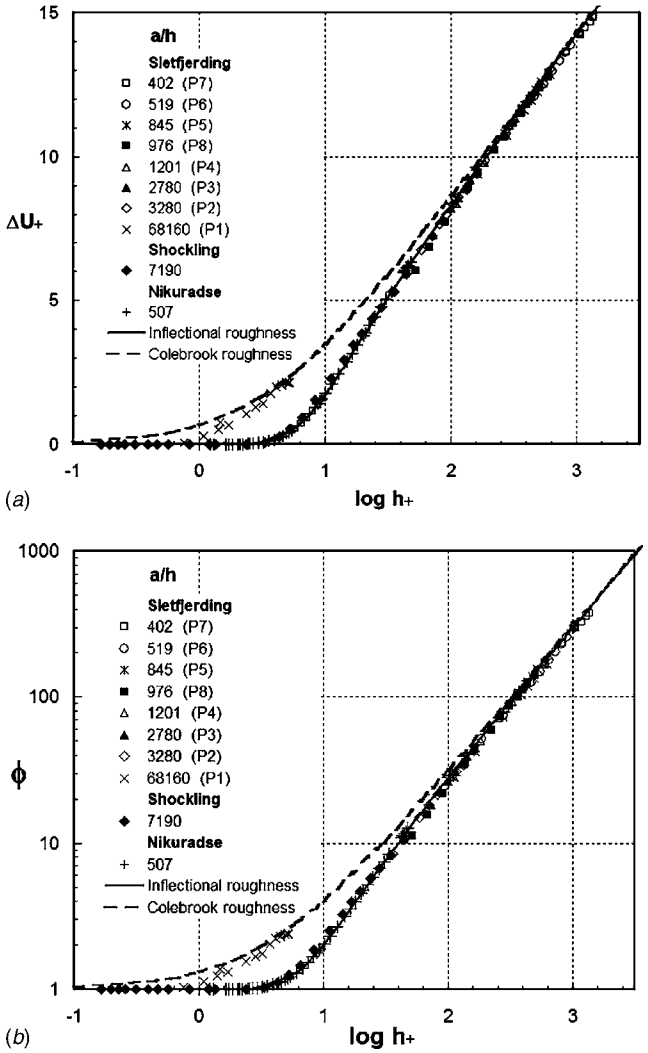

Fig. 1 Comparison of the roughness characteristics of the pipes from P2-P7 data of Sletfjerding, $a/h=7190$ data of Shockling, and $a/h=507$ data of Nikuradse for inflectional roughness with present prediction (29) for $j=11$ shown by a solid line. Comparison of P1 data of Sletfjerding with Colebrook monotonic roughness prediction (29) with $j=0$ shown by a dash line. (*a*) Roughness function ΔU_+ against h_+. (*b*) Roughness scale ϕ against h_+.

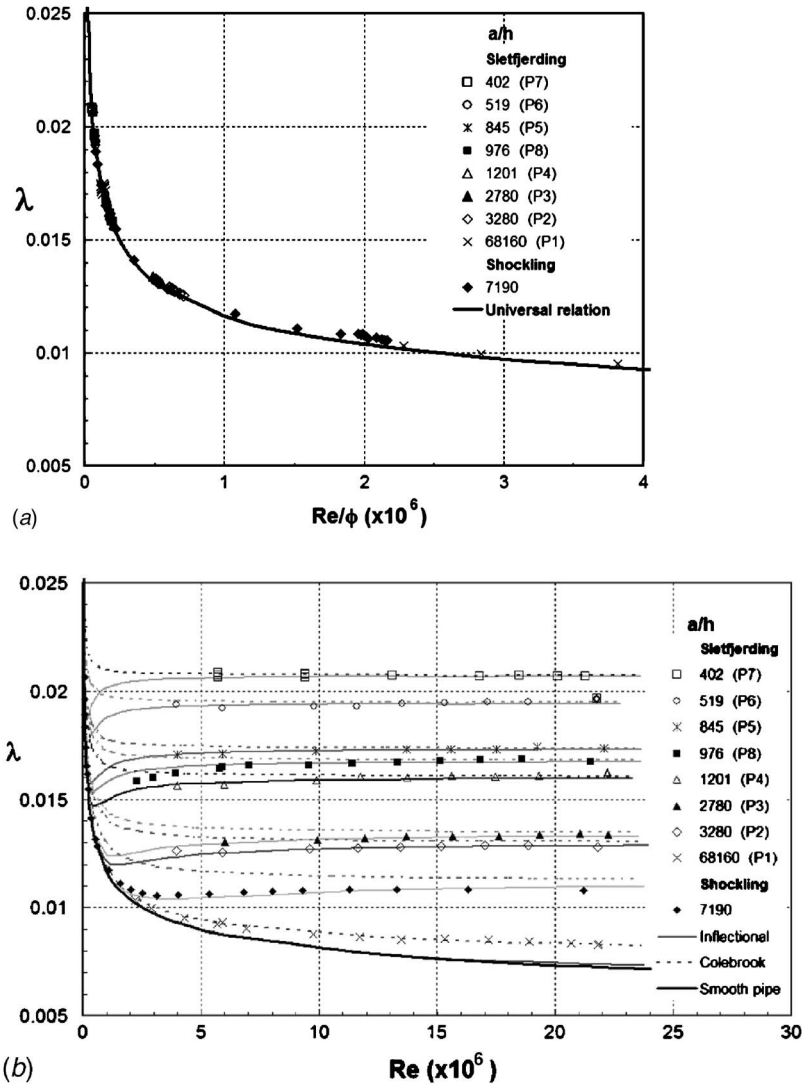

Fig. 2 Comparison of the roughness characteristics of the pipes from P2-P7 data of Sletfjerding, $a/h=7190$ data of Shockling, and $a/h=507$ data of Nikuradse showing inflectional roughness and P1 data of Sletfjerding showing monotonic roughness with present work. (*a*) Friction factor λ with roughness Reynolds number Re/ϕ from the data showing universal behavior, explicitly independent of transitional pipe roughness. (—) Present universal relation (25*b*). (*b*) Friction factor λ with traditional Reynolds number Re from data showing nonuniversal behavior that depends on transitional pipe roughness. (—) Present inflectional roughness prediction (34) with $j=11$, (----) Colebrook monotonic roughness prediction (34) with $j=0$.

The friction factor λ versus roughness Reynolds number $\mathrm{Re}_\phi = \mathrm{Re}/\phi$ from the data of Sletfjerding [3], Shockling [28], and Nikuradse [1], shown in Figs. 2(*a*) and 3(*a*), shows universality, which is explicitly independent of the transitional surface roughness. Our friction factor prediction (25*b*) also plotted in Figs. 2(*a*) and 3(*a*) describes the universal behavior very well for all kinds of roughnesses. The friction factor $1/\sqrt{\lambda}$ versus Re_ϕ from the data of Sletfjerding [3], Shockling [28], and Nikuradse [1] shown in Fig. 4(*a*) shows universal linear relation, explicitly independent of the transitional surface roughness. Our universal prediction $1/\sqrt{\lambda}$ versus Re_ϕ from relation (25*b*) also plotted in Figs. 4(*a*) also supports the universal linear relation very well for all kinds of roughnesses.

In contrast, the friction factor, in terms of traditional Reynolds number Re, is not universal, and depends on the nature of the surface roughness. The experimental data of Sletfjerding [3], however, did not include the data in the transition region between smooth and rough flows, and further experimental work is needed to verify the behavior of the friction factor in the transition region at high Reynolds numbers. Nevertheless, departure of their friction factor data from fully rough pipe relationships may throw some light on its nature, to show whether it is the inflectional roughness, Colebrook monotonic roughness, or any other type of roughness. Moreover, as shown earlier, Figs. 1(*a*) and 1(*b*) directly dealing with the roughness provide a guidance that the seven data sets of Sletfjerding [3] for $a/h=402$ (P7), 519 (P6), 845 (P5), 976 (P8), 1201 (P4), 2720 (P3), and 3280 (P2) and the data of Shockling [28] for $a/h=7091$ show inflectional-type roughness. The friction factor data P2-P8 of Sletfjerding [3], and $a/h=7190$ data of Shocking [28], shown in Fig. 2(*b*), show inflectional-type behavior, analogous to Nikuradse [1] sand grain roughness. Our predictions of the friction factor (34) for inflectional roughness with ($j=11$) using solid lines also shown in the

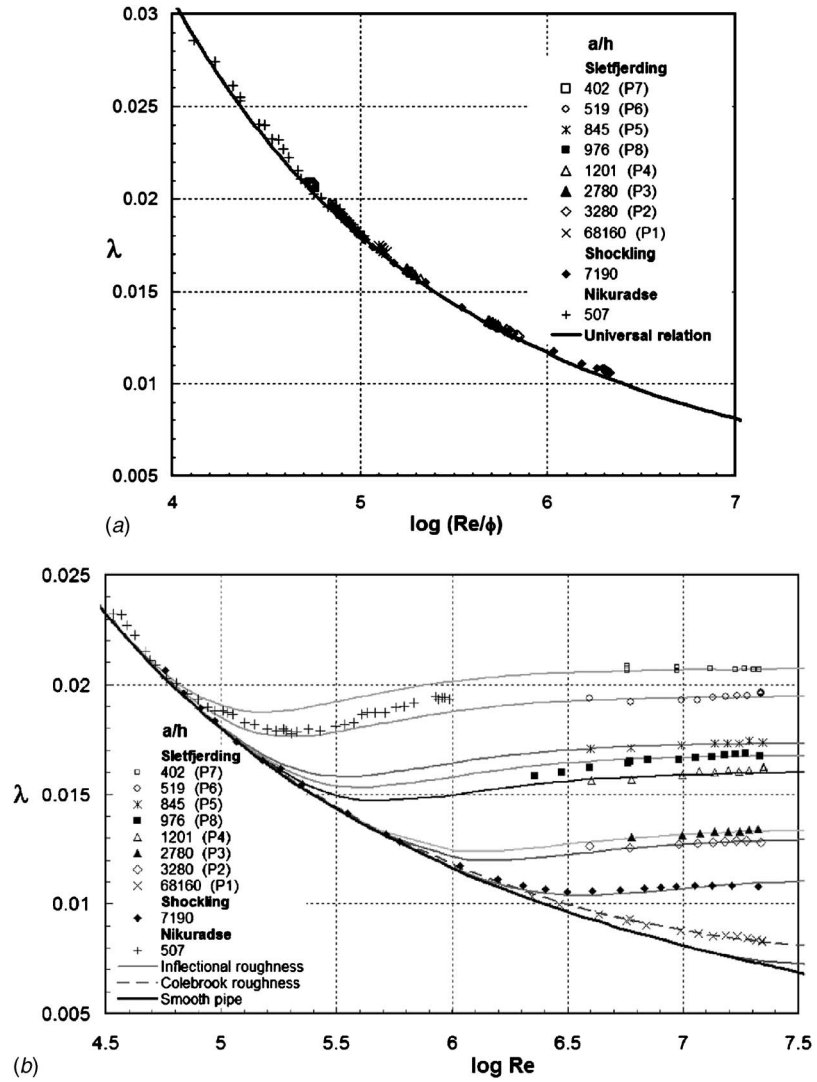

Fig. 3 Comparison of the roughness characteristics of the pipes from P2-P7 data of Sletfjerding, $a/h=7190$ data of Shockling, and $a/h=507$ data of Nikuradse showing inflectional roughness and P1 data of Sletfjerding showing monotonic roughness with present work. (*a*) Friction factor λ with roughness Reynolds number Re/ϕ from data showing universal behavior, explicitly independent of transitional pipe roughness. (—) Present universal relation (25*b*). (*b*) Friction factor λ with traditional Reynolds number Re from data showing nonuniversal behavior that depends on transitional pipe roughness. (—) Inflectional roughness, present prediction (34) with $j=11$ and comparison with the data of Sletfjerding (P2-P8), Shockling and Nikuradse, (----) Colebrook monotonic roughness prediction (34) with $j=0$ and comparison with the data of Sletfjerding (P1).

same figure compare very well with the data. The friction factor data P1 of Sletfjerding [3] also shown in Figs. 2(*b*) and 3(*b*) have monotonic behavior, which also compare well with Colebrook [2] monotonic roughness (34) with ($j=0$). In conclusion, the data P2-P8 of Sletfjerding [3] and $a/h=7190$ data of Shocking [28] compare very well with our prediction of friction factor, roughness function, and roughness scale for inflectional-type roughness, and so also P1 data of Sletfjerding [5] compare well with Colebrook monotonic roughness. The situation is further clearly expressed in Fig. 3(*b*) where predictions (34) for P2-P8 data of Sletfjerding [3] and $a/h=7190$ data of Shocking [28] compare very well with our predictions for the inflectional roughness ($j=11$) shown by solid lines and the P1 data of Sletfjerding [3] compare very well with monotonic roughness ($j=0$) shown by dotted line. Further, the data of Nikuradse [1] for $a/h=507$, also shown in Fig. 3(*b*), correspond to inflectional roughness, but the prediction line is not shown, which may be inferred from the neighborhood of P6 data for $a/h=519$. Our predicted friction factor based on Eq. (34), in terms of the traditional Reynolds number Re shown in Figs. 2(*b*) and 3(*b*), is also in good agreement with the data of Sletfjerding [3], Shocking [28], and Nikuradse [1]. The situation is further clearly expressed in Fig. 4(*b*) and no additional comment is needed.

Shockling [28] measurements on inflectional roughness in Princeton's superpipe proposed $(h_+,\Delta U_+)$ diagram. Allen et al. [39] arrived at this $(h_+,\Delta U_+)$ diagram, and estimated ΔU_+ for prescribed values of the roughness h_+. From one experiment to another Allen et al. adopted $h=3h_{\mathrm{rms}}$ for Nikuradse data, and $h=3h_{\mathrm{rms}}$ and $h=5.78h_{\mathrm{rms}}$ for their own data, for estimation of the friction factor. But, the present predictions are in better agreement

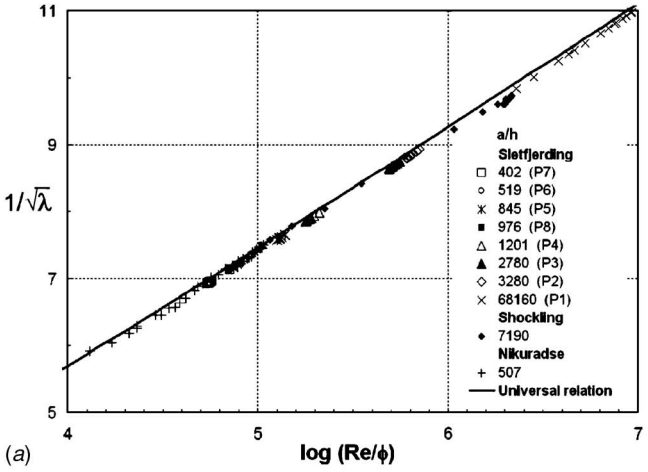

(a)

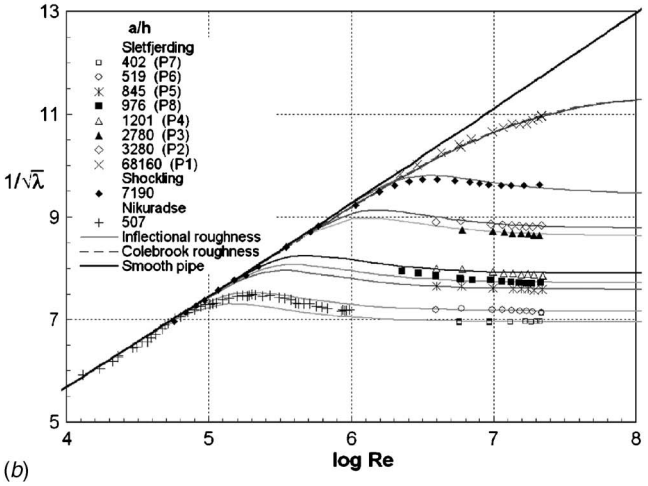

(b)

Fig. 4 Comparison of the roughness characteristics of the pipes from P2-P8 data of Sletfjerding, $a/h=7190$ data of Shockling, and $a/h=507$ data of Nikuradse showing inflectional roughness and P1 data of Sletfjerding showing monotonic roughness with present work. (*a*) Friction factor $1/\sqrt{\lambda}$ with roughness Reynolds number Re/ϕ from data showing universal behavior, explicitly independent of transitional pipe roughness. (—) Present universal relation (25*b*). (*b*) Friction factor λ with traditional Reynolds number Re from data showing nonuniversal behavior that depends on transitional pipe roughness. (—) Inflectional roughness, present prediction (34) with $j=11$ and comparison with the data of Sletfjerding (P2-P8), Shockling and Nikuradse, (----) Colebrook monotonic roughness prediction (34) with $j=0$ and comparison with the data of Sletfjerding (P1).

with the data of Shockling [28] and Nikuradse [1] when compared with the predictions of Allen et al. [39]. On the other hand, Shocking adopted $h=3h_{\mathrm{rms}}$ and Hama [13] adopted $h=5h_{\mathrm{rms}}$. In the present work, the equivalent sand grain roughness [1] $h=3.6h_{\mathrm{rms}}$ has been estimated from the friction factor data of Shockling [28]. Furthermore, for $h=3.6h_{\mathrm{rms}}$ and root mean square roughness $h_{\mathrm{rms}}/d=19.4\times10^{6}$, we get $a/h=7190$. The function $b_T=\lambda^{-1/2}-2\log(a/h)$ in the friction factor relation (31) has been estimated from λ and a/h data of Sletfjerding [3], Shocking [28], and Nikuradse [1]. These are shown in Fig. 5. The same figure also shows the prediction of b_T from relation (31) for inflectional roughness ($j=11$) and Colebrook monotonic roughness ($j=0$), which compare well with the data.

Sletfjerding [3] and Sletfjerding and Gudmundsson [4] have also measured alternative types of roughness R_a the arithmetic mean roughness, R_Z the mean peak to valley height roughness, R_q

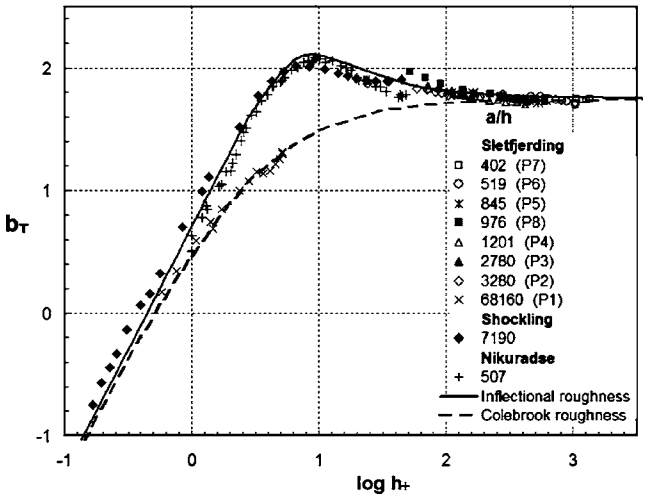

Fig. 5 Comparison of the present prediction (31) for $b_T=\lambda^{-1/2}-2\log(a/h)$ for inflectional roughness ($j=11$) and Colebrook monotonic roughness ($j=0$) with data of Sletfjerding, Shockling, and Nikuradse.

the root mean square (rms), and $R_q/H=$HT roughness (containing both a height measure and a texture measure), where H the Hurst exponent (a texture parameter), but no correlation was considered with equivalent sand grain roughness h. In the present work, the alternate roughness R_a, R_Z, R_q, and R_q/H plotted against h (equivalent sand grain roughness of Nikuradse) are shown in Fig. 6. The data are fitted by a linear relation and the correlation of the alternate roughness and equivalent sand grain roughness is as follows:

$$h=1.244R_Z \quad h=5.333R_q \quad h=6.45R_a \quad h=7.71R_q/H \tag{53}$$

The frction factors in terms of alternate roughness parameters R_a, R_q, R_z, and R_q/H in addition to h, based on correlations (53), are given in Table 1 for transitional rough pipes. Rows (1a)–(5a) in Table 1, respectively, give the relationship between λ and Re for each alternate roughness parameter R_a, R_Z, R_q, and R_q/H, respec-

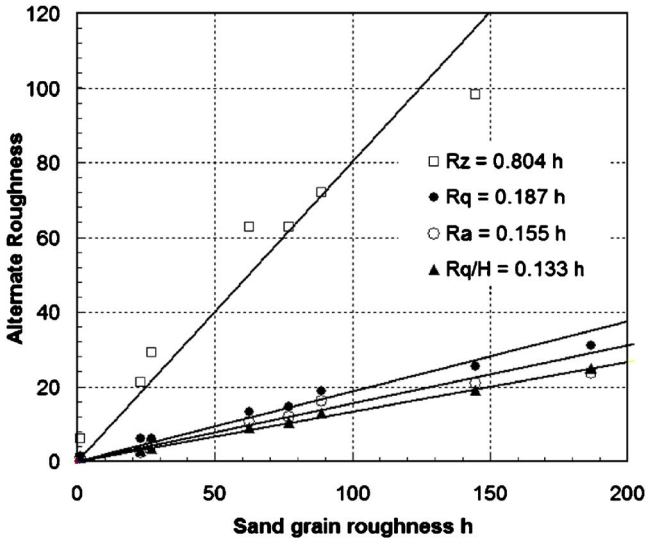

Fig. 6 Our prediction of the relationship between alternate roughnesses: R_a the arithmetic mean roughness, R_Z the mean peak to valley height roughness, R_q the root mean square (rms) roughness, and R_q/H the height-texture roughness, with respect to h the equivalent sand grain roughness from data of Sletfjerding and Gudmundsson.

tively, in terms of implicit relations. Furthermore, the explicit but approximate relations are also given in rows (1b)–(5b) in the same table. The work of Sletfjerding and Gudmundsson [4] and Sletfjerding [3]) provided support to some of these relations for Colebrook-type roughness $j=0$. For inflectional roughness, the data support to new friction factor relations would be provided in a subsequent publication.

It was shown by Afzal [28] that the second order effects from the extension of Izakson–Millikan argument needed a postulate about the order of the higher order terms. Afzal [30] regarded it as being of the order $(\mathrm{Re}\sqrt{\lambda})^{-1}$, and from the mesolayer theory of Afzal [21,22], he regarded it as being of the order $(\mathrm{Re}\sqrt{\lambda})^{-0.5}$. On the other hand, Zagarola and Smits [35] and McKeon et al. [36] friction factor relations (45) and (46) attributed the second order effect as the viscous corrections, empirically estimated from the deviation of log law velocity profile and Spalding's [37] empirical velocity profile in the sublayer. This deviation of the data was fitted with $(\mathrm{Re}\sqrt{\lambda})^{-0.9}$ by Zagarola and Smits [35] and with $(\mathrm{Re}\sqrt{\lambda})^{-0.55}$ by McKeon, et al. [36]. These authors neither made any link between the nature of their curve fit with Reynolds number power index −0.9 or −0.55 nor associated it with the physics of turbulent motion. Moreover, the comparison of friction factors (45) and (46) with experimental data was not explicitly shown in their work.

The second order effects in the friction factor for moderately large Reynolds number flows are studied in terms of a departure function Λ representing the difference between friction factor and log law, as defined below

$$\Lambda \equiv \frac{1}{\sqrt{\lambda}} - A\log(\mathrm{Re}_\phi\sqrt{\lambda}) \tag{54}$$

and our second order universal prediction (41) for transitional rough pipes becomes

$$\Lambda = C + \frac{C_{1/2}}{(\mathrm{Re}_\phi\sqrt{\lambda})^{1/2}} + \frac{C_1}{\mathrm{Re}_\phi\sqrt{\lambda}} + \cdots \tag{55}$$

The departure function data shown in Figs. 7(*a*), 7(*b*), 8(*a*), and 8(*b*) are from inflectional roughness data P2-P8 of Sletfjerding [3], Shockling [28] machine-honed surface roughness and Nikuradse [1] sand grain roughness, and monotonic roughness P1 data Sletfjerding [3], and Blasius-type 1/4 power law for transitional roughness given by Eq. (24) shown by dotted line, along with the fully smooth pipe data of McKeon [10], Oregon's data (Ref. [38]), and data of Patel and Head [33]. The computations from above mentioned data based on Prandtl constant $A=2$ are shown in Figs. 7(*a*) and 8(*a*) and McKeon constant $A=1.93$ are shown in Figs. 7(*b*) and 8(*b*). The friction factor departure functions Λ against $(\mathrm{Re}_\phi\sqrt{\lambda})^{-n}$, for traditional value $n=1$ (Ref. [28]) with the Prandtl constant $A=2$ and McKeon constant $A=1.93$ are, respectively, shown in Figs. 7(*a*) and 7(*b*) for $n=1$ and in Figs. 8(*a*) and 8(*b*) for $n=1/2$.

The friction factor departure Λ with $n=1$ and Prandtl constant $A=2$ is shown in Fig. 7(*a*) predicting $\Lambda=-0.88+75(\mathrm{Re}_\phi\sqrt{\lambda})^{-1}$, whereas Prandtl-type transitional roughness universal relation (25*b*) giving $\Lambda=-0.8$ is shown by a dash line. Using the McKeon constant $A=1.93$, shown in Fig. 7(*b*), the prediction is $\Lambda=-0.537-85(\mathrm{Re}_\phi\sqrt{\lambda})^{-1}$, whereas McKeon-type transitional roughness universal relation (26*b*) giving $\Lambda=-0.537$ is shown by a dash line. The friction factor departure Λ with $n=1/2$ and Prandtl constant $A=2$ is shown in Fig. 8(*a*) for which the prediction is $\Lambda=-0.88+2.2(\mathrm{Re}_\phi\sqrt{\lambda})^{-1/2}$, whereas Prandtl-type transitional roughness universal relation (25*b*) giving $\Lambda=-0.8$ is shown by a dash line. Also, for the McKeon constant $A=1.93$, shown in Fig. 8(*b*), the prediction is $\Lambda=-0.537-3.2(\mathrm{Re}_\phi\sqrt{\lambda})^{-1/2}$, whereas McKeon-type transitional roughness universal relation (26*b*) giving $\Lambda=-0.537$ is shown by a dash line. From the scatter of the data, it is not easy to draw an appropriate line that describes the second order effects in friction factor from smooth and rough pipe data. An approximate mean line is drawn in these figures with due emphasis on the high Reynolds number data of Sletfjerding [3] and the low Reynolds number Blasius-type [19] friction factor law (24) for transitional pipe roughness and smooth pipe data of Patel and Head [33]. The numerical values of the undetermined constants estimated from the data for the Prandtl constant $A=2$ are smaller when compared with the McKeon constant $A=1.93$. This is so both for the traditional case $n=1$ (Ref. [30]) and the mesolayer case $n=1/2$ (Refs. [21,22]). Furthermore, the scatter of data in each case requires a judicious choice for determination of the numerical constants for second order effects for moderately large Reynolds numbers. The behavior of the Shockling [28] rough superpipe data and McKeon et al. [38] smooth superpipe data shown

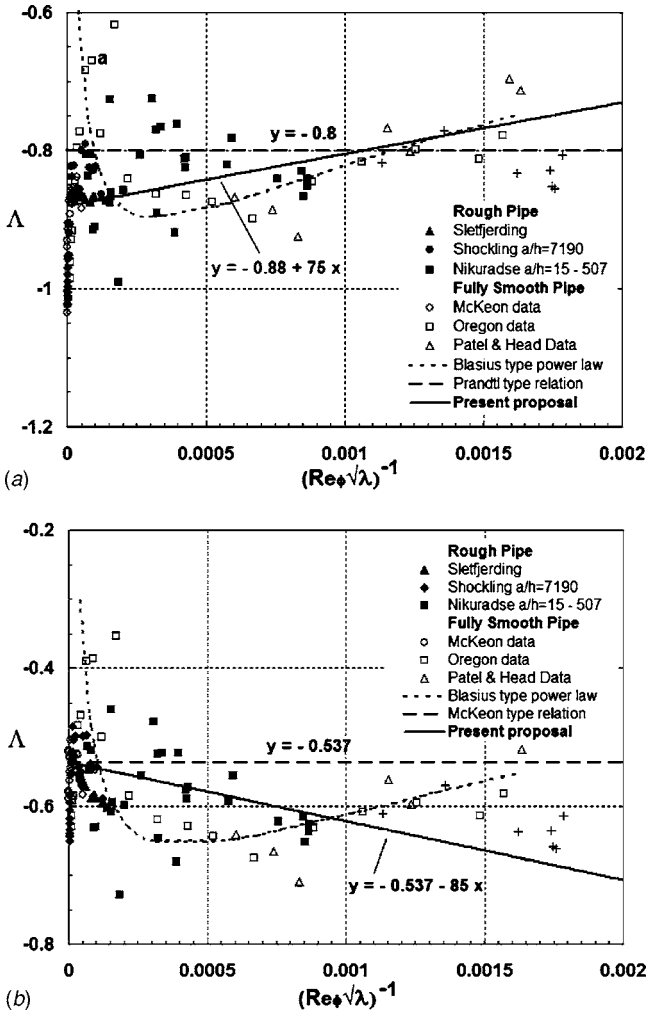

Fig. 7 Second order effect of order $(\mathrm{Re}_\phi\sqrt{\lambda})^{-1}$: The friction factor departure function $\Lambda\equiv 1/\sqrt{\lambda}-A\log(\mathrm{Re}\sqrt{\lambda})$ against $(\mathrm{Re}_\phi\sqrt{\lambda})^{-1}$ from Sletfjerding's [3] inflectional roughness data P2-P8 $a/h=402-3280$ (▲), Shockling's [28] machine-honed surface roughness data $a/h=7190$ (●), Nikuradse's [1] sand grain roughness data $a/h=15-507$ (■), and (·····) Blasius-type 1/4 power law for transitional roughness relation (24), along with fully smooth pipe data (McKeon [10] (○), Oregon data [38] (□), and Patel and Head [33] (△)). (*a*) Computations from the data based on Prandtl constant $A=2$. (—) Present prediction $\Lambda=-0.88+75(\mathrm{Re}_\phi\sqrt{\lambda})^{-1}$, (---) Prandtl-type relation (25*b*) with $\Lambda=-0.8$. (*b*) Computations from the data based on McKeon constant $A=1.93$. (—) Present prediction $\Lambda=-0.537-85(\mathrm{Re}_\phi\sqrt{\lambda})^{-1}$, (---) McKeon-type relation (26*b*) with $\Lambda=-0.537$.

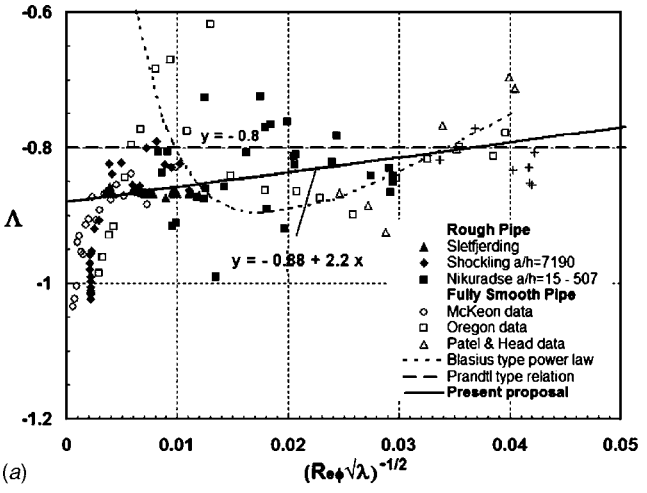

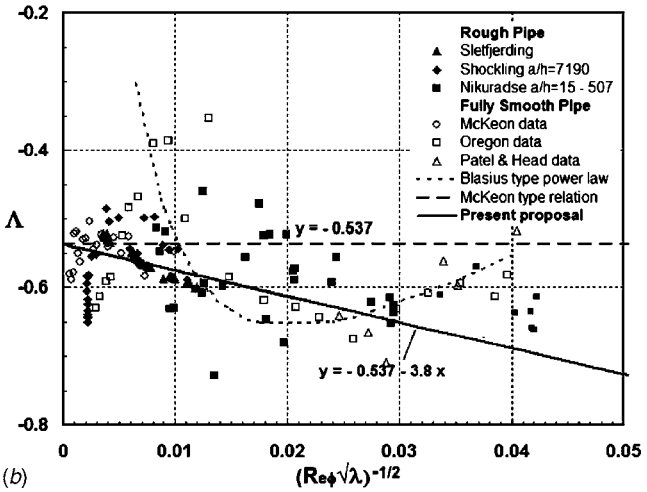

Fig. 8 Second order mesolayer effect of order $(\mathrm{Re}_\phi\sqrt{\lambda})^{-1/2}$: The friction factor departure function $\Lambda \equiv 1/\sqrt{\lambda} - A\log(\mathrm{Re}\sqrt{\lambda})$ against $(\mathrm{Re}_\phi\sqrt{\lambda})^{-1/2}$ from Sletfjerding's [3] inflectional roughness data P2-P8 $a/h=402-3280$ (▲), Shockling's [28] machine-honed surface roughness data $a/h=7190$ (●), Nikuradse's [1] sand grain roughness data $a/h=15-507$ (■), and (⋯ ⋯) Blasius-type 1/4 power law for transitional roughness relation (24) along with fully smooth pipe data (McKeon [10] (○), Oregon data [38] (□), and Patel and Head [33] (△)). (*a*) Computations from the data based on Prandtl constant $A=2$. (—) Present prediction $\Lambda=-0.88+2.2(\mathrm{Re}_\phi\sqrt{\lambda})^{-1/2}$, (---) Prandtl-type relation (25*a*) with $\Lambda=-0.8$. (*b*) Computations from the data based on McKeon constant $A=1.93$. (—) Present prediction $\Lambda=-0.537-3.8(\mathrm{Re}_\phi\sqrt{\lambda})^{-1/2}$, (---) McKeon-type relation (26*b*) with $\Lambda=-0.537$.

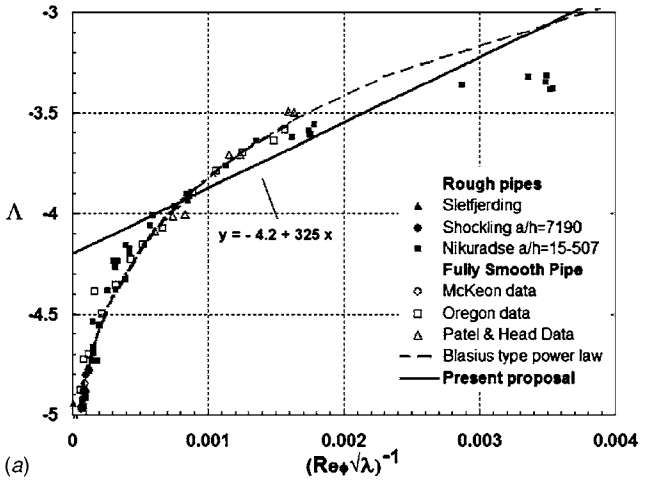

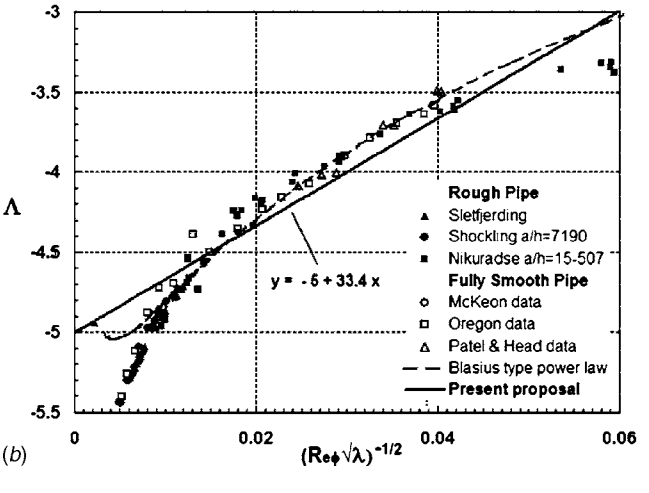

Fig. 9 Second order effect with substantive mesolayer: The friction factor departure function $\Lambda \equiv 1/\sqrt{\lambda} - A\log(\mathrm{Re}\sqrt{\lambda})$ with mesolayer $A=(A_i+A_0)/(\sqrt{32}\log_{10}e)\approx 3$ from Sletfjerding's [3] inflectional roughness data P2-P8 $a/h=402-3280$ (▲), Shockling's [28] machine-honed surface roughness data $a/h=7190$ (●), Nikuradse's [1] sand grain roughness data $a/h=15-507$ (■), and (⋯⋯) Blasius-type 1/4 power law for transitional roughness relation (24) along with fully smooth pipe data (McKeon [10] (○), Oregon data [38] (□), and Patel and Head [33] (△)). (a) Λ versus $(\mathrm{Re}_\phi\sqrt{\lambda})^{-1}$ and (—) Present prediction $\Lambda=-4.2+325(\mathrm{Re}_\phi\sqrt{\lambda})^{-1}$. (*b*) Λ versus $(\mathrm{Re}_\phi\sqrt{\lambda})^{-1/2}$ and (—) present prediction $\Lambda=-5+33.4(\mathrm{Re}_\phi\sqrt{\lambda})^{-1/2}$.

in Figs. 7(*a*), 7(*b*), 8(*a*), and 8(*b*) almost on a vertical line showing the scatter in the value intercept $C=-0.537$ in relation (55) do not reveal much about second order effects. On the other hand, the data of Sletfjerding [3] and Sletfjerding and Gudmundsson [4] show systematic variation of second order effects with respect to appropriate Reynolds number, but the sand grain data of Nikuradse [1] are more scattered about the proposed line of prediction shown in these figures. For example, Figs. 7(*a*) and 8(*a*) for $A=2$ and Figs. 7(*b*) and 8(*b*) for $A=1.93$ from the same data show the sign change in the order of magnitude of the second order low Reynolds number effects. Clearly, a more judicious criterion for choice of universal numerical value for the Karman constant k or $A=[k\sqrt{8}\log_{10}(e)]^{-1}$ is also needed for the estimation of the second order low Reynolds number effects.

It may be pointed out that to the lowest order, the mesolayer is trivial in Eqs. (49) and (50), and its implications on higher order effects have been investigated. If the mesolayer is a substantive or distinguished layer, then from the three layer theory, the friction factor has been analyzed here. The departure function Λ from Eq. (52) for substantive mesolayer friction factor equations (27) and (28) where $A_i=5$ and $A_o=2.5$ and $A\approx 3$ is shown in Fig. 9(*a*) with $(\mathrm{Re}_\phi\sqrt{\lambda})^{-1}$ and Fig. 9(*b*) with $(\mathrm{Re}_\phi\sqrt{\lambda})^{-1/2}$ from inflectional roughness data P2-P8 of Sletfjerding [3], Shockling [28] machine-honed surface roughness and Nikuradse [1] sand grain roughness, and monotonic roughness P1 data Sletfjerding [3], and Blasius-type 1/4 power law for transitional roughness given by Eq. (24) is shown by a dotted line, along with the fully smooth pipe data of McKeon [10], Oregon's data (Ref. [38]), and data of Patel and Head [33]. The entire data show more systematic behavior. An approximate mean line is drawn in these figures with due emphasis on the low Reynolds number Blasius-type [19] friction factor law (24) for transitional pipe roughness and smooth pipe data of

Patel and Head [33]. The proposed predictions in the two cases are $\Lambda=-4.2+325(\mathrm{Re}_\phi\sqrt{\lambda})^{-1}$ and $\Lambda=-5+33.4(\mathrm{Re}_\phi\sqrt{\lambda})^{-1/2}$ and later numerical value of second order effect is more appropriate. A more judicious criterion for choice of universal numerical value of the prefactor A of logarithmic term in the friction factor is also needed for the estimation of the second order low Reynolds number effects.

5 Conclusions

(1) The friction factor and roughness Reynolds number relationship are universal and explicitly independent of wall roughness. The universality is supported by transitional roughness data of Sletfjerding [3], Sletfjerding and Gudmundsson [4], Shocking [28], and Nikuradse [1].

(2) The roughness function ΔU_+ and the roughness scale ϕ, as predicted by our relations (19*a*) and (19*b*) for inflectional roughness ($j=11$) and Colebrook monotonic roughness ($j=0$), compare very well with the experimental data. The seven data sets of Sletfjerding [3] for $a/h=402$ (P7), 519 (P6), 845 (P5), 976 (P8), 1201 (P4), 2720 (P3), and 3280 (P2) and the data of Shockling [28] for $a/h=7091$ compare very well with our predictions for inflectional roughness, analogous to Nikuradse [1] sand grain roughness. Furthermore, the Sletfjerding [3] data $a/h=68160$ (P1) also compare well with $j=0$, the Colebrook [2] monotonic roughness.

(3) There is no universality of scaling while using the traditional variables and different expressions are needed for various types of roughness as suggested by inflectional roughness and monotonic Colebrook–Moody roughness. Our prediction for friction factor λ based on the traditional Reynolds number Re, for each roughness parameter a/h, is also in very good agreement with the entire data both for inflectional roughness and of Colebrook monotonic roughness.

(4) The friction factor versus roughness Reynolds number given by Prandtl-type equation (25*b*) is universal and explicitly independent of wall roughness, which compare well with the experimental data. The relation (25*b*) in terms of roughness function (29*a*) and (29*b*) leads to nonuniversal prediction equation (34), which also compare well with the inflectional roughness experimental data with $j=11$ and Colebrook monotonic roughness data with $j=0$. The friction factor versus roughness Reynolds number, McKeon-type equation (26*b*), is also universal and explicity independent of wall roughness. The relation (26*b*) in terms of roughness function (29*a*) and (29*b*) leads to nonuniversal prediction equation (34) for inflectional roughness for $j=11$ and Colebrook monotonic roughness with $j=0$.

(5) The implicit new expressions for friction factor λ have been proposed for alternate roughness parameters, viz., R_q the root mean square (rms) roughness, R_a the arithmetic mean roughness, R_Z mean peak to valley height roughness, and R_q/H, and also for h the equivalent sand grain roughness. The explicit approximate expressions of friction factor λ versus Re for various alternate roughness R_a, R_Z, R_q, and R_q/H, in addition to h, have also been proposed. The work of Sletfjerding [3]) and Sletfjerding and Gudmundsson [4] provided support to some of these relations for Colebrook-type roughness $j=0$. For inflectional roughness, the data support to new friction factor relations would be provided in a subsequent publication.

(6) The second order effect in friction factor (45) and (46) for fully smooth pipes was taken of the order $(\mathrm{Re}\sqrt{\lambda})^{-0.9}$ by Zagarola and Smits [35] and order by McKeon et al. [36]. These authors neither made any link between the nature of their curve fit with Reynolds number power index −0.9 or −0.55 nor associated it with the physics of turbulent motion. Moreover, the comparison of their friction factors (45) and (46) with experimental data was not explicitly shown in their work.

(7) The second order effect of the friction factor in transitional rough pipe for moderately large Reynolds numbers has been formulated and tested from P2-P8 data of Sletfjerding [3] for inflectional roughness, data of Shockling [28] for machine-honed surface roughness, data of Nikuradse [1] for sand grain roughness, *P*1 data of Sletfjerding [3] for Colebrook monotonic as well as that for fully smooth pipe data of McKeon [10], Oregon's data (Ref. [38]), and Patel and Head [33]. The perturbation constants estimated for Prandtl [9] constant $A=2$ are smaller when compared with McKeon [10] constant $A=1.93$ for traditional order $n=1$ of order $(\mathrm{Re}_\phi\sqrt{\lambda})^{-1}$ as well as for the mesolayer case $n=1/2$ of order $(\mathrm{Re}_\phi\sqrt{\lambda})^{-1/2}$. From the scatter of the data, it is not easy to draw an appropriate line that describes the second order effects in friction factor from smooth and rough pipe data. An approximate mean line is drawn in these figures with due emphasis on the high Reynolds number data of Sletfjerding [3], the low Reynolds number Blasius-type [19] friction factor law (24) for transitional pipe roughness, and smooth pipe data of Patel and Head [33].

(8) The behavior of Shockling [28] rough superpipe data and McKeon et al. [36] smooth superpipe data shown in Figs. 7(*a*), 7(*b*), 8(*a*), and 8(*b*) almost falls on a vertical line. This implies that the scatter in the value of the intercept $C=-0.537$ [10] in Eq. (53) does not reveal much about the second order effects. The data of Sletfjerding [3] and Sletfjerding and Gudmundsson [4] show systematic variation of the second order effects with respect to appropriate Reynolds number, but Nikuradse [1] sand grain data are more scattered about the proposed line of prediction. For example, Figs. 7(*a*) and 8(*a*) for $A=2$ and Figs. 7(*b*) and 8(*b*) for $A=1.93$ from the same data show the sign change in the order of magnitude of the second order low Reynolds number effects. The departure function for substantive mesolayer friction factor is shown in Figs. 9(*a*) and 9(*b*), in contrast to Figs. 7(*a*) and 8(*b*) for lowest order trivial mesolayer implication on higher order effects. Clearly, a more judicious criterion for choice of universal numerical value of the prefactor A of logarithmic term in the friction factor is also needed for the estimation of the second order low Reynolds number effects.

Acknowledgment

The author is grateful for the support of All India Council of Technical Education, New Delhi.

References

[1] Nikuradse, J., 1933, *Laws of Flow in Rough Pipe*, VDI, Forchungsheft No. 361, English translation NACA T.M. 1292, 1950.

[2] Colebrook, C. F., 1939, "Turbulent Flow in Pipes With Particular Reference to the Transition Region Between the Smooth and Rough Pipe Laws," Journal of Institution of Civil Engineers, London, **11**, pp. 133–156.

[3] Sletfjerding, E., 1999, "Friction Factor in Smooth and Rough Gas Pipelines," Dr.-Ing. thesis, Norwegian University of Science and Technology, Trondheim.

[4] Sletfjerding, E., and Gudmundsson, J. S., 2003, "Friction Factor Directly From Roughness Measurements," J. Energy Resour. Technol., **125**, pp. 126–130.

[5] Barr, D. I. H., 1972, "New Forms of Equations for the Correlation of Pipe Resistance Data," Proc. Inst. Civil Engg. London, **53**(2), pp. 383–390; see also 1977, "Discussion of Accurate Explicit Equation for Friction Factor," J. Hydr. Div. ASCE, **103**(HY3), pp. 334–337.

[6] Churchill, S. W., 1973, "Empirical Expressions for the Shear Stress in Turbulent Flow in Commercial Pipe," AIChE J., **19**, pp. 375–376.

[7] Swamee, P. K., and Jain, A. K., 1976, "Explicit Equations for Pipe Flow Problems," J. Hydraul. Eng. ASCE, 102(5), pp. 657–664; Collins, M. A., *ibid.* 102(11), pp. 1707–1709; Barr, D. H., *ibid.* 103(4), pp. 460–463.

[8] Haaland, S., 1983, "Simple and Explicit Formulas for the Friction Factor in Turbulent Pipe Flow," J. Fluids Eng., **105**, pp. 89–90.

[9] Prandtl, L., 1935, "The Mechanics of Viscous Fluids," in *Aerodynamic Theory*,

edited by Durand, W. F., California Institute of Technology, Pasadena, CA, Vol. 3, pp. 34–208.
[10] McKeon, B. J., 2003, "High Reynolds Number Turbulent Pipe Flow," Ph.D. thesis, Princeton University, Princeton.
[11] Warburton, C., 1974, "Surface Roughness of Graphite and Its Effect on Friction Factor," Proc. Inst. Mech. Eng., **188**, pp. 457–460.
[12] Clauser, F. H., 1954, "Turbulent Boundary Layers in Adverse Pressure Gradients," J. Aeronaut. Sci., **21**, pp. 91–108.
[13] Hama, F. R., 1954, "Boundary-Layer Characteristics for Rough and Smooth Surfaces," Soc. Nav. Archit. Mar. Eng., Trans., **62**, pp. 333–351.
[14] Afzal, N., Seena, A., and Bushra, A., 2006, "Power Law Turbulent Velocity Profile in Transitional Rough Pipes," J. Fluids Eng., **128**(3), pp. 548–558.
[15] Raupach, M. R., Antonia, R. A., and Rajagopalan, S., 1991, "Rough-Wall Turbulent Boundary Layer," Adv. Appl. Mech., **44**, pp. 1–25.
[16] Jimenez, J., 2004, "Turbulent Flow Over Rough Walls," Annu. Rev. Fluid Mech., **36**, pp. 173–196.
[17] Bendrict, R., 1980, *Fundamentals of Pipe Flow*, Wiley, New York, p. 240.
[18] Balachandar, R., Hager, K., and Blackely, D., 2002, "Velocity Distribution in Decelerating Flow Over a Surface," Can. J. Civ. Eng., **29**, pp. 211–221.
[19] Hager, W. H., 2003, "Blasius: A Life in Research and Education," Exp. Fluids, **34**, pp. 568–571.
[20] Nikuradse, J., 1932, *Laws of Turbulent Flow in Smooth Pipes*, VDI, Forchungsheft No. 356, English translation NASA TT F-10, 1966.
[21] Afzal, N., 1982, "Fully Developed Turbulent Flow in a Pipe: An Intermediate Layer," Arch. Appl. Mech., **52**, pp. 355–377.
[22] Afzal, N., 1984, "The Mesolayer Theory of Turbulent Flows," AIAA J., **22**, pp. 437–439.
[23] Afzal, N., and Seena, A., 2007, "Alternate Scales for Turbulent Flow in Transitional Rough Pipes: Universal Log Law," J. Fluids Eng., **129**(1), pp. 80–90.
[24] Moody, L. F., 1944, "Friction Factors for Pipe Flow," Trans. ASME, **66**, pp. 671–684.
[25] Yen, B. C., 2002, "Open Channel Flow Resistance," J. Hydraul. Eng., **128**, pp. 20–39.
[26] Grigson, C., 1987, "The Full Scale Drag of Ship Surface and the Effects of Quality Roughness on Predicted Power," J. Ship Res., **31**, pp. 189–206.
[27] Cebeci, T., 2004, *Analysis of Turbulent Flows*, Elsevier, New York.
[28] Shockling, M. A., 2005, "Turbulent Flow in Rough Pipe," MSE thesis, Princeton University, Princeton.
[29] Shockling, M. A., Allen, J. J., and Smits, A. J., 2006, "Roughness Effects in Turbulent Pipe Flow," J. Fluid Mech., **564**, pp. 267–285.
[30] Afzal, N., 1976, "Millikan Argument at Moderately Large Reynolds Numbers," Phys. Fluids, **19**, pp. 600–602.
[31] Izakson, A. A., 1937, "On Formula for the Velocity Distribution Near Walls," Zh. Tekh. Fiz., **4**, pp. 155–159.
[32] Millikan, C. B., 1938, "A Critical Discussion of Turbulent Flows in Channels and Circular Tubes," *Proceedings of the Fifth International Congress on Applied Mechanics*, edited by J. P. Den Hartog, and H. Peters, Wiley, New York, pp. 386–392.
[33] Patel, V. C., and Head, M. R., 1969, "Some Observations on Skin Friction and Velocity Profile in Fully Developed Pipe and Channel Flow," J. Fluid Mech., **38**, pp. 181–201.
[34] Afzal, N., and Yajnik, K., 1973, "Analysis of Turbulent Pipe and Channel Flows at Moderately Large Reynolds Number," J. Fluid Mech., **61**, pp. 23–31.
[35] Zagarola, M. V., and Smits, A. J., 1998, "Mean Flow Scaling in Turbulent Pipe Flow," J. Fluid Mech., **373**, pp. 33–79.
[36] McKeon, B. J., Zagarola, M. V., and Smits, A. J., 2005, "A New Friction Factor Relationship for Fully Developed Pipe Flow," J. Fluid Mech., **538**, pp. 429–443.
[37] Spalding, D. B., 1961, "A Single Formula for the Law of the Wall," J. Appl. Mech., **28**, pp. 455–458.
[38] McKeon, B. J., Swanson, C. J., Zagarola, M. V., Donnelly, R. J., and Smits, A. J., 2004, "Friction Factor for Smooth Pipe Flow," J. Fluid Mech., **511**, pp. 41–44.
[39] Allen, J. J., Shockling, M. A., and Smits, A. J., 2005, "Evaluation of a Universal Transitional Resistance Diagram for Pipes With Honed Surfaces," Phys. Fluids, **17**, p. 121702.

Chungpyo Hong
e-mail: cphong@comp.metro-u.ac.jp

Yutaka Asako

Department of Mechanical Engineering,
Tokyo Metropolitan University,
Minami-Osawa, Hachioji,
Tokyo, 192-0397, Japan

Stephen E. Turner
Naval Undersea Warfare Center,
Newport, Rhode Island, 02841

Mohammad Faghri
Department of Mechanical Engineering,
University of Rhode Island,
92 Upper College Road,
Kingston, Rhode Island 02881

Friction Factor Correlations for Gas Flow in Slip Flow Regime

*Poiseuille number, the product of friction factor and Reynolds number (fRe) for quasi-fully-developed gas microchannel flow in the slip flow regime, was obtained numerically based on the arbitrary-Lagrangian-Eulerian method. Two-dimensional compressible momentum and energy equations were solved for a wide range of Reynolds and Mach numbers for constant wall temperatures that are lower or higher than the inlet temperature. The channel height ranges from 2 μm to 10 μm and the channel aspect ratio is 200. The stagnation pressure p_{stg} is chosen such that the exit Mach number ranges from 0.1 to 1.0. The outlet pressure is fixed at atmospheric conditon. Mach and Knudsen numbers are systematically varied to determine their effects on f*Re*. The correlation for f*Re *for the slip flow is obtained from that of f*Re *of no-slip flow and incompressible theory as a function of Mach and Knudsen numbers. The results are in excellent agreement with the available experimental measurements. It was found that f*Re *is a function of Mach and Knudsen numbers and is different from the values by 96/(1+12Kn) obtained from the incompressible flow theory.* [DOI: 10.1115/1.2776966]

Keywords: friction factor, correlation, gas flow, microchannel, slip regime

Introduction

Design and fabrication of the microelectromechanical system (MEMS) have increased the need for understanding fluid flow and heat transfer in microgeometries. In the case of gaseous flow in a microchannel, it is well known that the rarefaction (the slip on the surface), the surface roughness, and the compressibility have significant effects, separately or simultaneously, on the results. Since the experimental work by Wu and Little [1,2], who measured the friction coefficient and Nusselt number for nitrogen, argon, and helium flows in silicon or glass microchannels, many experimental and numerical investigations have been undertaken.

The rarefaction effects can be studied by solving the momentum and energy equations with slip velocity and temperature jump boundary conditions (e.g., Refs. [3,4]). These effects are dominant when the characteristic length of the channel is less than about 10 μm and lead to a reduction in friction factor and heat transfer coefficient with increasing Kn number, as can be seen by Beskok et al. [5], Ameel et al. [6], Ahmed and Beskok [7], and Renksizbulut et al. [8].

The compressibility effects on fluid flow characteristics cause the flow to accelerate due to the decrease (variation) of the pressure and density along the channel, which leads to an increase in friction factor. This effect has been investigated by many researchers, e.g., Prud'homme et al. [9], Berg et al. [10], Guo [11], Sayegh et al. [12], Sun and Faghri [13], and Araki et al. [14,15].

Recently, the effects of surface roughness, rarefaction, and compressibility were experimentally investigated by Turner et al. [16,17]. The local pressure along the channel was measured, but only the average friction factor between the first and the last pressure taps was reported. Asako et al. [18,19] performed computational simulations on the effect of the compressibility for a wide range of Reynolds and Mach numbers in microchannels and microtubes. They found that *f*Re in the quasi-fully-developed region where the gas flow is accelerated is a function of Mach number and obtained a correlation for the result. They also compared their numerical results with experimental data by Turner et al. [17] for microchannels and with experimental data obtained from the tube cutting method for microtubes. They found that both results have similar trends. Ji et al. [20] performed a numerical analysis for a 2D compressible gas flow and heat transfer through a microchannel in the slip flow regime to investigate the effect of wall roughness. They found that in the case of the slow flow, *f*Re for high Kn flows are significantly lower than for low Kn flows. In the case of a high velocity flow at Ma_{out}=0.527, *f*Re increases along the smooth channel and reaches to 138. This value is lower than the local *f*Re correlation suggested by Asako et al. [18].

As can be seen above, there seems to be no literature on the parametric study of compressibility and rarefaction effects on local friction factor of slip flows. The motivation of the present study is to conduct numerical computations to obtain *f*Re in a quasi-fully-developed region of a microchannel with channel heights in the range of 2–10 μm.

Formulation

Description of the Problem and Conservation Equations. The problem is modeled as a parallel-plate channel, as shown in Fig. 1, with a chamber at the stagnation temperature T_{stg} and pressure p_{stg} attached to its upstream section. The flow is assumed to be steady, two dimensional, and laminar. The fluid is assumed to be an ideal gas. For the parallel-plate channel, the governing equations can be expressed as

$$\frac{\partial \rho u}{\partial x} + \frac{\partial \rho v}{\partial y} = 0 \tag{1}$$

$$\frac{\partial \rho u u}{\partial x} + \frac{\partial \rho u v}{\partial y} = -\frac{\partial p}{\partial x} + \mu\left(\frac{\partial^2 u}{\partial x^2} + \frac{\partial^2 u}{\partial y^2}\right) + \frac{\mu}{3}\frac{\partial}{\partial x}\left(\frac{\partial u}{\partial x} + \frac{\partial v}{\partial y}\right) \tag{2}$$

$$\frac{\partial \rho u v}{\partial x} + \frac{\partial \rho v v}{\partial y} = -\frac{\partial p}{\partial y} + \mu\left(\frac{\partial^2 v}{\partial x^2} + \frac{\partial^2 v}{\partial y^2}\right) + \frac{\mu}{3}\frac{\partial}{\partial y}\left(\frac{\partial u}{\partial x} + \frac{\partial v}{\partial y}\right) \tag{3}$$

$$\frac{\partial \rho u i}{\partial x} + \frac{\partial \rho v i}{\partial y} = -p\left(\frac{\partial u}{\partial x} + \frac{\partial v}{\partial y}\right) + \lambda\left(\frac{\partial^2 T}{\partial x^2} + \frac{\partial^2 T}{\partial y^2}\right) + \phi \tag{4}$$

where

Contributed by the Fluids Engineering Division of ASME for publication in the JOURNAL OF FLUIDS ENGINEERING. Manuscript received November 14, 2006; final manuscript received April 11, 2007. Review conducted by Dimitris Drikakis.

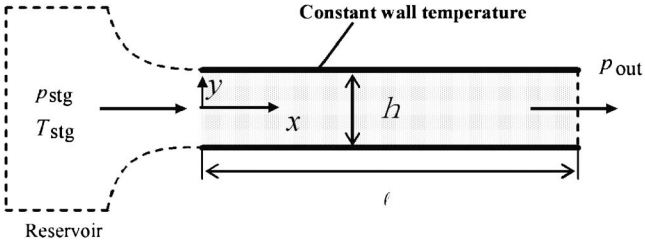

Fig. 1 A schematic diagram of problem

$$\phi = 2\mu\left[\left(\frac{\partial u}{\partial x}\right)^2 + \left(\frac{\partial v}{\partial y}\right)^2\right] - \frac{2\mu}{3}\left(\frac{\partial u}{\partial x} + \frac{\partial v}{\partial y}\right)^2 + \mu\left(\frac{\partial u}{\partial y} + \frac{\partial v}{\partial x}\right)^2 \tag{5}$$

The equation of the state for the ideal gas is expressed by

$$i = \frac{1}{\gamma - 1}\frac{p}{\rho} = \frac{R}{\gamma - 1}T \tag{6}$$

For slip flows, it is known that the rarefaction effects depend on the Knudsen number ($\mathrm{Kn} = \sigma/D_h$), which is the ratio of the gas mean free path to a characteristic length and is dominant when the characteristic length is less than 10 μm. These effects can be studied by solving Navier–Stokes equation with slip boundary conditions. In terms of flow field, when the Knudsen number is greater than 0.05, not only the velocity slip but also the Knudsen layer effects are accounted for the slip boundary conditions [21]. For Poiseuille flow, with a Knudsen number of Kn=0.05, the mass flow rate is approximately 15% greater than that of no-slip flow condition. About 70% of this mass flow rate increase is due to the velocity slip at the wall, and the remaining 30% is due to the Knudsen layer effects. However, in the present study, Knudsen number ranges from 0.0035 to 0.0175 when the channel height varies from 2 μm to 10 μm. Therefore, change in the mass flow rate due to the Knudsen layer effects is only 2%, and it is relatively small.

Rarefaction effects are studied by solving the momentum and energy equations with the slip boundary conditions, in which the velocity slip, temperature jump, and shear stress work on the wall are taken into account. With the assumptions of slip boundary conditions, uniform inlet velocity, pressure, density, and specified pressure, p_{out}, at the outlet, the boundary conditions can be expressed as follows:
at the inlet,

$$(x = 0):\ u = u_{in} \quad v = 0 \quad p = p_{in} \quad \rho = \rho_{in} \tag{7}$$

at the outlet,

$$(x = \ell):\ p = p_{out} \tag{8}$$

on the walls,

$$(y = \pm 0.5h):\ T = T_w \tag{9}$$

Furthermore, the slip boundary conditions at the walls, $y = \pm 0.5h$, are expressed as follows [22]:
the slip velocity at the wall,

$$u_{y=\pm 0.5h} = u_s = \mp \frac{2 - f}{f}\sigma\left(\frac{\partial u}{\partial y}\right)_{y=\pm 0.5h} \qquad v = 0 \tag{10}$$

the temperature jump at the wall,

$$T_{y=\pm 0.5h} = T_w \mp \frac{2 - \alpha}{\alpha}\frac{2\gamma}{\gamma + 1}\frac{\sigma}{\mathrm{Pr}}\left(\frac{\partial T}{\partial y}\right)_{y=\pm 0.5h} \tag{11}$$

the shear stress work at the wall,

$$\lambda\left(\frac{\partial T}{\partial y}\right)_{y=\pm 0.5h} = \dot{q}_w - \mu u_s\left(\frac{\partial u}{\partial y}\right)_{y=\pm 0.5h} \tag{12}$$

where σ is the mean free path, f is Maxwell's reflection coefficient, and α is the thermal accommodation coefficient. For fully diffuse reflection, $f=1$, and if it is assumed that the impinging molecules are accommodated to the wall temperature, $\alpha=1$ can be used.

The velocity, the pressure, and the density at the inlet of the channel are obtained by the stagnation treatment given by Karki [23]. The stagnation pressure can be expressed in terms of the inlet pressure, velocity, and specific internal energy as follows:

$$p_{stg} = p_{in}\left(1 + \frac{1}{2}\frac{u_{in}^2}{\gamma i_{in}}\right)^{\gamma/\gamma - 1} \tag{13}$$

Also, from the ideal gas law, the relationship for pressure and density between stagnation and inlet points can be expressed as

$$\frac{p_{stg}}{\rho_{stg}{}^{\gamma}} = \frac{p_{in}}{\rho_{in}{}^{\gamma}} \tag{14}$$

The static pressure at the inlet can be obtained from a linear extrapolation from the interior of the computational domain. By substituting the extrapolated pressure and the stagnation pressure into Eq. (14), the inlet density is obtained. Then, using the equation of state, the specific internal energy at the inlet can be found. Finally, the inlet velocity can be determined by substituting these values into Eq. (13). The procedure is repeated until convergence is achieved.

Dimensionless Variables. Attention will now be focused on the calculation of the Reynolds number, Mach, number and Knudsen number, which will be defined as

$$\mathrm{Re} = \frac{2\dot{m}}{\mu} = \frac{\bar{u}D_h}{\mu/\bar{\rho}} \quad \mathrm{Ma} = \frac{\bar{u}}{\sqrt{\gamma(\gamma - 1)\bar{i}}} \quad \mathrm{Kn} = \frac{\sigma}{D_h} = \sqrt{\frac{\pi\gamma}{2}}\frac{\mathrm{Ma}}{\mathrm{Re}} \tag{15}$$

where $\dot{m}$ is the mass flow and D_h is the hydraulic diameter. $\bar{u}$, $\bar{\rho}$, and $\bar{i}$ are the average velocity, density, and specific internal energy at a cross section,

$$\bar{u} = \frac{1}{A}\int udA \quad \bar{\rho} = \int \rho udA \Big/ \int udA$$

$$\bar{p} = \frac{1}{A}\int pdA \quad \bar{i} = \frac{1}{\gamma - 1}\frac{\bar{p}}{\bar{\rho}} \tag{16}$$

It is noteworthy that Re is constant but Ma varies along the channel, and for higher Re the effect of Ma (compressibility) is significant but for lower Re the Kn effect (rarefaction) is dominant.

The product of friction factor and Reynolds number is called Poiseuille number [24]. The friction factors based on Darcy's and Fanning's definitions will be introduced. The Darcy friction factor is defined as

$$f_d = \frac{-2D_h}{\overline{\rho u}^2}\left(\frac{d\bar{p}}{dx}\right) \tag{17}$$

The modified Fanning friction factors (four times of Fanning friction factor) is based on the wall shear stress and is defined as

$$f_f = \frac{4\tau_w}{(1/2)\overline{\rho u}^2} = \frac{4\mu(\partial u/\partial y)_{y=\pm h}}{(1/2)\overline{\rho u}^2} \tag{18}$$

Numerical Solutions. The numerical methodology is based on the arbitrary-Lagrangian-Eulerian (ALE) method proposed by Amsden et al. [25]. The detailed description of the ALE method is documented in the literature by Amsden et al. [25] and will not be given here. The computational domain is divided into quadrilat-

Table 1 Effect of grid size on Ma, f_fRe, and f_dRe

	Ma	f_fRe	f_dRe
Coarse grid (200×10)	0.1680	95.73	91.38
Medium grid (200×20)	0.1698	94.80	90.79
Fine grid (200×40)	0.1703	94.46	90.15
GCI between the fine grid and the medium grid	0.17%	0.28%	0.30%
GCI between the medium grid and the coarse grid	0.61%	0.76%	0.80%

Table 2 Channel height, length, p_{stg}, Re, Ma, and Kn

	h (μm)		
	2	5	10
ℓ (mm)	0.4	1	2
p_{stg} (kPa)	$400\rightarrow2200$	$300\rightarrow1200$	$200\rightarrow800$
Re	$8\rightarrow276$	$25\rightarrow466$	$37\rightarrow741$
Ma_{in}	$0.023\rightarrow0.146$	$0.038\rightarrow0.183$	$0.044\rightarrow0.221$
Ma_{out}	$0.098\rightarrow1.043$	$0.124\rightarrow1.042$	$0.091\rightarrow1.274$
Kn_{in}	$0.0043\rightarrow7.8\times10^{-4}$	$0.0023\rightarrow3.8\times10^{-4}$	$0.0017\rightarrow4.3\times10^{-4}$
Kn_{out}	$0.0184\rightarrow0.0058$	$0.0074\rightarrow0.0034$	$0.0037\rightarrow0.0025$

eral cells. The velocity components are defined at the vertices of the cell, and other variables such as pressures, specific internal energy, and density are assigned at the cell centers. The number of cells in the x direction was 200. The cell size gradually increases in the x direction from the inlet to the middle of the channel, and it gradually decrease to the exit. Since the velocity profile is almost parabolic in the quasi-fully-developed region, the number of cells in the y direction are fixed at 20 for all the computations. This grid alignment was determined from the results based on the generalized Richardson extrapolation and grid convergence index (GCI) suggested by Roche [26]. To determined the grid alignment, the supplementary runs were preformed with coarse grids (200×10) and fine grids (200×40). The grid size effects on Ma, f_fRe, and f_dRe were investigated for $T_w=350$ K of $h=5$ μm and $p_{stg}=400$ kPa. The results are tabulated in Table 1. The maximum GCI between the fine grid (200×40) and the medium grid (200×10) is 0.3%, and GCI between the medium grid (200×20) and the coarse grid (200×10) is 0.8%. Numerical uncertainties are reduced with the increase in grid density. By considering the balance between computation time and accuracy, all the computations were performed with the medium grid (200×20).

The ALE method is a time marching method. The value of 10^{-3} was used for the convergence criterion of the Newton–Raphson iteration, and the convergence for the time increment was confirmed by inequalities $|\Delta\dot{m}/\dot{m}|<10^{-10}$, where $\Delta\dot{m}$ represents change in the mass flow rate $\dot{m}$.

Results and Discussions

The computations were performed for three microchannels of 2 μm, 5 μm and, 10 μm. When air temperature ranges from 250 K to 350 K, C_p, μ, and λ of air vary, respectively, from 1.005 kJ (kg K)$^{-1}$ to 1.019 kJ (kg K)$^{-1}$, from 1.59×10^{-5} Pa s to 2.025×10^{-5} Pa s, and from 0.0226 W (m K)$^{-1}$ to 0.0293 W (m K)$^{-1}$. The changes in the values are relatively small. Therefore, constant properties are assumed except for the density. $R=287$ J (kg K)$^{-1}$, $\gamma=1.4$, $\mu=1.862\times10^{-5}$ Pa s, and $\lambda=0.0261$ W (m K)$^{-1}$ were assumed for the working fluid. The channel height ranges from 2 μm to 10 μm. The aspect ratio, which is the length to height ratio of the channel, is 200 and the developing length for the incompressible flow, ℓ/D_h, is 100 at Re=2000. The constant wall temperature was 250 K or 350 K, which is higher or lower than the stagnation temperature. The stagnation temperature was kept at $T_{stg}=300$ K. The stagnation pressure p_{stg} was chosen in such a way that the Mach number at the exit ranges from 0.1 to 1.0. The outlet pressure was maintained at atmospheric condition, $p_{out}=10^5$ Pa. The channel height, the channel length, the stagnation pressure, and the corresponding Reynolds, Mach, and Knudsen numbers in the case of $T_w=250$ K and 350 K are listed in Table 2. The Reynolds number obtained ranges from 8 to 741, and the Mach number at the outlet ranges from 0.098 to 1.274. The Knudsen number decreases with increasing Mach number for the slip flow. In other words, it was shown that the compressibility effect is important for higher Re and that the rarefaction effect is significant for lower Re.

Pressure and Temperature Distributions and Velocity Vector. The contour plots of the pressure and temperature for the flow in a channel of $h=5$ μm and $\ell=1$ mm are presented in Figs. 2(a) and 2(b), respectively, and the velocity vectors are presented in Fig. 2(c). The reference arrow in the figure represents a velocity of 100 m/s. The results are for the stagnation pressure of $p_{stg}=600$ kPa and the wall temperature of $T_w=350$ K. Figure 2(b) represents the temperature contours in the channel. The temperature in the core region of the channel decreases as a result of the energy conversion into kinetic energy. Figure 2(c) shows the gas flow with a uniform velocity at the inlet. Because of the viscosity, the velocity profile is nearly parabolic. However, the flow in the channel is accelerated and the average velocity increases. This is due to the volume expansion of the gas caused by the pressure drop. The pressure at any cross section of the channel is almost uniform and decreases along the channel. The pressure gradient becomes steep near the outlet, as seen in Fig. 3.

Velocity Profile. The velocity profiles of the quasi-fully-developed region for the channel of $h=2$ μm, $\ell=0.4$ mm, and $p_{stg}=1200$ kPa are plotted in Fig. 4. The Knudsen numbers of these results are 0.01 and 0.015. Corresponding Mach numbers are 0.46 and 0.67, respectively. The dotted line and the dashed line in the figure represent analytically obtained slip velocity profiles of Kn=0.01 and Kn=0.015, respectively, for a fully developed flow of the incompressible fluid. Also, the solid line represents the no-slip velocity profile. The velocity profiles of the incompressible flow are parabola. As seen in the figure, the velocity profiles of the compressible flow differ from those of the incompressible flow. The velocity of the compressible flow near the wall is faster than that of the incompressible flow, and a slightly higher friction factor is predicted. It can be seen that with increasing Kn, the maximum velocity at the center decreases whereas the slip velocity at the wall increases.

Poiseuille Numbers f_fRe and f_dRe. In the case of $h=2$ μm, Poiseuille numbers f_fRe and f_dRe for both $T_w=250$ K and 350 K are plotted as a function of x in Figs. 5(a) and 5(b), respectively. Using the Knudsen number that is calculated from Eq. (15), the value of fRe is obtained from $f\text{Re}=96/(1+12\text{Kn})$ and are plotted in the figure. As can be seen in Figs. 5(a) and 5(b), the channel can be divided into two regions. The region from the inlet to $x=0.1\ell$ can be considered as the entrance region where the friction factor decreases sharply. The region from $x=0.1\ell$ to the exit can be considered as the quasi-fully-developed region.

The value of f_dRe is higher than that of f_fRe because f_dRe includes the acceleration loss effect. The value of f_dRe for $T_w=250$ K (Fig. 5(a)) falls sharply near the entrance since the pressure drop is small and the density change strongly depends on the temperature near the inlet.

In the case of the slow flow (see $p_{stg}=400$ kPa and $p_{stg}=800$ kPa in Figs. 5(a) and 5(b)), the values of f_fRe and f_fRe

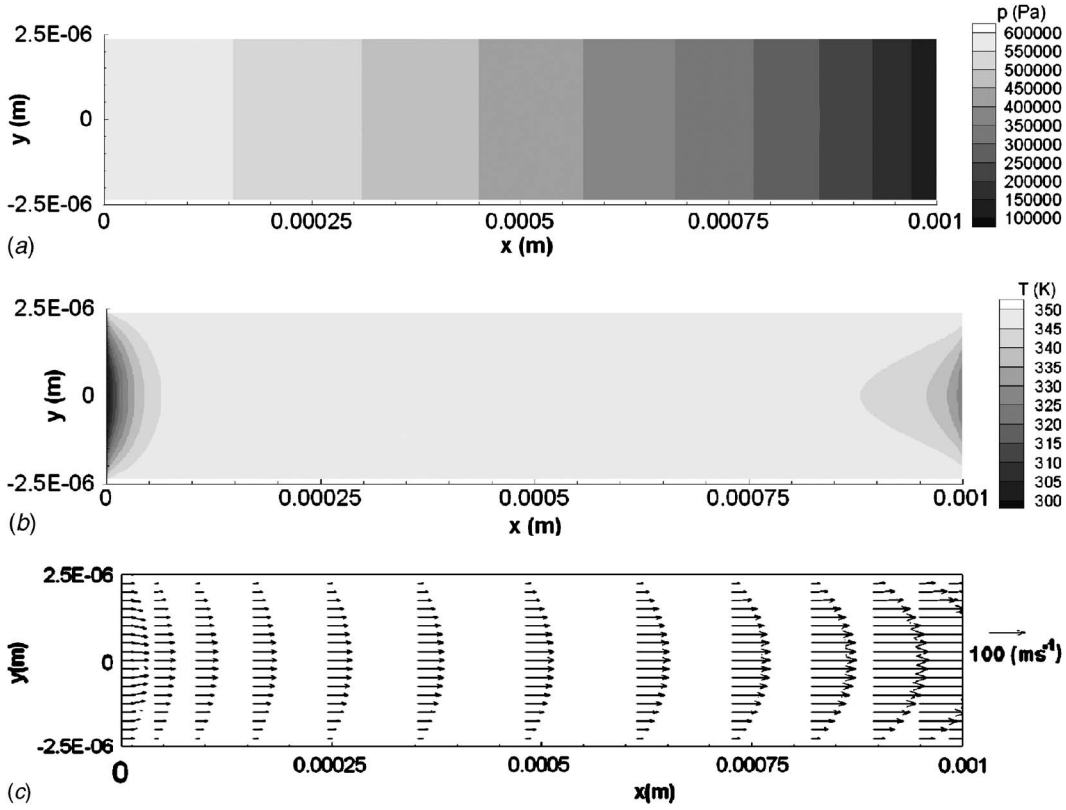

Fig. 2 Contour plot of (*a*) pressure, (*b*) temperature, and (*c*) velocity vector (T_w=350 K, h=5 μm, ℓ =1 mm, and p_{stg}=600 kPa)

decrease sharply near the entrance and decrease slightly along the channel due to the rarefaction effect. Then, the values of f_fRe almost coincide with those of incompressible flow for T_w =250 K and 350 K except at the entrance region. But the values of f_dRe depart from those of incompressible flow. On the other hand, in the case of the fast flow (see p_{stg}=1500 kPa and p_{stg} =2200 kPa in Figs. 5(*a*) and 5(*b*)), the values of f_fRe and f_dRe also decrease sharply near the entrance but increase along the channel due to the acceleration of the flow. Then, the values of f_fRe and f_dRe are higher than those of the incompressible flow. Therefore, the values of f_fRe and f_dRe in the slip flow cannot be predicted from the correlation of the incompressible theory. Qualitatively similar results are also obtained for the channels of h =5 μm and h=10 μm.

Correlation for *f*Re and Mach Number in the No-Slip Flow. In the previous work (Asako et al. [18]), it was found that the Poiseuille numbers f_fRe and f_dRe for Ma$<$0.4 and Re$<$500 are mainly functions of the Mach number, and the effect of Reynolds number is small in no-slip flow regime. However, the range of Ma and Re of the previous work is narrower compared with the present study. Therefore, in order to obtain the corresponding correlations of the Poiseuille numbers f_fRe and f_dRe for the slip flow,

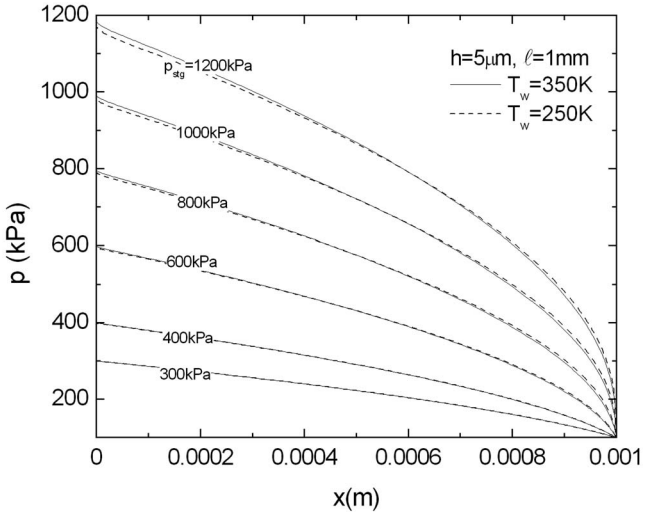

Fig. 3 Pressure variation along the channel (h=5 μm and ℓ =1 mm)

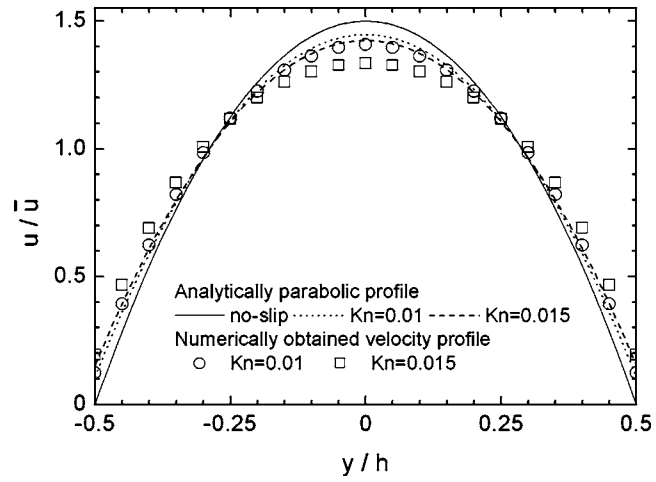

Fig. 4 Velocity profile

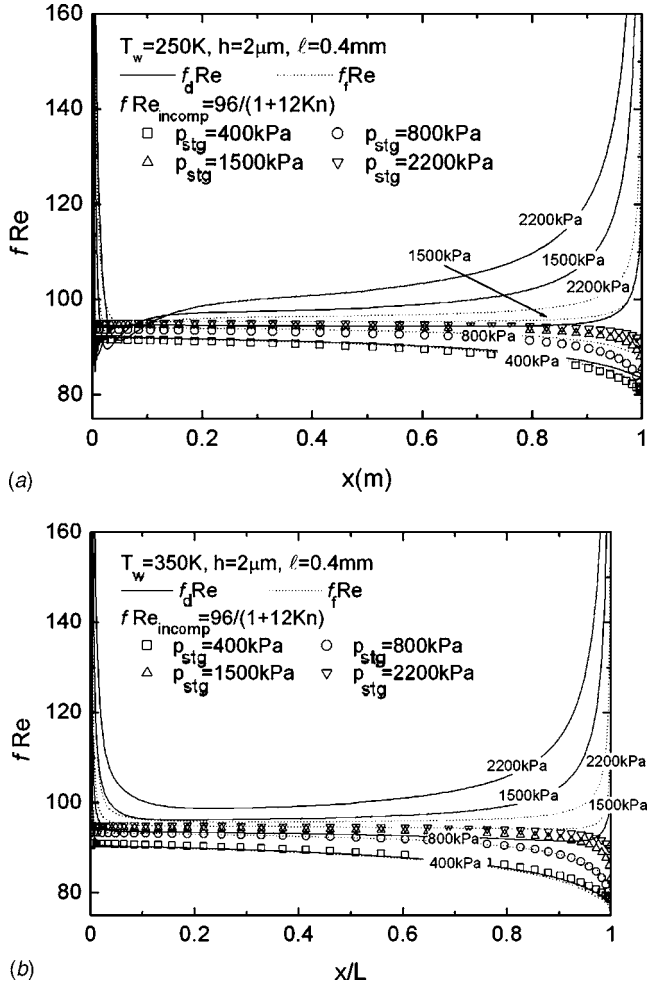

Fig. 5 ***f*Re as a function of *x* for *h*=2 μm: (*a*) T_w=250 K (*b*) T_w=350 K**

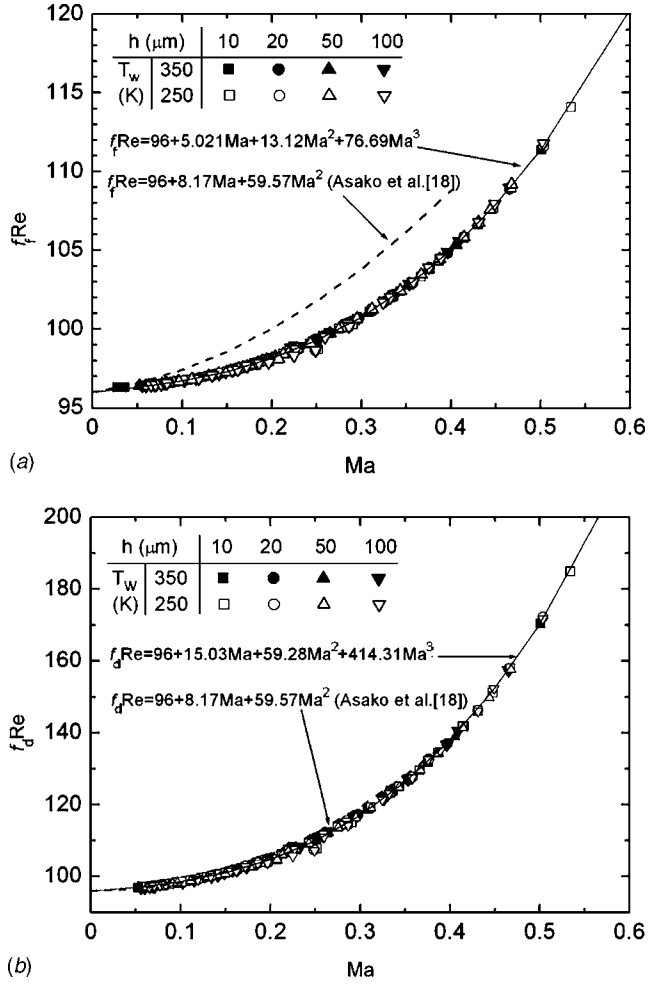

Fig. 6 ***f*Re as a function of Mach number for both T_w=250 K and T_w=350 K in the no-slip flow: (*a*) f_fRe (*b*) f_dRe**

supplementary calculations for T_w=350 K and T_w=250 K were also conducted for the channel of h=10, 20, 50, and 100 μm with no-slip boundary conditions.

The values of f_fRe and f_dRe at x=0.4ℓ, 0.6ℓ, 0.8ℓ, 0.9ℓ, and 0.95ℓ obtained are plotted as a function of the Mach number in Figs. 6(*a*) and 6(*b*), respectively. The results for both T_w=250 K and T_w=350 K are plotted in the same figures. The solid line in the figure represents the correlation for the *f*Re and the Mach number that is obtained by a polygonal curve fit as

$$f_f\mathrm{Re} = 96 + 5.02\mathrm{Ma} + 13.12\mathrm{Ma}^2 + 76.69\mathrm{Ma}^3 \tag{19}$$

$$f_d\mathrm{Re} = 96 + 15.03\mathrm{Ma} + 59.28\mathrm{Ma}^2 + 414.31\mathrm{Ma}^3 \tag{20}$$

The dashed lines in the figures represent the correlations obtained in the previous work [18]. The f_dRe correlation of the previous work coincides with Eq. (20). However, the f_fRe correlation of the previous work differs from Eq. (19). In the previous work, the f_tRe correlation was obtained from

$$f_f = 2D_h\left(\frac{d\bar{p}}{dx}\right)\left(\frac{1}{\bar{\rho}} - \frac{1}{\overline{\rho u^2}}\right) \tag{21}$$

However, the f_fRe difference between the previous and present works is less than 4%. The above correlations are obtained for the constant wall temperature, which is lower or higher than the stagnation temperature in the range of Re$<$3600 and Ma$<$0.6.

Contour Plots of f_fRe and f_dRe. Supplementary runs for T_w=350 K were performed for the channels of h=2 μm, 5 μm, and 10 μm with no-slip boundary conditions to investigate their influence on f_fRe and f_dRe from Mach and Knudsen numbers. The values of f_fRe at x=0.4ℓ, 0.6ℓ, 0.8ℓ, 0.9ℓ, and 0.95ℓ obtained for both no-slip flow and slip flow are presented in the form of a contour plot in Figs. 7(*a*) and 7(*b*) as a function of Ma, Re, and Kn. In the case of slow flow, the values of f_fRe and f_dRe decrease with increasing Kn due to the rarefaction effect. On the other hand, in the case of fast flow, the values of f_fRe and f_dRe increase with increasing Ma due to the compressibility effect.

For higher Re, f_fRe and f_dRe are mainly functions of the Mach number, and the effects of Reynolds and Knudsen numbers are small. However, for lower Re, f_fRe and f_dRe are not functions of the Mach number but mainly functions of the Knudsen number. Therefore, Mach and Knudsen numbers are systematically varied to determine their influence on f_fRe.

In the case of no-slip flow, as can be seen in Fig. 7(*a*), the values of f_fRe in the range of Ma$<$0.1 are not less than 96. The value of f_fRe at Ma=0.072 approaches 96.5 with Kn=0.013. On the other hand, in the case of slip flow, the values of f_fRe in the range of Ma$<$0.1 decrease less than 96 due to the rarefaction effect (Fig. 7(*b*)). The value of f_fRe at Ma=0.078 approaches 81.2 with Kn=0.013. However, the values of f_fRe for Ma$>$0.3 are almost the same for both no-slip and slip flow. Kn is less than 0.005, and the rarefaction effect cannot be seen. In the case of no-slip flow, the values of f_fRe at Ma=0.494 approaches 110.7,

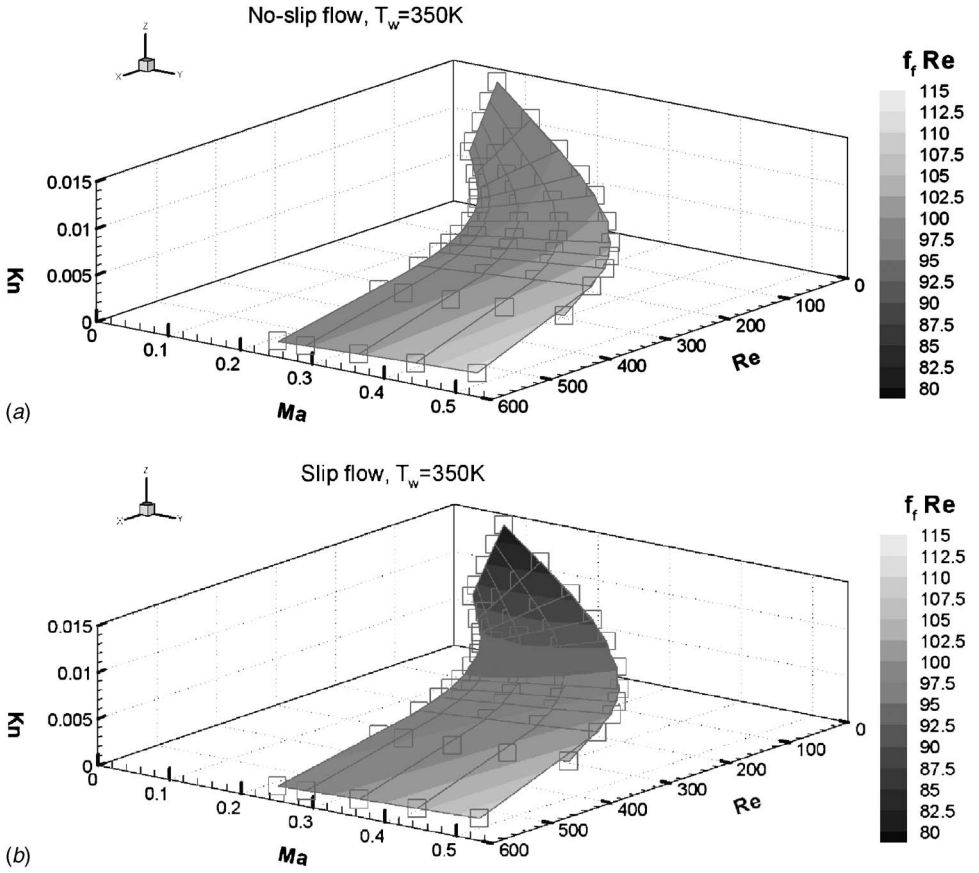

Fig. 7 Contour plot of f_fRe for T_w=350 K: (*a*) no-slip flow (*b*) slip flow

and in the case of slip flow, the values of f_fRe at Ma=0.497 approaches 109.1. Qualitatively similar results are also obtained for the values of f_dRe.

Correlation for *f*Re, Mach, and Knudsen Numbers in the Slip Flow. The values of f_fRe and f_dRe at $x=0.4\ell$, 0.6ℓ, 0.8ℓ, 0.9ℓ, and 0.95ℓ obtained for $T_w=350$ K and for $h=2$ μm to $h=10$ μm are presented in the form of a contour plot as a function of Ma and Kn in Figs. 8(*a*) and 8(*b*), respectively. In the slip flow, the flow is affected by the compressibility and rarefaction effects simultaneously, as shown in Fig. 7(*b*). It can be found that f_fRe and f_dRe are functions of Ma and Kn. The plains in the figures represent the correlation for *f*Re, Ma, and Kn, which is obtained from the correlation for *f*Re and Ma in no-slip flow (Eqs. (19) and (20)) and *f*Re of the incompressible theory in slip flow as

$$f_f\mathrm{Re} = \frac{96}{1+12\mathrm{Kn}} + \frac{5.02\mathrm{Ma} + 13.12\mathrm{Ma}^2 + 76.69\mathrm{Ma}^3}{(1+12\mathrm{Kn})^2} \quad (22)$$

$$f_d\mathrm{Re} = \frac{96}{1+12\mathrm{Kn}} + \frac{15.03\mathrm{Ma} + 59.28\mathrm{Ma}^2 + 414.31\mathrm{Ma}^3}{(1+12\mathrm{Kn})^2} \quad (23)$$

The values of f_fRe and f_dRe obtained from Eqs. (22) and (23) are also plotted as functions of Ma and Kn in the figures for $T_w=350$ K, respectively. White circles in the figures represent the calculation data. Vertical solid lines from the circles represent the discrepancies from Eqs. (22) and (23). As can be seen in the figures, f_fRe and f_dRe obtained by Eqs. (22) and (23) almost coincide with the calculation data within the range of ±2%. Qualitatively similar results are also obtained for $T_w=250$ K.

In the case of slow flow, the values of f_fRe and f_dRe decrease along the channel with increasing Ma and Kn due to the rarefaction effect. On the other hand, in the case of fast flow, the values of f_fRe and f_dRe increase along the channel with increasing Ma due to the compressibility effect. Namely, in the case of $\mathrm{Kn}_{\mathrm{in}} < 0.001$, the values of f_fRe and f_dRe increase along the channel with increasing Ma and Kn due to the compressibility effect. However, the rarefaction effect is relatively small with increasing Kn. On the other hand, in the case of $\mathrm{Kn}_{\mathrm{in}} > 0.001$, the values of f_fRe and f_dRe decrease along the channel with increasing Ma and Kn due to the rarefaction effect. However, the compressibility effect is relatively small.

For instance, the values of f_fRe for $T_w=350$ K and $h=5$ μm are plotted as a function of x in Fig. 9. Those obtained from the correlation for the f_fRe, Ma, and Kn (Eq. (22)) are also plotted in the figures. It can be seen that the values of f_fRe of calculations almost coincide with those of correlations except near the entrance region. The values of f_dRe coincide with those obtained (Eq. (23)), except near the entrance region. Qualitatively similar results are also obtained for $T_w=250$ K.

As a result of that, the values of f_fRe and f_dRe for both $T_w=250$ K and $T_w=350$ K in the slip flow can be predicted from the correlation for the *f*Re, Ma, and Kn (Eqs. (22) and (23)).

Comparisons With Experimental Data. Turner et al. [17] measured the local pressure of nitrogen, helium, and air flow along microchannels with a rectangular cross section. The microchannels were etched into silicon wafers and capped with a smooth glass. The channel length was about 27 mm and the hydraulic diameter ranges from 4 μm to 100 μm. Five pressure taps were located along the channel with equal spacing of 5 mm, and additional two pressure taps were at the inlet and outlet ports. The details of the experiment were well documented in the previous papers [16,17].

The semilocal friction factors were obtained from the pressure

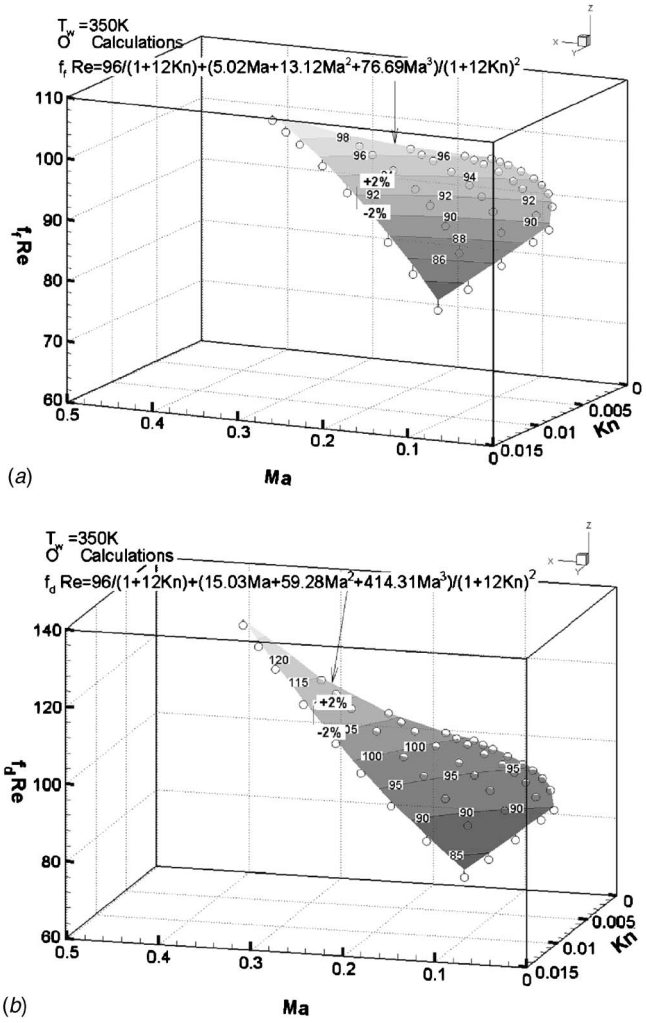

Fig. 8 *f*Re as a function of Ma and Kn for T_w=350 K: (*a*) f_fRe (*b*) f_dRe

data for nitrogen flows through the microchannels. The dimensions of the channels and the range of the inlet pressure and the Mach and Knudsen numbers are listed in Table 3. The outlet pressure was maintained at atmospheric condition for nitrogen flow. To facilitate the presentation of experimental data, Eqs. (22) and (23) obtained in a parallel-plate channel were arranged with the Poiseuille number of the incompressible flow, $f\mathrm{Re}_{\mathrm{incomp}}$ determined from the channel geometry (e.g., Ref. [27]) as

$$f_f\mathrm{Re} = \frac{f\mathrm{Re}_{\mathrm{incomp}}}{1+12\mathrm{Kn}} + \frac{5.02\mathrm{Ma}+13.12\mathrm{Ma}^2+76.69\mathrm{Ma}^3}{(1+12\mathrm{Kn})^2} \quad (24)$$

$$f_d\mathrm{Re} = \frac{f\mathrm{Re}_{\mathrm{incomp}}}{1+12\mathrm{Kn}} + \frac{15.03\mathrm{Ma}+59.28\mathrm{Ma}^2+414.31\mathrm{Ma}^3}{(1+12\mathrm{Kn})^2} \quad (25)$$

$f\mathrm{Re}_{\mathrm{incomp}}$ of Nos. 024 and 319 are 94.52 and 89.89, respectively. Then, contour plots of f_fRe obtained by Eq. (24) for Nos. 024 and 319 are presented in Figs. 10(*a*) and 10(*b*) as a function of Ma and Kn, respectively. The semilocal friction factors between the third and fourth pressure taps and fourth and fifth pressure taps were obtained from the experimental data using Eq. (21). Experimental results are also presented in the figures as a function of Ma and Kn. White circles in the figures represent experimental data. Vertical solid lines from the circles represent the discrepancies between Eq. (24) and experimental results. As can be seen in the figures, f_fRe obtained by Eq. (24) almost coincide with experimental data within ±2% for No. 024 and within 1% for No. 319.

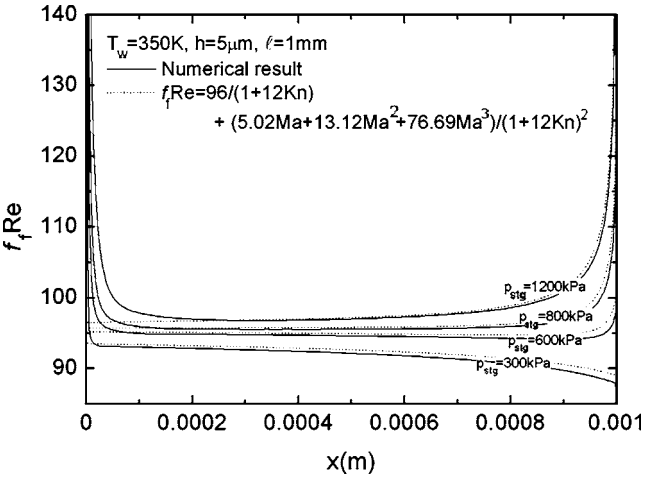

Fig. 9 f_fRe as a function of *x* for T_w=350 K

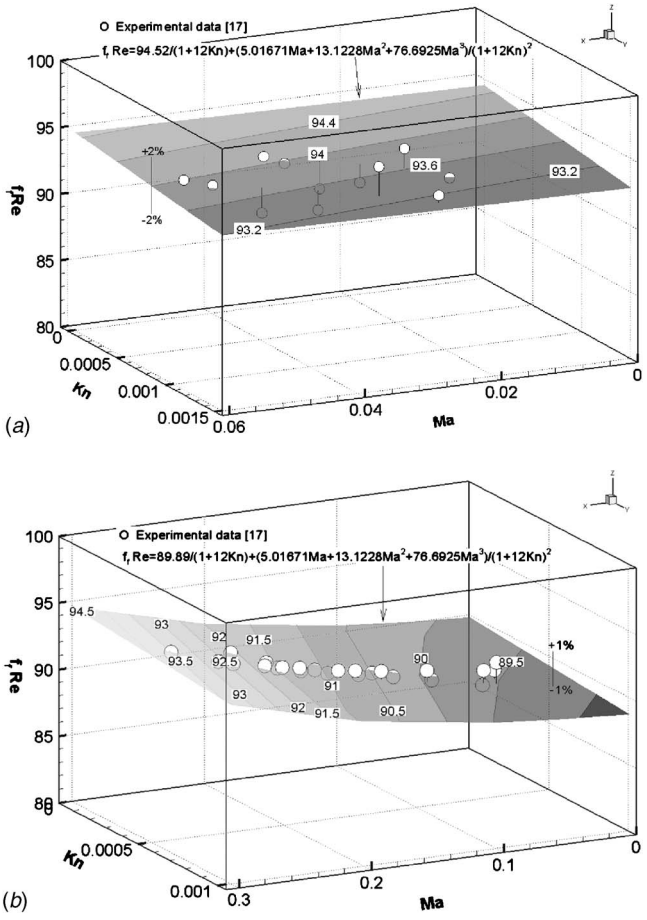

Fig. 10 Comparison of f_fRe with experimental data: (*a*) No. 024 (*b*) No. 319

Concluding Remarks

Two-dimensional compressible momentum and energy equations are solved for a parallel-plate microchannel in the slip flow regime. The computations were performed for constant wall temperature, which is lower or higher than the stagnation temperature. The following conclusions are reached.

(1) In the case of no-slip flow, both f_fRe and f_dRe are functions

Table 3 Channel dimensions, p_{in}, Ma, and Kn number [17]

No.	W (μm)	H (μm)	L (mm)	D_h (μm)	p_{in} (kPa)	Ma	Kn
024	1061	12.285	26.82	24.289	140–320	0.013–0.056	6.0×10^{-4}–0.0014
319	994	50.097	26.87	95.384	140–320	0.046–0.274	2.5×10^{-4}–6.3×10^{-4}

of the Mach number, and they differ from the incompressible value of 96 for a parallel-plate duct. The following correlations are obtained for the constant wall temperature, which is lower or higher than the stagnation temperature for $\mathrm{Re}<3600$ and $\mathrm{Ma}<0.6$.

$$f_f\mathrm{Re} = 96 + 5.02\mathrm{Ma} + 13.12\mathrm{Ma}^2 + 76.69\mathrm{Ma}^3$$

$$f_d\mathrm{Re} = 96 + 15.03\mathrm{Ma} + 59.28\mathrm{Ma}^2 + 414.31\mathrm{Ma}^3$$

(2) In the case of slip flow, both f_fRe and f_dRe are the functions of the Mach and Knudsen numbers, and they also differ from the incompressible value of $96/(1+12\mathrm{Kn})$ for a parallel-plate duct. The following correlations are obtained from the correlation for fRe and Ma in no-slip flow and fRe of the incompressible flow in slip flow as follows:

$$f_f\mathrm{Re} = \frac{96}{1+12\mathrm{Kn}} + \frac{5.02\mathrm{Ma} + 13.12\mathrm{Ma}^2 + 76.69\mathrm{Ma}^3}{(1+12\mathrm{Kn})^2}$$

$$f_d\mathrm{Re} = \frac{96}{1+12\mathrm{Kn}} + \frac{15.03\mathrm{Ma} + 59.28\mathrm{Ma}^2 + 414.31\mathrm{Ma}^3}{(1+12\mathrm{Kn})^2}$$

(3) The values of f_fRe and f_dRe of slip flow increase with increasing Mach number due to the compressibility effect such as those of no-slip flow and are lower than those of no-slip flow with increasing Kn.

(4) In the range of $0.2<\mathrm{Ma}<0.3$, the values of f_fRe and f_dRe obtained by the correlations of the slip flow almost coincide with the experimental data with an accuracy of 2%. To facilitate the presentation of experimental data, correlations of f_fRe and f_dRe are generalized by $f\mathrm{Re}_{\mathrm{incomp}}$ determined from the channel geometry.

Acknowledgment

Financial support from the Japan Society for the Promotion of Science (Grant-in-Aid for Scientific Research (C) No. 16560189) is greatly acknowledged.

Nomenclature

A = per-cycle transfer area per unit depth, m
C_p = specific heat, J kg^{-1} K^{-1}
D_h = hydraulic diameter (=$2h$), m
f = Maxwell's reflection coefficient
h = channel height, m
i = specific internal energy, J kg^{-1}
Kn = Knudsen number
ℓ = channel length, m
$\dot{m}$ = total mass flow rate per unit depth, kg (m s)$^{-1}$
Ma = Mach number
Nu = Nusselt number
p = pressure, Pa
Pr = Prandtl number
$\dot{q}_w$ = wall heat flux, W m^{-2}
R = gas constant, J kg^{-1} K^{-1}
Re = Reynolds number
T = temperature, K
T_w = wall temperature, K
u,v = velocity components, m s^{-1}
x,y = coordinates, m

Greek Symbols

α = thermal accommodation coefficient
ϕ = dissipation function
γ = specific heat ratio
λ = thermal conductivity, W m^{-1} K^{-1}
μ = viscosity, Pa s
ρ = density, kg m^{-3}
σ = molecular mean free path, m
τ = shear stress, N m^{-2}

Subscripts

in = inlet
out = outlet
stg = stagnation value

References

[1] Wu, P., and Little, W. A., 1983, "Measurement of Friction Factors for the Flow of Gases in Very Fine Channels Used for Microminiature Joule-Thomson Refrigerator," Cryogenics, **23**, pp. 273–277.
[2] Wu, P., and Little, W. A., 1984, "Measurement of the Heat Transfer Characteristics of Gas Flow in Fine Channel Heat Exchangers Used for Microminiature Refrigerators," Cryogenics, **24**, pp. 415–420.
[3] Arkilic, E. B., Schmidt, M. A., and Breuer, K. S., 1994, "Gaseous Flow in Microchannel," *ASME Symposium on Micro Machining and Fluid Mechanics*, pp. 1–10.
[4] Beskok, A., and Karniadakis, G. E., 1994, "Simulation of Heat and Momentum Transfer in Complex Microgeometries," J. Thermophys. Heat Transfer, **8**(4), pp. 647–655.
[5] Beskok, A., Karniadakis, G. E., and Trimmer, W., 1996, "Rarefaction and Compressibility Effects in Gas Microflows," ASME J. Fluids Eng., **118**, pp. 448–456.
[6] Ameel, T. A., Wang, X., Barron, R. F., and Warrington, R. O., 1997, "Laminar Forced Convection in a Circular Tube With Constant Heat Flux and Slip Flow," Microscale Thermophys. Eng., **1**(4), pp. 303–320.
[7] Ahmed, I., and Beskok, A., 2002, "Rarefaction, Compressibility, and Viscous Heating in Gas Microfilters," J. Thermophys. Heat Transfer, **16**(2), pp. 161–170.
[8] Renksizbulut, M., Niazmand, H., and Teracan, G., 2006, "Slip-Flow and Heat Transfer in Rectangular Microchannels With Constant Wall Temperature," Int. J. Therm. Sci., **45**, pp. 870–881.
[9] Prud″homme, R. K., Chapman, T. W., and Bowen, J. R., 1986, "Laminar Compressible Flow in a Tube," Appl. Sci. Res., **43**, pp. 67–74.
[10] Berg, H. R., Seldam, C. A., and Gulik, P. S., 1983, "Compressible Laminar Flow in a Capillary," J. Fluid Mech., **246**, pp. 1–20.
[11] Guo, Z. Y., 2000, "Size Effect on Flow and Heat Transfer Characteristics in MEMS," *Proceedings of the International Conference on Heat Transfer and Transport Phenomena in Microscale*, Banff, Canada, pp. 24–31.
[12] Sayegh, R., Faghri, M., Asako, and Y., Sunden, B., 1999, "Direct Simulation Monte Carlo of Gaseous Flow in Micro-Channel," *Proceedings of the ASME National Heat Transfer Conference*, Albuquerque, NM, Paper No. HTD99-256.
[13] Sun, H., and Faghri, M., 1999, "Effect of Rarefaction and Compressibility of Gaseous Flow in Microchannel Using DSMC," Numer. Heat Transfer, Part A, **38**, pp. 153–158.
[14] Araki, T., Kim, M. S., Inaoka, K., and Suzuki, K., 1999, "An Experimental Investigation of Gaseous Flow Characteristics in Micro-Tubes," *Proceedings of Kyoto University-Tsinghua University Joint Conference on Energy and Environment*, pp. 7–12.
[15] Araki, T., Kim, M. S., Inaoka, K., and Suzuki, K., 2002, "An Experimental Investigation of Gaseous Flow Characteristics in Microchannels," Microscale Thermophys. Eng., **6**, pp. 117–130.
[16] Turner, S. E., Sun, H., Faghri, M., and Gregory, O. J., 2000, "Effect of Surface Roughness on Gaseous Flow Through Microchannels," *IMECE*, HTD-Vol 366, pp. 291–298.
[17] Turner, S. E., Lam, L. C., Faghri, M., and Gregory, O. J., 2004, "Experimental Investigation of Gas Flow in Microchannel," ASME J. Heat Transfer, **127**, pp. 753–763.
[18] Asako, Y., Pi, T., Turner, S. E., and Faghri, M., 2003, "Effect of Compressibility on Gaseous Flows in Micro-Channels," Int. J. Heat Mass Transfer, **46**, pp. 3041–3050.

[19] Asako, Y., Nakayama, K., and Shinozuka, T., 2005, "Effect of Compressibility on Gaseous Flows in a Micro Tube," Int. J. Heat Mass Transfer, **48**, pp. 4985–4994.
[20] Ji, Y., Yuan, K., and Chung, J. N., 2006, "Numerical Simulation of Wall Roughness on Gaseous Flow and Hea Transfer in a Microchannel," Int. J. Heat Mass Transfer, **49**, pp. 1329–1339.
[21] Lockerby, D. A., Reese, J. M., and Gallis, M. A., 2005, "The Usefulness of Higher-Order Constitutive Relations for Describing the Knudsen Layer," Phys. Fluids, **17**(10), p. 100609.
[22] Sparrow, E. M., and Lin, S. H., 1962, "Laminar Heat Transfer in Tubes Under Slip-Flow Conditions," ASME J. Heat Transfer, **84**(4), pp. 363–369.
[23] Karki, K. C., 1986, "A Calculation Procedure for Viscous Flows at All Speeds in Complex Geometries," Ph.D. thesis, University of Minnesota, Minneapolis.
[24] Churchill, S. W., 1988, *Viscous Flows: The Practical Use of Theory*, Butterworths, Boston.
[25] Amsden, A. A., Ruppel, H. M., and Hire, C. W., 1980, "SALE a Simplified ALE Computer Program for Fluid Flow at All Speeds," Los Alamos Scientific Laboratory Report No. LA-8095.
[26] Roche, P. J., 1994, "Perspective: A Method for Uniform Reporting of Grid refinement Studies," ASME J. Fluids Eng., **116**, pp. 405–413.
[27] Shah, R. K., and London, A. L., 1978, *Laminar Flow Forced Convection in Ducts, Advances in Heat Transfer Supplement, 1*, Academic, New York.

Linear Instability of Entry Flow in a Pipe

Kirti Chandra Sahu

Rama Govindarajan
e-mail: rama@jncasr.ac.in

Engineering Mechanics Unit,
Jawaharlal Nehru Centre for Advanced
Scientific Research,
Bangalore-560 064, India

We show that flow in the entry region of a circular pipe is linearly unstable at a Reynolds number of 1000, a factor of 10 smaller than assumed hitherto. The implication that dynamics in this region could greatly hasten the transition to turbulence assumes relevance because in spite of major recent progress, the issue of how pipe flow becomes turbulent is far from settled. Being axisymmetric and close to the centerline, the present instability would be easily distinguishable in an experiment from other generators of turbulence. [DOI: 10.1115/1.2776965]

1 Introduction

The fully developed laminar flow through a circular pipe is linearly stable at any Reynolds number (see, e.g., Ref. [1]). The mechanisms driving the flow to turbulence are being investigated avidly [2–7]. When and whether the transient algebraic growth of disturbances is crucial or whether the route is entirely nonlinear [8] is still not clear. In this paper, we do not address this debate. Our purpose is to bring to light a factor, which has hitherto been considered unimportant, namely, the exponential growth of disturbances in the entry region. Thus, the very assumption that the flow is fully developed could obscure the complete route to turbulence. The distance l_e from the pipe entrance required to reach the fully developed parabolic profile can be very long [9–11] and scales linearly with the Reynolds number Re, roughly as $l_e/R \sim \mathrm{Re}/20$, where R is the pipe radius. This means that high Reynolds number laminar flow through a pipe of limited length may never reach a parabolic state. With many recent demonstrations [2,12] that pipe flow may be maintained laminar up to very high Reynolds numbers (of the order of hundred thousand), an understanding of the instability of the entry flow is increasingly relevant. Even at much lower Reynolds numbers, observations [10,13,14] indicate that turbulent slugs and spots most often originate in the entry region.

We show that exponential growth of disturbances in the entry region occurs at a Reynolds number of 1000, an order of magnitude lower than predicted by earlier theoretical work. Thus, linear instability can play a more important role on the route to turbulence than estimated up to now. We bring a recently developed sophisticated solution method for nonparallel stability to bear on this problem. This is the first time, to our knowledge, that this problem is solved in a consistent manner. Recent work on entry flow is either on finite amplitude perturbations [15,16] or on estimates of transient growth [17], not on linear instability. The existence of exponential growth, even over a short axial extent, means that transient growth and nonlinearities will be enhanced significantly, hastening the transition to turbulence.

A body of work on linear instability was done several decades ago, with large discrepancy among the theoretical results. For example, Tatsumi [18], Huang and Chen [19], Garg [20], and Gupta and Garg [21] obtained critical Reynolds numbers for linear instability, $\mathrm{Re}_{\mathrm{cr}}$, of 9700, 19,750, 13,250, and 11,700, respectively. The typical pipe is known to undergo a transition to turbulence at a far lower Reynolds number, of about 2000, in which case the linear instability in the entry region may be deemed to be of only academic interest. Probably due to this, the disagreements were never resolved. It is only recently that laminar flow has been achievable at Reynolds number exceeding 100,000, see, e.g., Ref. [2], in such cases the entry region will obviously play an important role in the transition to turbulence. The contrast with experiment, where linear instabilities were seen at a Reynolds number as low as 3800 [13], was not investigated. All theoretical studies of linear instability, to our knowledge, have made two major approximations: (i) the basic flow, whose stability is being studied, is taken in an approximate form, usually of boundary-layer type, and (ii) the stability is studied under the assumption of locally parallel flow. Both of these represent physics inadequately, as we find. Given the current interest in pipe transition, it is imperative to study this flow with better technique, which includes all the physics. As described in Sec. 2, we obtain the basic flow in a long entry region accurately. A nonparallel stability analysis is conducted, correct to $O(\mathrm{Re}^{-1})$ as described in Sec. 3.

2 Mean Flow

The flow studied here is through a straight pipe (shown in Fig. 1) with a uniform streamwise velocity U_i at the inlet. We solve the axisymmetric Navier–Stokes equations for steady, incompressible Newtonian flow in the stream function-vorticity formulation using a six-level full-multigrid method on a parallel machine. The equations are nondimensionalized by the streamwise velocity U_i at the inlet and the radius of the pipe R. The Reynolds number is thus $\mathrm{Re} \equiv U_i R/\nu$, where ν is the kinematic viscosity. A large enough length of pipe is considered for the Neumann condition to be applicable at the outlet, and the exit profile is checked to be parabolic. The details of the solution method and its validation are given in Refs. [22,23]. Axial (U) and radial (V) velocity profiles at different axial locations for $\mathrm{Re}=5000$ are shown in Figs. 2(a) and 2(b), respectively. The exact solution is found to be considerably different from all the approximate profiles used in earlier studies.

3 Nonparallel Stability Analysis

3.1 Formulation. To study the stability of this flow, each quantity is expressed as the sum of a mean and a three-dimensional perturbation, e.g.,

$$u_{\mathrm{tot}} = U(x,r) + \hat{u}(x,r,\theta,t) \tag{1}$$

where x, r, and θ are the axial, radial, and azimuthal coordinates respectively; u, v and w are the corresponding velocity components; the subscript tot stands for "total;" and t is time. For $\mathrm{Re} \gg 1$, we have $\partial/\partial x \ll \partial/\partial r$, and therefore $V \sim O(\mathrm{Re}^{-1})$, as is verified numerically, see Fig. 2(b). This simplifies our approach, since it enables us to express the x dependence of the perturbations as the product of a rapidly varying wavelike part, $\exp[i\int \alpha(x)\mathrm{d}x]$, and a slowly varying function, $u(x,r)$, such that $\partial u/\partial x \sim O(\mathrm{Re}^{-1})$. The approach followed is thus similar to Ref. [22]. In combination with a normal mode form in θ and t, the streamwise velocity perturbation may be written as

Contributed by the Fluids Engineering Division of ASME for publication in the JOURNAL OF FLUIDS ENGINEERING. Manuscript received November 10, 2006; final manuscript received May 22, 2007. Review conducted by Dimitris Drikakis.

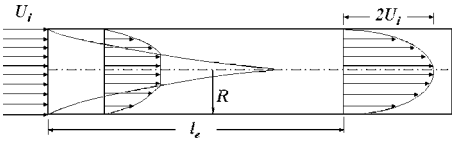

Fig. 1 Schematic of the developing flow in the entry region of a pipe; not to scale

$$\hat{u} = \mathrm{Re}\left\{ u(x,r)\exp\left[i\left(\int \alpha(x)\mathrm{d}x + n\theta - \beta t \right) \right] \right\} \tag{2}$$

where n is the number of waves in the azimuthal direction, and β is the disturbance frequency. The continuity and momentum equations are linearized, and terms of $O(\mathrm{Re}^{-2})$ and smaller terms are neglected. The final equation is of the form

$$\mathcal{H}\phi(x,r) + \mathcal{G}\frac{\partial\phi(x,r)}{\partial x} = \beta\mathcal{B}\phi(x,r) \tag{3}$$

Here $\phi=[u,v,w,p]^T$, and the nonzero elements of the 4×4 matrix operators $\mathcal{H}$, $\mathcal{G}$, and $\mathcal{B}$ are given by

$$h_{11} = Ui\alpha + \mathcal{D}_x U + V\mathcal{D}_r + \mathcal{Q} - \frac{1}{\mathrm{Re}}\frac{1}{r^2} \quad h_{12} = \mathcal{D}_y U$$

$$h_{14} = i\alpha \quad h_{23} = \frac{2}{\mathrm{Re}}\frac{in}{r^2} \quad h_{22} = V\mathcal{D}_r + \mathcal{D}_r V + Ui\alpha + \mathcal{Q}$$

$$h_{24} = \mathcal{D}_r \quad h_{32} = -\frac{2}{\mathrm{Re}}\frac{in}{r^2} \quad h_{33} = V\mathcal{D}_r - \frac{V}{r} + Ui\alpha + \mathcal{Q}$$

$$h_{34} = \frac{in}{r} \quad h_{41} = \frac{i\alpha}{\mathrm{Re}}\mathcal{D}_r \quad h_{42} = V\mathcal{D}_r + \mathcal{D}_r V + Ui\alpha + \frac{1}{\mathrm{Re}}\left(\frac{n^2}{r^2} + \alpha^2\right) \quad h_{43} = \frac{in}{\mathrm{Re}}\left(\frac{1}{r^2} + \frac{\mathcal{D}_r}{r}\right) \quad h_{44} = \mathcal{D}_r$$

$$g_{11} = g_{22} = g_{33} = g_{42} = U \quad g_{14} = 1$$

and

$$b_{11} = b_{22} = b_{33} = b_{42} = i \quad \text{where } \mathcal{D}_r = \frac{\partial}{\partial r}$$

$$\mathcal{D}_x = \frac{\partial}{\partial x}$$

and

$$\mathcal{Q} = \frac{1}{\mathrm{Re}}\left[\alpha^2 + \frac{(1+n^2)}{r^2} - \frac{1}{r}\frac{\partial}{\partial r} - \frac{\partial^2}{\partial r^2} \right]$$

The boundary conditions are

$$u = v = w = p = 0 \quad \text{at } r = 0 \quad \text{for } n \neq 1 \tag{4}$$

$$u = p = 0 \quad v + iw = 0 \quad \text{at } r = 0 \quad \text{for } n = 1 \tag{5}$$

$$u = v = w = 0 \quad \text{at } r = 1 \tag{6}$$

Incidentally, Eq. (3) may be obtained from the stability equation in Ref. [22] by setting the angle of pipe divergence to zero. The system of partial differential equations obtained here may be solved as an eigenvalue problem of larger size as described in the following section.

3.2 Solution Method. The streamwise derivative in Eq. (3) couples neighboring axial locations in the flow field to one another. Consider two streamwise Locations 1 and 2 separated by an incremental distance, i.e., $x_2=x_1+\Delta x$. To first order in Δx, and noting that β remains constant downstream, we may express Eq. (3) as

$$\begin{bmatrix} \mathcal{H}_1 - \mathcal{G}_1/\Delta x & \mathcal{G}_1/\Delta x \\ -\mathcal{G}_2/\Delta x & \mathcal{H}_2 + \mathcal{G}_2/\Delta x \end{bmatrix}\begin{bmatrix} \phi_1 \\ \phi_2 \end{bmatrix} = \beta\begin{bmatrix} \mathcal{B}_1 & 0 \\ 0 & \mathcal{B}_2 \end{bmatrix}\begin{bmatrix} \phi_1 \\ \phi_2 \end{bmatrix} \tag{7}$$

The partial differential equation now has the appearance of an eigenvalue problem of twice the size of the corresponding parallel stability problem. The discretization and solution of the eigensystem are done using a Chebyshev collocation spectral method, described, for example, in Ref. [24]. The collocation points given by

$$y_i = \cos(i\pi/N) \quad i = 1,N \tag{8}$$

are naturally denser near the wall and sparser close to the centerline, so no further grid stretching is necessary. The results shown here have been obtained with 81 grid points; the accuracy is discussed later in this section.

Note that in Eq. (2), the x dependence may be apportioned arbitrarily between α and the eigenfunction u as long as all rapid variations in the axial direction are included in the wavelike part, to ensure that $\partial u/\partial x$ is small. To do this, we first set the operator $\mathcal{G}$ to zero and solve the resulting eigenvalue problem at Locations 1 and 2 independently. At each location, we choose a guess value of α and iterate it until the desired complex frequency β_0 is obtained. The operators $\mathcal{H}$, $\mathcal{G}$, and $\mathcal{B}$ are then known at Locations 1 and 2, so Eq. (7) can be solved. This procedure works since the ordinary differential equation differs from the partial differential equation only in terms nominally of $O(\mathrm{Re}^{-1})$. We have verified numerically that choosing other suitable initial guesses for $\mathcal{G}$ makes no difference to the results.

The growth rate g of the disturbance kinetic energy, $E=1/2(\hat{u}^2+\hat{v}^2+\hat{w}^2)$, is given by

$$g = \frac{1}{E}\frac{\partial E}{\partial x} = -2\alpha_i + \left.\frac{1}{E_e}\frac{\partial E_e}{\partial x}\right|_r \tag{9}$$

where $E_e=1/4(uu^*+vv^*+ww^*)$, the asterisk denotes a complex conjugate. It is characteristic of developing flow that a disturbance may amplify at one radial location and decay at another. Secondly, one disturbance quantity (e.g., $\hat{u}$) could be amplified while others decay.

Typical values of α obtained by using different numbers of

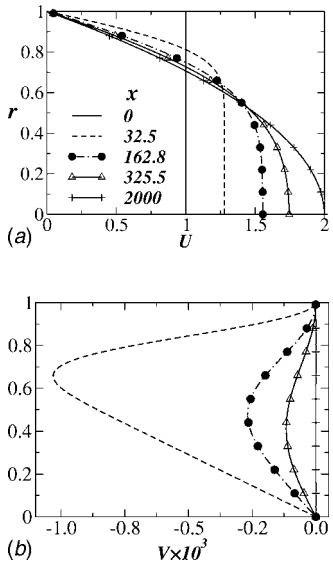

Fig. 2 (*a*) Axial and (*b*) radial velocity profiles at different streamwise locations; Re=5000

Table 1 Sensitivity of wavenumber and growth rate to the number of collocation points used

No. of grid points (N)	α_r	α_i
51	0.499990	−0.000748914
61	0.490003	−0.000744894
81	0.490001	−0.000743789

collocation points for Re=5000, $x=183.5$, and $\beta_d=0.5$ are shown in Table 1. It is seen that 81 grid points are sufficient to make a statement about stability.

4 Results and Discussion

Present eigenvalues for fully developed pipe flow match with those of Ref. [25] up to the tenth decimal place. While the least stable mode for fully developed flow is the helical ($n=1$) mode, the axisymmetric ($n=0$) mode is found to be the most unstable here, consistent with experiment [13]. At Re=5000, the variation with axial distance of amplitude of disturbance kinetic energy is shown in Fig. 3. Disturbances of frequencies outside the range shown are found to be less unstable. The variation is monitored here at $r=0.08$. The flow is linearly unstable within a certain axial extent. Too far upstream, the effective Reynolds number of the shear layer is too low for instability, and downstream; the flow is closer to fully developed and thus linearly stable. It is found (not shown) that the disturbance kinetic energy decays for $r>0.6$, and that its growth is maximum close to the centerline. Thus an experiment where the probe is positioned within $0<r<0.6$ would measure exponential growth of disturbances of the right frequency, while probes placed closer to the wall would register a stable flow. The disturbance kinetic energy integrated across the pipe decays at these Reynolds numbers. We thus expect a greater tendency toward turbulence close to the centerline, in contrast with other mechanisms.

Under the parallel flow approximation, earlier studies neglected the "small" variations in the downstream direction, as well as the small radial mean flow. With consistent matched asymptotic expansions in the distinguished limits, it has been shown that these effects are not small [26]. In fact, the axial development of the flow makes $O(1)$ contributions over some radial extent. The largest effects come from the terms in the stability equations containing V multiplied by a radial derivative of the eigenfunction, as we found numerically and from the estimates of order of magnitude. What is happening physically is that the negative radial mean flow sweeps disturbance vorticity away from the wall and toward the centerline, which affects stability dramatically. The parallel flow approximation, even using the accurate basic flow, completely misses this physics and finds the flow to be stable, as seen in Fig. 3.

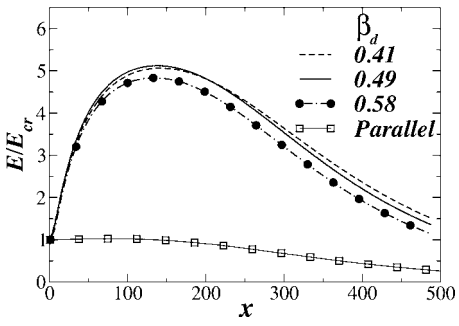

Fig. 3 Amplification of the disturbance kinetic energy for the axisymmetric ($n=0$) mode for typical disturbance frequencies for Re=5000 at $r=0.08$. The result with a parallel flow assumption is shown by the solid line with squares.

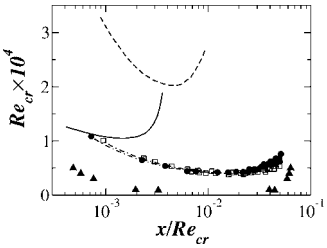

Fig. 4 Axial variation of the critical Reynolds number. Filled triangles, axisymmetric mode at $r=0.25$. Filled circles and open squares, experimental results [13]. The theoretical results of Refs. [18,19] for axisymmetric disturbances are shown by the dashed and solid lines, respectively. The results of Refs. [13,18,19] were compliled in this manner in Ref. [15].

In the experiments compiled by [13], the variation in amplitude of the axial disturbance velocity $\hat{u}$ was the quantity measured, which gives the result integrated over all eigenmodes. Since only a small range of frequencies is unstable at the Reynolds numbers considered, we expect the experiment to display a significantly lower level of instability than predicted by the stability analysis. We also do not expect $\hat{u}$ to correlate exactly with E. Also, stability is a function of r, and the measurements were made at one or more unspecified radial locations. Figure 4 shows the present zero growth curve at $r=0.25$. The region above the curves is unstable, indicating the axial extent of possible exponential growth at a given Reynolds number. The qualitative behavior is the same as the experiments, with a larger region of instability, as expected. Note that at a Reynolds number of 1000, the flow is already linearly unstable over a short axial extent. The growth rates (not shown) at this Reynolds number, however, are extremely small and would be difficult to see in an experiment. The effect of these modes on the transition at this Reynolds number would be indirect, via transient growth, but probably already not insignificant. It is clear from the same figure that the critical Reynolds numbers predicted by earlier theoretical studies are unrealistically high. Figure 5(a) demonstrates that at $r=0.25$, while the predicted neutral boundary is larger than in the experiments, the extent over which the kinetic energy grows by 1.8 times or more of its original amplitude matches very well with the experimental neutral boundary. A modern experiment where instability of a given frequency could be detected accurately at a specified radial location would be very valuable. The regions of instability at different radial locations are shown in Fig. 5(b). In accordance with the expectations above, disturbance growth is much higher closer to the centerline rather than at the wall. In the existing experiments, the radial location at which measurements were made is not mentioned; the prediction here that disturbance growth is a sensitive function of the radial location will hopefully motivate further experimental work.

To summarize, flow in the entry region of a pipe is already linearly unstable at a Reynolds number of 1000, an order of magnitude lower than computed hitherto, so this region could play a more important role in transiiton to turbulence than realized. The advection toward the centerline of the disturbance vorticity by the small radial mean flow is the generator of this instability. We have made no approximation in solving for the mean flow and have performed a complete nonparallel analysis correct to $O(\mathrm{Re}^{-1})$. Our results are in qualitative agreement with existing experiment, but more accurate experiments are needed. The present instability is axisymmetric and most active near the centerline, which clearly distinguishes it from other mechanisms of transition to turbulence, such as low-speed streaks. This would make it more appealing to the experimenter.

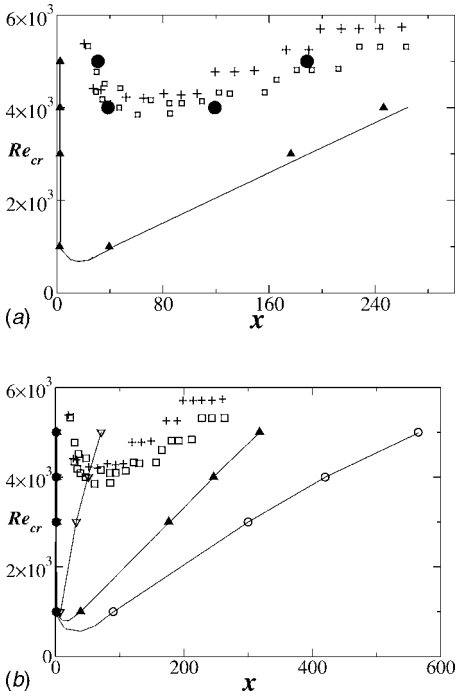

Fig. 5 Axial variation of the critical Reynolds number ($n=0$ mode). Plus and open squares: experimental results [13] for nonaxisymmetric and axisymmetric disturbances, respectively. (*a*) At $r=0.25$. Filled triangles, neutral boundary; filled circles, where $E/E_{cr}=1.8$. (*b*) Open circles, $r=0.5$; filled triangles, $r=0.25$; open triangles, $r=0.08$. The lines are shown to guide the eye.

Acknowledgment

Grateful thanks to Professor Tom Mullin for the thesis of S. D. Williams and for discussions. We acknowledge the Defense Research and Development Organisation, India for financial support.

References

[1] Lessen, M., Sadler, S. G., and Liu, T. Y., 1968, "Stability of Pipe Poiseuille Flow," Phys. Fluids, **11**, pp. 1404–1409.
[2] Hof, B., van Doorne, C. W. H., Westerweel, J., Nieuwstadt, F. T. M., Faisst, H., Eckhardt, B., Wedin, H., Kerswell, R. R., and Waleffe, F., 2004, "Experimental Observation of Nonlinear Traveling Waves in Turbulent Pipe Flow," Science, **305**, pp. 1594–1598.
[3] Hof, B., Juel, A., and Mullin, T., 2003, "Scaling of the Turbulence Transition Threshold in a Pipe," Phys. Rev. Lett., **91**, pp. 244502.
[4] Peixinho, J., and Mullin, T., 2006, "Decay of Turbulence in Pipe Flow," Phys. Rev. Lett., **96**, pp. 094501.
[5] Kerswell, R. R., 2005, "Recent Progress in Understanding the Transition to Turbulence in a Pipe," Nonlinearity, **18**, pp. R17–R44.
[6] Faisst, H., and Eckhardt, B., 2006, "Traveling Waves in Pipes," Phys. Rev. Lett., **91**, pp. 224502.
[7] Hof, B., van Doorne, C. W. H., Westerweel, J., and Nieuwstadt, F. T. M., 2005, "Turbulence Regeneration in Pipe Flow at Moderate Reynolds Numbers," Phys. Rev. Lett., **95**, pp. 214502.
[8] Waleffe, F., 1998, "Three-Dimensional Coherent States in Plane Shear Flows," Phys. Rev. Lett., **81**(19), pp. 4140–4143.
[9] Ekman, V. W., 1910, "On the Change From Laminar to Turbulent Motion of Liquids," Ark. Mat., Astron. Fys., **6**, pp. 1–16.
[10] Wygnanski, I. J., and Champagne, F. H., 1973, "On Transition in a Pipe. Part 1. The Origin of Puffs and Slugs and the Flow in a Turbulent Slug," J. Fluid Mech., **59**, pp. 281–335.
[11] Reshotko, E., 1958, "Experimental Study of the Stability of Pipe Flow I. Establishment of an Axiallary Symmetric Poiseuille Flow," *JPL Progress Report* No. 20-364.
[12] Huerre, P., and Rossi, M., 1998, *Hydrodynamics and Nonlinear Instabilities*, C. Godreche and P. Manneville, eds., Cambridge University Press, Cambridge, p. 81.
[13] Sarpkaya, T., 1975, "A Note on the Stability of Developing Laminar Pipe Flow Subjected to Axisymmetric and Non-axisymmetric Disturbances," J. Fluid Mech., **68**, pp. 345–351.
[14] Sarpkaya, T., 1966, "Experimental Determination of the Critical Reynolds Number for Pulsating Poiseuille Flow," ASME J. Basic Eng., **88**, pp. 589–598.
[15] Williams, S. D., 2001, "An Investigation of the Stability of Developing Pipe Flow," Ph.D. thesis, University of Manchester, Manchester, UK.
[16] Moss, E. A., and Abbot, A. H., 2002, "The Effect of Finite Amplitude Disturbance Magnitude on Departures from Laminar Conditions in Impulsively Started and Steady Pipe Entrance Flows," ASME J. Fluids Eng., **124**(1), pp. 236–240.
[17] Duck, P. W., 2005, "Transient Growth in Developing Plane and Hagen Poiseuille Flow," Proc. R. Soc. London, Ser. A, **461**, pp. 1311–1333.
[18] Tatsumi, T., 1952, "Stability of the Laminar Inlet-flow Prior to the Formation of Poiseuille Regime. II," J. Phys. Soc. Jpn., **7**, pp. 495–502.
[19] Huang, L. M., and Chen, T. S., 1974, "Stability of the Developing Laminar Pipe Flow," Phys. Fluids, **17**(1), pp. 245–247.
[20] Garg, V. K., 1981, "Stability of Developing Flow in a Pipe Flow: Non-axisymmetric Disturbances," J. Fluid Mech., **110**, pp. 209–216.
[21] Gupta, S. C., and Garg, V. K., 1981, "Effect of Velocity Distribution on the Stability of Developing Flow in a Pipe," Phys. Fluids, **24**(4), pp. 576–578.
[22] Sahu, K. C., and Govindarajan, R., 2005, "Stability of Flow Through a Slowly Diverging Pipe," J. Fluid Mech., **531**, pp. 325–334.
[23] Sahu, K. C., 2003, Master's thesis, Jawaharlal Nehru Centre for Advanced Scientific Research, Bangalore, India.
[24] Canuto, C., Hussaini, M. Y., Quarteroni, A., and Zang, T. A., 1987, *Spectral Methods in Fluid Dynamics*, Springer-Verlag, New York.
[25] Schmid, P. J., and Henningson, D. S., 2001, *Stability and Transition in Shear Flows*, Springer-Verlag, New York.
[26] Govindarajan, R., and Narasimha, R., 1999, "A Low-order Parabolic Theory for Two-dimensional Boundary Layer Stability," Phys. Fluids, **11**(6), pp. 1449–1458; Bhattacharya, P., Manoharan, M. P., Govindarajan, R., and Narasimha, R., 2006, "The Critical Reynolds Number of a Laminar Incompressible Mixing Layer from Minimal Composite Theory," J. Fluid Mech., **565**, pp. 105–114.

Development-Length Requirements for Fully Developed Laminar Pipe Flow of Inelastic Non-Newtonian Liquids

R. J. Poole[1]
e-mail: robpoole@liv.ac.uk
Department of Engineering,
University of Liverpool,
Brownlow Street,
Liverpool L69 3GH, United Kingdom

B. S. Ridley[2]
e-mail: blake.ridley@mwhglobal.com
Department of Engineering,
University of Liverpool,
Brownlow Street,
Liverpool L69 3GH, United Kingdom

*In the current study, we report the results of a detailed and systematic numerical investigation of developing pipe flow of inelastic non-Newtonian fluids obeying the power-law model. We are able to demonstrate that a judicious choice of the Reynolds number allows the development length at high Reynolds number to collapse onto a single curve (i.e., independent of the power-law index n). Moreover, at low Reynolds numbers, we show that the development length is, in contrast to existing results in the literature, a function of power-law index. Using a simple modification to the recently proposed correlation for Newtonian fluid flows (Durst, F. et al., 2005, "The Development Lengths of Laminar Pipe and Channel Flows," J. Fluids Eng., **127**, pp. 1154–1160) to account for this low Re behavior, we propose a unified correlation for X_D/D, which is valid in the range* $0.4 < n < 1.5$ *and* $0 < \mathrm{Re} < 1000$. [DOI: 10.1115/1.2776969]

1 Introduction

The importance of knowing the length of pipe required for laminar Newtonian pipe flow to fully develop, i.e., for the velocity profile to become nonvarying in the axial direction, has long been recognized. Not only is this "development length" of great practical use, in the design of pipe flow systems, for example, but it is also important for scientists and engineers studying such flows and their transition to turbulence [1].

This importance is reflected in the number of studies which have attempted to provide a definitive relationship between the nondimensional entrance length (X_D/D) and the Reynolds number in a functional form $X_D/D = C_1\mathrm{Re}$. Numerous papers have used either analytical [2–4], numerical [5–7], or experimental [8,9] means to determine $X_D = f(\mathrm{Re})$. This extensive literature is succinctly described in the recent paper of Durst et al. [10] who also point out that virtually all of these studies incorrectly provide the variation of X_D as being of the form $X_D/D = C_1\mathrm{Re}$. Such a relationship incorrectly implies that in the creeping-flow limit (i.e., $\mathrm{Re} \to 0$), the flow will instantaneously develop. In fact, at low Reynolds number, diffusion plays an important role and the correct functional form of the relationship between the development length and Re should be

$$X_D/D = C_0 + C_1\mathrm{Re} \tag{1}$$

To address the inconsistencies and confusion in the literature, Durst et al. [10] conducted a detailed numerical study and proposed the following nonlinear correlation:

$$X_D/D = [(0.619)^{1.6} + (0.0567\mathrm{Re})^{1.6}]^{1/1.6} \tag{2}$$

which is valid in the range $0 < \mathrm{Re} < \infty$ (provided, of course, that the flow remains laminar. As is well known, with great care, transition in pipe flow can be delayed to very high Reynolds numbers [1]). Thus, the situation for Newtonian fluids is finally well understood and an accurate correlation is now available. For non-Newtonian fluid flows, in contrast to the situation for Newtonian fluid flows, the literature is considerably scarcer although by no means less contradictory. In Table 1, we summarize most of the previous investigations using the "power-law" model in this area. Much as Durst et al. [10] observed for Newtonian fluid flows, nearly all of these previous studies predict a relationship of the form

$$X_D/D = C(\mathrm{Re}) \tag{3}$$

where $C = f(n)$ and n is the power-law index. Such correlations clearly neglect the role played by diffusion, which becomes increasingly important with decreasing Reynolds number. Based on our own numerical results, described in detail in this paper, a correlation of the form of Eq. (3) is probably only valid for Reynolds numbers greater than about 20. Moreover, there are considerable differences for even this "high Reynolds number" estimation in the Newtonian limit (i.e., $n = 1$). Only three studies are within ±10% of the robust value of 0.0567Re determined recently in the numerical study of Ref. [10]: Collins and Schowalter [3], 0.061Re; Mehrota and Patience [14], 0.056Re; and Ookawara et al. [15], ~0.0575Re. This latter paper (i.e., Ref. [15]) is the only study in the literature that proposes both a correlation of the correct form and is in reasonable (maximum 5.8% error) agreement with the correlation of Durst et al. [10] in the Newtonian limit. However, the correlation proposed by Ookawara et al. [15] predicts that, in the creeping-flow limit, the development length is independent of the power-law index n and equal in magnitude to the Newtonian development length. Such a result seems surprising given the nonlinearity that is retained in the governing equations through the power-law equation (in contrast to the corresponding equations for creeping Newtonian flow, which are, of course, linear).

In the current study, we conduct a detailed and systematic numerical investigation of developing pipe flow for inelastic non-Newtonian fluids obeying the power-law model. We show that a judicious choice of the Reynolds number allows the development length at high Re to collapse onto a single curve (i.e., independent of n). Moreover, at low Re, we show that the development length is, in contrast to the results of Ookawara et al., a function of power-law index. Using a simple modification to the correlation proposed by Durst et al., to account for this low Re behavior, we propose a unified correlation for X_D/D, which is valid in the range $0.4 < n < 1.5$ and $0 < \mathrm{Re} < 1000$.

[1]Corresponding author.
[2]Present address: MWH-Process and Hydraulics Department, Dominion House, Birchwood Warrington, UK.

Contributed by the Fluids Engineering Division of ASME for publication in the JOURNAL OF FLUIDS ENGINEERING. Manuscript received January 2, 2007; final manuscript received April 20, 2007. Review conducted by Dennis Siginer.

Table 1 Summary of previous investigations of development-length requirements for non-Newtonian power-law pipe flows

Author	Method	Parameter range	Re definition	Re range	$X_D=f(\mathrm{Re})$	Newtonian prediction
Collins and Schowalter [3]	A	$0<n<1$	Re_{CS}	No range provided	$X_D/D=C(\mathrm{Re})$ where $C=f(n)$	$X_D/D=0.061(\mathrm{Re})$
Mashelkar [11]	A	$0<n<1$	Re_{CS}	"High Re"	$X_D/D=C(\mathrm{Re})$ where $C=f(n)$	$X_D/D=0.049(\mathrm{Re})$
Soto and Shah [12]	N	$n=0.5$, 0.75 and 1.5	Re_{CS}	No range provided	$X_D/D=(0.15-0.085n)\mathrm{Re}$[a]	$X_D/D=0.065(\mathrm{Re})$
Matros and Nowak [13]	A	No limit provided	Re_{MR}	No range provided	$X_D/D=\mathrm{Re}\left\{0.0865\left[\frac{2(n+1)}{3n+1}\right]^{-2}\right\}$	$X_D/D=0.0865(\mathrm{Re})$
Mehrota and Patience [14]	N	$0.6<n<1.5$	Re_{MR}	>200	$X_D/D=0.056(\mathrm{Re})$	
Ookawara et al. [15]	N	No limit provided	Consult ref	<50	$X_D/D=\sqrt{((0.655)^2+(0.0575)^2(\mathrm{Re})^2)}$	
Gupta [16]	A	$0.3<n<2.0$	Re_{MR}	No range provided	$X_D/D=C(\mathrm{Re})$ where $C=f(n)$	$X_D/D=0.04(\mathrm{Re})$
Chebbi [17]	A	$0<n<1.5$	Re_{CS}	No range provided	$X_D/D=C(\mathrm{Re})$ where $C=f(n)$	$X_D/D=0.09(\mathrm{Re})$

[a]Extracted by the current authors from graphical data

2 Numerical Method

To compute the developing flow field within a pipe for inelastic non-Newtonian liquids, we make use of the fact that the flow is laminar, incompressible, steady, and axisymmetric (i.e., two dimensional). The governing equations are then those expressing conservation of mass (Eq. (4)) and momentum (Eq. (5)) in combination with a suitable rheological constitutive equation,

$$\frac{\partial u_i}{\partial x_i}=0 \tag{4}$$

$$\rho\left[\frac{\partial(u_iu_j)}{\partial x_i}\right]=\frac{\partial p}{\partial x_i}+\frac{\partial}{\partial x_j}\left[\eta(\dot\gamma)\left(\frac{\partial u_i}{\partial x_j}+\frac{\partial u_j}{\partial x_i}\right)\right] \tag{5}$$

For reasons of simplicity, we choose to use a purely viscous generalized Newtonian fluid (GNF) based on the power-law model, which gives the following "viscosity function":

$$\eta(\dot\gamma)=k\dot\gamma^{n-1} \tag{6}$$

where the shear rate $\dot\gamma$ is related to the second invariant of the rate of deformation tensor (D_{ij}) by

$$\dot\gamma=\sqrt{2D_{ij}D_{ij}}\quad\text{where } D_{ij}=\frac{1}{2}\left(\frac{\partial u_i}{\partial x_j}+\frac{\partial u_j}{\partial x_i}\right) \tag{7}$$

Equations (4)–(7) are solved using the commercial package FLUENT (Version 6.2). This well-established code has been used extensively in the calculation of complex flows (see Refs. [18–22] for recent examples) and is adequate to model the inelastic laminar flows under consideration here. The differencing schemes used are both formally second order in accuracy: central differencing is used for the diffusive terms and a second-order upwinding scheme for the convective terms. Some limited calculations were also carried out using a theoretically third-order quadratic upstream interpolation for convective kinematics (QUICK) type scheme for the convective terms to ascertain the effect of discretization scheme on the accuracy of our results. Coupling of the pressure and velocity was achieved using the well-known semi-implicit method for pressure-linked equations (SIMPLE) implementation of Patankar [23].

Double precision (14 d.p.) was used for all the calculations so that round-off errors are negligible. The iterations were stopped whenever the scaled residuals (see Ref. [24]) for the solutions for the two components of velocity and the continuity equation approached an asymptotic value; in general, the scaled residuals were observed to reach a level between 10^{-12} and 10^{-15}.

A schematic representation of the computational domain is given in Fig. 1. At inlet ($x=0$), we apply a uniform velocity U_B and we define the development length X_D as the axial distance required for the centerline velocity to reach 99% of its fully developed value. We use the well-known no-slip boundary condition at the wall and impose zero axial gradients at the outlet. The length of the domain is dependent on the Reynolds number of the flow in question ($L=f(\mathrm{Re})$); in general, the domain was at least five times as long as the calculated development length. Calculations with extended domain lengths confirmed that this criterion was sufficient to allow X_D to be independent of this length.

A preliminary series of calculations was carried out for a Newtonian fluid, at a moderate Reynolds number (Re=10), with 10×20, 20×40, 40×80, 80×160, and 160×320 quadrilateral cells of constant dimension, $\Delta x=2\Delta r$, to determine a suitable mesh density and to investigate the accuracy of our simulations. In addition to the variation in X_D, to allow us to estimate this accuracy, we define a relative error

$$E=\frac{u_c-U_{C,\mathrm{FD}}}{U_{C,\mathrm{FD}}} \tag{8}$$

where u_c is the calculated centerline velocity at the outlet plane and $U_{C,\mathrm{FD}}$ is the corresponding fully developed analytical value. The analytical solution for the fully developed pipe flow of a power-law fluid is well known (see Ref. [25], for example) and is given by

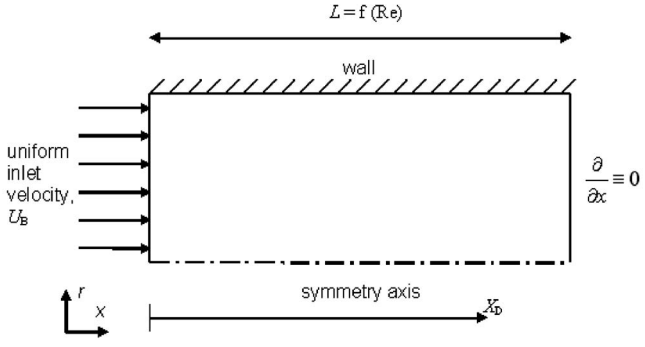

Fig. 1 Schematic of computational domain and boundary conditions

Table 2 Mesh characteristics and development lengths for a Newtonian fluid Re=10 using either a second-order upwind or QUICK-type discretization scheme

					Second order upwind		
Mesh	$\Delta r/R$	$\Delta x/R$	NC	u_c	E (%)	X_D	e_r (%)
M1	0.1	0.2	200	1.980	0.9821	0.8897	1.81
M2	0.05	0.1	800	1.995	0.2472	0.8789	0.52
M3	0.025	0.05	3200	1.999	0.06256	0.8747	0.15
M4	0.0125	0.025	12800	2.000	0.01678	0.8734	0.04
M5	0.00625	0.0125	51200	2.000	0.00534	0.8730	0.02
Richardson extrapolation						0.8729	
					QUICK		
M1	0.1	0.2	200	1.980	1.026	0.8946	1.71
M2	0.05	0.1	800	1.995	0.2611	0.8768	0.53
M3	0.025	0.05	3200	1.999	0.06704	0.8749	0.16
M4	0.0125	0.025	12800	2.000	0.01778	0.8735	0.05
M5	0.00625	0.0125	51200	2.000	0.00534	0.8730	0.02
Richardson extrapolation						0.8728	

$$\frac{u}{U_B} = \frac{(1+3n)R^{-(1+n)/n}}{(1+n)}(R^{(1+n)/n} - r^{(1+n)/n}) \tag{9}$$

Thus, the centerline velocity is simply $U_{C,\mathrm{FD}}=[(1+3n)/(1+n)]U_B$ and the velocity profile becomes increasingly flat with increasing degree of shear thinning index (i.e., decreasing n).

The results of our grid-dependency study are tabulated in Table 2. Firstly, we note that the variation of X_D between meshes is at most about 2%. Secondly, fitting these points to an equation of the form $a(\Delta r)^p+b$ allows us to estimate the order of accuracy (p) of our simulations and the mesh-independent (extrapolated) X_D value, b [26]. Using this order to estimate the "Richardson" extrapolation value for this quantity (i.e., the value extrapolated to zero mesh size), shown in Table 2, we still find that the error in our simulations, defined as $e_r=(X_{D,\mathrm{extrap}}-X_{MX})/X_{D,\mathrm{extrap}}$, especially for meshes M4 and M5, is exceedingly small ($<0.05\%$). Also shown in Table 2 are the corresponding results obtained using a QUICK type of discretization scheme for the convective fluxes. With increasing mesh refinement, differences between the two schemes become increasingly slight and reassuringly the extrapolated values for both schemes agree to better than 0.005%. Based on these levels of error, and the amount of computing time required for a specific mesh density, we conducted all remaining calculations using a mesh density corresponding to mesh M4 which, for the case studied above, gives "errors" (both based on our E parameter and in comparison with the zero grid-size extrapolation e_r) less than 0.05%. Using this mesh density (which at the highest Re studied, and therefore the longest domain lengths, led to grids with 640,000 cells) resulted in very accurate simulations for the whole range of Reynolds numbers and power-law indices studied. Our E parameter, for example, which essentially measures the difference between the fully developed calculation and the corresponding analytical solution, although exhibiting a slight dependency on n, was always less than 0.03%.

3 Validation of Newtonian Results

In Fig. 2, we plot the variation of the development length with Reynolds number for our Newtonian simulations. Also shown is the nonlinear correlation proposed by Durst et al. [10], i.e., Eq. (2). As can be seen, there is good agreement between the current simulations and the correlation. The maximum percentage difference between our data and the correlation proposed by Durst et al. [10] is about 4.5%. Such a level of discrepancy is slightly greater than the error between the original data of Durst et al. [10] and their correlation (3%).

4 Power-Law Model Results

4.1 Definition of Re. As discussed in detail by Chhabra and Richardson [27], as a consequence of their variable viscosity, one of the intrinsic difficulties with analyzing flows of non-Newtonian liquids is in the correct definition of a Reynolds number (i.e., the ratio of inertia to viscous forces within the flow). Perhaps, the most straightforward Reynolds number is that based on a characteristic shear rate $\dot{\gamma}=U_B/D$, which here we call the Collins–Schowalter Reynolds number

$$\mathrm{Re}_{\mathrm{CS}} = \frac{\rho U_B^{2-n} D^n}{K} \tag{10}$$

Such a Reynolds number also arises naturally from a simple dimensional analysis of the problem. Although the simplicity of Eq. (10) is appealing, it is well known that it is not always the most appropriate definition. For example, in turbulent pipe flows [28] or in pipe flows with abrupt changes in cross-sectional area [29], the viscosity at the wall is usually more useful,

$$\mathrm{Re} = \frac{\rho U_B D}{\mu_{\mathrm{wall}}} \tag{11}$$

This Reynolds number has the advantage that it is physically based on some quantity within the flow but has the disadvantage that it requires a detailed knowledge of the flow field and cannot be easily estimated in a complex flow. In a developing flow field, such as the current case, it also has the disadvantage that it will vary with axial location until the flow is fully developed. Nevertheless, if we consider the fully developed region in our flow, it is relatively straightforward to show that $\dot{\gamma}_{\mathrm{wall}}=(2(1+3n)/n)\times(U_B/D)$ and therefore that

$$\mathrm{Re}_{\mathrm{wall}} = \frac{\rho U_B^{2-n} D^n}{K}\left(\frac{n}{2+6n}\right)^{n-1} \tag{12}$$

Alternatively, one may take a different approach and select a generalization of the Reynolds number such that the data under investigation collapse in some manner. Metzner and Reed [30] used such an approach to correlate the pressure drop data required to drive the fully developed non-Newtonian flow in a pipe. They defined a Reynolds number

$$\mathrm{Re}_{\mathrm{MR}} = \frac{\rho U_B^{2-n} D^n}{K} 8\left(\frac{n}{6n+2}\right)^n \tag{13}$$

so that $f=16/\mathrm{Re}_{\mathrm{MR}}$ in laminar flow. An identical definition of this Reynolds number was also derived by Bird [31] using an elegant

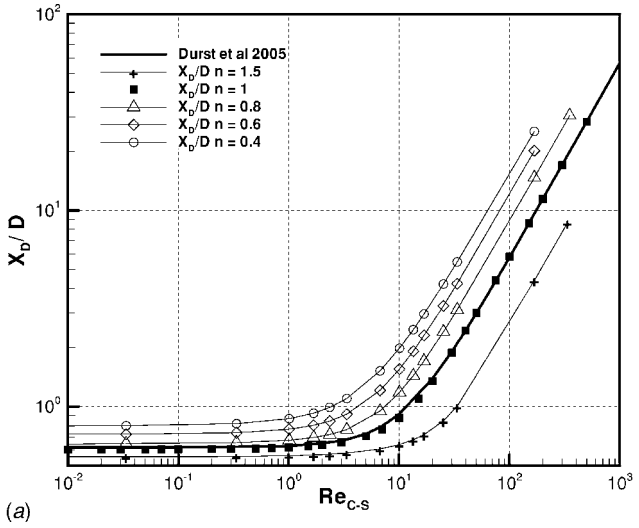

(*a*)

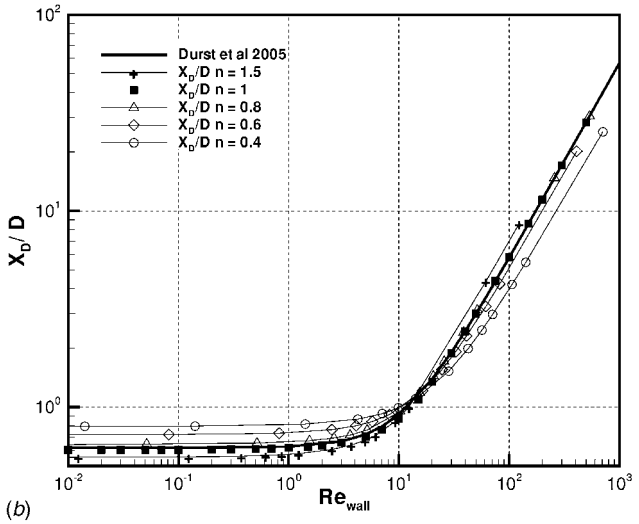

(*b*)

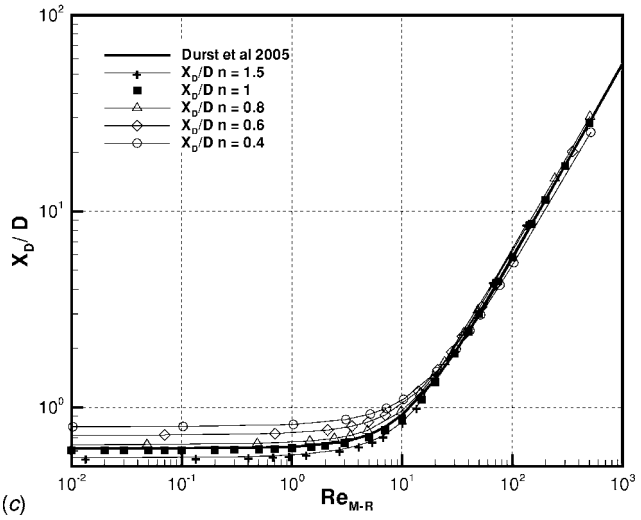

(*c*)

Fig. 2 Variation of development length for Newtonian and power-law fluids versus (*a*) Reynolds number based on Collins and Schowalter [3], (*b*) Re based on wall viscosity in fully-developed flow, and (*c*) Re based on definition of Metzner and Reed [30]

dimensional analysis approach. Finally, it is worth noting that all of these definitions are inter-related; thus,

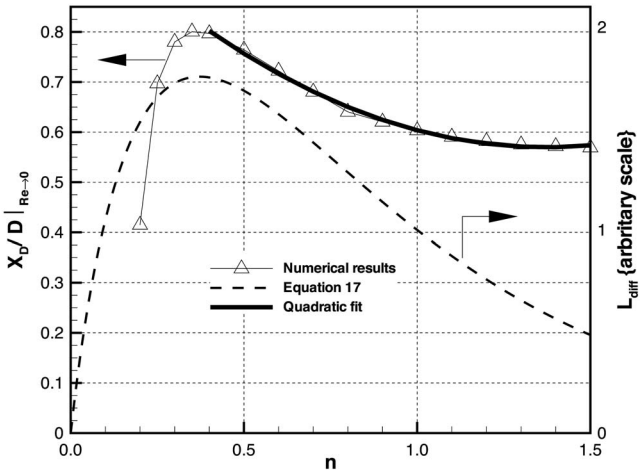

Fig. 3 Variation of creeping-flow ($Re_{CS}=0.001$) development length with power-law index

$$Re_{MR} = 8\left(\frac{n}{6n+2}\right)^{n} Re_{CS} \tag{14}$$

$$Re_{wall} = \left(\frac{n}{6n+2}\right)^{n-1} Re_{CS} \tag{15}$$

4.2 Discussion of Power-Law Simulations. The development length variation for the power-law model is shown for the three different definitions of the Reynolds number, Re_{CS}, Re_{wall}, and Re_{MR}, in Figs. 2(*a*)–2(*c*). Depending on the Re definition used, different conclusions can be drawn regarding the effect of power-law index on X_D. Using a Reynolds number based on a "characteristic" shear rate, Re_{CS}, a monotonic progressive increase in development length is observed for decreasing power-law index, i.e., X_D increases with increasing shear thinning ($n<1$) and decreases with shear thickening ($n>1$). Below a certain Reynolds number, $Re_{CS}\approx 1$, the flow is essentially governed by diffusion and, for a given value of n, the development length is approximately constant. At higher Re, the slope (i.e., $d[\log(X_D/D)]/d[\log(Re_{CS})]$) also appears to be approximately constant. Plotting the data using a Re based on the wall viscosity in the fully developed region, Re_{wall} (Fig. 2(*b*)), reveals a different overall trend; although at low Re, the trend is the same, at a critical Reynolds number ($Re_{wall}\approx 15$), there is a crossover past which the effect of power-law index on development length is reversed compared to the trend observed with Re_{CS}.

If we plot the data using the generalized Reynolds number of Metzner and Reed [30], we see that, at higher Reynolds number at least, the development lengths "collapse" onto the Newtonian curve. At high Reynolds numbers, our results are thus in practical agreement with the most recent numerical simulations in the literature (Mehrota and Patience [14] and Ookawara et al. [15]). At lower Re, where the development length is determined by diffusion, the constant development length is a function of power-law index. Such dependency is previously unreported in the literature, although most previous studies neglected this low-Re region.

We plot the variation of this constant creeping-flow development length with power-law index in Fig. 3. Further simulations were conducted in this low-Re regime (at $Re_{CS}=0.001$) to map out this variation in detail. Also included in Fig. 3 is a quadratic fit to these data over the range of power-law index for which we have conducted detailed simulations (i.e., $0.4<n<1.5$). With increasing shear thinning, i.e., progressively decreasing n, iterative convergence became increasingly time consuming and below $n=0.2$ we could no longer obtain convergence. A maximum development

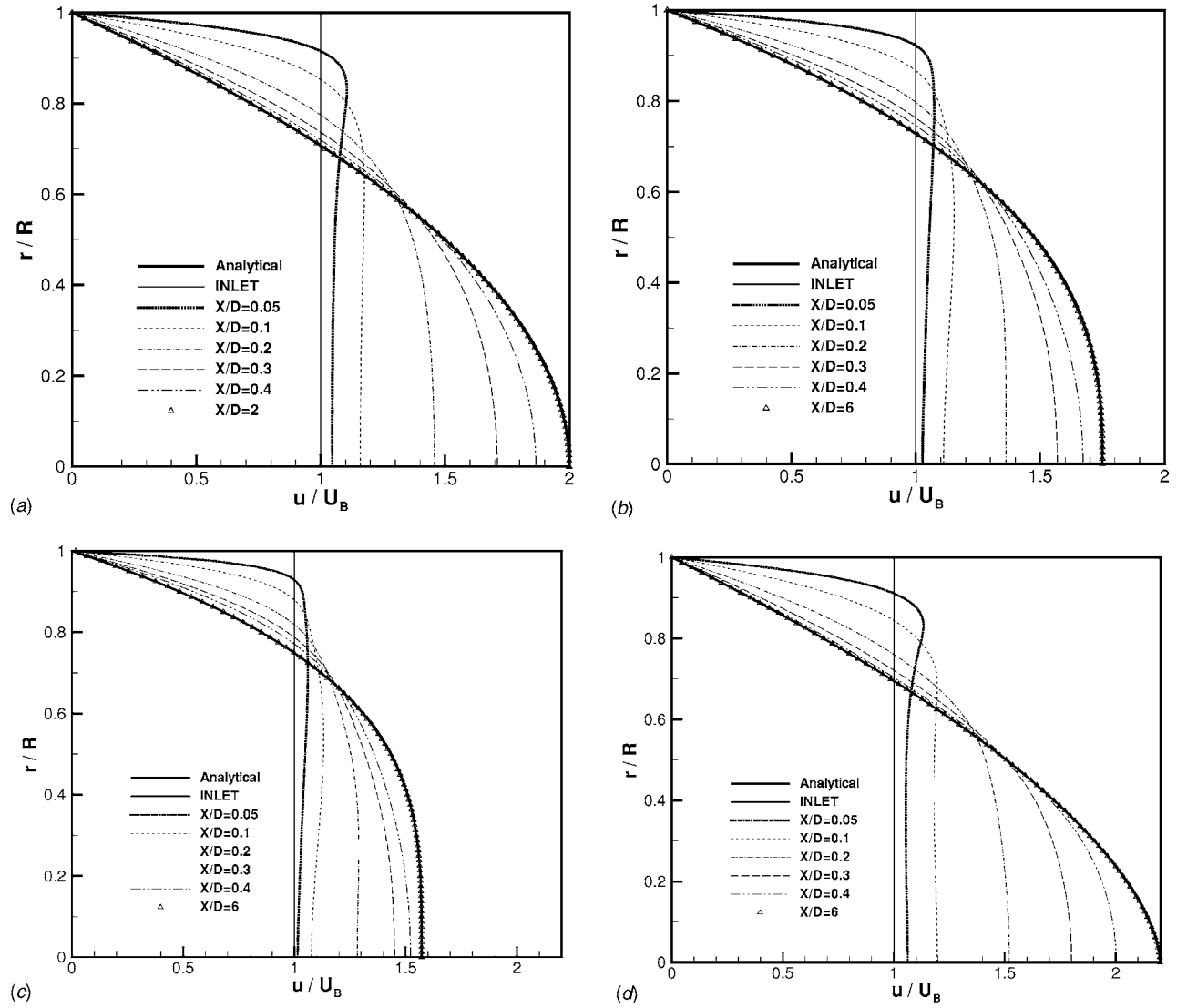

Fig. 4 Creeping-flow ($Re_{CS}=0.001$) axial velocity development at various axial locations for (*a*) Newtonian fluid, (*b*) $n=0.6$, (*c*) $n=0.4$, and (*d*) $n=1.5$

length occurs for $n \approx 0.35$; for fluids more shear thinning than this, the fully developed velocity profile becomes increasingly flat until the limiting behavior of $n=0$ the velocity profile is itself uniform and "instantaneously" fully developed. A possible explanation for the complex variation of the development length with power-law index is that there are two "competing" effects. In this creeping-flow regime, the development length is essentially diffusion dominated and so with decreasing n, it is plausible that the diffusion time will increase and so you might expect the development length to increase. However, with increased shear thinning, the fully developed velocity profile becomes increasingly uniform and so less rearrangement of the uniform inlet velocity profile needs to occur before it attains its fully developed shape. Using a simple scaling argument, it is possible to show that a characteristic diffusion time must be inversely proportional to the "effective" viscosity (at least in the range $0<n<2$),

$$t_{\text{diff}} \propto \frac{C^*}{\mu_{\text{eff}}} \tag{16}$$

where $\mu_{\text{eff}}=(1/8)K[(6n+2)/n]^n$ (i.e., from the Metzner-Reed Reynolds number) and C^* is an order-one constant, which has the units s^{n-1} kg/m. If we also define a characteristic velocity scale, to account for the fact that the fully developed velocity profile becomes increasingly flat with decreasing n, as the difference between the centerline fully developed value and the bulk velocity (i.e., $U_{C,\text{FD}}-U_B$), the development length should be of the form

$$L_{\text{diff}} \propto U^* t_{\text{diff}} \propto (U_{C,\text{FD}} - U_B)\frac{C^*}{\mu_{\text{eff}}} \tag{17}$$

The variation of this length scale with power-law index is included in Fig. 3. Although such a simple scaling argument based on bulk variables is unable to completely capture the full complexity of the development-length variation, it does correctly predict the power-law index at which the development length attains a maximum and it also predicts the form of the variation above and below this n value.

To further understand this complex low-Re behavior, in Fig. 4 we show the axial velocity distribution at various axial locations together with the fully developed analytical solution and the corresponding, virtually indistinguishable, fully developed numerical solution. As has been observed previously for the Newtonian case (Durst et al. (2005)), close to the uniform velocity inlet, a significant off-centerline velocity overshoot is apparent for all fluids, although this peak is enhanced for the shear-thickening fluid ($n=1.5$) and increasingly diminished with decreasing power-law in-

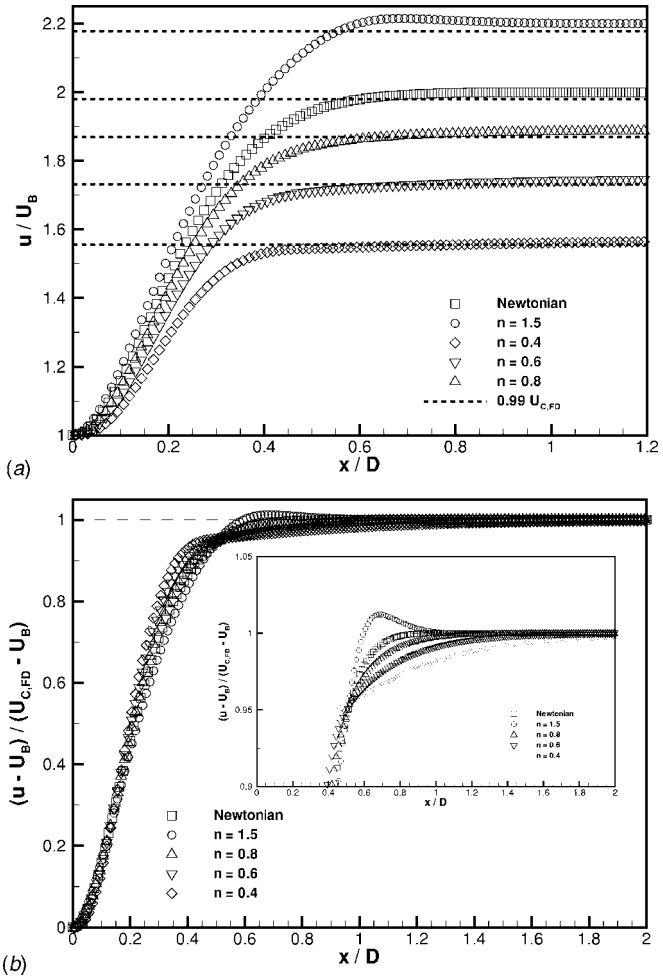

Fig. 5 Variation of centerline velocity for creeping-flow cases ($Re_{CS}=0.001$): (*a*) normalized by bulk velocity and (*b*) scaled to remove influence of flattened velocity profile

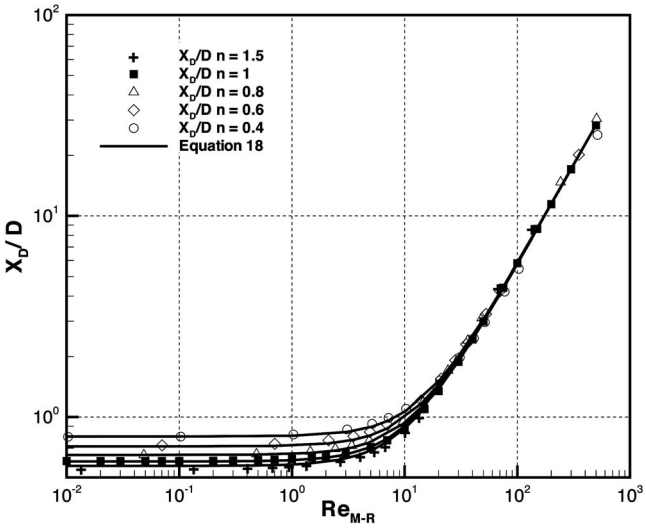

Fig. 6 Variation of development length for Newtonian and power-law fluids versus Re_{MR} together with universal correlation based on a modification to correlation of Durst et al. [10]

dex. As a consequence of the flattening of the velocity profiles, which accompanies shear thinning, it is difficult to differentiate this effect from any development-length effects. Therefore, in Fig. 5(*a*), we plot the centerline velocity variation, and in Fig. 5(*b*), we plot the same velocity data but scaled such that it varies between 0 and 1: 0 corresponds to the bulk uniform inlet velocity and 1 to the fully developed centerline value. Rescaling the data, as in Fig. 5(*b*), highlights some interesting effects. Close to inlet, $x/D < 0.3$, the centerline velocities collapse onto a single curve for all values of n. Downstream of $x/D > 0.5$, the rate of change of the centerline axial velocity decreases with decreasing n, at least in the range $0.4 < n < 0.8$, in agreement with the observed increase in X_D for increasing amounts of shear thinning (cf. Fig. 2). For the shear-thickening fluid, $n=1.5$, the centerline velocity initially overshoots its fully developed value. Thus, although using our definition of X_D, the shear-thickening fluids appear to develop quicker; in fact, if we were to refine our definition of X_D, perhaps to the more robust "length at which the centerline velocity attains a monotonically varying value within 1% of its fully developed value," this trend would be altered.

Finally, if we use the polynomial fit to the variation of creeping-flow development length with power-law index (shown in Fig. 3), we can make a simple modification to the correlation of Durst et al. to account for shear-thinning and mildly shear-thickening effects,

$$X_D/D = [(0.246n^2 - 0.675n + 1.03)^{1.6} + (0.0567\mathrm{Re}_{MR})^{1.6}]^{1/1.6} \quad (18)$$

This equation is only valid for power-law indices in the range $0.4 < n < 1.5$. The correlation is shown in Fig. 6 together with the numerical data for the various levels of power-law index. In general, the agreement of Eq. (18) to the data is better than 5% except at the highest Reynolds numbers where, especially for $n=0.4$ and 1.5, the agreement deteriorates somewhat (maximum 15% difference).

5 Conclusions

We have reported the results of a detailed and systematic numerical investigation of developing pipe flow of inelastic non-Newtonian fluids obeying the power-law model. Use of the Reynolds number developed by Metzner and Reed [30] allows the development length at high Reynolds number to collapse onto a single curve (i.e., independent of the power-law index n). Moreover, at low Reynolds numbers, the development length is, in marked contrast to existing results in the literature, a function of power-law index. Using a simple modification to the recently proposed correlation for Newtonian fluid flows [10] to account for this low-Re behavior, we have proposed a unified correlation for X_D/D, which is valid in the range $0.4 < n < 1.5$ and $0 < \mathrm{Re} < 1000$.

Acknowledgment

The authors would like to thank Professor Marcel Escudier, University of Liverpool, and Professor Manuel Alves, Universidade do Porto, for useful discussions about the work reported in this paper.

References

[1] Darbyshire, A. G., and Mullin, T., 1995, "Transition to Turbulence in Constant-Mass-Flux Pipe Flow," J. Fluid Mech., **289**, pp. 83–114.

[2] Siegel, R., 1953, "The Effect of Heating on Boundary Layer Transition for Liquid Flow in a Tube," Sc.D. thesis, Massachusetts Institute of Technology, Cambridge.

[3] Collins, M., and Schowalter, W. R., 1963, "Behaviour of Non-Newtonian Fluids in the Inlet Region of a Channel," AIChE J., **9**, pp. 98–102.

[4] Chen, R. Y., 1973, "Flow in the Entrance Region at Low Reynolds Numbers," J. Fluids Eng., **95**, pp. 153–158.

[5] Hornbeck, R. W., 1964, "Laminar Flow in the Entrance Region of a Pipe," Appl. Sci. Res., Sect. A, **13**, pp. 224–236.

[6] Friedmann, M., Gillis, J., and Liron, N., 1968, "Laminar Flow in a Pipe at Low

and Moderate Reynolds Numbers," Appl. Sci. Res., **19**(6), pp. 426–433.
[7] Atkinson, B., Brocklebank, M. P., Card, C. C. H., and Smith, J. M., 1969, "Low Reynolds Number Developing Flows," AIChE J., **15**, pp. 548–553.
[8] Nikuradse, J., 1950, *Applied Hydro and Aerodynamics*, McGraw-Hill, New York, p. 27.
[9] McComas, S. T., and Eckert, E. R. G., 1965, "Laminar Pressure Drop Associated With the Continuum Entrance Region and for Slip Flow in a Circular Tube," ASME J. Appl. Mech., **32**, pp. 765–770.
[10] Durst, F., Ray, S., Unsal, B., and Bayoumi, O. A., 2005, "The Development Lengths of Laminar Pipe and Channel Flows," J. Fluids Eng., **127**, pp. 1154–1160.
[11] Mashelkar, R. A., 1975, "Hydrodynamic Entrance-Region Flow of Pseudoplastic Fluids," Proc. Inst. Mech. Eng., **177**, pp. 683–689.
[12] Soto, R. J., and Shah, V. L., 1976, "Entrance Flow of a Yield-Power Law Fluid," Appl. Sci. Res., **32**, pp. 73–85.
[13] Matros, Z., and Nowak, Z., 1983, "Laminar Entry Length Problem for Power Law Fluids," Acta Mech., **48**, pp. 81–90.
[14] Mehrota, A. K., and Patience, G. S., 1990, "Unified Entry Length for Newtonian and Power Law Fluids in Laminar Pipe Flow," Can. J. Chem. Eng., **68**, pp. 529–533.
[15] Ookawara, S., Ogawa, K., Dombrowski, N., Amooie-Foumeny, E., and Riza, A., 2000, "Unified Entry Length Correlation for Newtonian, Power Law and Bingham Fluids in Laminar Pipe Flow at Low Reynolds Number," J. Chem. Eng. Jpn., **33**, pp. 675–678.
[16] Gupta, R. C., 2001, "On Developing Laminar Non-Newtonian Flow in Pipes and Channels," Nonlinear Anal.: Real World Appl., **2**, pp. 171–193.
[17] Chebbi, R., 2002, "Laminar Flow of Power-Law Fluids in the Entrance Region of a Pipe," Chem. Eng. Sci., **57**, pp. 4435–4463.
[18] Escudier, M. P., O'Leary, J., and Poole, R. J., 2007, "Flow Produced in a Conical Container by a Rotating Endwall," Int. J. Heat Fluid Flow (to be published).
[19] Fellouah, H., Castelain, C., El Moctar, A. O., and Peerhossaini, H., 2006, "A. Numerical Study of Dean Instability in Non-Newtonian Fluids," ASME Trans. J. Fluids Eng., **128**, pp. 34–41.
[20] Huang, Z., Olsen, J. A., Kerekes, R. J., and Green, S. I., 2006, "Numerical Simulation of the Flow Around Rows of Cylinders," Comput. Fluids, **35**, pp. 485–491.
[21] Taha, T., and Cui, Z. F., 2006, "CFD Modeling of Slug Flow in Vertical Tubes," Chem. Eng. Sci., **61**, pp. 676–687.
[22] Hu, L. Y., Zhou, L. X., Zhang, J., and Shi, M. X., 2005, "Studies on Strongly Swirling Flows in the Full Space of a Volute Cyclone Separator," AIChE J., **51**(3), pp. 740–749.
[23] Patankar, S., 1980, *Numerical Heat Transfer and Fluid Flow*, Hemisphere, Washington.
[24] Celik, I. B., and Li, J., 2005, "Assessment of Numerical Uncertainty for the Calculations of Turbulent Flow Over a Backward-Facing Step," Int. J. Numer. Methods Fluids, **49**(9), pp. 1015–1031.
[25] Bird, R. B., Armstrong, R. C., and Hassager, O., 1987, *Fluid Mechanics*, Dynamics of Polymeric Fluids, Vol. 1, 2nd ed., Wiley-Interscience, New York.
[26] Ferziger, J. H., and Peric, M., 2001, *Computational Methods for Fluid Dynamics*, Springer, New York.
[27] Chhabra, R. P., and Richardson, J. F., 1999, *Non-Newtonian Flow in the Process Industries: Fundamentals and Engineering Applications*, Butterworth-Heinemann, Oxford.
[28] Escudier, M. P., Poole, R. J., Presti, F., Dales, C., Nouar, C., Desaubry, C., Graham, L., and Pullum, L., 2005, "Observations of Asymmetrical Flow Behaviour in Transitional Pipe Flow of Yield-Stress and Other Shear-Thinning Liquids," J. Non-Newtonian Fluid Mech., **127**, pp. 143–155.
[29] Poole, R. J., and Escudier, M. P., 2004, "Turbulent Flow of Viscoelastic Liquids Through an Axisymmetric Sudden Expansion," J. Non-Newtonian Fluid Mech., **117**, pp. 25–46.
[30] Metzner, A. B., and Reed, J. C., 1955, "Flow of Non-Newtonian Fluids—Correlation of the Laminar, Transition, and Turbulent-Flow Regions," AIChE J., **1**, pp. 434–440.
[31] Bird, R. B., 1956, "Correlation of Friction Factors in Non-Newtonian Flow," AIChE J., **2**, pp. 428–429.

Influence of Reynolds Number on the Evolution of a Plane Air Jet Issuing From a Slit

P. R. Suresh

Sarit K. Das
Professor
e-mail: sarit_das@hotmail.com
e-mail: skdas@iitm.ac.in

T. Sundararajan
Professor

Department of Mechanical Engineering,
Indian Institute of Technology Madras,
Chennai 600036, India

Jet flows are encountered in a variety of industrial applications. Although from the points of view of manufacturing with ease and small spatial requirement it is convenient to use short slit nozzles, most of the available studies deal with turbulent jets issuing from contoured nozzles. In the present work, experiments have been conducted in the moderate Reynolds number range of 250–6250 for a slit jet. Mixing characteristics of slit jets seem to be quite different from those of jets emerging out of contoured nozzles. This is primarily due to the differences in the decay characteristics and the large scale eddy structures generated in the near field, which are functions of the initial momentum thickness. It is evident that, in the range of $250 \leqslant Re \leqslant 6250$*, the overall spreading characteristics of the slit jet flow have stronger Reynolds number dependence than those of contoured nozzle jets. In particular, the slit jets exhibit slower mean velocity decay rates and slower half-width growth rates. Normalized power spectra and probability distribution functions are used to assess the spatial evolution and the Reynolds number dependence of jet turbulence. It is seen that the fluctuating components of velocity attain isotropic conditions at a smaller axial distance from the nozzle exit than that required for mean velocity components to become self-similar.* [DOI: 10.1115/1.2776959]

Keywords: jets, transition to turbulence, self-similarity in jets, shear layer, Reynolds number, jet structures

1 Introduction

Jet flows are encountered in a variety of industrial applications dealing with cooling, mixing, or drying processes. Flow patterns associated with jets involve mechanisms of vortex evolution and interaction, flow instabilities, and fine scale turbulence augmentation. Most of the past experimental works on plane jets have considered higher Reynolds number turbulent jets issuing from contoured nozzles or long channels [1–5]. This is because jet flows are found to be very sensitive to the initial velocity profile, and well-defined nozzle or channel shapes allow accurate characterization of the initial profile. In industrial applications, it is impractical to provide long nozzles or channels, and short nozzles are usually employed. Quite often, it proves equally effective to form jets by allowing a gas to escape through slit shaped perforations on the wall of a plenum. Therefore, slit jets arising in such instances need to be characterized in their typical application range of low to moderate Reynolds numbers to aid their effective usage.

Several researchers have analyzed the flow structure of jets issuing from contoured nozzles or long channels. Thomas and Goldschmidt [1] indicated that in jets issuing from long channels, shear layer merging occurred between $6 < x/d < 12$. According to Antonia et al. [2], organized structures are developed well downstream of the nominal merging point of the mixing layers, but upstream of the onset of self-preservation. It was further concluded that interaction of the structures from the opposite mixing layers results in their destruction and new structures are formed subsequently. A detailed experimental investigation by Heskestad [3] showed that the channel jet becomes self-preserving at 100 slot widths. Experiments by Bradbury [5] indicated that all free turbulent shear flows may have similar structure. A low velocity free stream air supply was provided in the above study to control the outer layers of the jets. It was concluded that similarity should not be restricted by local isotropy considerations but should apply to the larger eddies as well.

Klein et al. [6] studied the Reynolds number effect on plane jets using direct numerical solution. The Re was in the range $1000 < \mathrm{Re} < 6000$. Flow is not independent of Re but close to a converged state with very weak Re dependence at $\mathrm{Re} = 6000$. The axial distance covered in these studies was of the order of 30–40 times the diameter of the jet. Suyambazhahan et al. [7] studied oscillations in a 2D laminar jet over a range of Reynolds and Grashof numbers and for various jet orientations. For isothermal jets, the frequency of velocity oscillations and the axial location for the onset of oscillations increase with Reynolds number. Studies were conducted by Namer and Otugen [8] at moderate Reynolds numbers ($\mathrm{Re} \geqslant 1000$) for a jet having an aspect ratio of 56. In plane jets, the transition from laminar to turbulent flow is known to occur at a low Reynolds number of the order of 500. Hence, the range of $\mathrm{Re} < 1000$ is also of interest for obtaining a complete picture of jet flow behavior. Jo and Kim [9] conducted a linear stability analysis to study transition in the range of $50 \leqslant \mathrm{Re} \leqslant 1000$. Hussain and Clark [10] studied the effects of the mean and fluctuating flow characteristics of the upstream boundary layer on the evolution of flow in the near field of a plane jet.

It is clear from the above survey of literature that most of the earlier studies have dealt with jets from contoured nozzles or long channels, and the Reynolds number range corresponding to laminar to turbulent flow transition has not been investigated in detail. Also, it is evident that studies that characterize plane jets issuing from simple slits are rare. The jet spread rates in the transverse and axial directions, as well as the jet instability modes, are likely to be different due to the change in the jet inlet geometry and the consequent changes in the initial flow conditions. Hence, there is a need to characterize slit jets for their optimal usage in applications such as air curtains or pollutant dispersion devices, where low spread rate could be of interest.

The primary objective of the present work is to study the evolution of a plane jet issuing from a slit. It is also aimed to high-

Contributed by the Fluids Engineering Division of ASME for publication in the JOURNAL OF FLUIDS ENGINEERING. Manuscript received November 22, 2005; final manuscript received May 17, 2007. Review conducted by Timothy J. O'Hern.

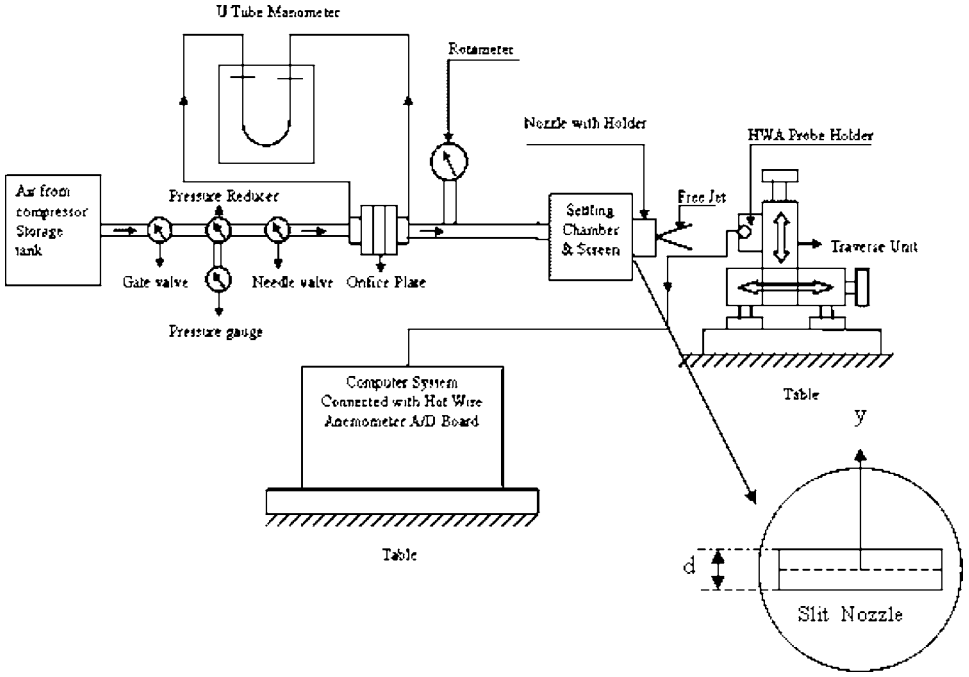

Fig. 1 Schematic of the experimental setup

light the influence of Reynolds number on the development of turbulent structures. Jets are studied experimentally starting from a very low Reynolds number of 250 up to a value of 6250 in order to bring out the complex mechanisms involved in the transitional regime. The data obtained include mean streamwise velocity, time-averaged turbulence statistics, autocorrelations, spectra of streamwise fluctuating velocity, and also the fluctuating velocity components in the transverse directions.

2 Experimental Setup

A schematic of the experimental setup is given in Fig. 1. Compressed air (10 bar maximum pressure) from a storage vessel is admitted through a pressure regulator and a needle valve that regulates the flow rate. An accurately calibrated orifice meter and a rotameter fitted in the line are used to measure the air flow rate. The average jet exit velocity is computed from the measured air flow rate. A two-dimensional traverse system is used to investigate the flow field in the axial and transverse directions. The present study is conducted for a two-dimensional plane air jet issuing from a slit into quiescent atmospheric air. Additional precautions have been enforced to prevent any stray air circulation, which might interfere with the jet flow. The region is covered by two side plates in order to preserve the two dimensionality of the jet expansion (primarily in the vertical plane). The slit dimensions are 50×2 mm^2 so as to get an aspect ratio of 25 (Fig. 1). A disk of 4 mm in thickness houses the slit of rectangular cross section, and the disk is directly fitted at one end of the settling chamber. The sudden contraction at the slit accelerates the air flow, and a jet with a top hat velocity profile with a small momentum thickness emerges from the slit nozzle. The slit has sharp edges to prevent the occurrence of flow nonuniformities at the nozzle exit.

The initial turbulence level of the jet is controlled to about 0.5% by a honeycomb and fine screen structure. Turbulence measurements are carried out with a Dantec hot wire anemometer model 90N10. The probe used is Dantec model 55P11 made of 5 μm diameter platinum coated tungsten wire, with a maximum frequency response of 500 kHz. The hot wire anemometer is calibrated using a Pitot tube in conjunction with a micromanometer (Furness Control FCO12), with an accuracy of $\pm 1\%$ and linearity better than 1% of the reading. Velocity is varied from 2.1 m/s to 51.9 m/s so as to vary Re from 250 to 6250.

Voltage-velocity calibration data are fitted with a power law form $E=A+BU^n$, where A and B are constants. The probe is recalibrated daily in a wind tunnel after cleaning with acetone solution. The mean and rms values are taken at a sampling rate of 1 kHz for a sampling time of 60 s. A few measurements of fluctuating components v and w are taken with the help of the Dantec 55P12, 45 deg slant probe using the procedure suggested by Brunn [11] and Fujita and Kovasznay [12]. Repeatability of results was checked for similar runs and was found to be satisfactory. In order to check the accuracy of the method, Reynolds stress $(-\rho u'v')$ variation is estimated over the cross section of a fully developed pipe flow using the present slant probe. The Reynolds stress is also derived from pressure drop data and the measured mean velocity profile in the radial direction. The Reynolds stresses obtained by the two methods agreed within an error of 2%, indicating that the slant probe used here for measuring v and w fluctuations is accurate enough.

For estimation of the power spectra of velocity fluctuations, data are acquired at a sampling frequency of 50 kHz for the highest Reynolds number with the low pass filter fixed at 20 kHz for locations up to an axial distance of 140 times jet height (d). The signals are digitized using a 12 bit analog-to-digital (A/D) converter. A temperature compensation scheme is implemented, and a correction is applied to the data in order to reduce error due to temperature variation during the experiment. Reynolds number at the exit is calculated based on the mass flow rate measured using the orifice meter. Uncertainties in mass flow rate, cross sectional area of the nozzle, and nozzle height d are, respectively, 1.13%, 0.71%, and 0.5%. Uncertainty involved in the acquisition and conversion of mean and rms values of velocity samples are 1.2% and 2%, respectively, for 95% confidence level with reference to the calibration. Using the propagation method suggested by Moffat [13], uncertainties in Re and longitudinal turbulence intensity are estimated as 1.42% and 2.33%, respectively. The maximum uncertainty in the dimensionless fluctuations of v/U_c and w/U_c components measured by the slant probe is 3.9%.

Fast Fourier transform (FFT) analysis was performed on the velocity data to evaluate the dominant spectral components and their amplitudes along the jet axis. Four traces of 262,144 points were averaged for each spectrum. For each data trace, a Blackman

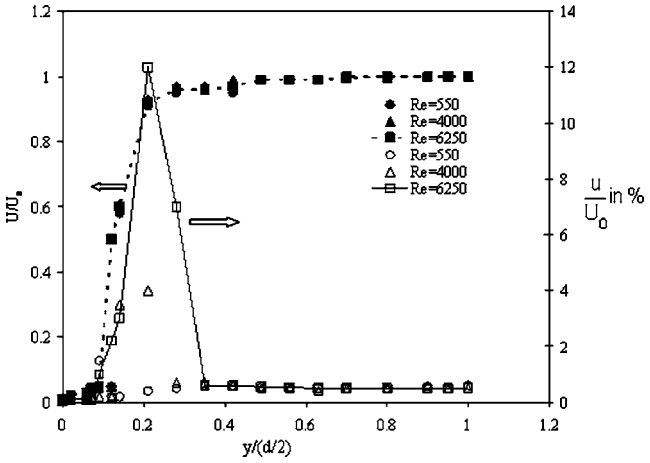

Fig. 2 Mean and rms velocity variation across the jet cross section. Note: Solid symbols represent axial velocity and open symbols represent turbulence intensity.

window and an averaging routine were used with 62 overlapping data segments of 2048 points. The experiments were carefully conducted by switching off electrical appliances nearby and during night times, so as to minimize any acoustic disturbances emanating from machines or traffic. From the mean velocity measurement, the jet half-width variation was estimated at different locations and Reynolds numbers. Probability distribution functions (PDFs) have been used as a tool to assess the Re and location dependence of turbulent fluctuations. Maximum uncertainty in the frequency calculation by FFT is estimated as $f \pm 6$ Hz, and the propagation of uncertainty in Strouhal number is 1.11%. The window width in PDF estimation is limited to 0.2σ so as to control the uncertainty to 1%.

3 Results and Discussion

Evolution of a free jet depends on the velocity profile of the initial boundary layer as well as the Reynolds number, as illustrated by Hussain and Clark [10]. Mean and fluctuating velocity components measured at a section located 1 mm from the slit-nozzle exit are shown in Fig. 2. The measured mean velocity has a top hat profile, which indicates an incomplete laminar boundary layer development inside the nozzle. It is also evident that a major portion of the interior region of the jet lies in the potential core. The displacement thickness (δ) obtained by numerical integration is $0.0355d$ and momentum thickness (θ) is $0.0133d$ for Re $=6250$ (where d is the height of the slit). The ratio of the displacement to momentum thickness is the shape factor, and the value obtained here is 2.68 for Re$=6250$, which is slightly higher than the value of 2.5 obtained for the Blasius profile of laminar flow over a flat plate. The turbulence intensity profile exhibits a peak near the edge of the shear layer. As the Reynolds number increases the maximum turbulence intensity in the shear layer also increases but remains below 0.5% over a considerable portion of the cross section. According to Ref. [10], these two features together can be taken as an indication for the existence of a laminar boundary layer within the slit, up to the jet inlet.

3.1 Mean and Fluctuating Velocity Components. Mean velocity decay along the central axis in the near region is plotted in Fig. 3(*a*). This shows that the near field flow is almost unaffected by Re up to $x/d=5$. Namer and Otugen [8] found that the mean velocity decay in the near region is influenced by the Reynolds number and that the potential core length decreases with Re for the jet flow from a contoured nozzle. The present results for the slit-nozzle jet show that the mean velocity decay in the near field ($x/d \leqslant 5$) and the potential core length are nearly independent of

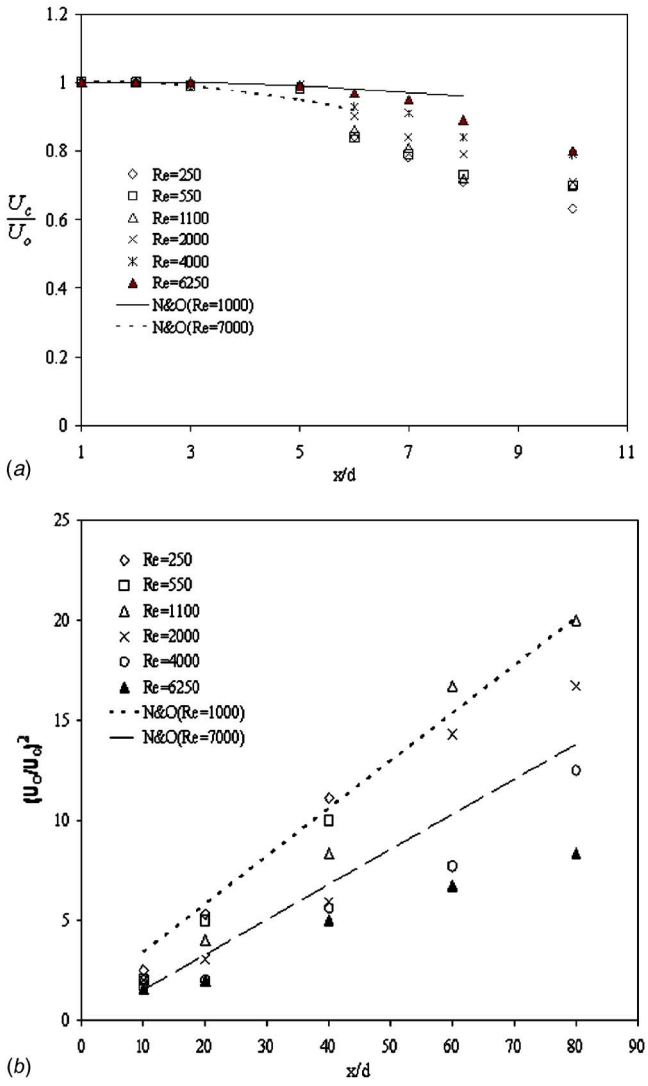

Fig. 3 (*a*) Development of mean velocity in the near field. Note: N&O represents Ref. 8. (*b*) Inverse of the mean square velocity decay. N&O represents Ref. 8.

Reynolds number. Beyond the potential core, decay is slower for higher Re values. The above mentioned trends can be explained as follows. For a contoured nozzle, a well grown boundary layer whose thickness depends on the Reynolds number is present at the nozzle exit. This, in turn, results in larger vortices in the near field region, which increase the mixing in the jet shear layer as well as the rate of shear layer growth. Consequently, the potential core length is less for a contoured jet. In order to understand the effect of jet Reynolds number on potential core length, one needs to keep in mind both the decrease in the inlet momentum thickness and the increase in inlet turbulence intensity with Reynolds number. For a slit jet, the boundary layer growth (i.e., momentum thickness) is negligible at the nozzle exit. Also, due to the strong influence of the sudden contraction, the effect of Reynolds number appears to be negligible in the potential core length.

The quantity $(U_o/U_c)^2$ is plotted in Fig. 3(*b*) for six Reynolds numbers between 250 and 6250. The results show that a correlation can be obtained in the form

$$\left(\frac{U_o}{U_c}\right)^2 = K_1\left(\frac{x}{d} - C_1\right) \tag{1}$$

Here, the value of K_1 varies from 0.21 to 0.1 as Re changes from 1100 to 6250. This compares with the values of 0.239 and 0.175

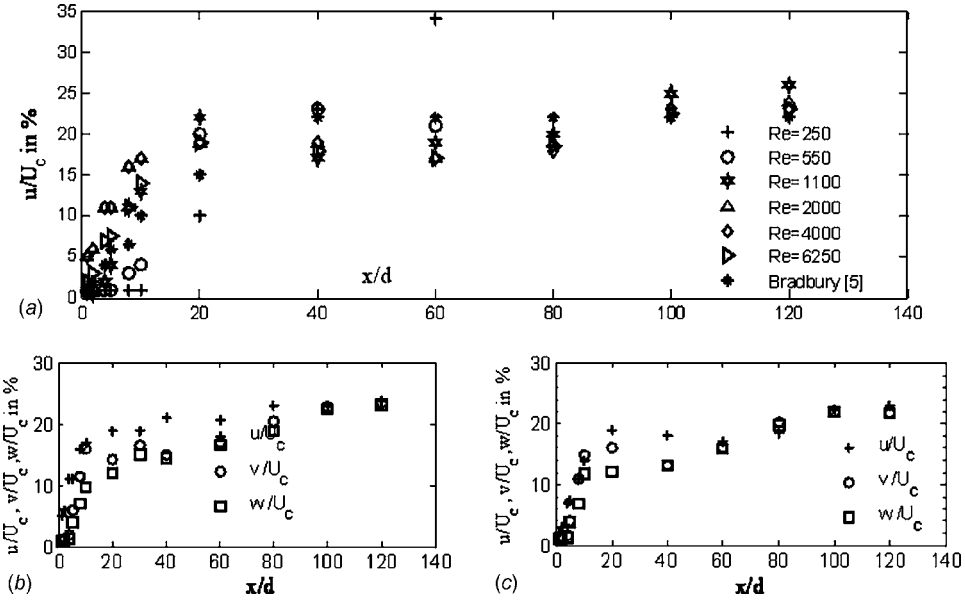

Fig. 4 (*a*) Axial evolution of turbulence intensity (u/U_c). (*b*) Axial evolution of fluctuating velocity components for Re=2000. (*c*) Axial evolution of fluctuating velocity components for Re=6250.

for the contoured nozzle jets obtained at Re of 1000 and 7000, respectively, by Namer and Otugen [8]. The value of K_1 reported by Thomas and Goldschmidt [1] is 0.22. These differences observed in the value of K_1 can be attributed to the change in nozzle shape, i.e., slit geometry employed in the present study as opposed to contoured nozzles in Refs. [1,8].

The axial growth of turbulence intensity is plotted in Fig. 4(*a*). The domain of plotting is restricted to $x/d=60$ for Re=250 and 550, considering the high measurement uncertainties for the mean and fluctuating components in the far field, at low Re values. It is seen that at a Reynolds number of 250, large turbulence intensity occurs in the far region. In such cases, it is possible that the flow has three-dimensional features due to axis switching and asymptotic approach toward axisymmetric shape. As the Reynolds number increases, turbulence intensities decrease in the far field. Early hot wire measurements of Heskestad [3] also indicated higher turbulence intensities with smaller Reynolds numbers, but the corresponding axial distributions did not level off by $x/d=160$ even at a high Re of 36,900. The present measurements show that the turbulence intensity increases fast up to $x/d=20$, followed by minor variations up to about $x/d=100$, eventually attaining an asymptotic value for $x/d>120$. In the case of contoured nozzles, Hussain and Clark [10] and Krothapalli et al. [14] observed that the turbulence intensity peaks at $x/d=20$, after which it slows down and attains an asymptotic value. The physics was explained in terms of interactions between the shear layers and the merging of vortices with opposite senses of rotation. It was suggested by Krothapalli et al. [14] that the presence of a large centerline peak of fluctuating component u in the interaction region may depend on the initial boundary layers at the nozzle lip being laminar or turbulent. In the present results, only a mild peak is identified at $x/d=20$ for high Re jets and at $x/d=40$ for low Re jets. The absence of a large peak whose location is dependent on Re (as discussed in the Refs. [8,14]) probably indicates that the mechanism involved in the growth of the shear layer is different for the slit jet under consideration. For the same reason, while a contoured plane jet is able to attain an asymptotic value of turbulence intensity at $x/d=40$ [5], for a slit jet, the position is considerably shifted to a larger value of x/d. Beyond $x/d=100$, turbulence intensity attains an asymptotic value of about 23%, in close agreement with the result obtained by Bradbury [5].

At a higher Reynolds number, the structure of the flow develops faster and turbulence intensity values become almost Re independent at moderate axial distances from the jet exit plane. The differences in turbulence intensity evolution for low Re and high Re jets, especially in the far field, can be attributed to the fact that the low Re jet spreading is dominated by the growth of shear layer instabilities, whereas high Re jets are also influenced by turbulence development. A lower value of turbulence intensity and prevailing laminar nature for low Re jets in the near field also suggest that the underlying large structures are more coherent and organized in these regions. These coherent structures grow toward the far region due to intermittent engulfment of low velocity ambient fluid. In turn, higher fluctuation amplitudes and lower mean velocities occur, resulting in large turbulence intensities in the far field. As mentioned earlier, it is more appropriate to attribute such velocity fluctuations to shear layer instabilities rather than to the growth of turbulence. At a higher Reynolds number, turbulent shear layers develop in the near region ($x/d<20$) itself. After the merger of the shear layers, when jet development is complete, turbulence intensity attains an asymptotic value on the centerline.

The turbulence intensities in other directions (v/U_c and w/U_c) are plotted for two Reynolds numbers (Figs. 4(*b*) and 4(*c*)). It is evident that the magnitudes of the above two components are almost equal throughout the axial length. In the near region, their magnitudes are lower than u/U_c. However, for $x/d>100$, all the three components of turbulence intensities are equal, indicating the occurrence of isotropic turbulence. The probability distribution function plots, discussed later in Figs. 9(*b*) and 9(*c*), exhibit Gaussian profiles beyond $x/d=80$, further corroborating the attainment of isotropic turbulence. This is contrary to the contoured jet results obtained by Gutmark and Wygnanski [4] in which jet turbulence had not become isotropic until about $x/d=120$.

3.2 Evolution of Spectral Components and Strouhal Number. The evolution of different spectral components and the variations of Strouhal number based on the frequency of the spectral component with peak amplitude along the centerline and in the shear layer are presented in Figs. 5–8. At a low Re of 550 (Fig. 5), only certain isolated peaks are present in the spectrum, indicating the truly laminar nature of the flow and the presence of coherent vortical structures due to jet instability. With increase in axial distance, subharmonics appear at $x/d=5$, which grow in amplitude at larger distances ($x/d=10$). The changes in the spec-

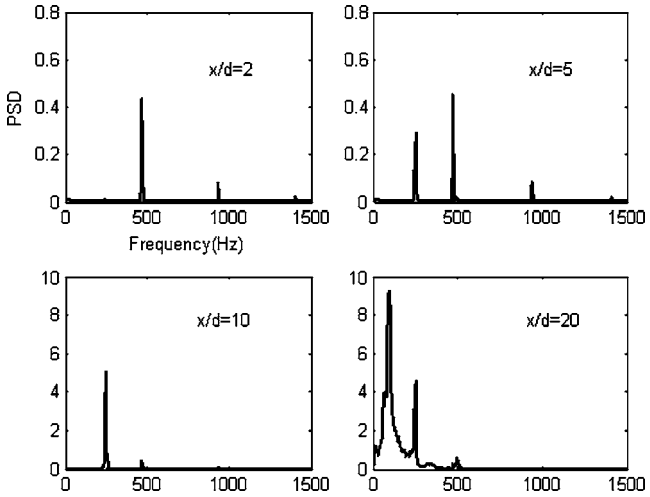

Fig. 5 Spectral variation of velocity fluctuations along the axis for Re=550

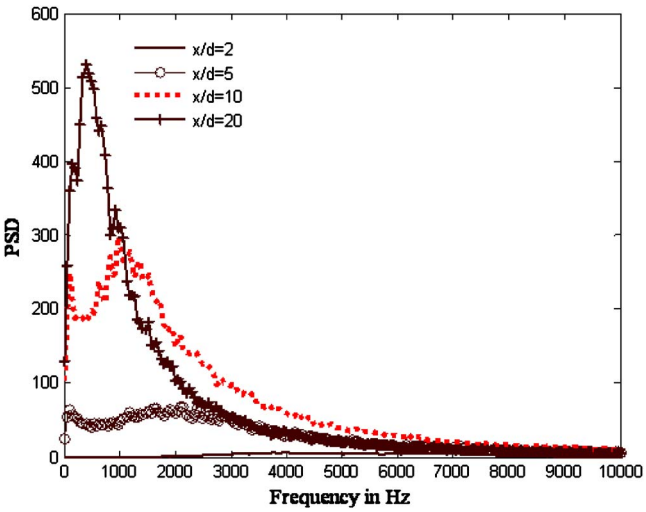

Fig. 7 Spectral variation of velocity fluctuations along the axis for Re=6250

tra toward lower frequency isolated peaks with higher amplitudes imply that the jet oscillations (due to shear layer instability) grow with distance because of entrainment of ambient fluid. At larger distances, a broader spectrum develops due to eddy coalescence and bifurcation phenomena. Large eddies appear to dominate even at an axial distance of $x/d=20$. At Re of 1100 (Fig. 6), isolated spectral components in the range of 0.8 kHz are observed in the near field ($x/d=2$). For larger axial distances, these components get amplified and other isolated spectral components also appear, primarily at lower frequencies. This trend can be attributed to the growth of vortex structures, which are initiated within the shear layer, in the near field region. Coalescence of small vortices into larger ones (vortex pairing) and growth due to entrainment of ambient fluid may result in the occurrence of low frequency, larger amplitude fluctuations. At still larger axial distances, while the peak amplitude shifts toward lower frequencies, the spectrum becomes broadbanded. These features for Re=1100 indicate the evolution of a turbulent flow field in the far region from an initially laminar jet flow near the nozzle with narrow band fluctuations arising from shear layer instabilities. At higher Reynolds number (Re=6250), broadband fluctuations are observed in the vicinity of the nozzle itself, although a few isolated frequency components are also superimposed on the broadband spectrum

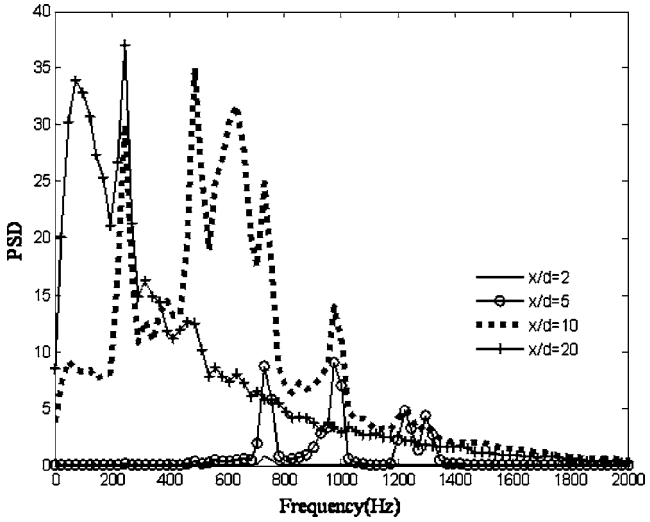

Fig. 6 Spectral variation of velocity fluctuations along the axis for Re=1100

(Fig. 7). At higher axial distances, the frequency of peak amplitude shifts toward lower values, even though the overall growth in amplitudes and the broadening of the spectra are evident. Thus, for Re=6250, it can be inferred that the incipience of turbulence occurs in the near field itself.

It is possible to define a Strouhal number for the jet flow as

$$\mathrm{St} = \frac{f_p d}{U} \tag{2}$$

where f_p is the frequency having the maximum amplitude in the power spectrum. Variations of St with axial distance are plotted in Fig. 8 for Re=1100 and Re=6250. Strouhal number has been calculated based on the frequency of dominant spectral component monitored along the jet centerline and also at the location where the mean velocity becomes half of the centerline velocity. These have been termed as "Strouhal number at centerline ($\mathrm{St_{CL}}$)" and "Strouhal number in shear layer ($\mathrm{St_{SL}}$)," respectively. It is clear that the centerline Strouhal number ($\mathrm{St_{CL}}$) is higher than the shear layer Strouhal number ($\mathrm{St_{SL}}$) near the nozzle, and beyond some axial distance, both become nearly equal. However, for the higher Re (Fig. 8(*b*)) situation, an earlier convergence of the two Strouhal number values is seen at $x/d=20$. At lower Re of 1100, the convergence occurs at a spatial location beyond $x/d=60$, indicating that shear layer development is delayed in such a case. It is to be noted that for a jet issuing from a long channel [1], the convergence distance was observed to be $x/d=40$ for Re=6250, as compared to the value of $x/d=20$ observed in the present study. Moreover, Re dependence for the convergence distance was also noticed by Thomas and Goldschmidt [1]. The values of Strouhal number obtained in the present work are comparable with those reported in the literature (Gutmark and Ho [15]). The convergence of the two Strouhal numbers for the centerline and the shear layer in the far region shows the nonexistence of two separate preferred modes of instability for a slit jet, namely, the jet column mode and the shear column mode. In general, the slit jet studied here behaves quite differently from the conventional contoured or channel jet as far as the St variation is concerned, which is important from the point of view of passive or active control of such jets.

3.3 Probability Distribution Function of Longitudinal Fluctuations. As discussed by Townsend [16], the PDFs of velocity fluctuations are Gaussian for homogeneous isotropic turbulent flows. Estimates of the axial variations of the third and fourth moments of fluctuating velocity (skewness and kurtosis, respectively) for different Reynolds numbers show that there are signifi-

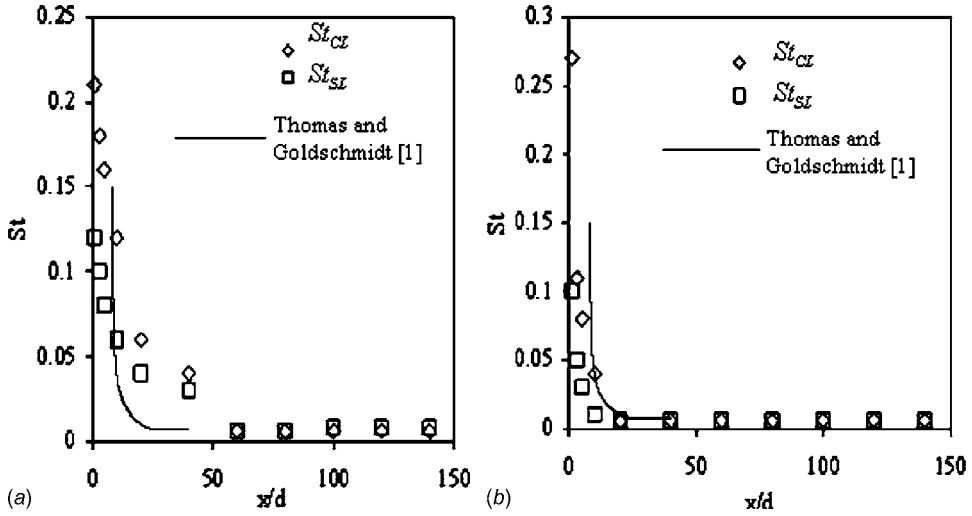

Fig. 8 Variation of St along the centerline and shear layer for Re=1100 and Re=6250

cant deviations from the Gaussian values of 0 and 3 for these quantities. Only in the far field, when jet evolution is almost complete, asymptotic approach to isotropic turbulence and the corresponding occurrence of a Gaussian probability distribution function are expected.

The probability density estimate **p** is the vector of density values evaluated at any spatial point x_i. The estimate is based on a normal Kernel function using a window parameter of "width" w that is a function of the number of points in w. The density is evaluated at 100 equally spaced points covering the range of the data in w. The turbulent velocity fluctuation is nondimensionalized by the respective rms velocities for calculating the PDFs.

Figures 9(*a*)–9(*c*) show the near and far field nature of PDFs. In the near field i.e., at $x/d=10$, we can see that the PDFs are not self-similar and Gaussian. At far regions ($x/d=80$), all the curves approach the Gaussian distribution but still deviate slightly from each other. Further away at $x/d=140$, low Re PDFs (Fig. 9(*c*))

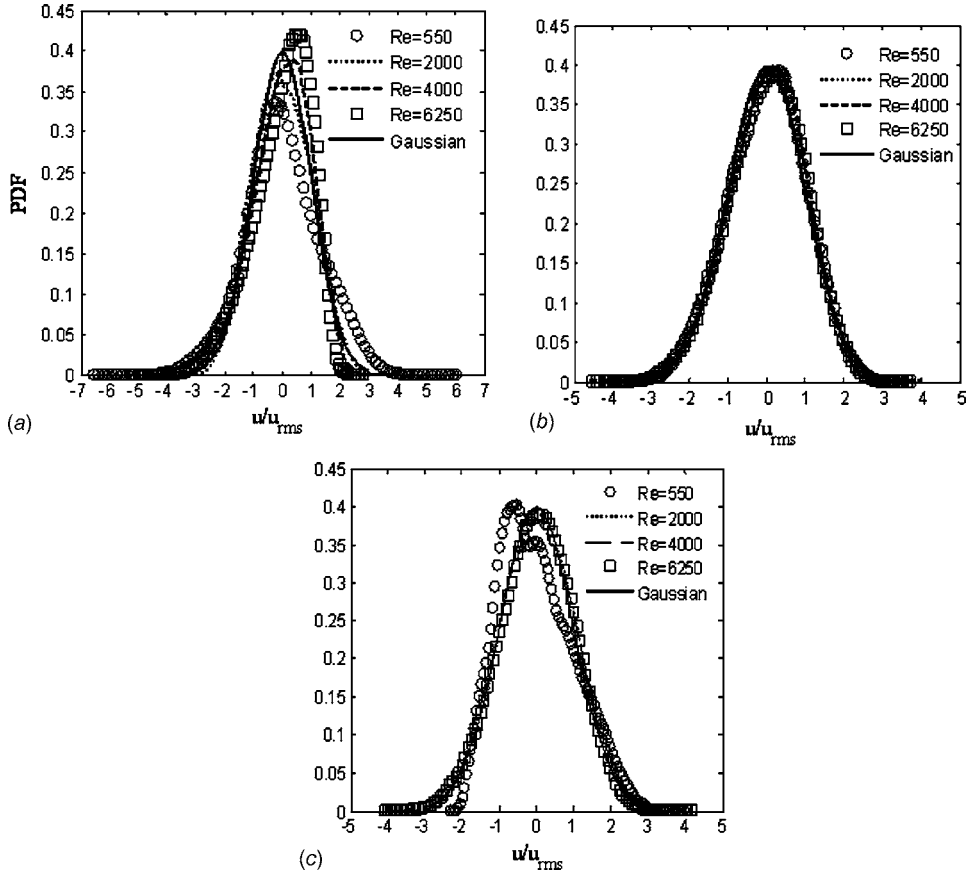

Fig. 9 (*a*) Reynolds number dependence of PDF in the near field ($x/d=10$). (*b*) Reynolds number dependence of PDF in the far field ($x/d=80$). (*c*) Reynolds number dependence of PDF in the very far field ($x/d=140$).

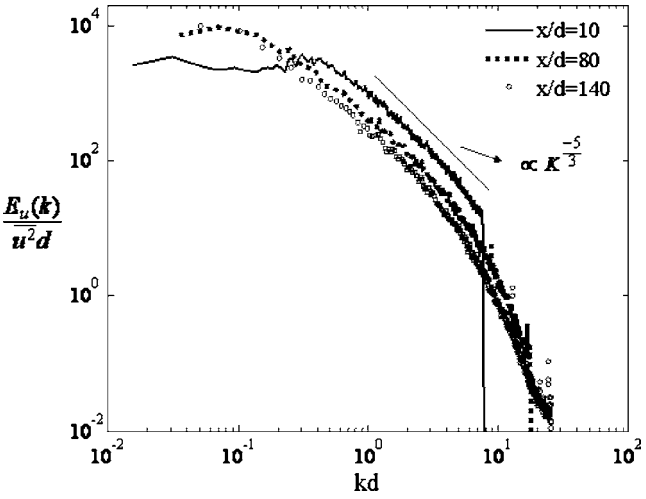

Fig. 10 Variation of wave number spectrum along the axis for Re=6250

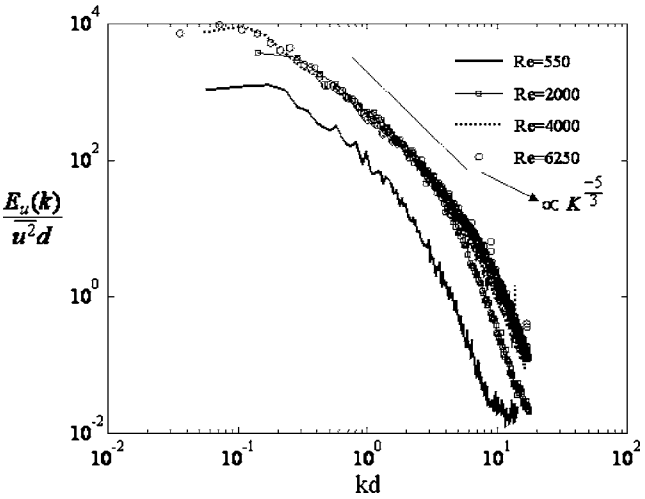

Fig. 11 Reynolds number dependence of wave number spectrum at $x/d=80$

deviate significantly from the Gaussian distribution; especially, the PDF of Re=550 becomes highly skewed due to the large intermittency and jet oscillations. This corroborates the idea that the jet is basically governed by coherent structure formation in the shear layer associated with the entrainment process and also phenomena such as axis switching. In the far field ($x/d>80$), full grown isotropic turbulent flow features are observed, except at very low Reynolds numbers. At such locations, the turbulent fluctuations achieve self-similarity, and they essentially become Re independent at high values of Re. However, from the mean velocity square decay (Fig. 3(*b*)), it is evident that in the far region of a slit jet, the mean flow field in the moderate Reynolds number regime of $250<\mathrm{Re}<6250$ still retains a memory of the nozzle exit conditions, though turbulent quantities have become Re independent. This trend is consistent with the observation of George [17].

3.4 Wave Number Spectra of Velocity Fluctuations. Bashir [18] reported a weak dependence of velocity spectra on the axial distance. However, Namer and Otugen [8] did not find any effect even at the near field location of $x/d=20$ and observed that the nondimensionalized wave number spectra collapse to a single curve for a contoured nozzle jet. Reynolds number dependence of the spectrum has been studied by Bashir and Uberoi [19] who carried out turbulence measurements in the Reynolds number range of 7000–18,000. Their results also indicate that normalized spectra are Reynolds number independent. In the present work, the power spectra of velocity fluctuations for a slit jet are estimated from raw data using MATLAB software, and variations with respect to jet Reynolds number and axial distance are studied.

The power spectra of velocity fluctuations in the wave number space, $E_u(k)$, are normalized with rms velocity and nozzle width. The wave number is defined as

$$k=\frac{2\pi f}{U} \tag{3}$$

where f is the frequency and U is the mean velocity at a particular location. The wave number spectra at different axial distances are plotted in Fig. 10 for Re=6250. A considerable region in the inertial subrange with slope close to the value of $-5/3$ is seen in the plots. It is clear that the length of the dissipation region is increasing with axial distance. So, the idea that larger distances support broader spectra is clear from this figure. Beyond $x/d=80$, variation in the spectrum with axial distance is minimal and limited to only the high wave number region of the normalized spectral distribution. At $x/d=10$, a drift is observed in the normalized spectrum. This can be attributed to the development of large vortical structures in the region due to the shear layer interactions. The minimum wave number decreases with a decrease in axial distance, showing that energy containing larger eddies are present in the near region. Figure 11 indicates that eddies of similar relative size contain the same fraction of turbulent kinetic energy in the developed region. A broadening of the spectra is also observed with an increase of Re.

It is clear that the curve for Re=550 in Fig. 11 fails to collapse with the higher Re data in the far region at $x/d=80$. This shows that the low Re jet never attains full grown turbulent flow conditions even in the far region. As discussed earlier, this trend can be attributed to the occurrence of shear layer instability modes and axis switching.

3.5 Length Scales. The value of the integral length scale L can be calculated from the autocorrelation coefficient function

$$\rho_u(t)=\frac{\overline{u(t)u(t+\tau)}}{\overline{u^2}} \tag{4}$$

where $u(t)$ is the measured time history record of longitudinal-velocity fluctuation and τ is a variable time delay. An integral time scale T_1 can be defined as

$$T_1=\int_0^\infty \rho_u(t)dt \tag{5}$$

Using Taylor's hypothesis, the value of L may be estimated from

$$L=UT_1 \tag{6}$$

The variation of integral length scale with axial distance is plotted for Re=550 and Re=6250 in Fig. 12. The figure shows that the integral length scale increases with axial distance, which, in turn, ensures better mixing in the far field region. At around $x/d=60$, a sudden increase of length scale is noticed. This region corresponds to the attainment of the asymptotic turbulence intensity and isotropic turbulence. The trends observed here are different from the near-linear increase seen by Namer and Otugen [8]. Since the aspect ratio of the slit jet considered here is less from that employed by Namer and Otugen [8] for their contoured nozzles, it is possible that transition to an axisymmetric jet profile occurs prior to the attainment of complete self-similarity. The integral length scales (i.e., the average size of energy containing large eddies) depend on the Reynolds number at any axial distance. Although small scale mixing will be more or less the same irrespective of Re, the sizes of inertial subrange eddies decrease

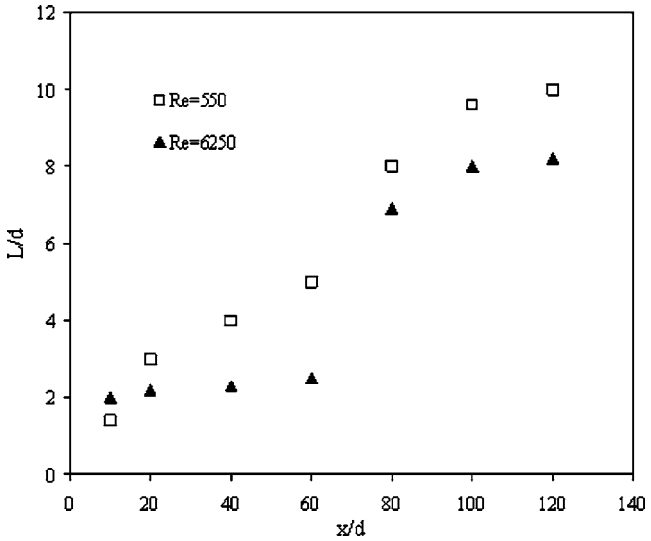

Fig. 12 Variation of integral length scale along the axis

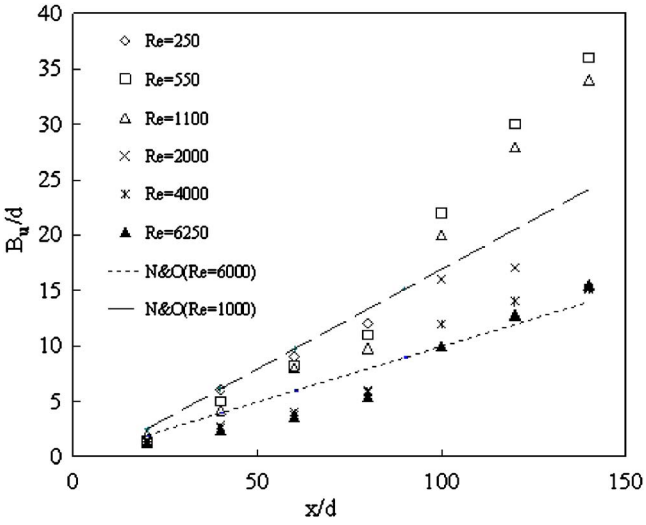

Fig. 14 Effect of Reynolds number on jet half-width variation. Note: N&O represents Ref. [8].

with Reynolds number. In other words, larger vortical structures are generated at lower Re values, as compared to those in the high Re range.

3.6 Turbulent Dissipation and Half-Width Growth Rate. The variations of dimensionless turbulent kinetic energy dissipation $\varepsilon d/U_c^3$ at different axial positions and various Reynolds numbers are plotted in Fig. 13. In the near region, the value of $\varepsilon d/U_c^3$ is observed to be high and nearly constant. The larger value of dissipation at the jet inlet implies nearly laminar conditions, and this is also the reason for the larger length of potential core observed in the present study as compared to that of Namer and Otugen [8]. Away from the nozzle exit, the dimensionless turbulence dissipation rate decreases at higher Re; correspondingly, the value of small scale turbulence production of $(1/2)(u^2+v^2+w^2)$ is expected to increase due to the decay of large eddies. The dissipation decreases with the increase of distance. This also illustrates the fact that smaller structures dominate in the far field, which are responsible for lower mixing. The far region flow field at high Re obeys the well known trend of $\varepsilon\alpha(x/d)^{-3/2}$.

The half-width (B_u) growth in x-y plane is plotted against the axial distance for various Reynolds numbers in Fig. 14. The growth rate is nearly linear up to a distance of $x/d=80$, and beyond this distance, nonlinearity appears, especially at low Reynolds numbers. As discussed earlier, three-dimensional phenomena such as axis switching and approach to axisymmetric profile may be responsible for such a nonlinear growth.

The half-width growth rate (also called spread rate) can be represented in the form

$$\frac{B_u}{d} = K_2\left(\frac{x}{d} - C_2\right) \tag{7}$$

where K_2 is the slope of spread rate and C_2 is the virtual origin. For low subsonic jets like the one in the present case, K_2 is expected to be constant for a given Reynolds number and independent of upstream conditions [20]. The variations of K_2 and C_2 are shown in Table 1 below.

At Re=6250, the slope K_2 and virtual origin C_2 are 0.07 and 2.81, with maximum uncertainty in the estimates being 8.75% and 10%, respectively, based on the methods suggested by Taylor [21] for least squares fit. The value of K_2 in the present work is lower by 30% from that of Ref. [8] at Re of 6250, showing a different spread rate for the slit jet used here. From the figure, it is also clear that for Re$<$1100, the spread is faster in line with the trends observed in Figs. 3, 4, and 13. The results presented above indicate that the turbulence level and spread rate depend on jet Reynolds number in the moderate Reynolds number regime. The large spread in the far field for the low Re cases may be attributed to the formation of large vortices in the shear layer due to convective

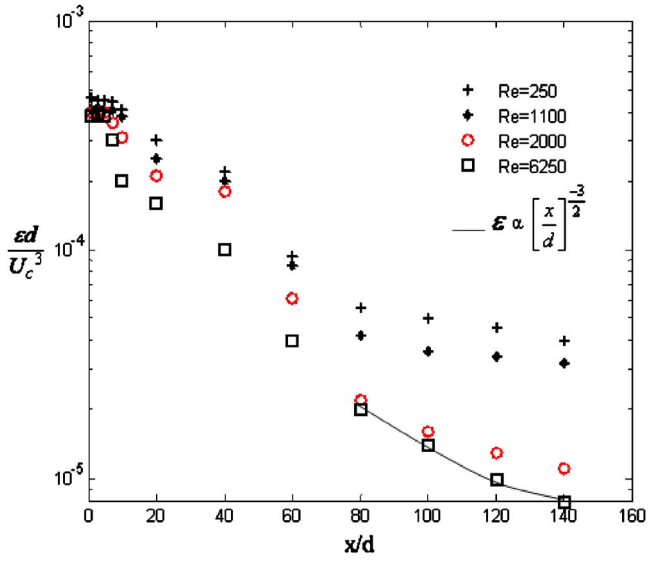

Fig. 13 Reynolds number effect on turbulent dissipation ε

Table 1 Variations of virtual origin and slope of spread rate with Reynolds number

Re	K_2	C_2
250	0.17	8.8
550	0.16	10
1100	0.14	5.71
2000	0.08	2.5
4000	0.074	4.05
6250	0.07	2.81
Namer and Otugen [8] (Re=1000)	0.179	6
Re=6000	0.1	0.6
Thomas and Goldschmidt [1] (Re=6000)	0.1	−3.2

instability, which result in greater level of mixing and eventually faster jet spreading, as observed in the flow visualization experiments of Hussain and Hussain [22]. In brief, the slit jet spread rates are considerably lower than those of contoured jet, as is clearly evident from the comparisons of mean velocity decay and half-width spread rates.

4 Conclusions

A jet issuing from a rectangular slit has been studied experimentally in the transition regime of Reynolds number, 250–6250. As compared with contoured nozzle jets, the spread rate of a slit jet is significantly lower. Based on the axial evolution of turbulence intensities, normalized spectral quantities, and PDFs, it is concluded that the two-dimensional slot jet becomes self-preserving at about 80 slot widths downstream of nozzle exit. At low Reynolds number, the development of turbulent structure into a self-preserving state is slow because of the effects due to shear layer instabilities and 3D phenomena such as transition from plane jet to a circular jet. Experiments reveal that the Reynolds number substantially affects many of the flow characteristics such as mixing, spread rate, and centerline decay during transition. Another feature brought out in the present study is the attainment of Reynolds number independence of turbulent quantities in the far region for $\mathrm{Re} > 1100$. The corresponding mean flow field, however, retains memory of the jet initial profile for the whole range of Reynolds number ($250 \leqslant \mathrm{Re} \leqslant 6250$) considered here. The practical significance of the findings may be concluded as follows. Due to slower near field mixing, this type of jet is suitable for air curtains and for pollutant dispersion into aquatic bodies or atmosphere where near field mixing is undesirable. In summary, from the mean and spectral properties of the simple slit jet flow studied here, it is possible to understand the nature of transition and identify conditions suitable for operation in engineering applications.

Nomenclature

B_u = half-width of the jet
$E_u(k)$ = spectral energy
d = height of the nozzle
f = frequency of fluctuations
f_p = frequency of component with peak amplitude value
k = wave number ($=2\pi f/U$)
L = integral length scale
PDF = probability density function
PSD = power spectral density
Re = Reynolds number ($=\rho U d/\mu$)
TI = turbulence intensity
St = Strouhal number ($=fd/U$)
$\mathrm{St_{CL}}$ = Strouhal number along the centerline
$\mathrm{St_{SL}}$ = Strouhal number along the shear layer
U_c = centerline velocity
U_0 = jet exit velocity
u = fluctuation velocity in the x direction
v = fluctuation velocity in the y direction
w = fluctuation velocity in the z direction
x = axial coordinate
y = transverse coordinate (along a height of 2 mm)

Greek Symbols

δ = displacement thickness
θ = momentum thickness
τ = lag time in autocorrelation
σ = standard deviation of the quantity
ε = turbulent dissipation

References

[1] Thomas, F. O., and Goldschmidt, V. W., 1986, "Structural Characteristics of a Developing Turbulent Planar Jet," J. Fluid Mech., **163**, pp. 227–256.
[2] Antonia, R. A., Browne, L. W. B., Rajagopalan, S., and Chambers, A. J., 1983, "On the Organized Motion of a Turbulent Plane Jet," J. Fluid Mech., **134**, pp. 49–66.
[3] Heskestad, G., 1965, "Hotwire Measurements in a Plane Turbulent Jet," ASME J. Appl. Mech., **32**, pp. 721–734.
[4] Gutmark, E., and Wygnanski, I., 1976, "The Planar Turbulent Jet," J. Fluid Mech., **73**(3), pp. 465–495.
[5] Bradbury, L. J. S., 1965, "The Structure of a Self Preserving Turbulent Jet," J. Fluid Mech., **23**, pp. 31–64.
[6] Klein, M., Sadiki, A., and Janicka, J., 2003, "Investigation of the Influence of the Reynolds Number on a Plane Jet Using Direct Numerical Simulation," Int. J. Heat Fluid Flow, **24**, pp. 785–794.
[7] Suyambazhahan, S., Das, S. K., and Sundararajan, T., 2004, "Hydrodynamic and Thermal Oscillations in a Non-Isothermal Laminar Jet," Int. J. Heat Mass Transfer, **47**(17), pp. 3957–3969.
[8] Namer, I., and Otugen, M. V., 1988, "Velocity Measurements in a Plane Turbulent Air Jet at Moderate Reynolds Numbers," Exp. Fluids, **6**, pp. 387–400.
[9] Jo, S. H., and Kim, M. U., 2002, "Hydrodynamic Stability of Two Dimensional Jet Near the Nozzle Exit," JSME Int. J., Ser. B, **45**(3), pp. 694–703.
[10] Hussain, A. K. M. F., and Clark, A. R., 1977, "Upstream Influence on the Near Field of a Plane Turbulent Jet," Phys. Fluids, **20**(9), pp. 1416–1426.
[11] Brunn, H. H, 1995, *Hotwire Anemometry*, Oxford University Press, New York.
[12] Fujita, H., and Kovasznay, S. G., 1968, "Measurement of Reynolds Stress by a Single Rotated Hot Wire Anemometer," Rev. Sci. Instrum., **39**(9), pp. 1351–1355.
[13] Moffat, R. J., 1985, "Using Uncertainty Analysis in the Planning of an Experiment," ASME J. Fluids Eng., **107**, pp. 173–182.
[14] Krothapalli, A., Banganoff, D., and Karamcheti, K., 1981, "On the Mixing of Rectangular Jet," J. Fluid Mech., **107**, pp. 201–220.
[15] Gutmark, E., and Ho, C. M., 1983, "Preferred Modes and the Spreading Rates of Jets," Phys. Fluids, **26**(10), pp. 2932–2938.
[16] Townsend, A. A., 1976, *The Structure of Turbulent Free Shear Flow*, 1976, Cambridge University Press, Cambridge, England.
[17] George, W. K., 2004, "Role of Initial Conditions in Establishing Flow Conditions," AIAA J., **42**(3), pp. 438–446.
[18] Bashir, J., 1973, "Experimental Study of the Turbulent Structure and Heat Transfer of a Two Dimensional Heated Jet," Ph.D. thesis, University of Colarado, Boulder, CO.
[19] Bashir, J., and Uberoi, M. S., 1975, "Experiments on Turbulent Structure and Heat Transfer in a Two Dimensional Jet," Phys. Fluids, **18**(4), pp. 405–410.
[20] James, J. F., and Lafayette, V., 1969, "Virtual Origins of a Plane Turbulent Jet," AIAA J., **7**(12), pp. 2344–2346.
[21] Taylor, J. R., 1997, *An Introduction to Error Analysis*, University Science Books, Herndon, VA.
[22] Hussain, H. S., and Hussain, A. K. M. F., 1983, "Flow Visualization of the Coherent Structure Interactions in the Near Field of a Plane Jet," *Proceedings of the Third International Symposium on Flow Visualization*, University of Michigan, Ann Arbor, MI, pp. 510–513.

Numerical Simulation of Vortex Shedding and Lock-in Characteristics for a Thin Cambered Blade

Baoshan Zhu[1]
e-mail: bszhu@mail.tsinghua.edu.cn

Jun Lei

Shuliang Cao

State Key Laboratory of Hydroscience and Engineering,
Department of Thermal Engineering,
Tsinghua University,
Beijing 100084, P.R.C.

In this paper, vortex-shedding patterns and lock-in characteristics that vortex-shedding frequency synchronizes with the natural frequency of a thin cambered blade were numerically investigated. The numerical simulation was based on solving the vorticity-stream function equations with the fourth-order Runge–Kutta scheme in time and the Chakravaythy–Oscher total variation diminishing (TVD) scheme was used to discretize the convective term. The vortex-shedding patterns for different blade attack angles were simulated. In order to confirm whether the vortex shedding would induce blade self-oscillation, numerical simulation was also carried out for blade in a forced oscillation. By changing the pitching frequency and amplitude, the occurrence of lock-in at certain attack angles was determined. Inside the lock-in zone, phase differences between the blade's pitching displacement and the torque acting on the blade were used to infer the probability of the blade self-oscillation. [DOI: 10.1115/1.2776964]

Keywords: vortex shedding, forced oscillation, lock-in, self-oscillation, thin cambered blade

Introduction

Sources of fluid-induced vibration and noise in turbomachinery include rotor-stator interaction, vortex shedding, cavitation, inlet distortion, flow separation, rotating stall, and so on. Among these sources, vortex shedding from runner blades, when attack angle of the blades is near their stall angle, is considered to be an important excitation source for the pressure fluctuations and vibrations in turbomachines. To remove blade resonance excited by the vortex shedding, the so-called lock-in zone, in which the vortex-shedding frequency synchronizes with the blade natural frequency, should be avoided when the incidence angle of the blade is changed during the operation of the machines. However, it is not easy to determine the lock-in zone of a blade at different attack angles.

One of the objectives of the present paper is to investigate lock-in characteristics for a thin cambered blade, which has a similar cross section shape as the blades used in an axial pump installed in a large-capacity drainage pump station. The pump was operated at a constant rotational speed, and the flow discharged through the runner was adjusted by changing the attack angle of the blades. Large pressure fluctuations were observed in the suction water tunnels when the pump was operated at some attack angles of the blade without a rated head [1]. Pressure fluctuations in the tunnels, lateral and torsional vibrations of the shaft, vibrations of bearing housing, vibrations of ground, as well as pressure fluctuations of oil in the hydraulic control system were measured simultaneously. The relations among these vibrations and the dependence of these vibrations on the attack angles of the blade and rotational speed were investigated. Detailed measurements suggested that the excitation source was the vortex shedding from the blade.

In order to investigate the correlations of large pressure fluctuations in the water tunnels of the pump station with the vortex shedding from the blade, model experiments have been carried out [2,3]. Undoubtedly, the impeller of the axial pump has a three-dimensional stacking of blade geometry; for simplicity the three-dimensional effects were neglected and a two-dimensional blade cross section at midspan of the impeller was used to generate the unsteady vortex shedding and the vortex induced in the experiments.

Most of the studies [4–12] on vortex lock-in have been restricted to flow past bluff bodies with simple geometry, such as cylinders and flat plates. Early research on vortex shedding from forced-oscillating bluff cylinders showed that lock-in took place when the cylinder was undergoing either in-line oscillations with the incident flow or cross-flow oscillations [4,5]. Tokumaru and Dimotakis [6] and Filler et al. [7] confirmed through experiments that lock-in could also be induced when the cylinder was subjected to rotational oscillations near the natural shedding frequency through experimental observations. Recently, numerical studies of Mahfouz and Badr [8], Cheng et al. [9], and Choi et al. [10] also explored many details of the vortex lock-in phenomena of a rotational and oscillating cylinder. Chen and Fang [11,12] investigated experimentally and numerically the lock-in of vortex shedding induced by rotational oscillations of a flat plate, which was normal to a uniform stream.

Although the flow field near foils undergoing pitching motion has been extensively investigated because of its historical importance not only in rotorcraft applications but also in turbomachinery [13–16], there are only few reported studies of lock-in phenomena for flow around an oscillating foil. Flow field around foils at large angles of attack is usually characterized by massive flow separation, reattachment, and unsteadiness. Periodic vortex shedding results in a considerable fluctuating load on the blade. When the blade is periodically oscillated by external forcing, the shedding frequency can be modified from its natural shedding frequency to the forcing frequency. The lock-in of vortex shedding may also be changed to the forcing frequency.

In the present study, vortex-shedding patterns and lock-in characteristics of the blade tested in the experiments [2,3] were numerically investigated. The numerical simulations were based on solving the vorticity-stream function equations using a finite dif-

[1]Corresponding author.

Contributed by the Fluids Engineering Division of ASME for publication in the JOURNAL OF FLUIDS ENGINEERING. Manuscript received July 4, 2006; final manuscript received April 28, 2007. Review conducted by Yu-Tai Lee.

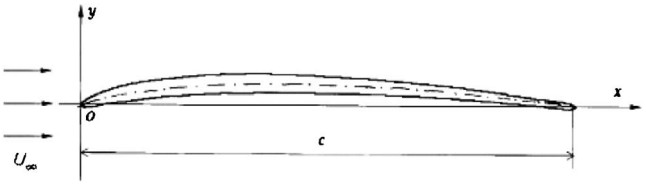

Fig. 1 The tested thin cambered blade with maximum camber $y/c=0.038$ at $x/c=0.40$ and blade thickness $t/c=0.036$ at $x/c=0.27$

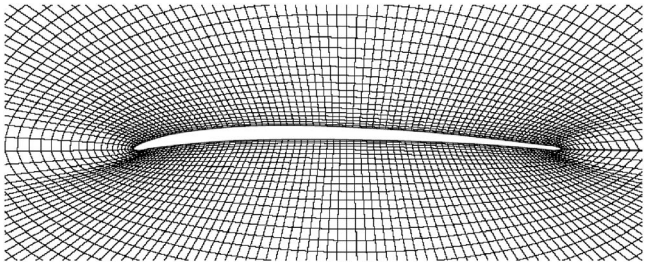

Fig. 2 *O* grid around the blade

ference method. The Chakravaythy–Oscher TVD scheme was used to discretize the convective term in the vorticity-transport equation. The stream function equation was solved with the Tschebyscheff successive linear overrelaxation (SLOR) method in alternative computational directions. The unsteady flows for different attack angles were first calculated. Then, the lock-in characteristics for vortex shedding corresponding to some attack angles were investigated by forcing the blade to oscillate. Inside the lock-in zone, the phase differences between the blade's oscillation displacements and the torques acting on the blade were evaluated, and the probability of the blade self-oscillation was inferred from the phase differences. The present investigation can help us to understand the mechanism of self-excited vibration of the conventional blade, and the results may be useful for practical application.

Equations and Solutions

Governing Equations. Consider an external incompressible two-dimensional flow in arbitrary motion. The governing equations in a vorticity-stream function (ω-ψ) formulation are written for a moving system,

$$\frac{\partial}{\partial t}(\omega + 2\Omega) + \nabla \cdot (\mathbf{u}\omega) = \nu \nabla^2 \omega \tag{1}$$

$$\nabla^2 \psi = -\omega \tag{2}$$

where $\mathbf{u}=(u,v)$ denoting the velocity components in the (x,y) directions in a moving system, Ω is the angular velocity, and ν is the kinematic viscosity. The vorticity ω and the stream function ψ are defined as

$$\omega = \frac{\partial v}{\partial x} - \frac{\partial u}{\partial y} \tag{3}$$

$$u = \frac{\partial \psi}{\partial y} \quad v = -\frac{\partial \psi}{\partial x} \tag{4}$$

A transformation from the Cartesian coordinates (x,y) to a boundary-fitted curvilinear coordinates (ξ, η) is carried out by introducing the general transformation $\xi=\xi(x,y)$ and $\eta=\eta(x,y)$. Equations (1) and (2) in the general curvilinear coordinates (ξ, η) are

$$\frac{\partial}{\partial t}[J(\omega + 2\Omega)] + \nabla \cdot (\mathbf{u}^c \omega) = \nu \nabla^2 \omega \tag{5}$$

$$\nabla^2 \psi = -J\omega \tag{6}$$

where J is the Jacobian transformation and $\mathbf{u}^c=(JU,JV)$ denotes the contravariant velocity components in the (ξ, η) directions.

Computational Domain and Boundary Conditions. Figure 1 shows the thin cambered blade investigated also in the experiments shown in Refs. [2,3]. The blade was supported by transverse wires at 40% chord. Although the experiments were carried out at Reynolds numbers, defined as $\mathrm{Re}=U_\infty c/\nu$, from 1.0×10^5 to 2.2×10^5, all the calculations were made at the smallest Reynolds number. Here, U_∞ denotes the freestream velocity and c denotes the chord length of the blade.

In order to confirm whether the blade vortex shedding would induce its self-oscillation, simulations were carried out for the blade under a forced sinusoidal oscillation about the axis $(x_0,y_0)=(0.40,0.038)$ with an attack angle given as

$$\alpha = \bar{\alpha} + \Delta\alpha \sin(2\pi f t) \tag{7}$$

where $\bar{\alpha}$ is the mean attack angle, $\Delta\alpha$ is the amplitude, and f is the frequency of the forced oscillation, which is expressed as an oscillating Strouhal number $\mathrm{St}=fc/U_\infty$.

In the calculation, the blade is embedded in a moving **O** grid, as shown in Fig. 2. A grid resolution study using grid densities $I\times J=180\times220$ and $I\times J=225\times275$ (I and J denote the circumferential and radial directions, respectively) showed that two grids produced nearly the same results for the forces acting on the blade and streamline contours around the blade for $\alpha=-8.3+5\sin(2\pi t)$; therefore the coarser grid was used for all calculations. Numerical tests of the effects of the nondimensional time step $\Delta T=\Delta t U_\infty/c$ used were done using values of 2.5×10^{-4}, 5.0×10^{-4}, and 1.0×10^{-3}. It was found that the time steps of 2.5×10^{-4} and 5.0×10^{-4} were identical, and thus the latter value was used for all computations.

The relation between the variables in the inertial frame of reference and the moving system is as follows:

$$\psi^* = \psi - \frac{\Omega}{2}[(x-x_0)^2 + (y-y_0)^2] \quad \omega^* = \omega + 2\,\Omega \tag{8}$$

$$u^* = u - \Omega(y-y_0) \quad v^* = v + \Omega(x-x_0) \tag{9}$$

where asterisk (*) denotes variables in the inertial frame of reference. In the far field, we have $u^*|_\infty=1$, $v^*|_\infty=0$, $\psi^*|_\infty=y^*-y_0^*$, and $\omega^*|_\infty=0$, where $\psi^*|_\infty=0$ when $y^*=y_0^*$. At the outflow boundary, the vorticity is assumed to be convected out of the computational domain by the freestream velocity.

On the blade surface Γ, the no-flux condition for the velocity is applied, resulting in $\psi|_\Gamma=0$. The boundary condition for the vorticity $\omega|_\Gamma$ is determined as

$$\omega|_\Gamma = \left.\frac{\partial^2 \psi}{\partial \mathbf{n}^2}\right|_\Gamma \tag{10}$$

which is subjected to the condition $\partial\psi/\partial\mathbf{n}|_\Gamma=0$, where $\mathbf{n}$ is the direction perpendicular to the surface. In the calculation, the so-called Wikes formula [17] was used to determine the vorticity on the body surface.

Numerical Method. Equations (5) and (6) are solved using the fourth-order Runge–Kutta scheme as follows:

$$\frac{\omega_1^* - \omega^{*(n)}}{\Delta t/2} = \frac{1}{J}\left[-\frac{\partial}{\partial\xi}(JU^n\omega^{*(n)}) - \frac{\partial}{\partial\eta}(JV^n\omega^{*(n)}) + \nu\nabla^2\omega^{*(n)}\right]$$

$$\nabla^2 \psi_1 = -J\omega_1 \tag{11}$$

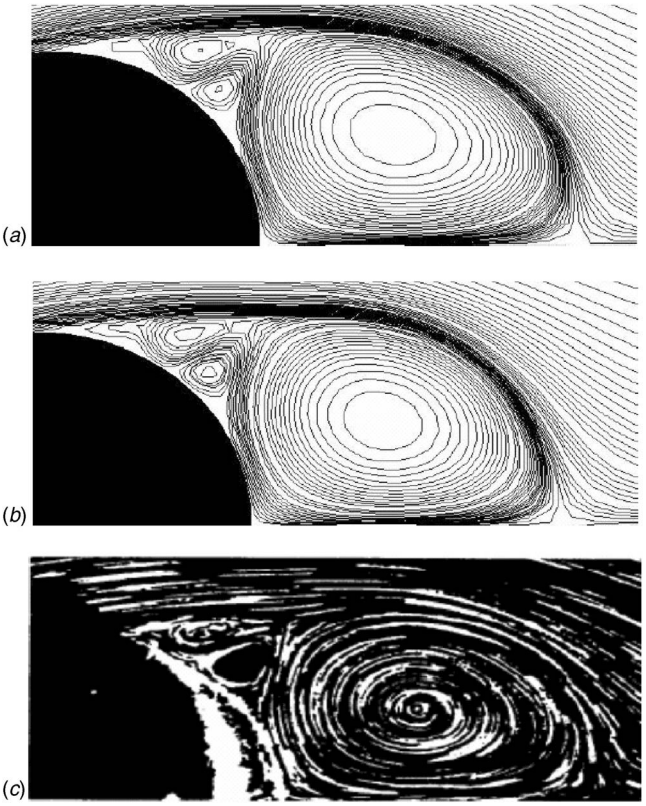

Fig. 3 Comparison of streamline for Re=3000 at T=5.0: (*a*) present method, grid density 120×150, ΔT=0.005; (*b*) present method, grid density 180×220, ΔT=0.0025; and (*c*) flow visualization by Bouard and Coutanceau [18]

$$\frac{\omega_2^* - \omega^{*(n)}}{\Delta t/2} = \frac{1}{J}\left[-\frac{\partial}{\partial \xi}(JU_1\omega_1^*) - \frac{\partial}{\partial \eta}(JV_1\omega_1^*) + \nu\nabla^2\omega_1^*\right]$$

$$\nabla^2\psi_2 = -J\omega_2 \tag{12}$$

$$\frac{\omega_3^* - \omega^{*(n)}}{\Delta t} = \frac{1}{J}\left[-\frac{\partial}{\partial \xi}(JU_2\omega_2^*) - \frac{\partial}{\partial \eta}(JV_2\omega_2^*) + \nu\nabla^2\omega_2^*\right]$$

$$\nabla^2\psi_3 = -J\omega_3 \tag{13}$$

$$\omega_4^* = \Delta t\frac{1}{J}\left[-\frac{\partial}{\partial \xi}(JU_3\omega_3^*) - \frac{\partial}{\partial \eta}(JV_3\omega_3^*) + \nu\nabla^2\omega_3^*\right]$$

$$\omega^{*(n+1)} = (-\omega^{*(n)} + \omega_1^* + 2\omega_2^* + \omega_3^*)/3 + \omega_4^*/6$$

$$\nabla^2\psi^{n+1} = -J\omega^{n+1} \tag{14}$$

where the variables with subscripts 1, 2, 3, and 4 denote the variables at the first, second, third, and fourth computational stages from time t to $t+\Delta t$, and the variables with superscripts n and $n+1$ denote the variables at time t and $t+\Delta t$, respectively.

At every stage, the convective term in the vorticity-transport equation is discretized with the third-order Chakravaythy–Oscher TVD scheme, and the diffusive term with the second-order central difference scheme. The stream function equation is solved with the Tschebyscheff SLOR method in two alternative computational directions. According to Eqs. (11)–(14), the vorticity-transport equation acts as the predictor and the stream function equation as the corrector. Although Eqs. (5) and (6) are solved independently, they are coupled on the surface of the blade. There is no explicit

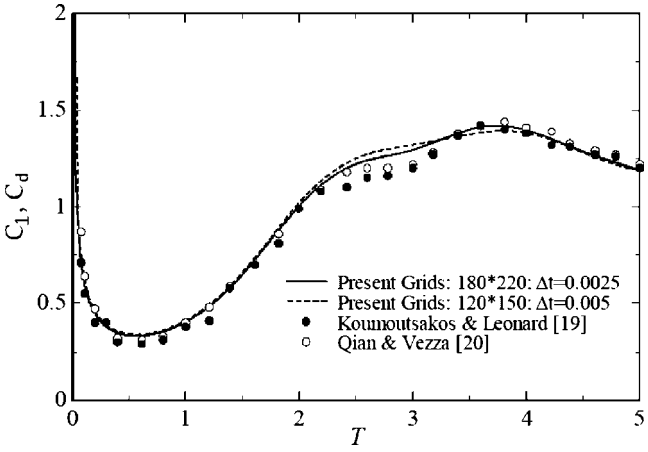

Fig. 4 Comparison of drag coefficient: Re=3000

boundary condition for the vorticity; this condition is established by employing Eq. (10) on the surface of the blade and enforcing $\partial\psi/\partial\mathbf{n}|_\Gamma = 0$ on the surface.

Calculation of Forces. On the surface of the blade, the following equation applied in the moving system must be satisfied:

$$\frac{\partial p}{\partial \mathbf{s}} = -\nu\frac{\partial \omega}{\partial \mathbf{n}} + \frac{\Omega}{2}\frac{\partial}{\partial \mathbf{s}}[(x-x_0)^2 + (y-y_0)^2] + \dot{\Omega}\left[(y-y_0)\frac{\partial x}{\partial \mathbf{s}} - (x-x_0)\frac{\partial y}{\partial \mathbf{s}}\right] \tag{15}$$

where p is the pressure on the surface of the blade, $\mathbf{s}$ is the tangential direction of the surface, and $\dot{\Omega}$ is the angular acceleration. The entire pressure distribution on the surface of the blade can be calculated by integrating of Eq. (15) with an assumed reference pressure.

The friction force exerted on the blade can be calculated as

$$\boldsymbol{\tau} = -\mu\mathbf{n} \times \boldsymbol{\omega} \tag{16}$$

where $\boldsymbol{\tau}$ is the shear stress, μ is the dynamical viscosity, and $\boldsymbol{\omega} = (0, 0, \omega)$. The drag force D, lift force L, and torque M acting on the blade are obtained from the following formulations:

$$D = \oint_\Gamma (-p\mathbf{n}\cdot\mathbf{i} + \boldsymbol{\tau}\cdot\mathbf{i})ds \tag{17}$$

$$L = \oint_\Gamma (-p\mathbf{n}\cdot\mathbf{j} + \boldsymbol{\tau}\cdot\mathbf{j})ds \tag{18}$$

$$M = \oint_\Gamma [(-p\mathbf{n}\cdot\mathbf{j} + \boldsymbol{\tau}\cdot\mathbf{j})\mathbf{r}\cdot\mathbf{i} - (-p\mathbf{n}\cdot\mathbf{i} + \boldsymbol{\tau}\cdot\mathbf{i})\mathbf{r}\cdot\mathbf{j}]ds \tag{19}$$

where $\mathbf{i}$ and $\mathbf{j}$ denote the unit vectors along the coordinate x and y, respectively. $\mathbf{r}$ is the distance vector and s is the surface arc length.

The nondimensional drag force C_d, lift force C_l, and torque C_m are calculated as

$$C_d = D \Big/ \left(\frac{1}{2}\rho U_\infty^2 c\right) \tag{20}$$

$$C_l = L \Big/ \left(\frac{1}{2}\rho U_\infty^2 c\right) \tag{21}$$

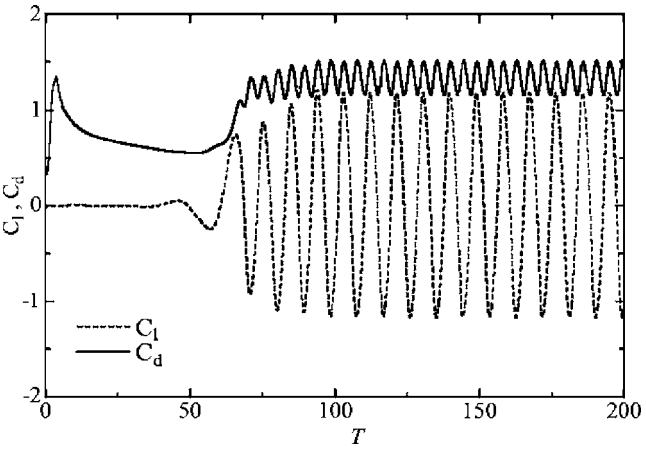

Fig. 5 Time variation in lift and drag coefficients: Re=3000

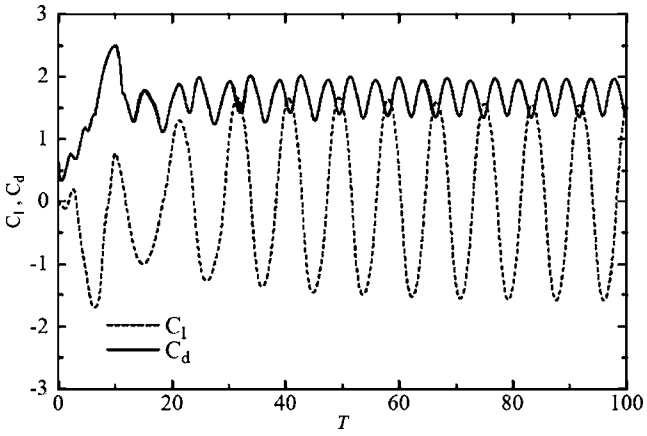

Fig. 7 Lift and drag coefficients at $f/f_s=1.0$ and $A_m=2.0$

$$C_m = M \Big/ \left(\frac{1}{2}\rho U_\infty^2 c^2\right) \tag{22}$$

where ρ is the density of the fluid.

Numerical Tests of the Present Method. We use the case of flow past a circular cylinder at a Reynolds number of Re $=2U_\infty R/\nu=3000$ to demonstrate the computational accuracy and the influence of grid density and time step size. For the coarser grid, we use a 120×150 grid in (r,θ) directions and the size of the first grid cell at the cylinder surface is $\Delta r_1=0.005$. The nondimensional time step adopted for the calculation is $\Delta T=\Delta t U_\infty/R=0.005$. For the finer grid, a 180×220 grid is used; Δr_1 and ΔT are set to 0.0025 and 0.0025, respectively. A comparison of the streamline patterns at nondimensional $T=5$ was made in Fig. 3 between the present results and the flow visualization results of Bouard and Coutanceau [18]. The calculated streamline patterns agree well with the flow visualization for both grid systems.

In Fig. 4, the drag coefficients calculated from two different grids are given. As discussed by Koumoutsakos and Leonard [19] at Re=3000, a series of separation phenomena appear on the circular cylinder surface, which poses a challenge for numerical method to capture all the flow structures. The interplay between the main vorticity and the secondary vorticity is reflected in the development of drag force as a drag plateau appears between $t=2.2$ and $t=3.0$. It can be seen that this phenomenon has been captured by the present method. Figure 4 also shows that the finer

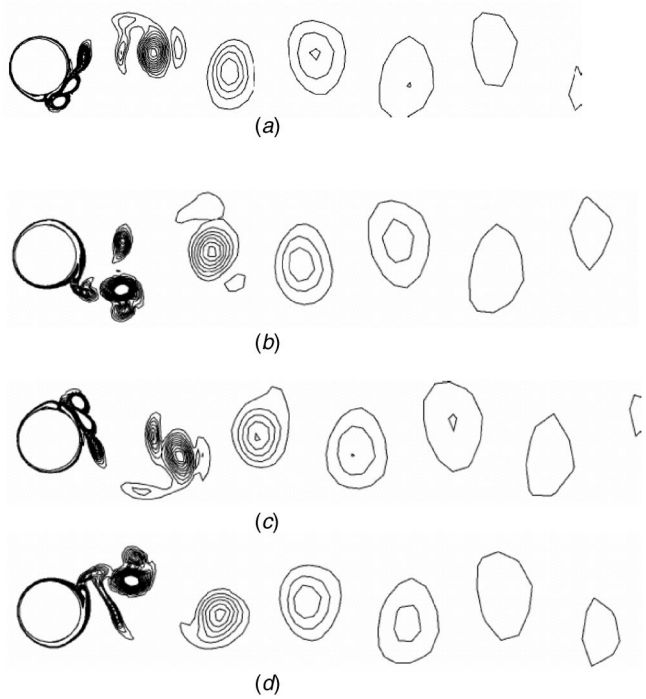

Fig. 6 Vortex patterns at $f/f_s=1.0$ and $A_m=2.0$ in a cycle T: (*a*) $T/4$, (*b*) $T/2$, (*c*) $3T/4$, and (*d*) T

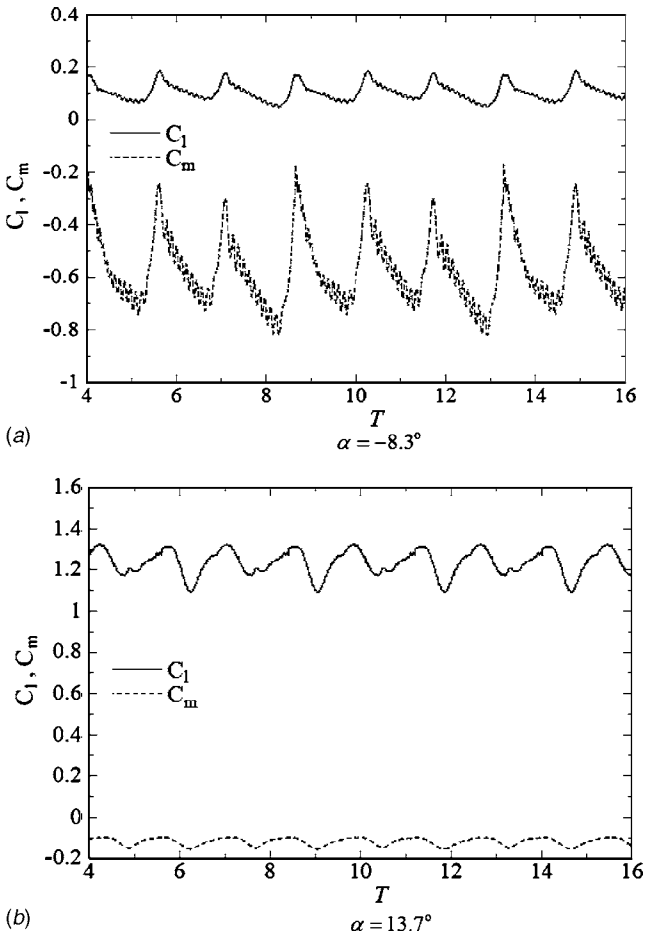

Fig. 8 Time variations for lift force and torque: (*a*) $\alpha=-8.3$ deg and (*b*) $\alpha=13.7$ deg

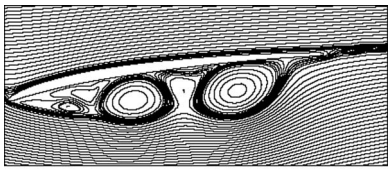

(a) Calculated streamline at $T=14.40$

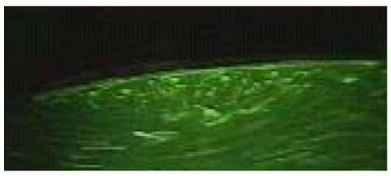

(b) Flow visualization [3]

Fig. 9 Instantaneous flow patterns for $\alpha=-8.3$ deg: (*a*) calculated streamline at $T=14.40$; (*b*) flow visualization [3]

grid with $\Delta t=0.0025$ gives a better agreement with the results from Koumoutsakos and Leonard [19] and Qian and Vezza [20]. The following results in this section are given using the finer grid.

The time histories of the drag and lift coefficients for a longer time period are given in Fig. 5. In the present study, no artificial perturbation was applied to the flow to initiate the alternate vortex shedding; rather, it is generated by the numerical diffusion during the calculation. After an extended time interval, i.e., $T>90$, the vortex-shedding process finally settles down, forming a steady vortex-shedding pattern in its wake. From Fig. 5, it can be calculated that the average C_d value after $T>90$ is about 1.34, and the Strouhal number St determined from the lift coefficient plot is about 0.22.

Using the present method, we have also investigated the unsteady flow past the cylinder undergoing rotational oscillation, i.e., $\Omega R/U_\infty=2.0\sin(0.22\pi t)$ at $\mathrm{Re}=3000$, which means that the rotating amplitude defined based on the maximum circumferential velocity of the cylinder surface is $A_m=\Omega R/U_\infty=2.0$ and the oscillating frequency $f=0.11$ or $f/f_s=1$, where f_s is a vortex-shedding frequency for flow past the stationary cylinder. Figure 6 shows the vorticity contours in an oscillating cycle of $T=9.02$. The vortex patterns shown in Fig. 6 indicate that two vortices of the same sign are shed in a half-cycle from the same side of the cylinder. The first vortex is induced by the opposite-sign vortex, i.e., the most recently generated one from the other side of the cylinder. Figure 7 shows the variation of the force coefficients. The lift coefficients vary at the vortex-shedding frequency, and the drag coefficients oscillate at twice the shedding frequency. Figure 7 also indicates that the value of the time-averaged drag ($C_d=1.70$) and the fluctuation amplitude of the lift coefficient are

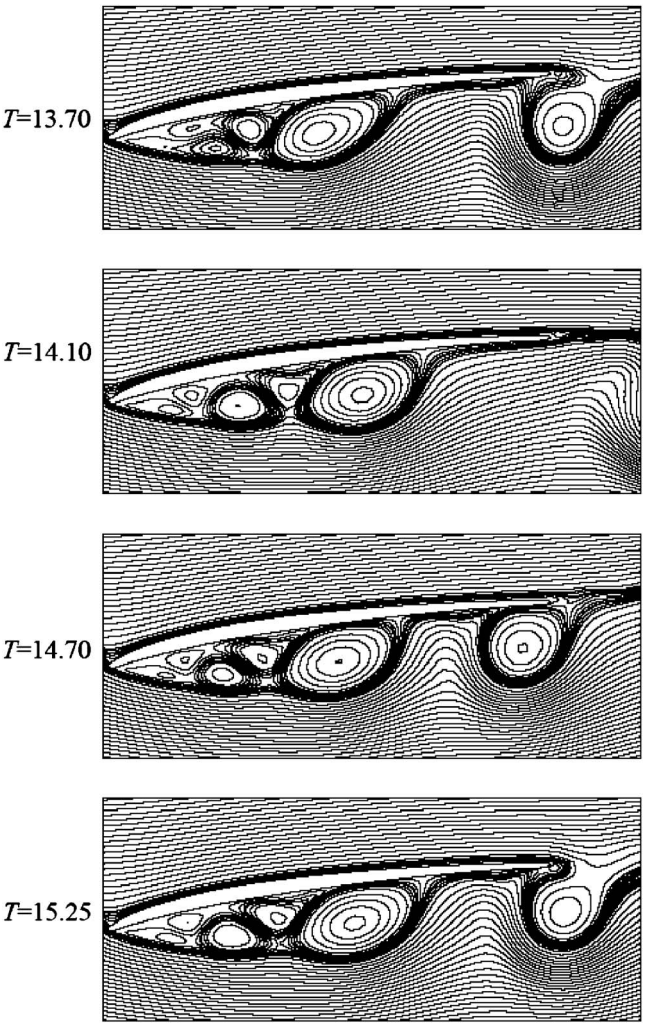

Fig. 10 Calculated streamline contours in a cycle: $\alpha=-8.3$ deg

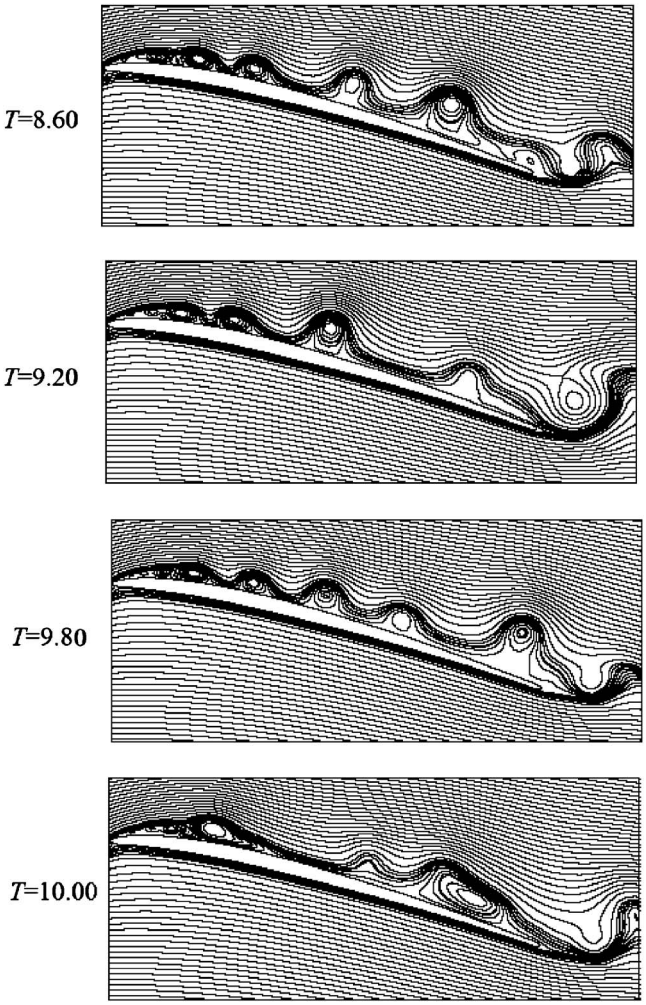

Fig. 11 Calculated streamline contours in a cycle: $\alpha=13.7$ deg

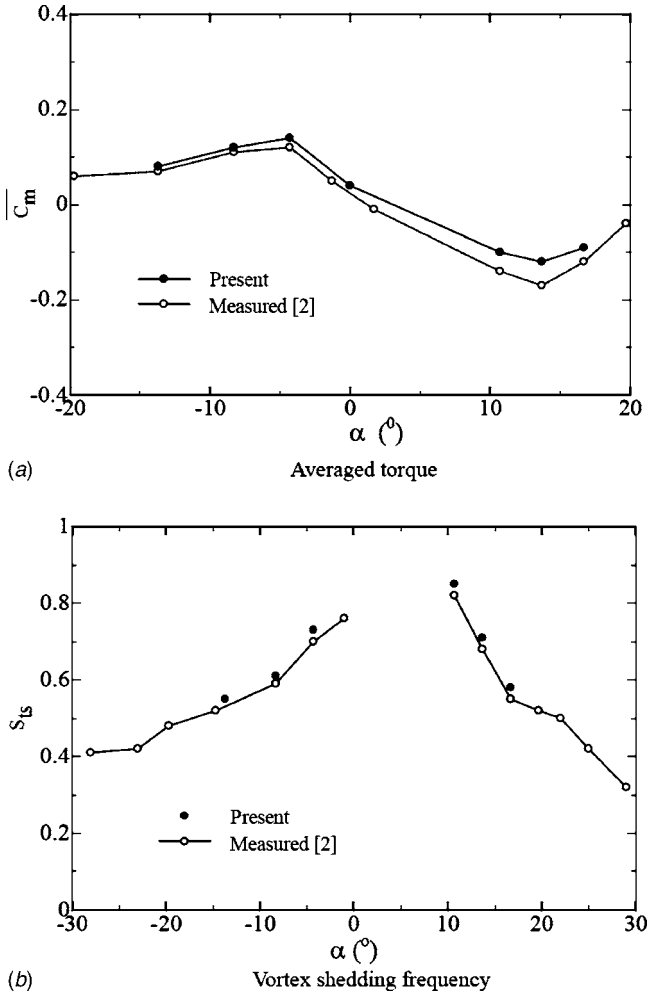

Fig. 12 Variation of averaged torque and vortex-shedding frequency with attack angle α: (*a*) $\alpha=-8.3$ deg and (*b*) $\alpha=13.7$ deg

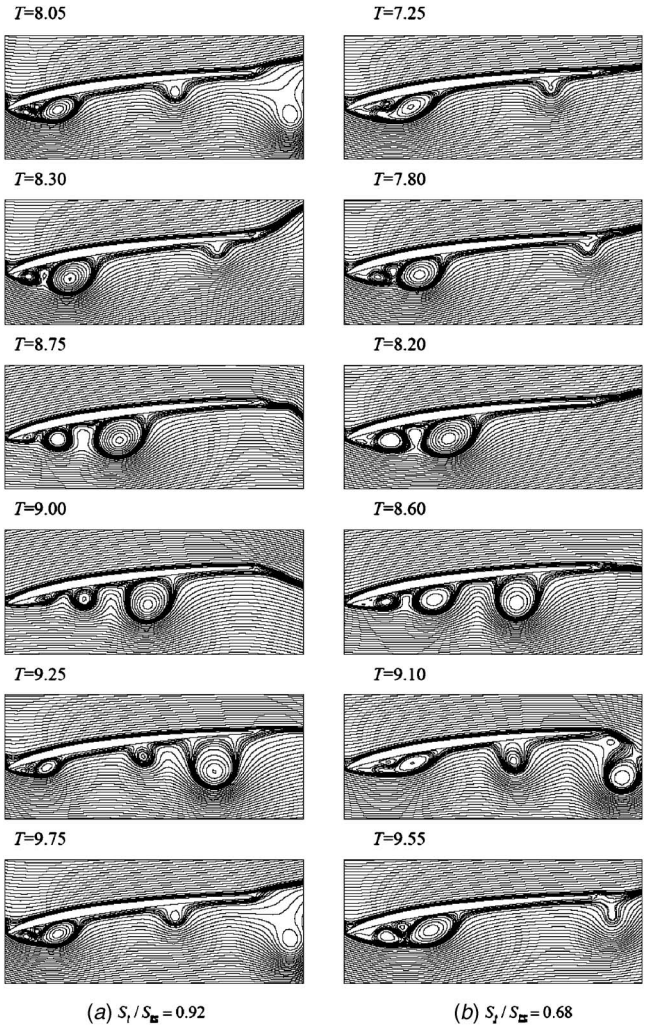

Fig. 13 Calculated streamline contours in an oscillation cycle for $\bar{\alpha}=-8.3$ deg, $\Delta\alpha=5.0$ deg: (*a*) $St/St_s=0.92$ and (*b*) $St/St_s=0.68$

larger than these for stationary cylinder, which are qualitatively similar to the experimental results in Refs. [6,7] and calculated results in Ref. [9].

Results and Discussions

Flow Characteristics of the Static Blade. Figure 8 shows the time histories for nondimensional lift force C_l and torque C_m acting on the blade for the attack angles $\alpha=-8.3$ deg and $\alpha=13.7$ deg. For $\alpha=-8.3$ deg, the mean values of nondimensional lift force and torque are $\bar{C}_l=-0.44$ and $\bar{C}_m=0.12$, respectively. The periodicity of the periodic vortex shedding is $f_s=1.55$, which is calculated based on the torque C_m shown in Fig. 8 using fast Fourier transtorm (FFT) analysis, and the Strouhal number is $St_s=f_s c/U_\infty=0.645$. For $\alpha=13.7$ deg, the corresponding values are $\bar{C}_l=1.23$, $\bar{C}_m=-0.12$, and $St_s=0.71$, respectively.

For the attack angle $\alpha=-8.3$ deg, the leading-edge vortex is formed on the downside surface of the blade, and the separated vortex reattaches to the blade; therefore, a long vortex bubble is formed, as shown in Fig. 9. In Fig. 9, an instantaneous flow pattern taken by the twinkle-laser-light sheet [3] at $Re=1.0\times10^5$ is also given. According to Fig. 9, the calculated streamline pattern agrees with the visualization. The experiments in Refs. [2,3] used two methods, i.e., a twinkling-laser-light sheet and a high-speed-camera (HSV-1000) photography, to view the flow patterns. The occurrence of the long separation bubbles was mainly observed and recorded in order to estimate the frequency of vortex shedding. Figure 10 shows that as the size and strength of the separated vortex bubble increase, another vortex separates from the bubble, moves to the trailing edge along the bottom surface, and finally escapes from the blade. The formation and separation of the surface vortices are periodical. Inside the vortex bubble, however, less vorticity can be found, and these vortex structures induce the high-frequency vibrations in the lift and torque curves shown in Fig. 8(*a*).

For the attack angle $\alpha=13.7$ deg, as shown in Fig. 11, a separated vortex is formed along the upper surface of the blade. The appearance of additional vortical formations is manifested by the structures observed above the upper surface of the blade. These vortical structures constitute the manifestation of a Kelvin–Helmholtz shear layer-type instability that can be found for flows at Reynolds numbers from $Re=1.0\times10^5$ to 2.2×10^5, which are investigated in this paper.

The averaged nondimensional torques and the vortex-shedding frequencies for different attack angles are shown in Fig. 12. The measured results [2] for Reynolds number $Re=2.2\times10^5$ are also given in the two figures for comparisons. Although there are some quantitative differences between the calculated and measured results, the predicted global characteristics of the vortex shedding with the attack angles agree well with the measurements.

In this paper, we calculate flows based on the vorticity-stream

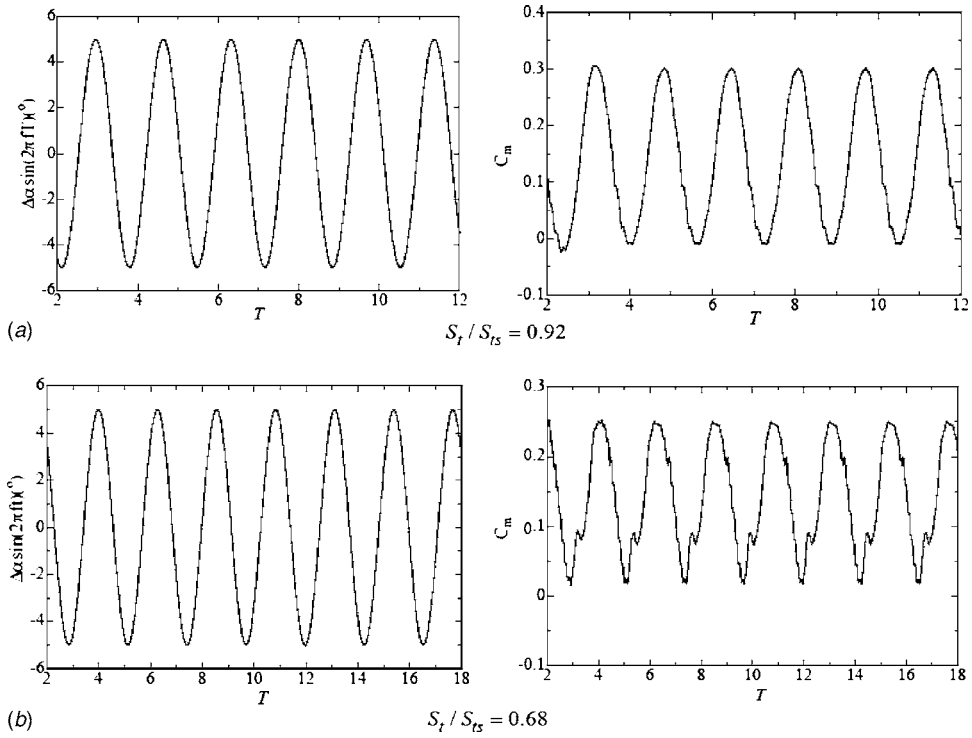

Fig. 14 Time histories of the oscillation displacement $\Delta\alpha \sin(2\pi ft)$ and torque C_m on the blade for $\bar{\alpha}=-8.3$ deg, $\Delta\alpha=5.0$ deg: (*a*) St/St$_s$=0.92 and (*b*) St/St$_s$=0.68

function for laminar flows only and do not account for flow turbulence. With the Reynolds numbers ranging from $\mathrm{Re}=1.0\times10^5$ to 2.2×10^5, flow transition from laminar to turbulent may occur in combination with a large laminar separation bubble (LSB) in the real world. Small disturbances existing in the laminar flow are strongly amplified in the shear layer of the separated flow and rapidly transitioned to turbulence, which, in turn, creates a large momentum transport normal to the shear layer, forces the flow reattaching to the surface quickly, and forms a short bubble. However, for convection-dominated flows at large Reynolds number, it is important to resolve the mean advection accurately. In the present investigation, the third-order Chakravaythy–Oscher TVD scheme has been used to discretize the convective terms and the fourth-order Runge-Kutta scheme has been used to advance time in the vorticity-transport equation. According to Figs. 9 and 12, global characteristics of the vortex shedding have been captured well. It is expected that the scheme used in the present paper provides a two-dimensional direct numerical simulation.

Lock-in Characteristics of the Blade. From Fig. 12, it can be found that the averaged torque reaches its peaks when the attack angles are −4.3 deg and 13.7 deg. Close to these two angles, the fluctuations in the instantaneous torque also become significant. It can be inferred that for this blade the stall angles are around these two angles: $\alpha=-4.3$ deg and 13.7 deg. As shown by Guo et al. [1], and Okamoto et al. [21], a prototype of this blade has been used in a pump station. When the blade is operated at the attack angles from $\alpha=-4.0$ deg to −7.0 deg, complex pressure fluctuations and vibrations [1,21] occur in the pump system from the blade tip. In simulating the flow over the oscillating blade, the authors selected the mean attack angles around $\bar{\alpha}=-8.3$ deg and $\bar{\alpha}=-4.3$ deg to match the experimental tests [2,3].

Figure 13 shows the calculated streamline contours in an oscillation cycle in the moving system for the mean attack angle $\bar{\alpha}=-8.3$ deg when the blade is forced to oscillate at an amplitude $\Delta\alpha=5$ deg, and the frequencies St/St$_s$ are 0.92 and 0.68. As mentioned before, the vortex-shedding frequency of the fixed blade expressed as a Strouhal number St$_s$ is 0.645 for the attack angle $\bar{\alpha}=-8.3$ deg.

The calculated unsteady flow patterns around the blade as well as the oscillation displacement of the blade were used to determine the lock-in state. As shown in Fig. 13(*a*), for St/St$_s$=0.92, the vortex-shedding frequency f_v is no longer equal to the vortex-shedding frequency f_s for the stationary blade. Vortices are shed at the oscillation frequency f. This means that the oscillating blade and the vortex shedding have the same characteristic frequency ($f_v=f$). The lock-in or resonance has taken place. The occurrence of the lock-in results in one dominant component in the torque curves shown in Fig. 14(*a*). The torque acting on the blade is in phase with the blade oscillation.

At the Stroubal number of 0.68 shown in Fig. 13(*b*), vortices shed at a frequency f_v that is approximately equal to the vortex-shedding frequency f_s of the static blade but different from the forcing frequency f of the blade oscillation. In addition to the strong vibration corresponding to the forced oscillation, periodic fluctuations occur in the time history of the calculated torque coefficient shown in Fig. 14(*b*) for St/St$_s$=0.68. These periodic fluctuation frequencies correspond to the vortex-shedding frequencies. This means that the vortex-shedding frequency is different from the forced oscillation frequency and the flow is not synchronized.

The onset of vortex lock-in due to the external forced oscillation depends on the combination of the forced oscillation frequency and amplitude. The results concerning the limits of lock-in regime for the mean attack angles $\bar{\alpha}=-8.3$ deg and $\bar{\alpha}=-4.3$ deg are shown in Fig. 15 based on the calculations for different forcing frequencies and angular displacement amplitudes. The measured results [2,3] are also given in the figure. The forcing ampli-

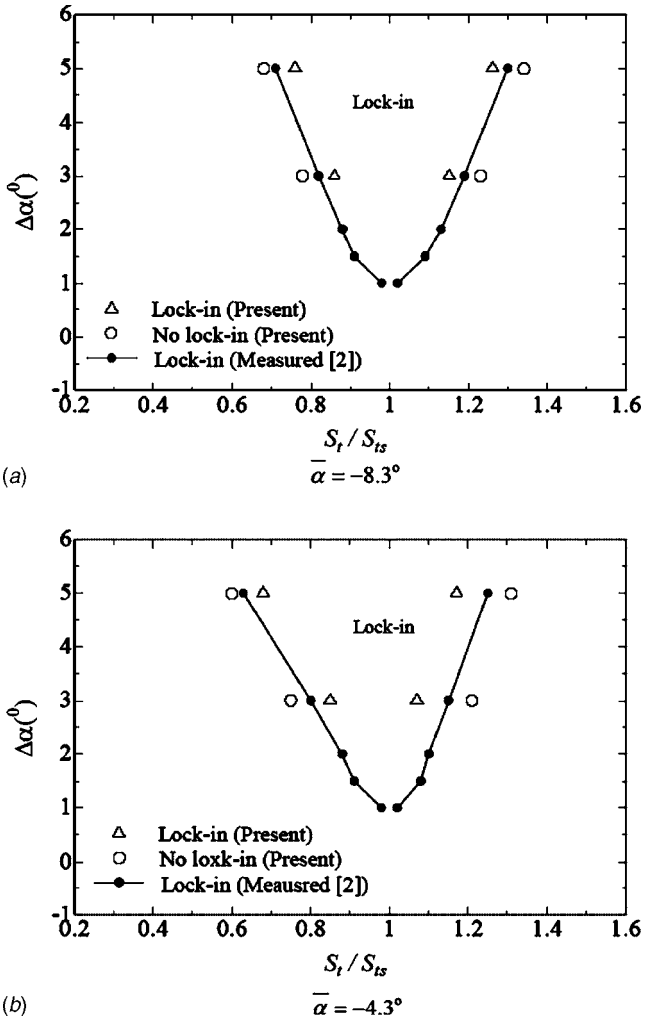

Fig. 15 Lock-in boundaries for two different attack angles: (*a*) $\bar{\alpha}=-8.3$ deg and (*b*) $\bar{\alpha}=-4.3$ deg

tude for the onset of lock-in increases with an increase in the difference between the forcing and natural shedding frequencies.

Possibility of Self-Oscillation. In the lock-in zone, the phase difference between the nondimensional torque C_m and the blade's oscillation displacement was evaluated. The phase differences were then used to infer the possibility of self-oscillation of the blade. For example, as shown in Fig. 14, for the case $\bar{\alpha}=-8.3$ deg, $\Delta\alpha=5.0$ deg, and $\mathrm{St}/\mathrm{St}_s=0.92$, the phase shift ϕ between the oscillating displacement and torque C_m is about −32.86 deg. When $-180\ \mathrm{deg} \leqslant \phi \leqslant 0$ deg, the energy calculated from the oscillation angular velocity and torque is negative. This implies that the energy is transferred from the oscillating blade to the flow. On the other hand, for $0\ \mathrm{deg} < \phi < 180$ deg, the energy is positive and the blade receives the energy from the flow. If the blade is free to move, vortex shedding will induce self-oscillation.

Table 1 lists the phase differences between the blade's oscillation displacements and the nondimensional torques inside the lock-in zone at the two mean attack angles, i.e., $\bar{\alpha}=-8.3$ deg and $\bar{\alpha}=-4.3$ deg. For the mean attack angle $\bar{\alpha}=-8.3$ deg, as the oscillation frequency approaches the vortex-shedding frequency for the stationary blade, the phase difference ϕ is $-180\ \mathrm{deg} < \phi < 0$ deg, and so the periodic vortex shedding will not induce the blade oscillation. However, for $\bar{\alpha}=-4.3$ deg, as the blade oscillates with the frequency close to the frequency of the vortex shedding for the fixed blade, the phase difference is $0\ \mathrm{deg} < \phi < 180$ deg, which implies that the blade will receive energy from the flow. Therefore, at the attack angle $\bar{\alpha}=-4.3$ deg, the periodic vortex shedding will induce the blade self-oscillation. This is consistent with the inference from the laboratory experimental data [2] and the prototype measurements [1,21].

4 Conclusions

In the present investigation, the vortex shedding and lock-in characteristics of a thin cambered blade were numerically investigated. The governing equations based on the vorticity-stream function formulation were solved numerically in a general curvilinear coordinate for the determination of the unsteady flow characteristics.

Vortex-shedding patterns change depending on the angles of attack for the static blade. For $\alpha=-8.3$ deg, a long vortex bubble forms along the bottom surface of the blade and a separated vortex generates from the bubble, moves to downstream, and finally escapes from the blade. This process is repetitive and results in periodic forces acting on the blade. For $\alpha=13.7$ deg, flow separation occurs on the upper surface of the blade and a complex vortex structure constitutes the manifestation of a Kelvin–Helmholtz shear layer instability.

The boundaries of the blade lock-in at two mean attack angles $\bar{\alpha}=-8.3$ deg and −4.3 deg have been determined to be the frequencies of oscillation around the vortex-shedding frequency. The onset of vortex-shedding lock-in depends on the combination of the forced oscillation frequency and amplitude. The phase differences between the blade's oscillating displacement and the torque acting on it were used to determine whether the vortex shedding will induce blade self-oscillation at $\bar{\alpha}=-8.3$ deg and −4.3 deg. For the attack angle $\alpha=-8.3$ deg, the periodic vortex shedding will not induce the oscillation even if the blade is free to vibrate. However, for $\alpha=-4.3$ deg, periodic vortex shedding will induce self-oscillation of the blade if it is free to move, which is consistent with the inference from the measurements.

This paper presents the vortex-shedding patterns and lock-in characteristics of a thin cambered blade used in an axial pump. As shown by Huang et al. [22], for conventional foils with a sharp trailing edge, the Strouhal number of vortex shedding depends on the angles of attack, Reynolds numbers, as well as the curvature at the ends of the foils. As organized and periodic vortex shedding occurs and the vortex shedding results in considerable fluctuating load on the foil, the blade self-oscillation induced by the vortex shedding may occur. The present investigation can provide some useful information to the problem of coupled vortex shedding and blade vibration in turbomachinery.

Table 1 Phase differences between the oscillating displacement and torque C_m

	$\Delta\alpha$ (deg)			$\Delta\alpha$ (deg)	
	5 deg	3 deg		5 deg	3 deg
$\mathrm{St}/\mathrm{St}_s$	Phase difference ϕ (deg)		$\mathrm{St}/\mathrm{St}_s$	Phase difference ϕ (deg)	
0.92	−32.86	−35.25	0.95	32.46	58.07
1.0	−46.44	−41.79	1.0	25.21	49.02
1.02	−49.31	−44.53	1.05	19.52	42.34

Acknowledgments

This work is partially supported by the National Science Foundation of China with the Grant No. 50679030. The authors would like to thank the reviewers for their constructive comments and suggestions.

Nomenclature

A_m = rotationally oscillating amplitude of cylinder, $\Omega R/U_\infty$
c = chord length
C_l = lift coefficient
C_d = drag coefficient
C_m = torque coefficient
f = frequency
$(\boldsymbol{i},\boldsymbol{j})$ = unit vectors along the Cartesian coordinate (x,y)
J = Jocobian, $\xi_x\eta_y-\eta_x\xi_y$
$\boldsymbol{n}$ = unit normal vector on the boundary surface
p = pressure
Re = Reynolds number
R = radius of cylinder
$\boldsymbol{r}$ = position vector
$\boldsymbol{s}$ = unit tangential vector on the boundary surface
St = Strouhal number, fc/U_∞
t = time
T = nodimensional time, tU_∞/c
(u,v) = velocity components in the Cartesian coordinate (x,y)
(U,V) = contravariant velocity components in the curvilinear coordinate (ξ,η)
α = angle of attack
Γ = boundary surface
$\Delta\alpha$ = amplitude of rotational oscillation in the attack angle
Δt = time step size
μ = viscosity coefficient of fluid
ν = kinematic viscosity coefficient of fluid
ρ = density of fluid
$\boldsymbol{\tau}$ = viscous shear stress
ψ = stream function
ϕ = phase difference
Ω = angular velocity
$\dot{\Omega}$ = angular acceleration
ω = vorticity

Superscripts

n = time step number
$\bar{}$ = mean value
* = variable in inertial frame of reference

Subscripts

1–4 = index of stages in the Runge–Kutta scheme
s = static cylinder or blade
v = vortex shedding
∞ = reference condition

References

[1] Guo, S., Maruta, Y., Okamota, H., Kanno, H., and Sato, K., 2003, "Complex Pressure Fluctuations and Vibrations in a Pump-Water Tunnel System," *ASME Fluids Engineering Division Summer Meeting*, Hl.
[2] Zhu, B., and Kamemoto, K., 2004, "Probability of Self-Oscillation Induced by Vortex Shedding From a Thin Cambered Blade," Exp. Therm. Fluid Sci., **29**, pp. 129–135.
[3] Miyake, T., 2002, "Study of Fluid-Induced Vibration on Two-Dimensional Thin Balde," MS thesis, Yokohama National University.
[4] Griffin, O. M., and Ramberg, S. E., 1976, "Vortex Shedding From a Cylinder Vibrating in Line With an Incident Uniform Flow," J. Fluid Mech., **75**, pp. 257–271.
[5] Koopmann, G. H., 1967, "The Vortex Wakes of Vibrating Cylinders at Low Reynolds Numbers," J. Fluid Mech., **28**, pp. 501–512.
[6] Tokumaru, P. T., and Dimotakis, P. E., 1991, "Rotary Oscillation Control a Cylinder Wake," J. Fluid Mech., **224**, pp. 70–90.
[7] Filler, J. R., Marston, P. L., and Mih, W. C., 1991, "Response of the Shear Layers Separating From a Circular Cylinder to Small-Amplitude Rotational Oscillations," J. Fluid Mech., **231**, pp. 481–499.
[8] Mahfouz, F. M., and Badr, H. M., 2000, "Flow Structure in the Wake of a Rotationally Oscillating Cylinder," ASME J. Fluids Eng., **122**, pp. 290–301.
[9] Cheng, M., Liu, G. R., and Lam, K. Y., 2001, "Numerical Simulation of Flow Past a Rotationally Oscillating Cylinder," Comput. Fluids, **30**, pp. 365–392.
[10] Choi, S., Choi, H., and Kang, S., 2002, "Characteristics of Flow Over a Rotationally Oscillating Cylinder at Low Reynolds Number," Phys. Fluids, **14**, pp. 2767–2777.
[11] Chen, J. M., and Fang, Y.-C., 1998, "Lock-on of Vortex Shedding Due to Rotational Oscillations of a Flat Plate in a Uniform Stream," J. Fluids Struct., **15**, pp. 779–798.
[12] Chen, J. M., and Fang, Y.-C., 2005, "On the Flow Over a Rotationally Oscillating Flat Plate: A Numerical Study," J. Fluids Struct., **20**, pp. 961–974.
[13] McCroskey, W. J., 1982, "Unsteady Airfoils," Annu. Rev. Fluid Mech., **14**, pp. 285–311.
[14] Tuncer, I. H., Wu, J. C., and Wang, C. M., 1990, "Theoretical and Numerical Studies of Oscillating Airfoil," AIAA J., **28**, pp. 1615–1624.
[15] Ohmi, K., Coutanceau, M., Loc, T. P., and Dulieu, A., 1990, "Vortex Formation Around an Oscillating and Translating Airfoil at Large Incidence," J. Fluid Mech., **211**, pp. 37–60.
[16] Sorensen, J. N., and Nygreen, P. J., 2001, "Unsteady Vorticity-Stream function Algorithm for External Flows," Comput. Fluids, **30**, pp. 69–97.
[17] Liu, J. G. and Weinan, E., 1996, "Vorticity Boundary Condition and Related Issues for Finite Difference Schemes," J. Comput. Phys., **124**, pp. 368–382.
[18] Bouard, R., and Coutanceau, M., 1980, "The Early Stage Development of the Wake Behind an Impulsively Started Cylinder for $40<R_e<10^4$," J. Fluid Mech., **101**, pp. 583–606.
[19] Koumoutsakos, P., and Leonard, A., 1995, "A High-Resolution Simulation of the Flow Around an Impulsively Started Cylinder Using Vortex Methods," J. Fluid Mech., **296**, pp. 1–38.
[20] Qian, L., and Veza, M. A., 2001, "A Vorticity-Based Method for the Incompressible Unsteady Viscous Flows," J. Comput. Phys., **172**, pp. 515–542.
[21] Okamoto, H., Maruta, Y., and Kanno, H., 2006, "Controlling Unsteady Flow Separation to Reduce Vortex-Induced Vibration in a Pump-Water-Tunnel System," *23rd IAHR Symposium*, Yokohama, Japan.
[22] Huang, R. F., Wu, J. Y., Jeng, J. H., and Chen, R. C., 2001, "Surface Flow and Vortex Shedding of an Impulsively Started Wing," J. Fluid Mech., **441**, pp. 265–292.

Flow Instability and Disk Vibration of Shrouded Corotating Disk System

S. Kanagai
LEXUS Body Engineering Division,
Toyota Motor Corporation,
1 Toyota-cho, Toyota,
Aichi 471-8571, Japan
e-mail: kana@earth.tec.toyota.co.jp

J. Suzuki
Machinery and Assembly Shop,
Mitsubishi Heavy Industries, Ltd.,
1-1-1 Wadasaki-cho, Hyogo-ku,
Kobe 652-8585, Japan
e-mail: jyo-suzuki@mhi.co.jp

S. Obi
e-mail: obsn@mech.keio.ac.jp

S. Masuda
e-mail: bzp01264@nifty.ne.jp

Department of Mechanical Engineering,
Keio University,
3-14-1 Hiyoshi, Kouhoku-ku,
Yokohama 223-8522, Japan

This paper focuses on the interaction between the flow unsteadiness and disk vibration of shrouded corotating disk system to identify the nature of the flow-induced vibration of disks in the wide range of rotation speed below critical. Special attention is paid to the role of the vortical flow structure on the disk vibration and vice versa. The water test rig for optical measurement and the air test rig for hot-wire and vibration measurements are employed, both being axisymmetric models of 3.5 in. hard disk drive. Before investigating fluid-solid interaction, the velocity and vorticity fields between disks are examined by employing a particle image velocimetry, in order to check the flow within our own apparatus to have the same characteristics as those commonly accepted. In the course of this preliminary experiment, it is found that "vortical structures" reported in the previous papers based on the flow visualization are actually "vortices" in the sense that it exhibits closed streamlines with concentrated vorticity at its center when seen from an observer rotating with the structure itself. The measurements of out-of-plane displacement of the disk employing different disk materials reveal that disk vibration begins to occur even in low subcritical speed range, and amplitude of nonrepeatable run out (NRRO) can be uniquely correlated by using the ratio between the rotating speed and the critical speed. The power spectral densities of disk vibration showed that the disk vibrates as a free vibration triggered by, but not forced by, the flow unsteadiness even in the high subcritical speed range. The disk vibration has negligible effect on the vortical flow structure suggesting the soundness of the rigid disk assumption employed in the existing CFD. However, RRO has significant influence on the flow unsteadiness even if the disks are carefully manufactured and assembled. Since the RRO is unavoidable in the real disk system, the flat disk assumption should be considered more carefully.
[DOI: 10.1115/1.2776958]

Keywords: flow instability, vortical structure, flow induced vibration, rotating disk, hard disk drive

1 Introduction

A flow between corotating disks enclosed in a stationary cylindrical shroud becomes unstable when the Reynolds number exceeds a certain critical level. This is manifested as a transition from a steady axisymmetric flow to an unsteady nonaxisymmetric flow. The time-dependent pressure force due to this flow may be one of the causes of disk vibration. Although fluid dynamic aspects of this problem have been reported by many investigators, very little attention has been paid to its relation to the disk vibration. For the future development of rotating storage devices such as magnetic or optical disk drives, a thorough study of flow-induced vibration of a rotating disk is critical.

The geometry of an unobstructed disk system and the definition of a coordinate system are shown in Fig. 1. Multiple disks with outer radius R_2 and thickness t are centrally clamped and closely packed in a cylindrical container with disk-to-disk spacing H and disk-to-shroud clearance a, and rotate at a constant angular velocity Ω. A ground-fixed coordinate system (r, θ, z) is defined as shown. The fluid between disks is forced to move as a solid body by the viscous stress on the disk and hub surfaces. Lennemann [1] has first found the unsteady asymmetric flow pattern. Later on, Abrahamson et al. [2] reported based on the dye visualization that this asymmetric pattern is caused by a "large-scale counter-rotating axial vortices" in the outer region. However, they recognized these structures in the flow visualization pictures and, strictly speaking, no one has actually observed "vortices" in the sense that the actual vortices must have closed streamlines with concentrated vorticity at its center when seen from an observer moving with the corresponding structure. For that, quantitative information on velocity and vorticity fields should be provided. Three-dimensional direct numerical simulations [3–7] and large eddy simulation (LES) [8,9] showed the nodal structures qualitatively similar to those observed by dye visualization and confirmed that they are actually axial vortices with concentrated vorticity.

In the experimental and numerical investigations cited above, the interest was focused mainly on the aerodynamics and the disks have been considered exclusively to be rigid and flat, and thus effects of out-of-plane movement of the disk surface have been completely ignored unless the disk speed approaches flutter speed [10–12]. Since the recent development of hard disk drives (HDDs) of high speed and high record density does not permit disk vibration of minute amplitude hitherto ignored in order to minimize the positioning error, the interrelation between disk and fluid must be examined more carefully even in the subcritical speed range.

As to the disk vibration, it has been reported that the disk vibration amplitude decreases with decreasing ambient pressure [13]. Fukaya et al. [14] performed measurements of disk vibration and velocity fluctuations with varying Reynolds number under the constant rotational speed and found that the disk vibration amplitude increases concurrently with increasing velocity fluctuation. They also postulated that the large-scale vortical structures on two sides of a disk may exert time-dependent differential pressure on a

Contributed by the Fluids Engineering Division of ASME for publication in the JOURNAL OF FLUIDS ENGINEERING. Manuscript received January 28, 2005; final manuscript received April 25, 2007. Review conducted by Joseph Katz.

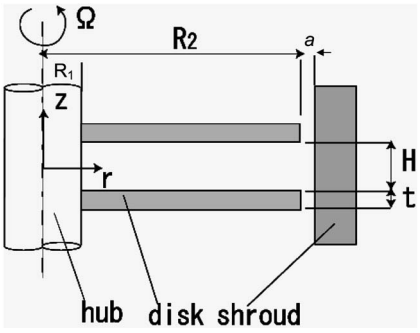

Fig. 1 Geometry and coordinate system of unobstructed corotating disks enclosed in cylindrical container (not to scale)

disk and excite disk vibration. Imai et al. [15] reported that the disk vibration is reduced by reducing the disk-shroud clearance. The measurement of the shroud surface pressure suggests that the reduction is caused by the decrease of the aerodynamic excitation [16]. On the contrary, Eguchi and Kouno showed theoretically that a clearance flow through a narrow shroud gap induced by the disk vibration causes its viscous damping [17]. Although rotational speeds in all cases cited above are much less than the critical speed of the disk, the results suggest the importance of the relation between disk vibration and unsteadiness of the surrounding flow. According to D'Angelo and Mote [18], the fluid-solid interaction problem might be increasingly important as the disk speed increases approaching the critical speed.

There might be several different types of interactions. When the unsteady aerodynamic force is very large, the disk vibrates as a forced vibration. This might be effective at supercritical or near flutter speed and might not be the case in the present subcritical range. When the amplitude of flow unsteadiness is small, the disk vibrates as a free vibration composed of the eigenmodes only. Inversely, the disk vibration may influence the flow unsteadiness through the unsteady boundary condition on the surface. Also, a statically deformed disk exerts similar unsteady boundary condition.

The purpose of the present investigation is to identify the nature of the interaction between disk and surrounding fluid in the whole subcritical speed range. Special attention is paid on the role of the asymmetric vortical structure on disk vibration and vice versa. First, flow visualization and velocity measurement are performed employing a particle image velocimetry (PIV) to identify the asymmetric vortical flow structure. Then, the unsteady characteristics of the velocity field and its relation to the disk vibration are investigated. Further, the effect of the disk out-of-plane movement on the flow unsteadiness is investigated and the appropriateness of the rigidity and flatness assumptions in numerical simulations of flow between disks is examined. The range of flow parameter covers the transition from steady axisymmetric to unsteady nonaxisymmetric, as shown in Fig. 1 of Ref. [14]. Upon changing the disk material, the rotation speed covers the whole subcritical range.

2 Preliminary Experiment to Identify Flow Structure

Before investigating the fluid-solid interactions, we check the flow structure in our experimental apparatus. A 2.5 in. (R_2 =32.5 mm) three-decker HDD has been reconstructed for the optical measurements by replacing the acrylic shroud and glass disks both being transparent and immersed in a water tank. The open part of the original shroud is closed to render the outer boundary axisymmetric. The disks are driven by a variable speed dc motor placed outside the tank. The Reynolds number based on the disk outer radius is $1.9\times10^4<\mathrm{Re}<7.6\times10^4$ and the aspect ratio $H/R_2=0.058$. For the flow visualization, a water solution of potassium permanganate is introduced into the spacing between the top and the second disks before starting rotation, and is illuminated from above by halogen lamps. For PIV measurement, tracer particles (Diaion, specific weight of 1.00, diameter of 75–150 μm) are dispersed uniformly in the working fluid and illuminated by a 1-mm-thick laser light sheet emitted from a 300 mW Ar-ion laser source, and are captured by an NTSC-type charge coupled device (CCD) camera. The velocity vectors in the $r-\theta$ plane between the disks are estimated by employing the density correlation algorithm [19]. The uncertainty of the present velocity measurement by PIV is ±2.1% with 95% confidence.

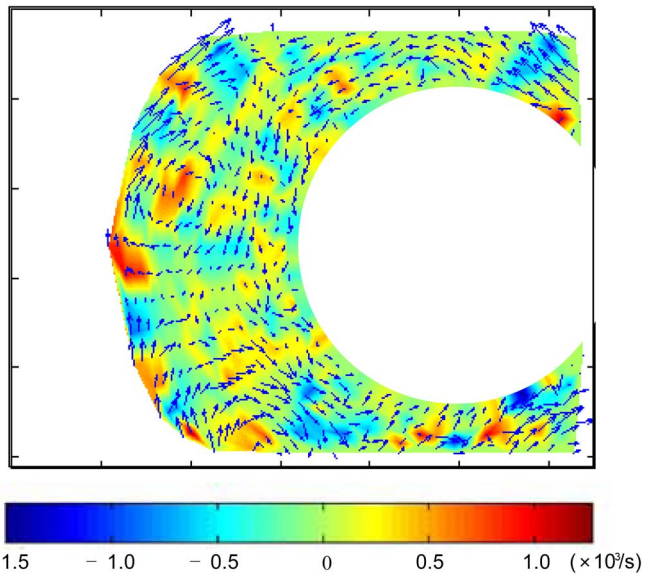

Fig. 2 Distribution of velocity vectors and axial component of vorticity relative to the rotating asymmetric structure obtained by PIV (Re=6.4×10⁴, H/R_2=0.061; disk rotation is counterclockwise)

The depthwise averages of the instantaneous velocity vectors relative to the frame of reference rotating with the structure are given in Fig. 2. The rotational speed is determined from the flow visualization video. The axial vorticity is also evaluated by the numerical differentiation of velocity components. In the region, $r\geqslant0.7R_2$, several closed streamlines with concentrated vorticity can be observed, whose direction of rotation is opposite to the direction of disk rotation. This result confirms that the asymmetric flow structure does exist in the present apparatus. More importantly, the "large-scale vortical structure" loosely called previously [1,2] is actually "vortex," which consists of closed streamlines and concentrated vorticity at its center when seen from an observer rotating with the corresponding structure. The present flow field exhibits common characteristics of enclosed spinning multidisk flow, such as the inner region of solid-body rotation, the outer region of quasifree vortex distribution and the boundary near $r\cong0.7R_2$.

Figure 3 shows the rotational speed ω of this vortical structure relative to the disk speed Ω, evaluated from the flow visualization video. It was estimated based on the phase difference obtained from the time correlations and the wave number spectra of the boundary shapes over 80–100 samples. The present results together with the results reported by other investigators [1,2,14,25] reveal that the structure always rotates at lower speed than the disk speed and that it decreases with increasing Reynolds number. This relative movement might induce the unsteady pressure force, and cause aerodynamic excitation of the disk. Its amplitude and frequency relative to the disk eigenfrequency as well as coherence and phase relation on both sides of the disk might be essential in considering the aerodynamic excitation of the disk vibration.

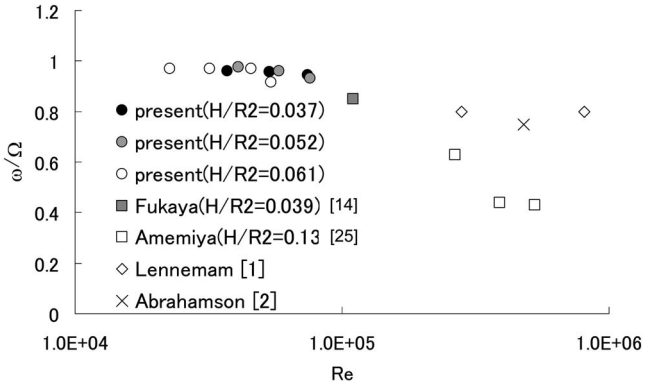

Fig. 3 Rotational speed ω of asymmetric structure as a function of disk Reynolds number (Vertical axis is normalized by disk speed Ω)

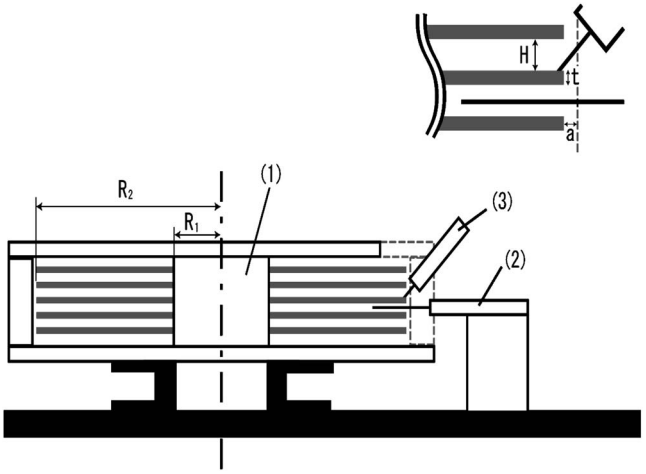

Fig. 4 Schematic of air test rig: (1) axisymmetric model of 3.5 in. five-decker HDD, (2) single-sensor hot-wire probe, and (3) capacitance-type displacement probe, R_1=12.35 mm, R_2=47.5 mm, H=2.45 mm, t=0.8 mm, and a=0.5 mm

3 Velocity and Vibration Measurements

3.1 Test Rig. In order to investigate the unsteady characteristics of velocity fluctuation associated with the large-scale vortical structure mentioned above and its relation to the disk vibration, velocity and vibration measurements are performed in the air test rig shown schematically in Fig. 4. It is consisted of an axisymmetric model of 3.5 in five-decker HDD (1), a single-sensor hot-wire probe (2), and a capacitance-type displacement probe (3). The probes are mounted on the three-axis micrometer stages with the minimum scale of 10 μm. All the equipment are fixed magnetically on the steel platen of $700\times700\times40$ mm^3 mounted on the thick concrete blocks.

The head-gimbal assembly and magnetic head were again removed and the original shroud was replaced by the circular cylinder to keep the geometry axisymmetric. A 10-mm-wide window is installed on the shroud for probe insertion. The rotation speed N is varied from 1000 rpm to 10,000 rpm with 200 rpm interval. This is realized by employing a dc servomotor with 1 rpm accuracy. The corresponding Reynolds number range is $15{,}700<\mathrm{Re}<157{,}000$, which covers the range of the water test mentioned in the previous section. The disk radii and thickness are $R_2=47.5$ mm and $R_1=12.35$ mm and $t=0.8$ mm. The interdisk spacing is $H=2.45$ mm (aspect ratio $H/R_2=0.05$) and the disk-to-shroud spacing is $a=0.5$ mm.

In order to cover the whole subcritical speed range, the aluminum disks and acrylic disks are used. Their critical speeds N_c are 30,100 rpm and 9670 rpm, respectively, which is defined as the lowest rotation speed at which a static force applied transversely to the disk can resonate a stationary wave [18]. Thus, the range of speed ratio is $0.033\leqslant N/N_c\leqslant0.33$ for aluminum and is $0.103\leqslant N/N_c\leqslant1.03$ for acrylic. Aluminum experiments are conducted by employing all five aluminum disks and as well in the acrylic experiments.

The out-of-plane displacement was measured using capacitance-type displacement meter (Iwatsu ST3511). For measurement at the outer rim of the intermediate disk, the probe head was cut to 45 deg, as shown in Fig. 5(*a*) and inserted obliquely from above. The uncertainty of the vibration measurement itself is estimated to be 0.8% with 95% confidence interval. However, the

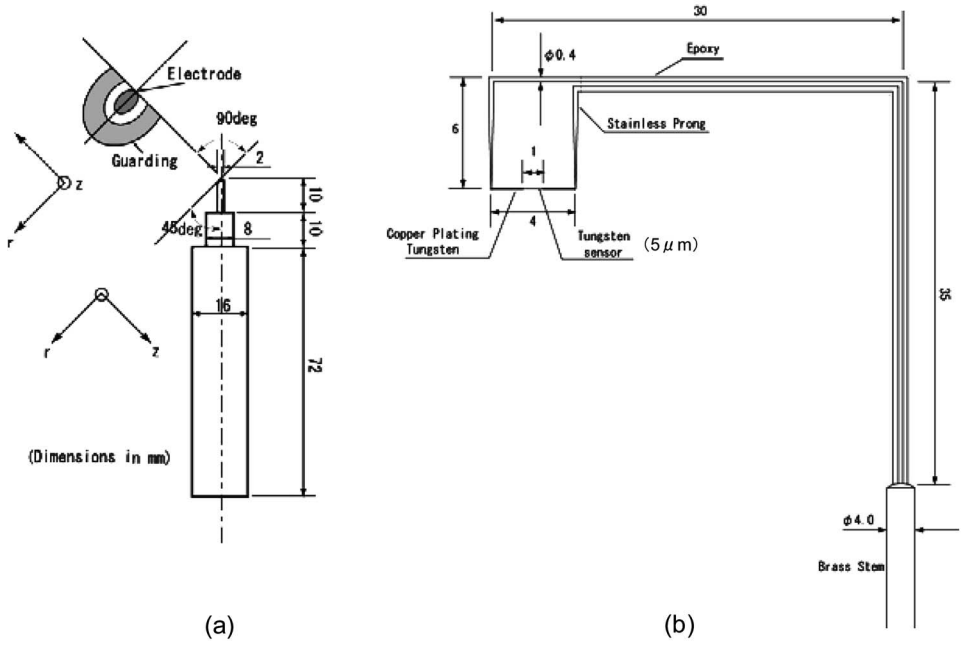

Fig. 5 Probe geometry: (*a*) Capacitance-type displacement meter probe for measuring disk vibration and (*b*) single hot-wire probe for measuring velocity fluctuation between disks

Table 1 Comparison of primary dimensions of water and air test rigs

	Water rig (mm)	Air rig (mm)	Ratio
Outer radius	32.5	47.5	1:1.46
Inner radius	12.0	12.35	1:1.03
Disk-to-disk clearance	1.9	2.45	1:1.29
Disk-to-shroud clearance	1	0.5	1:0.5

final result is sensitive to the time change of clamping condition. So, we have paid attention to minimize it during reassembling or even to avoid reassembling itself during a series of experiment. The flow in the peripheral region of 3 mm from the shroud inner surface is partially blocked by the sensor head, but the effect may be localized in the small circumferential region.

The circumferential component of velocity was measured by employing a single-sensor hot-wire anemometer probe, as illustrated in Fig. 5(*b*). It is made of 5-μm-diameter tungsten wire, coated by copper to a 30 μm diameter, soldered onto the tips of 0.4-mm-diameter prongs and then etched to fabricate 1-mm-long sensor. The blockage ratio amounts to 16%, but the difference of the mean velocity obtained by three-times thicker probe was less than 5%.

It was calibrated in a wind tunnel and the results were fitted to the fourth-order polynomials. To compensate for the temperature rise due to windage during operation, the air temperature inside the enclosure was measured by using a thermocouple. Overall, the uncertainty of hot-wire measurement is estimated to be 6% with 95% confidence interval.

Hot wire and displacement meter signals are low pass filtered at 2 kHz and then digitized through 12 bit analog-to-digital (AD) converter with a sampling rate of 5 kHz over 120 s and then processed by employing LABVIEW software. Fast Fourier transform (FFT) is performed over 5000 samples and averaged over 120 realizations. Overall resolution of displacement measurement is 12 nm.

Although the Reynolds number range of the air test overlaps with that of the water test mentioned in the previous section, the geometries of both test rigs are not strictly similar, as shown in Table 1. The largest difference is disk-to-shroud clearance. However, according to Tavener et al. [20] and Kong and Joo [21], we think that the flow between disks is not much affected by it. So, we consider the large-scale vortical structure in the air test rig to be qualitatively similar to that observed in the water test rig, although the wave number and speed of movement might not be exactly the same.

3.2 Disk Vibration. Figure 6 shows the rms of the disk out-of-plane displacement as functions of the speed ratio N/N_c, where

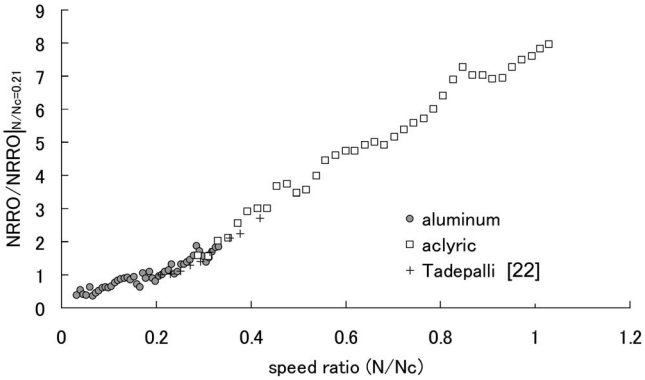

Fig. 6 NRRO of disk vibration versus speed ratio for different disk materials

N is the rotation speed of the disk and N_c is its critical speed. The vertical axis is the rms of nonrepeatable run-out (NRRO) components normalized by the value at $N/N_c=0.21$, for the sake of comparison with Tadepalli and Xia's data [22]. The signal of the displacement meter contains the so-called repeatable runout (RRO) caused by a static deformation and surface roughness of a disk as well as misalignment during assembly. Since this apparent vibration component always exhibits power spectral density (PSD) peaks at multiples of the rotation frequency, it can be easily removed by replacing them by zero, interpolating, integrating, and finally squaring to obtain pure vibration components (NRRO). The uncertainty of the final result is estimated to be 15%.

The result reveals that the rms of disk vibration begins to increase already in the low subcritical speed range of $N/N_c \leqslant 0.1$. Acrylic data show that it increases continuously above the critical speed. A nonmonotonic increase reflects the transition of vibration mode with the change of rotating speed. The single free disk experiment by D'Angelo and Mote [18] showed that the disk vibration is negligibly small in the subcritical range, begins to increase only at critical speed, and dramatically increases above the flutter speed. The present result confirms the finding of Fukaya et al. that the disk vibration of shrouded corotating disk is not negligible even well below critical [14].

The present results and Tadepalli and Xia's data of different geometries [22] can be put into a single curve by the present normalization. On the average, NRRO is nearly proportional to $(N/N_c)^{1.2}$, the exponent being smaller than 1.55 reported by Tadepalli and Xia. NRRO of acrylic disk is nearly four times larger than that of aluminum at the same disk speed. This large difference sets our expectation that the disk materials affect the flow instability through the unsteady boundary conditions imposed on the surface.

To investigate the effect of disk material on the vibration modes, the PSD of the displacement sensor signals has been evaluated and plotted in Fig. 7. In both aluminum and acrylic cases, there is a series of line spectra exactly at the multiples of the rotation frequency (10,000/60 Hz) corresponding to the RRO. During production process, the disk thickness was controlled within 10 μm. However, the amplitude of the RRO component of the disk out-of-plane movement after assembling amounts to 50 μm at worst. Also, it was hard to keep the cramping condition exactly the same during the reassembling. As a matter of fact, the peak levels of RRO are not the same for the two cases. Besides RRO peaks, several broader peaks with lower level can be recognized. They correspond to the NRRO. These peak levels are generally higher for acrylic than for aluminum in the entire frequency range tested.

To see the nature of the disk vibration in the whole subcritical speed range, the same measurements were performed by varying rotation speed from 1000 rpm to 10,000 rpm with 200 rpm interval. For each speed of rotation, the NRRO peaks are picked up and plotted in Fig. 8 as the form of waterfall plots. The lines indicate the frequencies of the eigenmodes obtained from finite element method (FEM) analysis without surrounding fluid, while the plots indicate the measured peak frequencies. The pairs of left- and right-running lines starting from the same point on the horizontal axis correspond to the backward (B) and forward (F) traveling waves of (m,n) mode, where m and n represent the number of nodal circles and nodal diameters. The vertical line corresponds to the (0,0) mode. The measured frequencies coincide well with the calculated results except for the shift of the eigenfrequency of a stationary disk. This inconsistency may partly be caused by the difference in the clamping condition.

For the aluminum disk, the dominant modes of vibration are (0,0), $(0,1)F$, $(0,1)B$, $(0,2)F$, $(0,2)B$, $(0,3)F$, $(0.3)B$, and $(0,4)B$, which are essentially the same as those in vacuum. The linearity of the plots indicates that the centrifugal stiffening is negligible in the aluminum case. For the acrylic disk, the peak frequencies are much lower than aluminum. The traveling speed is

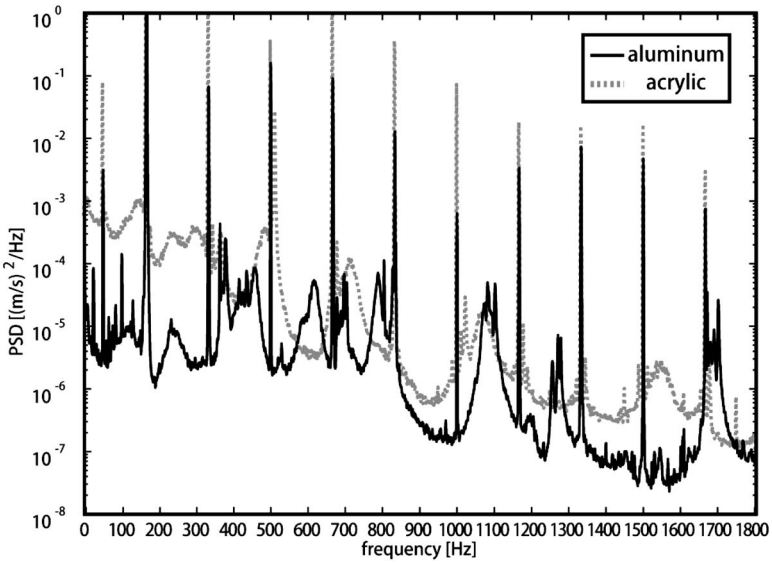

Fig. 7 PSD of displacement sensor signal for aluminum and acrylic disks (N=10,000 rpm)

slightly higher than that of aluminum and the slight curvature implies the centrifugal stiffening. Since the measured results in both cases coincide well with the eigenfrequencies obtained by FEM analysis without fluid, it is obvious that, in the subcritical speed range even close to critical, the disk vibration is a free vibration. It may be triggered by the flow unsteadiness but not forced by it.

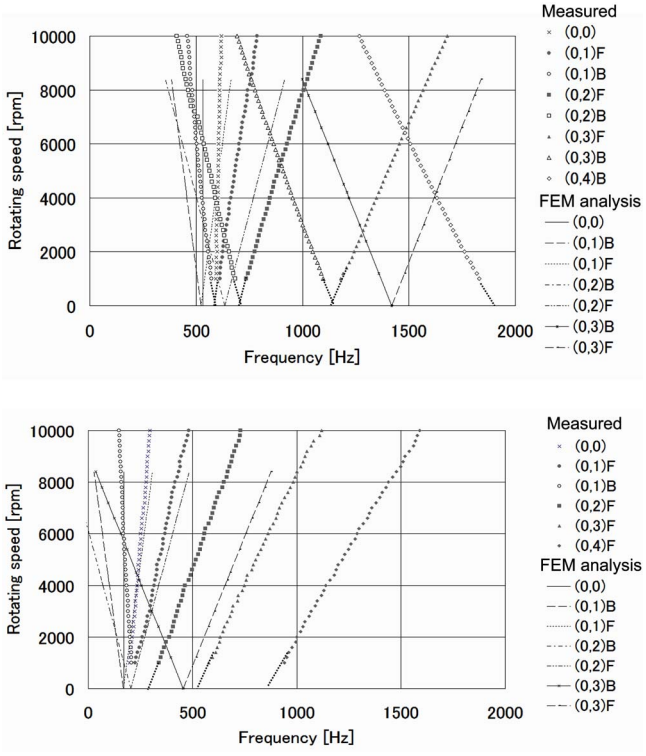

Fig. 8 Waterfall plots of disk vibration for aluminum and acrylic disks. Dominant PSD peaks of NRRO are plotted versus rotating speed (upper: aluminum; lower: acrylic; solid lines are from FEM analysis).

3.3 Velocity Fluctuation Near the Disk Outer Periphery. The large difference of NRRO shown in Figs. 6 and 7 suggests the possibility that the disk material somehow affects the flow unsteadiness through the vibrating boundary conditions. The velocity fluctuations near the disk periphery (r=0.96R_2) have been measured, where the largest amplitude of disk vibration is expected. The single hot-wire sensor is placed radially at the midway between the second and the third disks. In Fig. 9, the variations of rms velocity fluctuation with rotating speed are compared for the acrylic and aluminum disks. The velocity fluctuation of the acrylic disk exhibits slightly higher rms except in the intermediate speed range. Since the geometric and the aerodynamic conditions are kept unchanged, this difference is obviously attributed to the flow boundary condition on the disk surface. It may be caused by (i) inherent elastic properties of solid material (NRRO), (ii) difference of the static deformation (RRO), (iii) the different ranges of the speed ratio N/N_c, or (iv) a combination of them. As seen in Fig. 6, the NRRO amplitude of acrylic disk is more than four

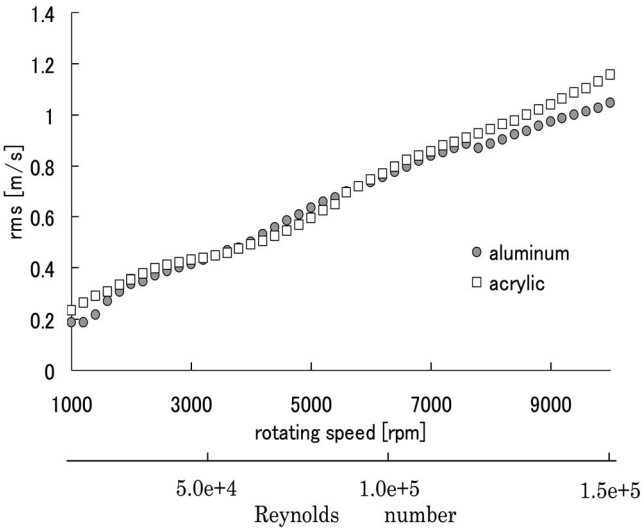

Fig. 9 Velocity fluctuation between disks near the outer periphery (r=0.96R_2)

times larger than that of aluminum at the same disk speed. This result seems to support our expectation that the vibrating boundary may affect the flow instability even in the subcritical speed range.

In this regard, however, it should be noted that the disk static deformation and the cramping conditions could not be kept exactly the same during the disk replacement. This means that not only NRRO but also RRO may be different for two cases. Since the flow perceives the sum of NRRO and RRO components, it cannot be concluded which is more strongly responsible before examining the frequency characteristics. This will be described in the next section.

Another point to be mentioned is that velocity fluctuation already begins far below critical and increases monotonically with increasing rotational speed. The numerical simulation assuming rigid flat disk by Herrero et al. [5] showed that the flow between disks remains steady and two dimensional at Reynolds number below 6×10^4. On the contrary, a laser Doppler velocimetry (LDV) measurement by Schuler et al. [23] and hot-wire measurement by Fukaya et al. [14] employing real flexible disks showed that the velocity fluctuation already begun at $\mathrm{Re}=(4.6-5.0)\times10^3$. The present results support the experiments [14,23] and suggest the importance of surface boundary condition in numerical calculations.

As to the reproducibility of velocity rms in Fig. 9, we have made the same measurement two times within several months and found that the tendency is well reproducible, although the quantitative disagreement amounts to more than 10%. It may partly be due to the unavoidable change of disk conditions and clamping conditions. As pointed out by D'Angelo and Mote [18], the vibration of a rotating disk is affected by friction and stiction at the disk/spacer interface and slippage of disk between the spacers. Stiction and slippage also cause hysteresis of the disk natural frequencies with start/stop cycles of rotation speed. These effects are more significant at higher rotational speed. In order to keep the clamping condition as constant as possible, we took care of fixing torque on the six bolts and the order of their fixing as well as the cleaning of the seating surface. In spite of it, the disk static deformation and cramping condition were difficult to reproduce. Insufficient reproducibility suggests the sensitivity of flow unsteadiness to the small change of wall boundary condition.

3.4 Solid-Fluid Interaction Near the Outer Periphery. In this section, the relationship between flow unsteadiness near the outer periphery and the disk out-of-plane movement is discussed on the basis of the frequency characteristics. In this region, unsteadiness is mainly related to the shroud boundary layer but not to the vortical structure inside. It is expected that the interrelation between flow and disk can be classified into three categories. (1) "Strong fluid-to-solid" interaction, which is from the flow unsteadiness to the disk vibration. If the amplitude of flow fluctuation is very high, the disk vibrates as a forced vibration and the PSD of the disk exhibits spectral peaks corresponding to the velocity peak other than the disk eigenfrequencies. This might be effective at supercritical or near flutter speed and might not be the case in the present subcritical range. (2) "Weak fluid-to-solid" interaction, in which the amplitude of flow unsteadiness is so small that the disk vibrates as a free vibration. In this case, the PSD of the disk exhibits spectral peaks coincident with the disk eigenfrequencies. As mentioned in Sec. 3.2, the vibration in the subcritical speed range belongs to this category. (3) Effect of NRRO, which is from the disk vibration to the flow unsteadiness. If the vibration amplitude is so large that the effect of unsteady boundary condition on the flow is not negligible, the velocity PSD shows new peaks other than its eigenfrequency. (4) Effect of RRO, which is expected when the disk static deformation is not negligible.

Figure 10 shows the PSDs of velocity fluctuations on the interdisk midplane for $N=10{,}000$ rpm. The hot-wire sensor is located near the periphery ($r=0.96R_2$). At the frequencies corresponding

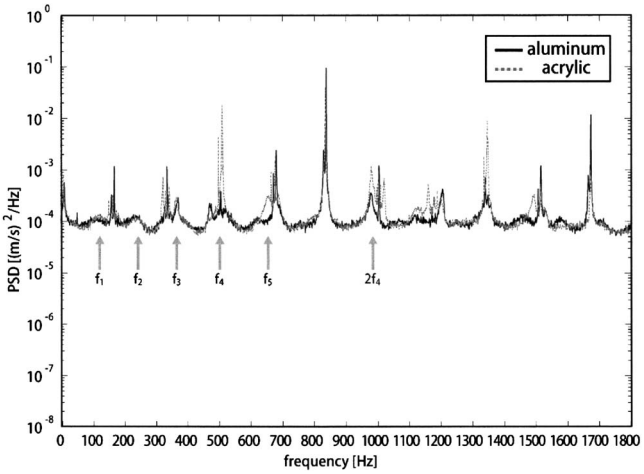

Fig. 10 PSD of velocity fluctuation on the interdisk midplane ($r=0.96R_2$, $N=10{,}000$ rpm, f_n denotes frequency of vortical flow mode)

to the disk RRO (multiples of 10,000/60 Hz), the velocity PSD shows sharp peaks. This result indicates that the RRO component affects the flow unsteadiness at the midway between disks. The statically deformed and/or misaligned disks make the distance between two disks circumferentially nonuniform. Since the fluid between them moves relative to the disks, it flows as if it were through the channel with a variable cross section. When it is observed from the ground-fixed coordinate, it gives rise to the apparent unsteadiness even if the disk does not vibrate. Since it is steady if seen from the disk-fixed coordinate, it does not directly trigger the vibration. This result implies that, in numerical simulations of flow between actual disks, RRO should be taken into account as the apparently unsteady boundary condition. Since this condition is given in advance, the numerical scheme may not be much different.

There are other lower and broader peaks. Some of them correspond to the asymmetric flow mode as denoted by f_1-f_5, but they are weak because the probe position is outside of the vortical flow region. Also, they do not coincide with the NRRO peaks shown in Fig. 7. The disk vibration amplitude of the acrylic disk is almost four times larger than that of the aluminum disk as shown in Fig. 6 and the vibration modes are much different with each other as shown in Fig. 7. However, the velocity PSDs for the two materials almost coincide, indicating that the flow at the midway between the disks is not affected by the vibration of the boundary. The distance of viscous diffusion of vorticity is estimated as the order of $\sqrt{\nu/f}$, which amounts only to the order of 100 μm in the present case. So, the sensor placed at the midway hardly detects the wall vibration. On the other hand, the RRO component is several orders of magnitude larger and also it is directly related to the entire depth between the disks through mass conservation, the sensor at the midway easily detects it.

3.5 Vortical Flow Structure and Disk Vibration. Finally, the relationship between vortical flow structure mentioned in Sec. 2 and disk vibration is discussed. The velocity fluctuation has been measured in the middle of the vortical flow region ($r=0.8R_2$). To avoid contamination by the shroud boundary layer turbulence and to concentrate our attention to the asymmetric vortical structure, the shroud boundary layer is kept away from the disk rim by employing a special shroud, as illustrated in Fig. 11. The aluminum disk is employed. The hot-wire traverse in the radial direction revealed that the thickness of the shroud boundary layer is less than 1.8 mm and the disk rim is located well outside of it [24].

PSDs of the disk vibration and velocity fluctuation are com-

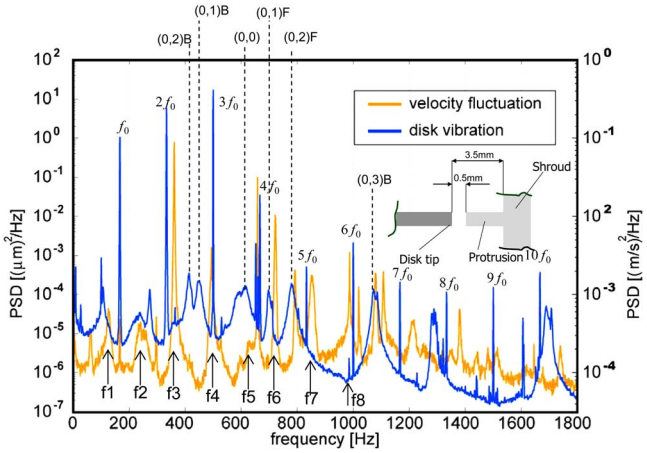

Fig. 11 Comparison of PSD of disk vibration at the periphery and velocity fluctuation at the middle of the vortical flow region (aluminum, N=10,000 rpm, N/N_c=0.33, a=0.5 mm, b=3.5 mm, hot-wire is located at $r=0.8R_2$; f1–f8 denote vortical flow mode, (m,n) denote vibration modes, and $nf0$ denotes disk RRO)

pared in Fig. 11 for N=10,000 rpm, in which fn indicate the frequency caused by the asymmetric flow structure of circumferential wave number n, and $(m,n)B$ and $(m,n)F$ indicate the backward and the forward traveling mode of disk vibration as before. The line specta denoted by nf_0 are at multiples of rotation frequency (166.6 Hz) and correspond to the disk RRO.

Although the PSD of the disk vibration exhibits peaks at the flow modes $f3$ and $f8$, it is negligibly small or might be accidental. Since at the other velocity peaks the vibration PSD does not generally show any peaks, the disk vibration in this speed range is free vibration, triggered by, but not forced by, the flow unsteadiness caused by the vortical structure.

Inversely, at RRO frequency f_0, the velocity PSD shows sharp peaks not corresponding to the flow instability mode. At $3f_0$, the velocity PSD exhibits an unusually high and sharp peak. This frequency is just equal to $f4$, and thus this flow mode might be excited by the RRO. At $2f_0$, the velocity PSD does not show a peak just at this frequency but the mode $f3$ nearby shows extremely high peak. At $4f_0$, the frequency of $f5$ is slightly shifted and enhanced by the RRO. These results infer that the RRO component of disk out-of-plane movement significantly influences the vortical flow structure. On the other hand, the velocity peaks and the NRRO peaks are essentially different. This result indicates that the vortical flow mode and vibration mode are decoupled at least in the frequency space.

Together with the facts mentioned in Secs. 3.3 and 3.4, we have come to the conclusions that the disk vibrates with its own modes even if they are excited by the flow unsteadiness including the vortical structure. This conclusion supports the idea of open loop of solid-fluid interaction proposed by Fukaya et al. [14]. In addition the RRO component of disk out-of-plane displacement may have a significant effect on the velocity fluctuation due to the differential velocity between disk and flow.

In the previous CFD studies, the disks have been treated exclusively as rigid and flat. The rigidity assumption is now confirmed appropriate even in the high subcritical speed range but the flatness assumption should be considered more carefully in the real system, since RRO is unavoidable as long as the disk rotates.

4 Summary and Conclusions

To identify the nature of the flow-induced vibration of disks in the wide range of rotation speed below critical, the structure and time-dependent behavior of unstable flow between disks together with disk vibration have been examined experimentally. By reconstructing the commercial hard disk drives to render them axisymmetric, and employing glass, aluminum, and acrylic disks, the flow visualization and measurements of velocity and out-of-plane displacement have been carried out. PIV and hot-wire anemometry have been employed for velocity measurements and a capacitance-type displacement meter has been employed for vibration measurements.

The velocity vector maps and vorticity contours between disks obtained by PIV revealed that the large-scale vortical structure loosely called previously is actually vortex, which consists of closed streamlines and concentrated vorticity at its center when seen from an observer rotating with the corresponding structure. After confirming that the asymmetric flow structure, well known in the enlarged low speed model, does exist in the present small size and high speed apparatus, the velocity fluctuations and disk vibration have been examined by varying disk speed and disk material.

It was found that the rms of disk vibration begins to increase already in the low subcritical speed range below 10% of disk critical speed and continues to rise until close to the critical speed. The data with different disk materials show that NRRO of disk vibration and disk speed is uniquely correlated when the disk speed is normalized by the critical speed. Comparisons of measured PSDs in the form of waterfall plots with that obtained by FEM without surrounding fluid indicate that the vibration modes in the subcritical speed range is essentially the same as in vacuum. It means that the disk vibration is a free vibration triggered by, but not forced by, the flow unsteadiness even in the high subcritical speed range.

Next, we have considered that the disk out-of-plane movement influences somehow the flow unsteadiness between disks. We want to know whether a real disk can be treated as a rigid flat surface, as has been assumed in previous CFD. To make it clear, the rms of velocity fluctuation at the interdisk midplane near the outer periphery of the disk has been examined. The velocity fluctuation is generally higher for the acrylic disk. Since the only difference is the disk boundary condition, it has been speculated that the disk out-of-plane movement influences the flow near the outer periphery of the disk. By inspection of PSD of velocity fluctuation, it has been revealed that the change of velocity fluctuation is mainly caused by the RRO component of disk out-of-plane movement, while the NRRO component is hardly detected by the fluid at the interdisk midplane in the outer periphery even in the high subcritical speed range.

Finally, the influence of disk out-of-plane movement on the vortical flow structure has been investigated by comparing PSD of the velocity fluctuation in the vortical flow region with that of disk vibration. It was found that the disk vibration has a negligible effect on the vortical structure suggesting the soundness of the rigid disk assumption employed in the existing CFD. However, RRO has a significant influence on the flow instability. Since the RRO is unavoidable in the real disk system, the flat disk assumption should be considered more carefully.

Acknowledgment

This work has been financially supported by the storage research consortium (SRC). Our thanks are also deu to Dr. M. Tokuyama of Hitachi, Ltd. for his efforts of preparing the facilities. We also thank H. Kusaka, S. Kisaki, and W. Yamamoto for their contributions in conducting the experiments.

Nomenclature

a = disk tip clearance
b = disk-to-shroud clearance
H = disk spacing
m = number of nodal circles
n = number of nodal diameters

$(m,n)F,(m,n)B$ = forward and backward traveling waves of (m,n) mode
N = speed of disk rotation (rpm)
N_c = critical speed of disk rotation
N/N_c = speed ratio
(r,θ,z) = cylindrical polar coordinate
R_1 = disk inner radius
R_2 = disk outer radius
Re = Reynolds number
t = disk thickness
μ = fluid viscosity
ρ = fluid density
Ω = angular velocity of disk rotation
ω = rotational speed of asymmetric structure relative to disk

References

[1] Lennemann, E., 1974, "Aerodynamic Aspects of Disk Files," IBM J. Res. Dev., pp. 480–488.
[2] Abrahamson, S. D., Eaton, J. K., and Koga, D. J., 1989, "The Flow Between Shrouded Corotating Disks," Phys. Fluids A, **1**(2), pp. 241–251.
[3] Humphrey, J. A. C., Schuler, C. A., and Webster, D. R., 1995, "Unsteady Laminar Flow Between a Pair of Disks Corotating in a Fixed Cylindrical Enclosure," Phys. Fluids, **7**(6), pp. 1225–1240.
[4] Iglesias, I., and Humphrey, J. A. C., 1998, "Two- and Three-Dimensional Laminar Flows Between Disks Co-Rotating in a Fixed Cylindrical Enclosure," Int. J. Numer. Methods Fluids **26**(5), pp. 581–603.
[5] Herrero, J., Giralt, F., and Humphrey, J. A. C., 1999, "Influence of the Geometry on the Structure of the Flow Between a Pair of Corotating Disks," Phys. Fluids, **11**(1), pp. 88–96.
[6] Randriamampianina, A., Schiestel, R., and Wilson, M., 2001, "Spatio-Temporal Behaviour in an Enclosed Corotating Disk Pair," J. Fluid Mech., **434**, pp. 39–64.
[7] Al-Shannag, M., Herrero, J., Humphrey, J. A. C., and Giralt, F., 2002, "Effect of Radial Clearance on the Flow Between Corotating Disks in Fixed Cylindrical Enclosures," J. Fluids Eng., **124**, pp. 719–727.
[8] Shimizu, H., Tokuyama, M., Imai, S., Nakamura, S., and Sakai, K., 2001, "Study of Aerodynamic Characteristics in Hard Disk Drives by Numerical Simulation," IEEE Trans. Magn., **37**(2), pp. 831–836.
[9] Tatewaki, M., Tsuda, N., and Maruyama, T., 2001, "An Analysis of Disk Flutter in Hard Disk Drives in Aerodynamic Simulation," IEEE Trans. Magn., **37**(2), pp. 842–846.
[10] Yasuda, K., Torii, T., and Shimizu, T., 1992, "Self-Excited Oscillations of a Circular Disk Rotating in Air," JSME Int. J., Ser. III, **35**, pp. 347–352.
[11] Renshaw, A. A., D'Angelo, C., and Mote, C. D., Jr., 1994, "Aerodynamically Excited Vibration of a Rotating Disk," J. Sound Vib., **177**(5), pp. 577–590.
[12] Hansen, M. H., Raman, A., and Mote, C. D., Jr., 2001, "Estimation of Non-Conservative Aerodynamic Pressure Leading to Flutter of Spinning Disks," J. Fluids Struct., **15**, pp. 39–57.
[13] McAllister, J. S., 1996, "The Effect of Disk Platter Resonance on Track Misregistration in 3.5 Inch Disk Drives," IEEE Trans. Magn., **32**(3), pp. 1762–1765.
[14] Fukaya, R., Obi, S., Masuda, M., and Tokuyama, M., 2002, "Flow Instability and Elastic Vibration of Shrouded Corotating Disk Systems," Exp. Fluids, **33**, pp. 369–373.
[15] Imai, S., Tokuyama, M., and Yamaguchi, Y., 1999, "Reduction of Disk Flutter by Decreasing Disk-To-Shroud Spacing," IEEE Trans. Magn., **35**(5), pp. 2301–2303.
[16] Imai, S., 2001, "Fluid Dynamics Mechanism of Disk Flutter by Measuring the Pressure Between Disks," IEEE Trans. Magn., **37**(2), pp. 837–841.
[17] Eguchi, T., and Kouno, T., 2005, "Theoretical Study on Aerodynamic Damping of Disk Flutter Caused by Narrow Disk-Shroud Gap," ASME Report No. ISPS-2005.
[18] D'Angelo, C., and Mote, C. D., Jr., 1993, "Aerodynamically Excited Vibration and Flutter of a Thin Rotating at Super Critical Speed," J. Sound Vib., **168**(1), pp. 15–30.
[19] 2002, *PIV Handbook*, The Visualization Society of Japan, Tokyo.
[20] Tavener, S. J., Mullin, T., and Cliff, K. A., 1991, "Novel Bifurcation Phenomena in a Rotating Annulus," J. Fluid Mech., **229**, pp. 483–497.
[21] Kong, D.-W., and Joo, W.-G., 2004, "Visualization of the Flow Pattern Between Corotating Disks in Shroud," *ASME Information Storage and Processing System Conference*, Santa Clara, CA, Jun. 2004.
[22] Tadepalli, S., and Xia, S., 2001, "Influence of Disc Spacing on Air Flow Excitation in Disc Drives," ASME Report No. ISPS-2001.
[23] Schuler, C. A., Weber, B., Humphrey, J. A. C., and Greif, R., 1990, "On the Flow in the Unobstructed Space Between Shrouded Corotating Disks," Phys. Fluids A, **2**(10), pp. 1760–1770.
[24] Suzuki, J., Yamamoto, W., Obi, S., and Masuda, S., 2005, "Exciting and Damping Effects of Flow Induced Vibration in Corotating Disk Systems," *ASME Information Storage and Processing System Conference*, Santa Clara, CA, Jun. 2005.
[25] Amemiya, K., Masuda, S., Obi, S., Tokuyama, M., and Imai, S., 2000, "Flow Between Shrouded Corotating Disks," Trans. Jpn. Soc. Mech. Eng., Ser. B, **65**(650B), pp. 2559–2564.

Velocity and Pressure Measurements Along a Row of Confined Cylinders

Barton L. Smith

Jack J. Stepan

Mechanical and Aerospace Engineering,
Utah State University,
Logan, Utah 84322

Donald M. McEligot

Idaho National Laboratory (INL),
Idaho Falls, Idaho 83415-3885;
University of Arizona,
Tucson, Arizona 85721;
IKE, University of Stuttgart,
D-70569 Stuttgart, Deutschland

The results of flow experiments performed in a row of confined cylinders designed to mimic a model of a prismatic gas-cooled reactor lower plenum design are presented. Pressure measurements between the cylinders were made. Additionally, the flow field was measured using particle image velocimetry at two different resolutions (one at high resolution and a second with wide angle that includes three cylinders). Based on these measurements, five regimes of flow behavior are identified that are found to depend on Reynolds number. It is found that the recirculation region behind the cylinders is shorter than that of half-cylinders placed on the wall representing the symmetry plane. Unlike a single cylinder, the separation point is always found to be on the rear of the cylinders, even at very low Reynolds number. [DOI: 10.1115/1.2776970]

1 Introduction

The present study is part of a broad program to assess and develop computational tools for advanced nuclear reactor systems [1,2]. One region of interest is the lower plenum of prismatic gas-cooled reactors (GCRs). There a finite array of short graphite posts supports the reactor core and—in an annular ring under the active core—heated flows from the vertical cooling channels enter as jets and then exit horizontally through a single core outlet duct. Typical designs of the posts have pitch-to-diameter ratios P/D of about 1.7 and height-to-diameter ratios H/D of 7. Consequently, it is a complicated flow through a geometry that cannot be considered to be an infinite, two-dimensional array of infinitely long rods. Furthest from the exit, the cross flow is nearly stagnant with the hot jets likely impinging on the plenum floor where a thermal design consideration is having sufficient insulation to protect the metallic plate supporting the posts. Near the exit, there is a cross flow from all the upstream jets and a thermal consideration is avoiding overheating the metallic hot-duct structural element (called thermal streaking). For the benefit of computational fluid dynamics (CFD) code developers, the first experiments address the limiting conditions where buoyancy effects and property variations are not important, i.e., an isothermal flow.

To assess the capabilities of CFD codes to treat the flow phenomena occurring in such a situation, an experiment has been designed to model them physically in the matched-index-of-refraction (MIR) flow system at INL [3]. The MIR experiment model is scaled to the application and consists of a row of full circular posts along its centerplane with half-posts on the two parallel walls, as shown in Fig. 1, to induce flow features somewhat comparable to those expected from the staggered adjacent rows of posts in the reactor design. Jet inlet ducts are located in one end wall in the MIR model. For meaningful assessment data, it is desired that the small experiment be operated in the same flow regimes as expected in the full-scale application. This desire translates into the questions: what flow regimes should be expected and what flow rates (or Reynolds numbers) are necessary to achieve these regimes.

With the annular reactor core, there are no cooling channels in a central near-cylindrical region. So no jets enter from the core in this region (Figs. 6 and 7 by Condie et al. [4]). It then provides a cross flow into which the jets from the section of the annular ring near the exit duct are injected. Based on the guidance of Žukauskas [5] for a two-dimensional situation, it is expected that this cross flow will be in his "mixed flow" regime. So the present study was undertaken with the prime objective of determining the flow behavior versus Reynolds number in the configuration of the MIR model. Alternatively, one could consider the purpose to be to examine whether the existing guidance for large arrays can provide useful predictions for this configuration. In the process, additional quantitative information has been obtained to assist in assessing CFD capabilities for this complicated flow and its interrelated phenomena.

For flows in GCRs in general, Schultz et al. [6] have surveyed available literature and have compiled lists of pertinent studies. Many studies have been conducted for individual phenomena separately. The references and investigators that they identified can provide significant tests of codes and their turbulence models for a wide variety of flow and mixing phenomena occurring in a lower plenum.

Flow over a single, 2D cylinder is perhaps the fundamental external flow problem and has thus been studied extensively for a number of years. More recently, modern measurement and simulation techniques have allowed detailed investigation of the wake region of a cylinder, which had been very difficult in the past due to large fluctuations and recirculation regions. Zhang et al. [7] investigated the wake of a cylinder numerically and experimentally for very low Reynolds numbers (less than 250) and identified four separate instability modes. Kim et al. [8] made detailed measurements of the shedding of a cylinder using time-resolved particle image velocimetry (PIV) measurements for a Reynolds number of 360. Reynolds stress distributions and mean separation streamlines were examined and correlated to drag behavior.

Flow across a pair of cylinders was studied experimentally by Wang and Zhou [9] in the Reynolds number range $100 < \mathrm{Re} < 1000$. The main focus of this study was the effect of the cylinder spacing on vorticity and frequency of structures in the wake of the cylinders.

Over decades, crossflows over large arrays of cylinders have been examined by Chilton and Genereaux [10], Grimison [11], Bergelin et al. [12], Kays and London [13], and many others. For engineering purposes, these efforts have concentrated on overall pressure drop and heat transfer coefficients with some flow visualization. While resulting correlations can imply differing flow regimes, apparently no systematic examination has considered the regime dependence on flow rate, particularly relating to the geom-

Contributed by the Fluids Engineering Division of ASME for publication in the JOURNAL OF FLUIDS ENGINEERING. Manuscript received August 1, 2006; final manuscript received March 2, 2007. Review conducted by Timothy J. O'Hern. Paper presented at the 2006 ASME Fluids Engineering Division Summer Meeting and Exhibition (FEDSM2006), Miami, FL, July 17–20, 2006.

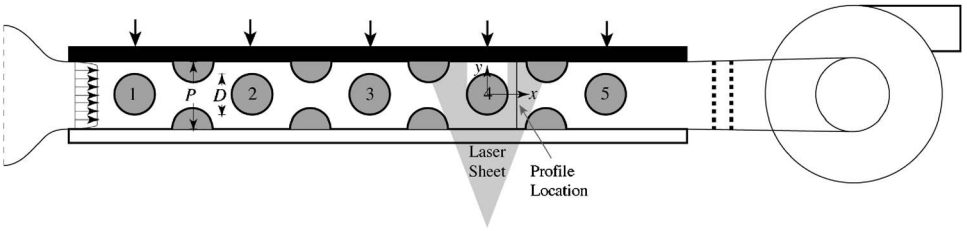

Fig. 1 The test section used in this study. Air enters through screens at the left, into a contraction and into the test section. The field of view for the wide-angle PIV data is shown (i.e., the laser sheet). The laser sheet moves through the near transparent side of the facility and terminates on the opaque far side. Streamwise locations of the pressure taps are indicated with arrows on the top wall. These taps are in the spanwise center of the channel. A second view of the facility is shown in Fig. 3.

etry of the INL model. For an equilateral triangular array of $P/D=1.5$, Bergelin et al. [12] arbitrarily designated the upper Reynolds number $U_{\max}D/\nu$ for their "viscous" (laminar) region as 200, a transition region from 200 to 5000, and turbulent above 5000. Žukauskas does provide graphical correlations for infinite equilateral arrays with $P/D=1.5$ and 2, bracketing the present application.

Pressure drop and local heat transfer coefficients were obtained by Achenbach [14] for staggered tube bundles at high Reynolds numbers. Velichko et al. [15] measured heat transfer and friction parameters for nontraditional tube bundle arrangements. Mean and fluctuating velocity components were measured at $2\times10^5<\mathrm{Re}<2\times10^6$ by Poskas and Survila [16] for staggered and inline bundles of tubes. Katinas et al. [17] measured tube vibrations induced at turbulence levels from one to 12% in the upstream flow to staggered and inline tubes; although the Reynolds number supposedly was varied from 10^3 to 2×10^5, effects were not presented in terms of Reynolds number. Fluctuations of heat transfer and velocity have been measured in a staggered tube array by Scholten and Murray [18]. Iwaki et al. [19] conducted PIV measurements for staggered bundles of $P/D=1.5$, five tubes wide, while their Reynolds number ranged from 5400 to 29,700, most results presented mean velocity distributions, vorticity contours, vortex structures, and turbulent intensities were at $\mathrm{Re}=27{,}000$.

Stanescu et al. [20] determined optimal spacing of cylinders to maximize the average heat transfer conductance for an entire bundle. Beale and Spalding [21] numerically predicted laminar flow and heat transfer across a variety of tube bundle geometries. Watterson et al. [22] applied a low-Reynolds-number $k-\epsilon$ model to flow around an array of staggered tubes. A $k-\epsilon$ model was also applied by Wilson and Bassiouny [23] to predict the laminar and turbulent flows of air across tube banks with apparently satisfactory agreement to data. From their large eddy simulation (LES) of flow through an inline array of $P/D=1.44$ at $\mathrm{Re}=70{,}000$, Benhamadouche et al. [24] observed evidence of eddy shedding in the shear regions. In addition to any turbulence present, such periodic oscillations would contribute to indicated mean fluctuations measured in an experiment.

These studies have typically been aimed at developing information applicable to infinite, two-dimensional arrays of infinitely long tubes, as approximated in some (very) large shell-and-tube heat exchangers. However, in the present situation, the row of posts is confined between sidewalls and the posts are short ($H/D\approx7$). Effects of blockage (confinement) by a single circular tube in a channel have been measured by Perkins and Leppert [25]. From these reports, Žukauskas [5] indicated that a change in blockage ratio alters the pressure distributions and flow patterns in the wake. Žukauskas et al. [26] measured the effects of blockage on the flow over a single cylinder centered in a channel, in terms of pressure distribution and drag coefficients. The study concentrated on conditions near the "critical" Reynolds number where the point of separation is shifted downstream so that the vortex region becomes narrower. They note that flow over a cylinder in a channel with finite dimensions differs from unbounded flow with the constrictions formed changing the pressure gradients from those existing without blockage. For their conditions, an increase in blockage increased the drag coefficient due to widening of the wake of the cylinder.

A flow somewhat comparable to a GCR lower plenum occurs in arrays of "pin fins" employed for internal cooling of turbine vanes and blades. These short circular cylinders are installed in the gap between the converging surfaces, which form the trailing edge of a blade for the purpose of increasing the overall heat transfer coefficient from metal blade surfaces to the internal coolant flow as shown, for example, in Figs. 2 and 3 of the paper by Ames et al. [27]. The measurements and predictions for pin fin arrays have been reviewed by Armstrong and Winstanley [28], Ames and Dvorak [29], and others. For effectiveness as extended surfaces, they are typically even shorter than the support posts in the lower plenum of a prismatic GCR. The pin fin experiments may also provide valuable data for assessment of CFD predictive techniques for GCRs.

Moulinec et al. [30] performed a 3D Direct Numerical Simulation (DNS) to study the effect of cylinder spacing on the wakes behind the cylinders. Their Reynolds number ranged from 50 to 6000. They reported that the vorticity behind a row of cylinders

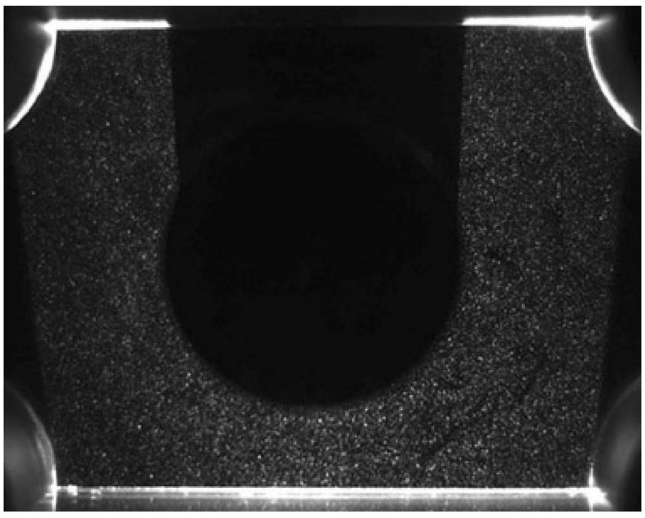

Fig. 2 A sample PIV raw-data image. No masking or other processing has been performed. The laser sheet enters from below. The edges of the wall cylinders are visible in all four corners of the image. The center cylinder generates a shadow on the far wall. An additional region around the cylinder is dark due to the effects explained in conjunction with Fig. 3.

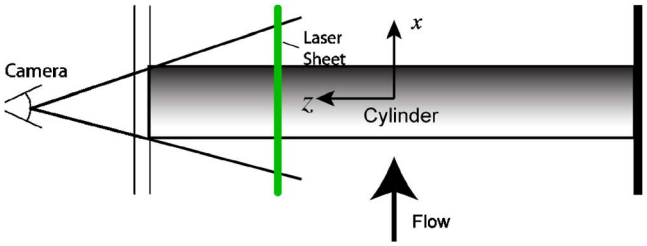

Fig. 3 A schematic diagram showing the cause of the dark region near the cylinder surface for the wide-angle data. The camera's view of the surface is blocked by the near end of the cylinder. The end of the cylinder is not visible in the images since it is not illuminated.

disappeared rapidly for low-Reynolds-number laminar flow due to cancellation of vorticity, while turbulent diffusion led to the disappearance of the wake for larger Reynolds number flow. As a result, the flow around each cylinder "cell" becomes independent of the others. PIV measurements of flow over inline and staggered tube banks were made by Iwaki et al. [19]. Similarities and difference between the two arrays were examined. It was noted that the flow in the staggered tube bank was more homogeneous than that for the inline bank, and that the flow therefore becomes fully developed more quickly.

We will most closely compare our data to that of Žukauskas [5]. In that study (which was based on flow visualization, pressure drop, and heat transfer measurements although the flow visualization images are not included in the paper), he describes three primary regimes of behavior that depend on Reynolds number $\mathrm{Re}=U_{\max}D/\nu$, where $U_{\max}$ is the bulk velocity at minimum area, D is the cylinder diameter, and ν is the kinematic viscosity. Presumably based on flow visualization results, the regimes are as follows:

1. Laminar flow ($\mathrm{Re}<1000$).
2. Mixed flow, where the boundary layers are laminar, while the flow contains turbulent regions ($500<\mathrm{Re}<2\times10^5$).
3. Turbulent or "critical" flow ($\mathrm{Re}>2\times10^5$).

This paper describes experiments performed at the Utah State University (USU) Experimental Fluid Dynamics Laboratory (EFDL) in support of other experiments performed in the INL MIR facility. In the present work, Reynolds numbers in this turbulent range described above are not achieved. However, detailed 2D velocity maps obtained using PIV provide considerably more information about the flow state than the earlier study. Based on these results, we are able to subdivide regimes 1 and 2.

It is not our intent to provide results applicable for infinite arrays with this unique model. Rather, we examine whether the guidance for infinite arrays is useful for noninfinite geometries such as ours. So far we have not found experiments, computations, or analyses for flow around a confined row of short posts with the approximate geometric ratios needed here.

2 Facility and Measurements

The facility consists of an inlet contraction, a test section, and an outlet that connects to ducting leading to the blower inlet as shown in Fig. 1. Atmospheric air (at 4500 ft, Logan air pressure is nominally 0.85 atm) is drawn through the facility by a frequency-controlled centrifugal blower. The inlet contracts 1.4:1 in the spanwise direction and 3:1 in the cross-stream direction. Turbulence is managed by a single bank of screen with 112 wires/cm at the inlet. The flow leaving the test section passes through two perforated plates placed in line to suppress separation and pulsations generated by the blower. The blower is connected to the outlet by a flexible hose. The effectiveness of the turbulence management is confirmed through hot wire measurements at $y=z=0$ (the spanwise and cross-stream center) and at the inlet of the test section. The rms level of the hot wire velocity magnitude signal varies from a minimum of 1.1% of the inlet mean velocity magnitude at low velocity up to 1.5% at the highest velocity; for the ultimate application, a "low" turbulence level is not expected.

A schematic diagram of the test section along with the coordinate system employed is given in Fig. 1. The test section is a channel 89.7 cm long in the streamwise direction (x), 8.53 cm in the cross-stream direction (y) and 34.8 cm in the spanwise (z) direction and is geometrically similar to the INL model. The channel contains an array of cylinders and half-cylinders designed to mimic an infinite array of cylinders arranged on an equilateral triangular pitch. Five cylinders, which represent vertical support posts in the lower plenum of a very high temperature reactor (VHTR) concept, are placed on the cross-stream centerline. The streamwise distance between these cylinders is 14.8 cm. The cylinders are 5.03 cm in diameter. Four sets of half-cylinders are placed on the cross-stream edges directly between the centerline cylinders.

The primary dimensionless parameter that describes this geometry is the cylinder pitch P/D, where P is the distance between adjacent cylinders (and equal to the channel width, 8.53 cm) and D is the cylinder diameter. Therefore, $P/D=1.7$, and the channel is 59% blocked by the cylinders. An additional parameter is the spanwise dimension relative to the cylinder diameter, $H/D=6.9$, which corresponds to the approximate height of the lower plenum represented.

Three types of measurements are made:

1. the pressure drop from each full cylinder to the next
2. the velocity field on the x-y plane between the fourth full cylinder and the next half-cylinder
3. three high-resolution overlapping x-y planes wrapping around the fourth cylinder

Pressure taps were drilled into the back wall of the facility as shown by the arrows in Fig. 1. The pressure taps were holes 1.59 mm in diameter. Care was taken to ensure that the wall was smooth after drilling. All taps were placed at the spanwise centerline and were at the same streamwise position as the axis of the full cylinders. The pressure measurements were made using a high-accuracy differential capacitance manometer with 0.0001 mm Hg resolution. This resolution is the major source of uncertainty in the pressure measurements. The positive and negative sides of the manometer were placed across the two successive ports. For each cylinder at each Reynolds number, data were recorded via a 12 bit analog-to-digital converter in a laboratory computer. The average of samples taken over 30 s is reported.

The PIV measurements were made using a system by LaVision Inc. consisting of a 12 bit 1.3 Mpixel (1280×1040) camera, a pair of 50 mJ Nd:YAG (yttrium aluminum garnet) lasers with sheet optics, and an acquisition personal computer including a frame grabber and a timing board. A fluorescent paint was applied to all surfaces to shift laser reflections to wavelengths that can be removed by a filter on the camera optics. The laser sheet entered the facility from one cross-stream side made of transparent plastic and was terminated on the other opaque side. The sheet was placed between the spanwise centerline ($z=0$) and the spanwise wall as a compromise between our desire to obtain 2D mean data and to minimize the extent of the region near the cylinder surface that cannot be observed due to parallax. Olive oil droplets formed by a Laskin nozzle apparatus (built in-house) were used as seeding particles. The droplets produced were estimated to be $1-2$ μm in diameter. The droplets were drawn into the facility at the inlet. Care was taken to ensure that the images of the droplets on the charge-coupled device (CCD) array were somewhat larger than 2 pixels to eliminate pixel locking while providing maximum accuracy [31]. Multiple cross-correlation passes with a final

interrogation-region size of 16 pixels were used. In each case, 500 image pairs were acquired at a rate of one pair per second.

An example of one image is shown in Fig. 2. Several features of this raw-data image should be noted: The data acquired are centered on the fourth cylinder, since this location was judged to be the most likely location to obtain a streamwise-periodic result based on the pressure drop data (cf. Fig. 7). Streamwise periodicity is confirmed by the pressure drop data below as well as a single case measured on the third cylinder (not shown). The half-cylinders upstream and downstream are visible on both sides of the channel. Both channel walls are easily found, and these locations are used for the PIV calibration since this distance is known (note that the laser reflections visible in the image do not extend into the measurement domain). The laser sheet is blocked by the lower half-cylinders but expands somewhat as it crosses the channel. The laser sheet is also blocked by the near end of the opaque centerline cylinder, forming a shadow on the far side of the channel. The shadow appears to be narrower than the cylinder. This situation occurs because the view of the surface of the cylinder is obscured by the part of the cylinder between the laser sheet and the camera lens. That is, due to the placement of the camera in line with the center of the cylinder, the angle subtended by the cylinder end is greater than the angle to the intersection of the cylinder and the light sheet further along, as shown in Fig. 3. Therefore, the entire boundary layer of the cylinder is not visible in these views. This effect is reduced by placing the laser sheet 10 cm from the spanwise center toward the side closest to the camera. Boundary layer data for a subset of these Reynolds numbers were acquired in the high-resolution data set described below.

The PIV data were first acquired with the blower outlet open and the blower operating between its minimum and maximum rotation rates. Reynolds numbers in the range $1473 < \mathrm{Re} < 55{,}900$ (see definition in Sec. 4) were generated. Since lower Re values were desired, the blower outlet was throttled, and a second set of data was recorded in the range $237 < \mathrm{Re} < 2620$. The camera field of view was not exactly repeated for both measurements. Therefore, the data locations for the two sets of data are somewhat different.

3 Uncertainty Analysis

PIV measures the displacement of the flow over a prescribed time interval. Modern timing boards are capable of precision that renders timing errors insignificant when assessing bias uncertainty on velocity measurements. The displacement measurement has many sources of bias error that are functions of particle image diameter, particle density, image noise, and particle displacements. It is now well established that, if the particle image is greater than 1 pixel, it is possible to measure displacements much smaller than a pixel [32]. Our estimates of the impact of these error sources are based on the guidance of Raffel et al. [33].

The particle image diameter is consistently near 2 pixels in all of the various data sets presented in this paper, resulting in a displacement uncertainty of 0.01 pixels [33]. Generally, particle displacements were in the range of 11–20 pixels, resulting in an uncertainty as large as 0.03 pixels [33]. Although the 12 bit camera used for all images has very low noise levels, a 5% background noise level is assumed for the sake of conservatism in the uncertainty estimate. This noise level results in an uncertainty of 0.01 pixels [33].

All of these sources prove to be small and insignificant when compared to the effect of velocity gradients within the interrogation window. Most regions of the flow have small gradients (0.02 pixels/pixel) resulting in a 0.1 pixel uncertainty. Larger gradients (0.14 pixels/pixel) can result in a 0.3 pixel uncertainty [33]. Clearly, these uncertainties dominate the displacement bias uncertainty and all other sources will be ignored. The bulk of the data presented is within the smaller range, and therefore, our estimate of bias error on the displacement measurement will be 0.1 pixel.

Generally, the mean displacements for the wide-angle cases vary from a minimum of 3 pixels (at maximum area) to a maximum of 5 pixels (at minimum area) resulting in a bias uncertainty of 2–3% of the mean. For the high-resolution cases, much larger displacements were achieved (6–19 pixels) resulting in uncertainties from of 0.5–1.5% [33].

Precision uncertainty is primarily due to fluctuations in the velocity as measured by $u_{\mathrm{rms}} = \sqrt{\overline{u'u'}}$, where u' is the streamwise velocity fluctuation and the overbar indicates time averaging. Since data were taken slowly enough to ensure independent samples, the precision uncertainty on the mean streamwise velocity is

$$\sigma_{U,p} = \frac{u_{\mathrm{rms}}}{\sqrt{N}} Z_c \tag{1}$$

where the numerator is the standard deviation of the velocity, N is the number of image pairs, and Z_c is 1.96 for 95% confidence [34]. The cross-stream uncertainty is similar. As shown below, fluctuations are typically 60% of the mean, resulting in a precision uncertainty of 2.7% of the mean. Therefore, the precision and bias uncertainties are of similar order, which is desirable. Based on the bias uncertainties above, the overall uncertainty on the mean ranges from 3% to 4% of the average velocity.

For Gaussian statistics, the uncertainty of fluctuation correlations such as u_{rms} is governed by the chi squared distribution. According to Beckwith et al. [34], the estimate of the standard deviation $S_{u_{\mathrm{rms}}}$ lies in an interval about the true value:

$$\frac{(N-1)S_{u_{\mathrm{rms}}}^2}{\chi_{\alpha/2}^2} < \sigma_{u_{\mathrm{rms}}}^2 < \frac{(N-1)S_{u_{\mathrm{rms}}}^2}{\chi_{1-\alpha/2}^2} \tag{2}$$

where $\alpha = 1-c$. For $N=500$ image pairs and $c=0.95$, $\chi_{\alpha/2}^2 = 564$ and $\chi_{1-\alpha/2}^2 = 440$. Based on these values, the error bars for $u'u'$ are 13% of the value.

4 Parameters and Parameter Space

The only independent dimensionless flow variable in this problem is the Reynolds number. Žukauskas [5] and Bergelin et al. [12] based the Reynolds number on the bulk velocity at the minimum area $((P-D)\times H)$ and the cylinder diameter, so that $\mathrm{Re} = U_{\max} D/\nu$. One may note that $U_{\max} = 2.4 U_{\mathrm{av}}$, where U_{av} is the bulk velocity at the maximum flow area. This average velocity is measured from the PIV data at a streamwise location half way between the half-cylinders and the center cylinder as marked in Fig. 1. Based on this definition, the Reynolds number for this study ranges over two orders of magnitude, or $237 < \mathrm{Re} < 55{,}900$, obtained from 27 total cases for the large field of view.

Pressure drop results are presented using the "minor loss factor" [35]

$$k = \frac{\Delta P_{1-5}}{(1/2) n \rho U_{\max}^2} \tag{3}$$

where ΔP_{1-5} is the pressure drop from the first to the last tap and n is the number of cylinders. For the array investigated here, we interpret the number of cylinders to be $n=8$, since the pressure taps do not sense the losses on the rear of the last cylinder. Note that although Žukauskas [5] uses the same definition, the loss factor used by Bergelin et al. [12] is a factor of 4 smaller.

5 Results

The primary purpose of this study is to identify Reynolds numbers that divide the flow behavior into identifiable regimes. One means of doing so is to observe instantaneous velocity vector fields for cases at various Reynolds numbers, such as those shown in Figs. 4 and 5. These plots reveal symmetry (or lack thereof) as

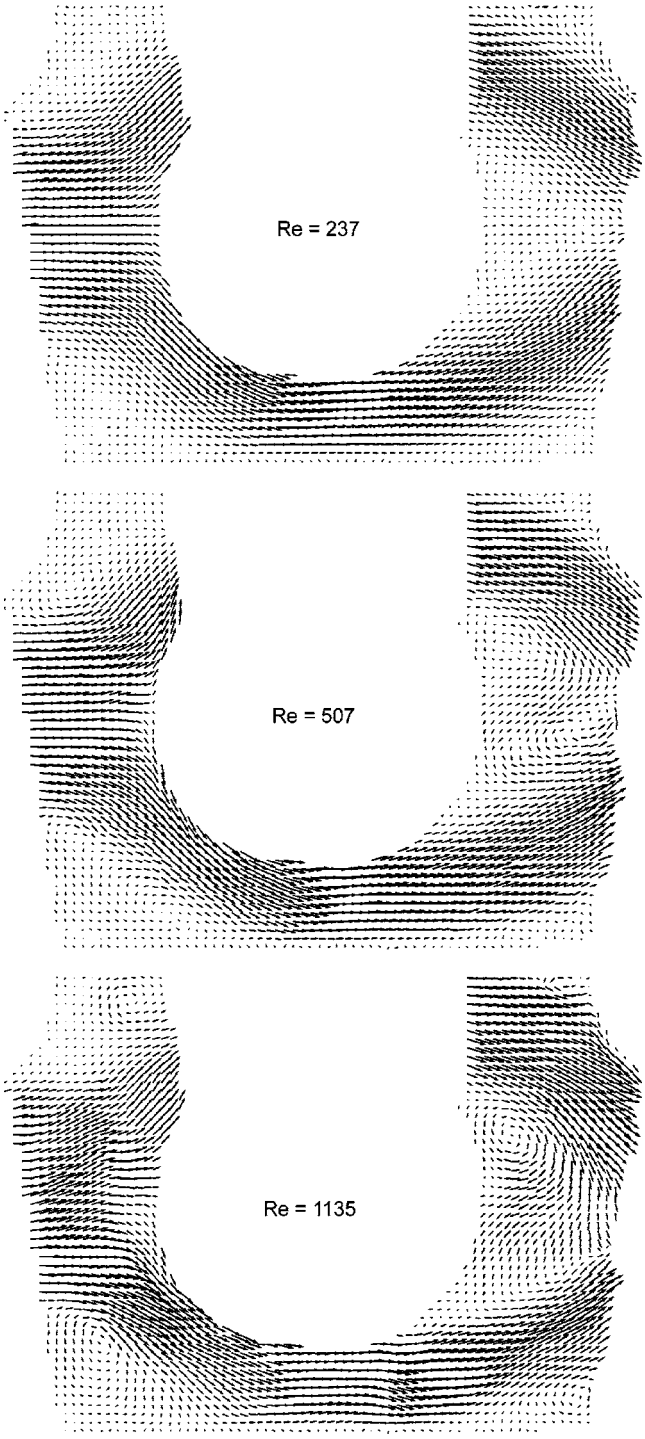

Fig. 4 Instantaneous velocity vectors normalized by U_{av}

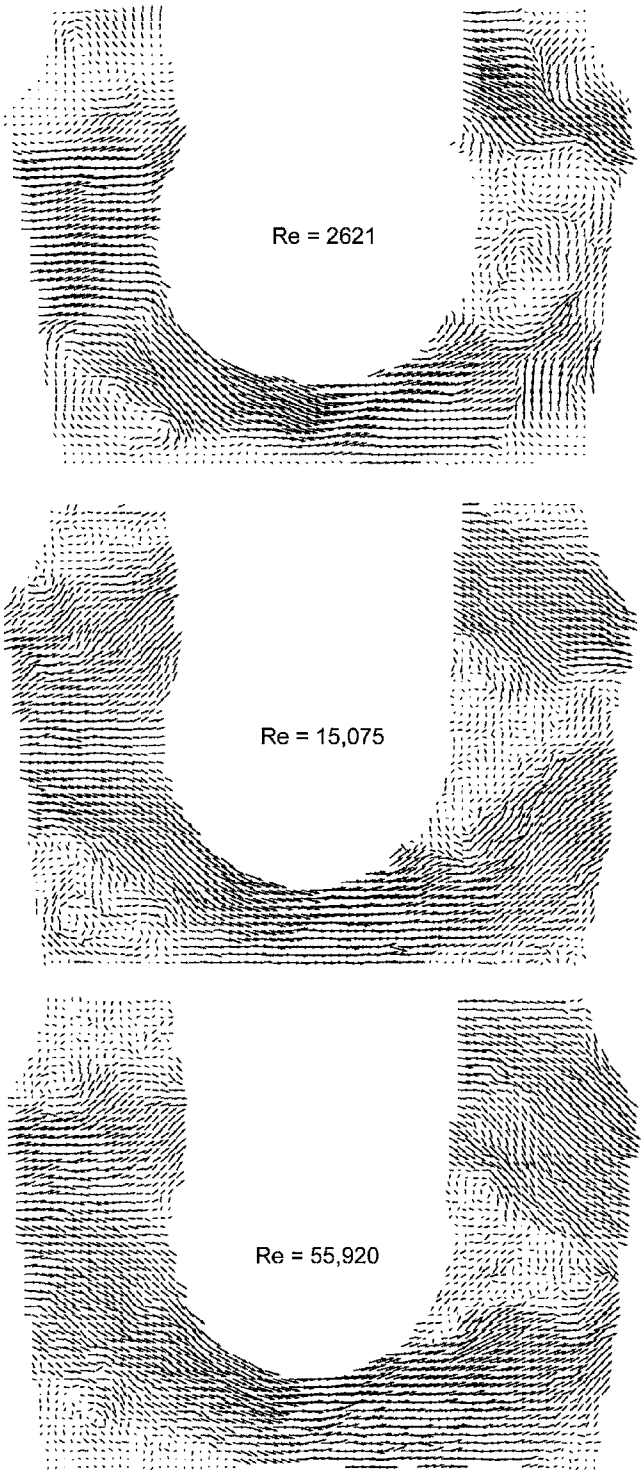

Fig. 5 Instantaneous velocity vectors normalized by U_{av}

well as the size of eddies present in the flow. Animated data for all cases discussed here are available on the EFDL website and may also be helpful [36].

At Re=237, the flow is laminar and steady. The flow in the wake of the cylinders is largely stagnant. Fluctuations of the wake position become apparent at Re=400. Some unsteady recirculation is apparent in the wake. Although this unsteadiness is not detectable in the still image for Re=507, the flow surges above and below the cylinder resulting in elevated streamwise velocity fluctuations (cf. Fig. 10). No turbulent mixing is present, and no small scale motions are present (this is further evidenced by the low value of the Reynolds shear stress in Fig. 12). For $600 < Re < 1900$, flow in regions of adverse pressure gradient (i.e., upstream and downstream of the centerline cylinder) is turbulent, while regions of favorable gradients (i.e., above and below the centerline cylinder) are laminar. Beginning at Re=1900, the flow is turbulent everywhere, with the exception of the boundary layer (this is determined based on the high-resolution measurements described below), which is not visible in these measurements. For the larger Reynolds numbers achieved in this study, the pattern remains largely unchanged. The primary differences between the

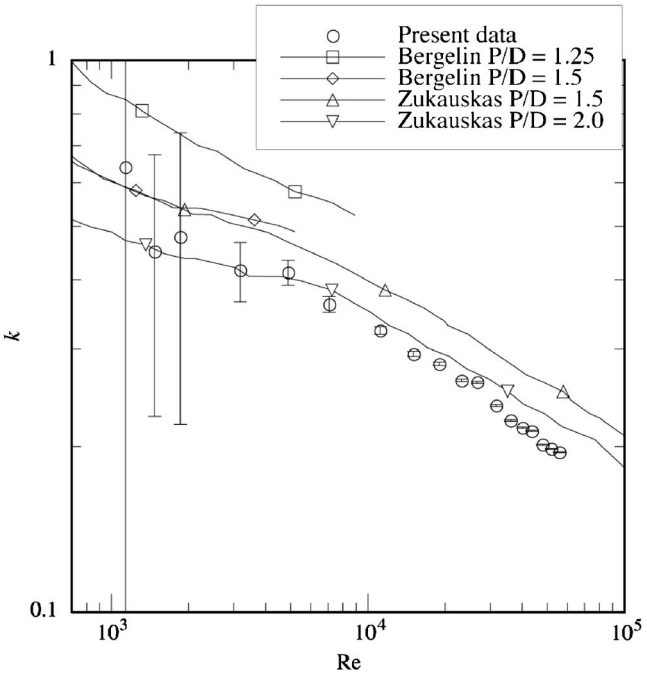

Fig. 6 Pressure losses represented by minor loss factors. Data for equilateral triangle arrays from Žukauskas [5] with $P/D=1.5$ and 2.0 and Bergelin et al. [12] with $P/D=1.25$ and 1.5 are also included.

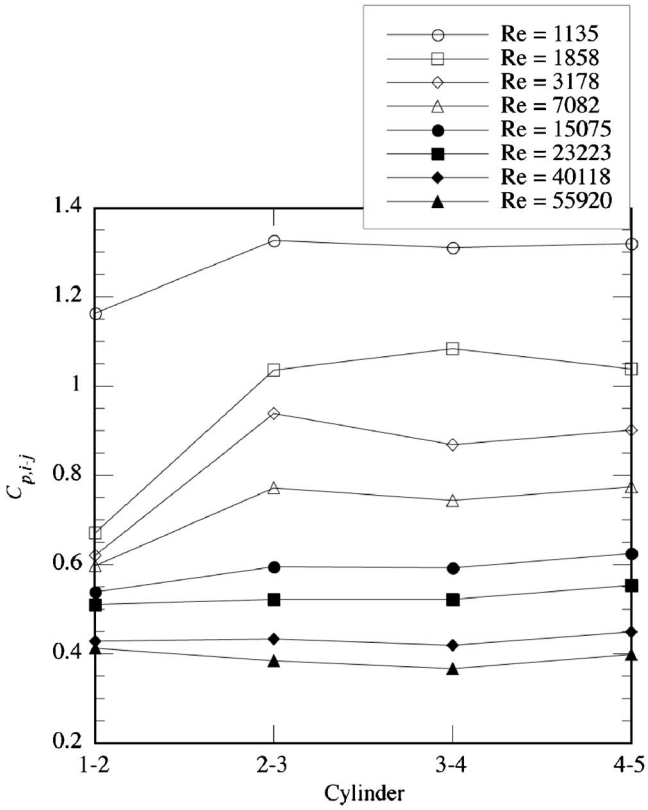

Fig. 7 Pressure drop coefficient $C_p=\Delta P/(1/2\rho U_{max}^2)$ in between taps for several values of Reynolds number

images for Re=2620, 15,075, and 55,900 are the sizes of the turbulent structures, which become smaller as Re grows, as expected.

The pressure drop results are shown in Figs. 6 and 7 for the range of Reynolds numbers over which they are within the resolution of the pressure transducer. The transducer resolution is indicated with error bars in Fig. 6. At low Reynolds numbers, the data lie between the results from Refs. [5,12] for P/D values just above and below that used here. At larger Re, the present data exhibit smaller losses than the infinite array of Ref. [5]. It may be that the presence of the cross-stream walls in the present case suppresses wake oscillations and thus inhibits losses.

It is also interesting to note how many cylinders must be traversed before periodic behavior is generated. This is investigated through measurement of the pressure coefficient from one pressure tap to the next $C_{p,i-j}=\Delta P_{i-j}/(1/2\rho U_{max}^2)$. The first subscript i refers to the cylinder (and pressure tap) at which the positive side of the pressure sensor is attached, while the second subscript j refers to the cylinder where the negative side is attached (see Fig. 1). The loss from the first cylinder to the second is much less than the losses across the remainder of the cylinders for lower Reynolds numbers (Re$<$15,000). This phenomenon is not present at larger Reynolds numbers. In all cases, the pressure drops between the remaining cylinders are similar.

Profiles of several flow quantities on a line midway between the centerline cylinder and the half-cylinders downstream (see Fig. 1) are now presented. The time-averaged profiles of the streamwise and cross-stream components of velocity (U and V, respectively) are shown in Figs. 8 and 9, respectively.

Starting with the streamwise component, in each case, the profile is symmetric with velocity peaks on either side of the centerline cylinder, and reverse flow is present in the cylinder wake in the center of the channel for all but the largest Reynolds number. Generally, as the Reynolds number is increased, the magnitudes of peaks decrease as the peaks become broader. The wake deficit also becomes smaller at this location, notably for the highest Reynolds number. In fact, the wakes for this case show no reverse flow here. The peaks have moved toward the centerline considerably, and the shape of the peak is modified compared to lower Re values.

In the cross-stream component profiles (Fig. 9), all cases with Re$\leqslant$2620 have a flat region of low cross-stream velocity in the wake. The largest Reynolds number exhibits a continuous variation of V across the wake, indicating that this measurement is downstream of the recirculation region for these two cases. This observation is confirmed below in Fig. 14.

Profiles of the measured Reynolds stresses are shown in Figs. 10–12. It should be noted that slow PIV measurements such as these cannot distinguish between turbulence and oscillations generated by vortex shedding or shear-layer instabilities. Also, while some of the profiles do not appear completely symmetric, the asymmetries generally fall within the 13% uncertainty reported above. At this location, the streamwise fluctuations (Fig. 10) in the wake of the cylinder are very small for the steady laminar (Re=237) case and increase with Reynolds number up to Re=15,100 before decreasing for the highest Reynolds numbers measured. Closer to the channel walls, the largest fluctuation values are for Re=2621. These peaks are very large for 1140$<$Re$<$2621 and become smaller while moving toward the centerline for higher Reynolds numbers.

Interestingly, unlike the streamwise fluctuations, the cross-stream fluctuations (Fig. 11) are very small for Re=507, similar to lower Reynolds numbers. Again, the largest fluctuations are at two peaks on either side of the centerline for Re=2621, and these peaks diminish in size while moving closer to the centerline for higher Reynolds numbers as the wake of the cylinder becomes smaller.

Reynolds shear stresses (Fig. 12) are essentially zero for Re$\leqslant$507 indicating no significant turbulent transport. The Reynolds shear stress profiles do not vary much for larger Reynolds numbers. The peak values become somewhat smaller as the peaks move inward, similar to the planar stresses.

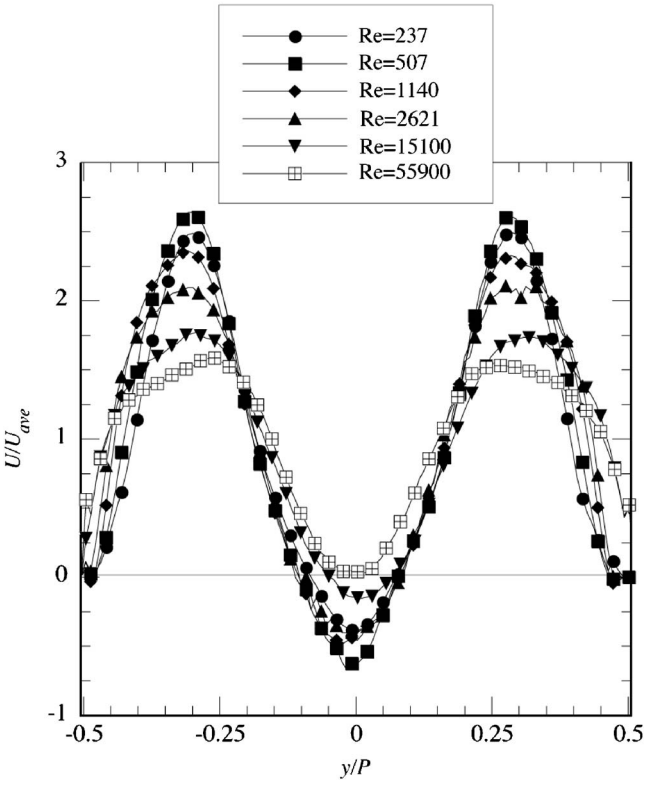

Fig. 8 Cross-stream profiles of the mean streamwise velocity for a range of Reynolds numbers halfway between the fourth cylinder and the following half-cylinders (as indicated in Fig. 1). Every third data point is shown.

Streamline plots (lines drawn parallel to the velocity vector) can be used to find the mean stagnation point that represents the edge of the recirculation region. We define the distance from the base of the cylinder to this point as the wake length L_w. An example of a streamline plot is shown in Fig. 13. The wake length for the full cylinder as well as the half-cylinder on the wall below and upstream of it can be found from the wide-angle data. A value reported more often is the recirculation length L_c or the streamwise distance from the separation point to the end of the wake (this definition is also shown in Fig. 13). Unfortunately, the separation points are not visible in the wide-angle data. They are known for the subset of Reynolds numbers for which high-resolution data are acquired (cf. Fig. 25). We note that the high-resolution data do not include the ends of the wake regions.

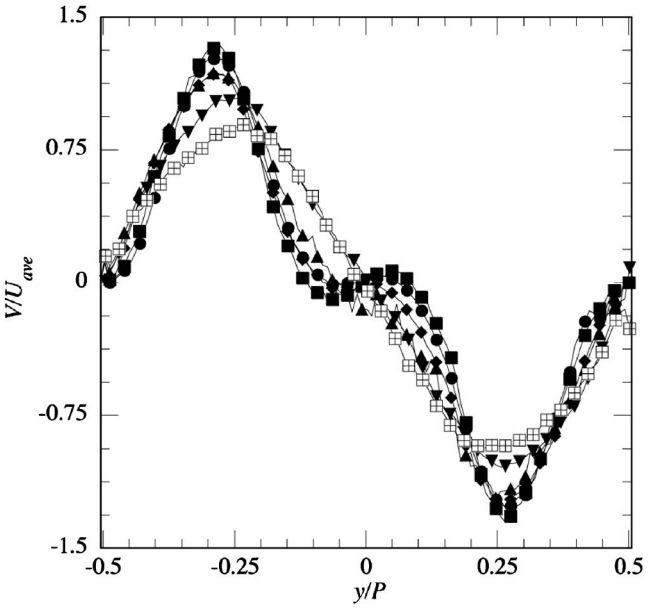

Fig. 9 Cross-stream profiles of the mean cross-stream velocity for a range of Reynolds numbers halfway between the fourth cylinder and the following half-cylinders (as indicated in Fig. 1). Every third data point is shown. Symbols as in Fig. 8.

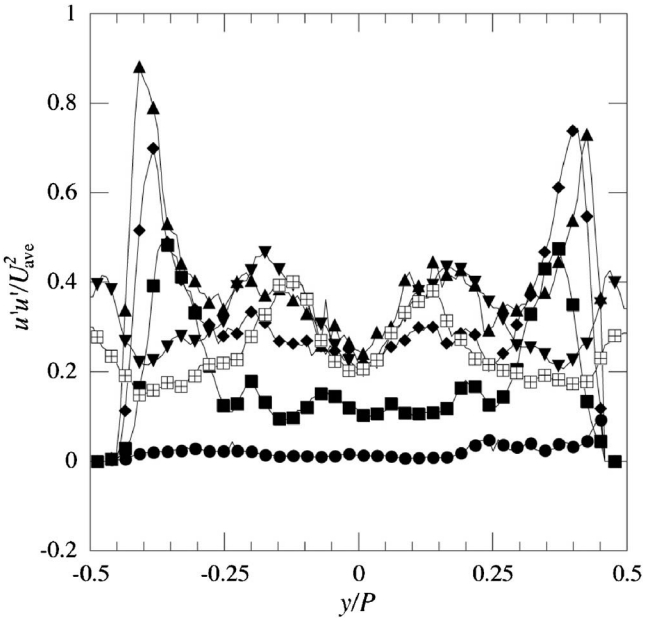

Fig. 10 Cross-stream profiles of the streamwise Reynolds normal stress $\overline{u'u'}/U_{av}^2$ halfway between the fourth cylinder and the following half-cylinders (as indicated in Fig. 1). Every third data point is shown. Symbols as in Fig. 8.

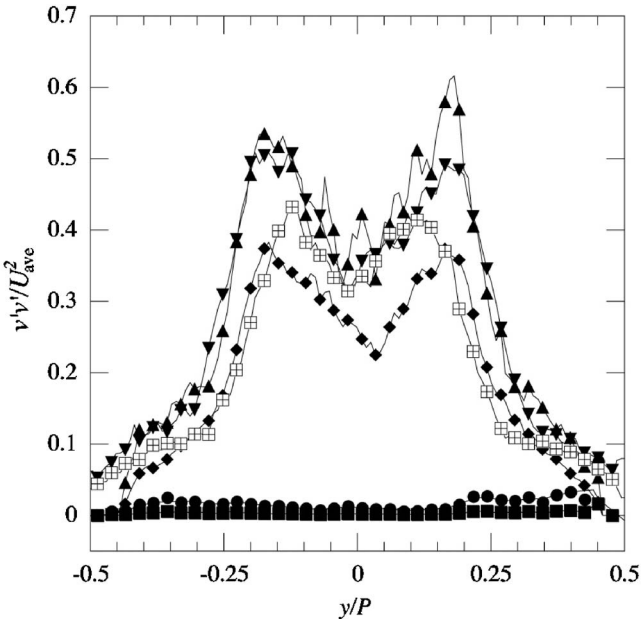

Fig. 11 Cross-stream profiles of the cross-stream Reynolds normal stress $\overline{v'v'}/U_{av}^2$ halfway between the fourth cylinder and the following half-cylinders (as indicated in Fig. 1). Every third data point is shown. Symbols as in Fig. 8.

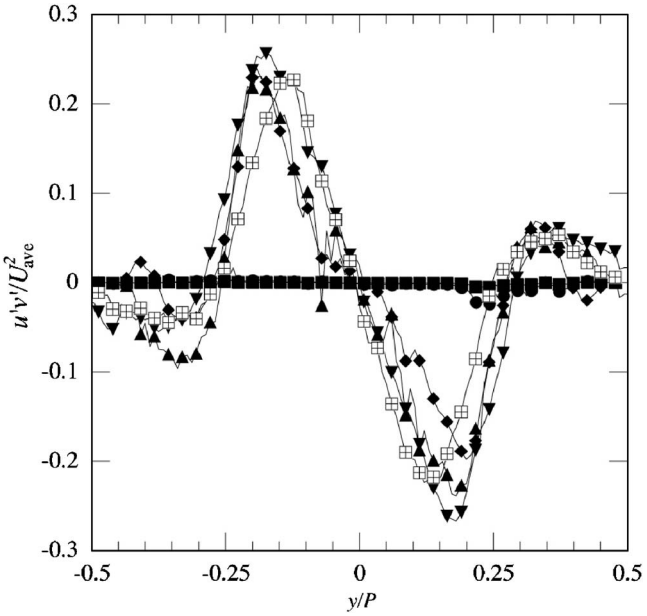

Fig. 12 Cross-stream profiles of the Reynolds shear stress $\overline{u'v'}/U_{av}^2$ halfway between the fourth cylinder and the next half-cylinders (as indicated in Fig. 1). Every third data point is shown. Symbols as in Fig. 8.

Therefore, L_c is determined for the center cylinder using a combination of the wide-angle and high-resolution data. The distance from the base of the cylinder to the separation point is determined from the high-resolution data (the missing Reynolds number values are interpolated based on a smooth fit of the data shown later in Fig. 25) and is added to the wake length to get the recirculation length. These data are shown in Fig. 14 along with data from other studies for cylinder arrays and single cylinders. At very low Reynolds numbers, the recirculation region length increases before reaching a maximum at about Re=400. The recirculation region shrinks with increasing Reynolds number beyond this value. It is interesting to note that the wake lengths for the wall cylinders tend to be larger than that of the center cylinder, and that the difference becomes larger with Reynolds number. The numerical data of Moulinec et al. [30] for an array of equally spaced staggered cylinders with spacings $P/D=2$ and 3 lie below and above

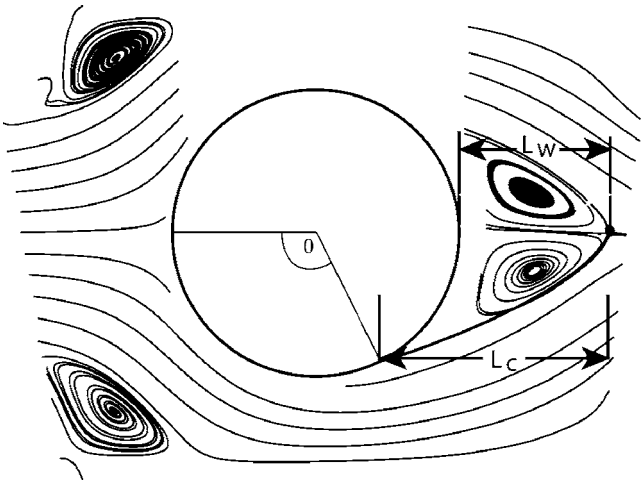

Fig. 13 Definition of the separation angle θ, wake length L_w, and recirculation length L_c. Streamlines are for flow at Re =237.

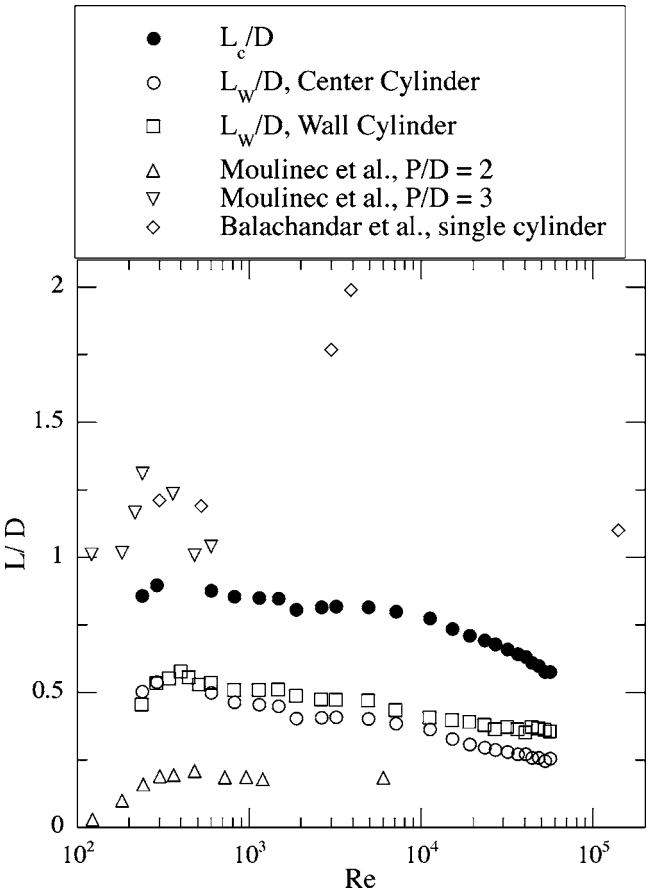

Fig. 14 Measures of the wake length relative to the diameter as a function of Reynolds number for the centerline cylinder and for the half-cylinder on the lower wall. Data from Moulinec et al. [30] and Balachandar et al. [37] are also shown for reference.

the present data, respectively. These data show no decrease in the recirculation length with Reynolds number. One cannot make a direct comparison here, since these data are for cylinders arranged in a square array rather than equilateral triangles as in the present case. These authors found the extent of the wake to be a strong function of the cylinder spacing in this range, with the wakes essentially disappearing for smaller P/D values. Data from Balachandar et al. [37] for a single cylinder are also shown. The recirculation lengths are similar to the P/D cylinder array from Ref. [30], and like the present case, the recirculation length grows before becoming smaller at larger Reynolds numbers. For the single cylinder, the maximum occurs at a larger Re value than for the arrays.

6 High-Resolution Results

Since it is not possible to examine the cylinder boundary layer in the initial set of data, a second data set was acquired at much higher resolution. Since the camera was not centered on the cylinder for these data, the surface of the cylinder is visible to the camera. For several values of Reynolds number, three fields of view were acquired, as shown in Fig. 15. These three views were chosen to ensure that the boundary layer could be examined from the stagnation point to the separation point. The spatial resolution of these data (i.e., the size of the final interrogation region) is 0.185 mm or $0.00365D$.

Examination of the instantaneous vector fields reveals what initially appears to be very distinct differences between the boundary layers for Re=2621 and 15,075. Vector fields from the middle and

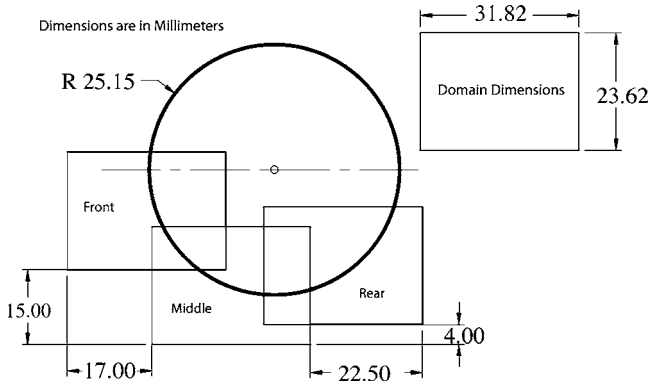

Fig. 15 The high-resolution data domains. The dimensions of each field of view are shown at top right. Three fields of view were acquired at each Reynolds number.

rear views for these two Reynolds number values are shown in Figs. 16 and 17. While the external flow fields are turbulent in both cases (with smaller eddies present in the higher Reynolds number case), the boundary layer is clearly laminar at Re=2621. This claim is based on the fact that the boundary layer is thick and steady (one must view several instances to appreciate the steadiness or lack thereof. Animations are available on the EFDL website [36]). The separated flow rolls into eddies that are easily resolved by the PIV system. At Re=15,075, the much thinner boundary layer separates from the cylinder. Very small eddies are present near the surface but not in the boundary layer. As shown below, the time-averaged separation point is nearly unchanged.

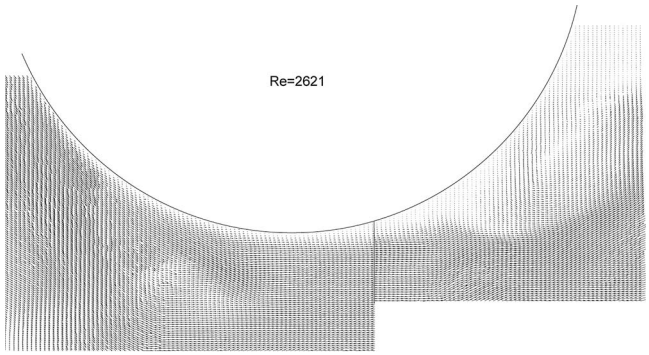

Fig. 16 Example of instantaneous vector field for Re=2621. We note that the plot is a composite of two different fields of view that were acquired at different times.

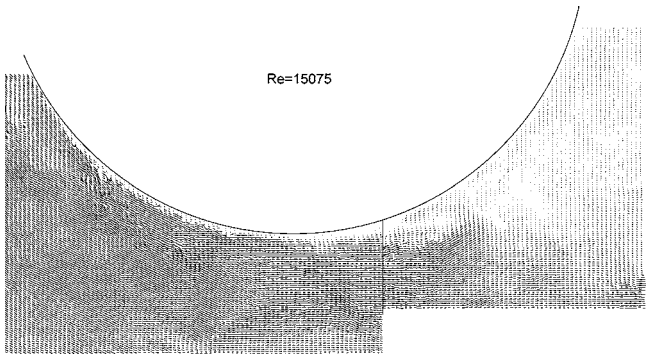

Fig. 17 Instantaneous vector field for Re=15,075. We note that the plot is a composite of two different fields of view that were acquired at different times.

Composites of the velocity fields and normalized statistics of the three views are shown in Figs. 18–23. As Re is increased, the flow velocity magnitude becomes more uniform (as evidenced by fewer magnitude contour levels). The magnitude behind the cylinder also increases steadily with Re. The Reynolds shear stress at Re=237 is very low (and is thus plotted at a smaller increment). The levels of all of the Reynolds stresses increase rapidly with Reynolds number. At Re=507, which is considered to be laminar but unsteady, the Reynolds stresses appear much larger. This is due to the oscillating flapping motion of this case and does not represent turbulence. Normal fluctuations (u_{rms} and v_{rms}) are very small for the lowest Re case and increase steadily with Re, especially in the wake of the cylinder where levels reach 60% of the mean velocity. At Re=237, there are significant streamwise fluctuations (20%) while the cross-stream fluctuations remain very small. We interpret this as a "surging" of flow along one side of the cylinder at the expense of the other. The unsteady laminar case (Re=507) has more than double this fluctuation level. The fluctuations in the boundary layer on the rear of the cylinder also increase significantly as Re increases from 2621 to 15,075. This may indicate transition of the boundary layer from laminar to turbulent on the rear of the cylinder or simply an increase in the large-scale fluctuations.

The y profiles of the U component of velocity at $\theta=90$ deg (which are identical to r profiles of the U_θ component) are shown in Fig. 24. Although the profiles appear to form two distinct groups, above and below Re=3000, we believe that this is simply a Reynolds number effect. Recasting these same data in wall coordinates (not shown) reveals that none of these profiles exhibit a log layer. We therefore conclude that in all cases, the boundary layer remains laminar at least up to 90 deg.

From these same velocity fields, the time-averaged separation point was found and is shown in Fig. 25. It is very interesting to note that unlike flow over a single cylinder, the separation never occurs on the front of the cylinder. The separation angle decreases with increasing Reynolds number and reaches a minimum near Re=15,000. For larger Reynolds number, the separation angle increases rapidly with Reynolds number. This may indicate that boundary layer transition is occurring and moving forward on the cylinder as Reynolds number increases.

7 Concluding Remarks

The present experiment was undertaken primarily to determine the variation of flow regime versus Reynolds number for a confined row of short cylinders simulating some aspects of flows in the lower plenum of a typical GCR design and to examine whether useful guidance is provided by existing data for large arrays of long circular cylinders. Streamwise central cylinders and wall-mounted half-cylinders formed an equilateral triangular pattern with P/D about 1.7 and H/D about 7. Reynolds numbers, based on minimum flow area and cylinder diameter, ranged from about 240 to 56,000. Measurements included pressure drop per row and PIV data for instantaneous and mean velocity fields plus related mean statistics. For the third cylinder and beyond, the flow was approximately streamwise periodic. The PIV fields were obtained away from the side-walls in the central region where the flow was essentially two dimensional in the mean. The loss coefficients are somewhat below the graphical correlations of Žukauskas' [5] for Reynolds numbers between 3000 and 56,000.

The detailed PIV results permitted categorizing the flow into five regimes in contrast to the three suggested by Žukauskas' [5]. These regimes are as follows:

1. steady laminar flow (Re$<$398)
2. unsteady laminar flow (444$<$Re$<$507)
3. mixed, partially turbulent flow (597$<$Re$<$1858)
4. mixed turbulent flow (Re$>$2621)
5. turbulent flow (none of the present cases are conclusively in this regime)

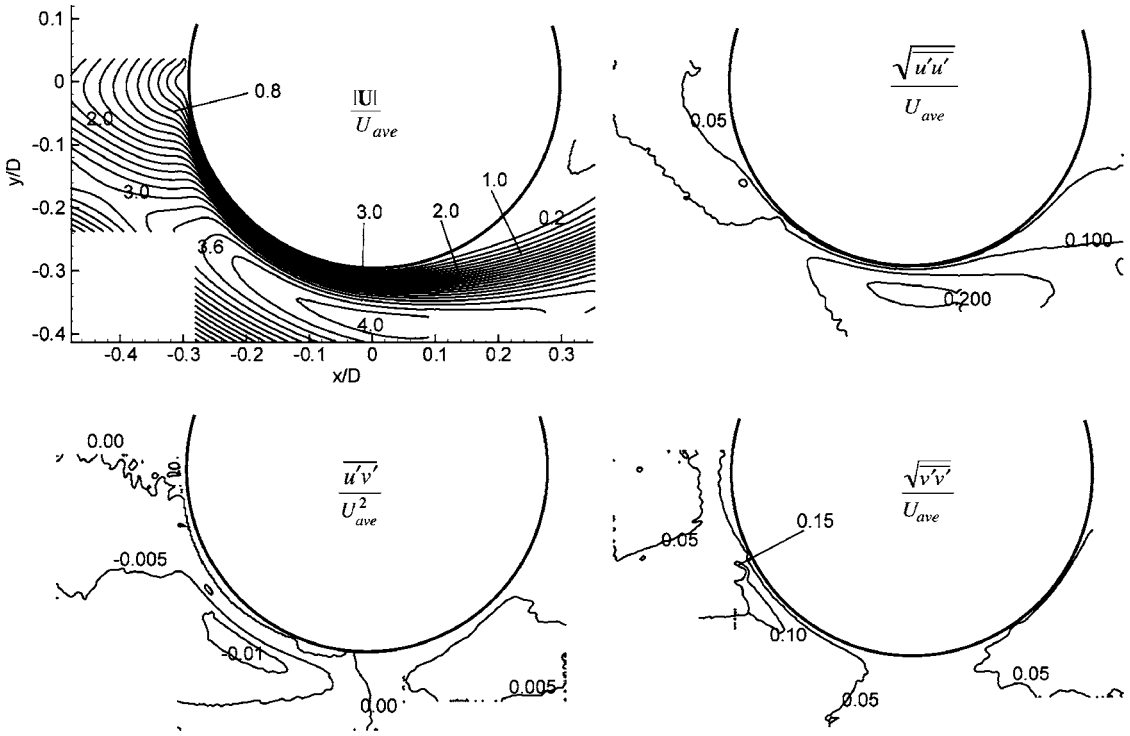

Fig. 18 The time-averaged contours of velocity magnitude (top left, increment is 0.2), Reynolds shear stress $\overline{u'v'}/U_{ave}^2$ (bottom left, increment is 0.005), relative streamwise rms level u_{rms}/U_{ave} (top right, increment is 0.05) and relative cross-stream rms level v_{rms}/U_{av} (bottom right, increment is 0.05) for Re=237.

These regimes were related to the Reynolds numbers of the present experimental runs but further measurements—beyond the present scope—would be desirable to define some boundaries more exactly. In particular, the transition from the mixed turbulent regime to the "fully" turbulent regime could be better defined if more data were available.

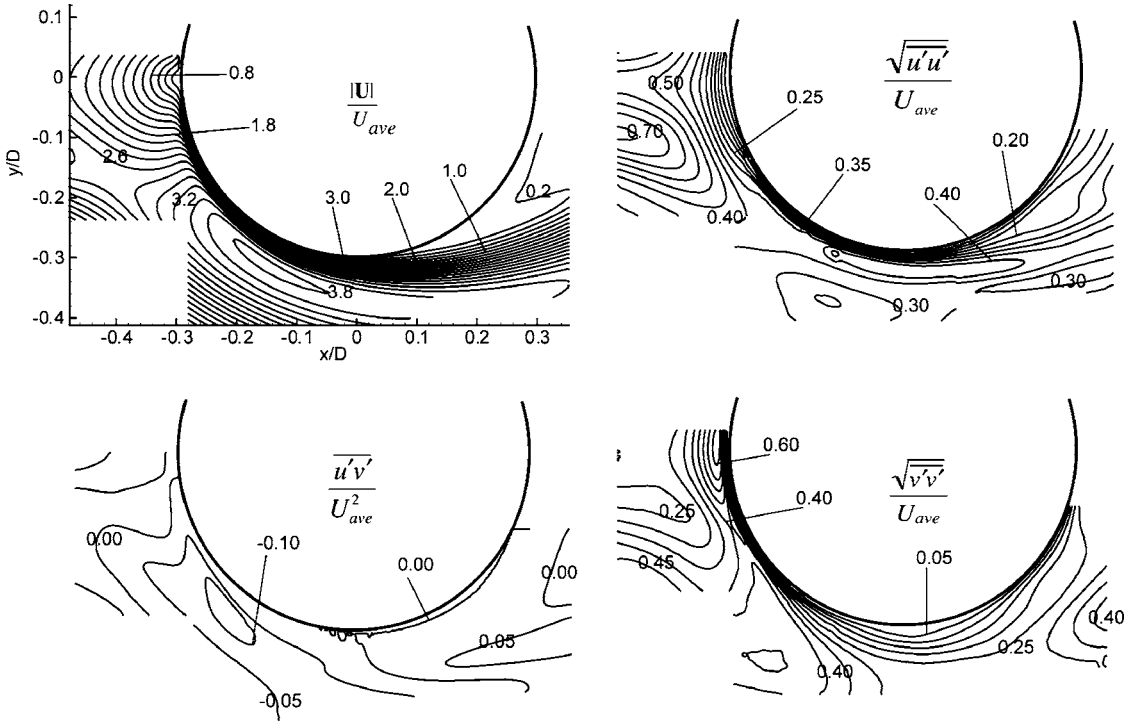

Fig. 19 The time-averaged contours of velocity magnitude (top left, increment is 0.2), Reynolds shear stress $\overline{u'v'}/U_{ave}^2$ (bottom left, increment is 0.05), relative streamwise rms level u_{rms}/U_{ave} (top right, increment is 0.05), and relative cross-stream rms level v_{rms}/U_{av} (bottom right, increment is 0.05) for Re=507.

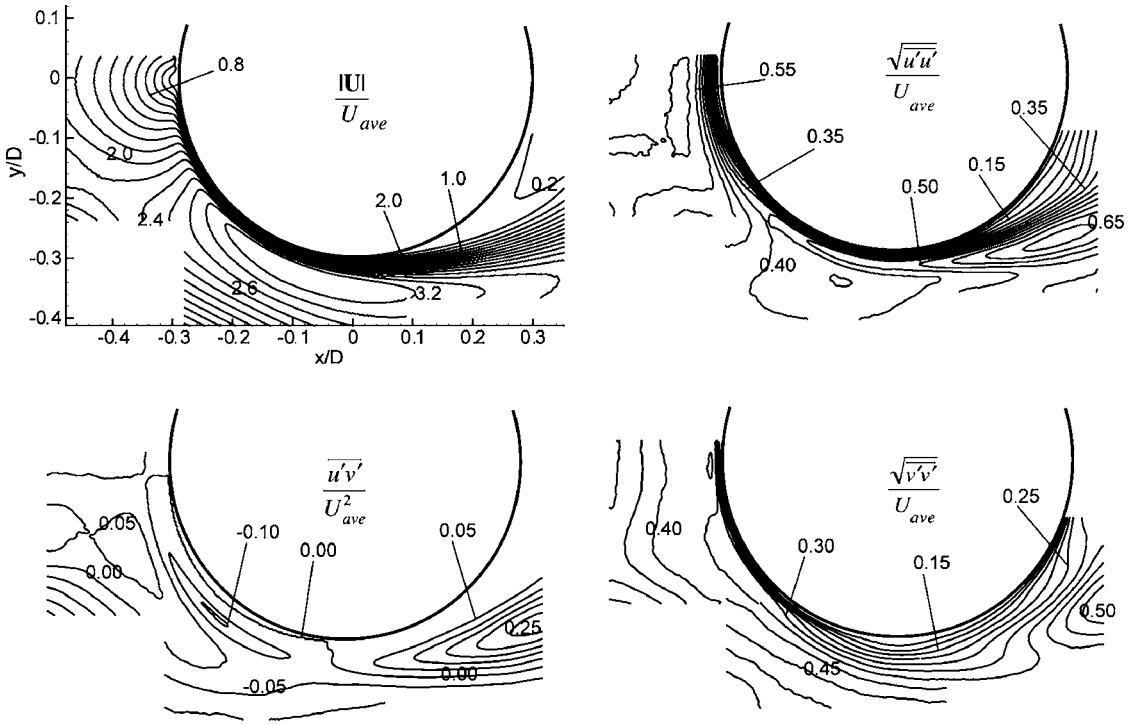

Fig. 20 The time-averaged contours of velocity magnitude (top left, increment is 0.2), Reynolds shear stress $\overline{u'v'}/U_{ave}^2$ (bottom left, increment is 0.05), relative streamwise rms level u_{rms}/U_{ave} (top right, increment is 0.05) and relative cross-stream rms level v_{rms}/U_{ave} (bottom right, increment is 0.05) for Re=1135

In addition to determination of the overall fields for the streamwise-periodic flow, PIV data from "high-resolution" views provide details of the boundary layer development around the central cylinder and, therefore, should serve as excellent benchmark data for the assessment of computer codes proposed for application to the lower plenums of gas-cooled nuclear reactors. For Reynolds numbers as high as 56,000, on the front face of the cylinder the apparent boundary layer thickness (defined as the distance to

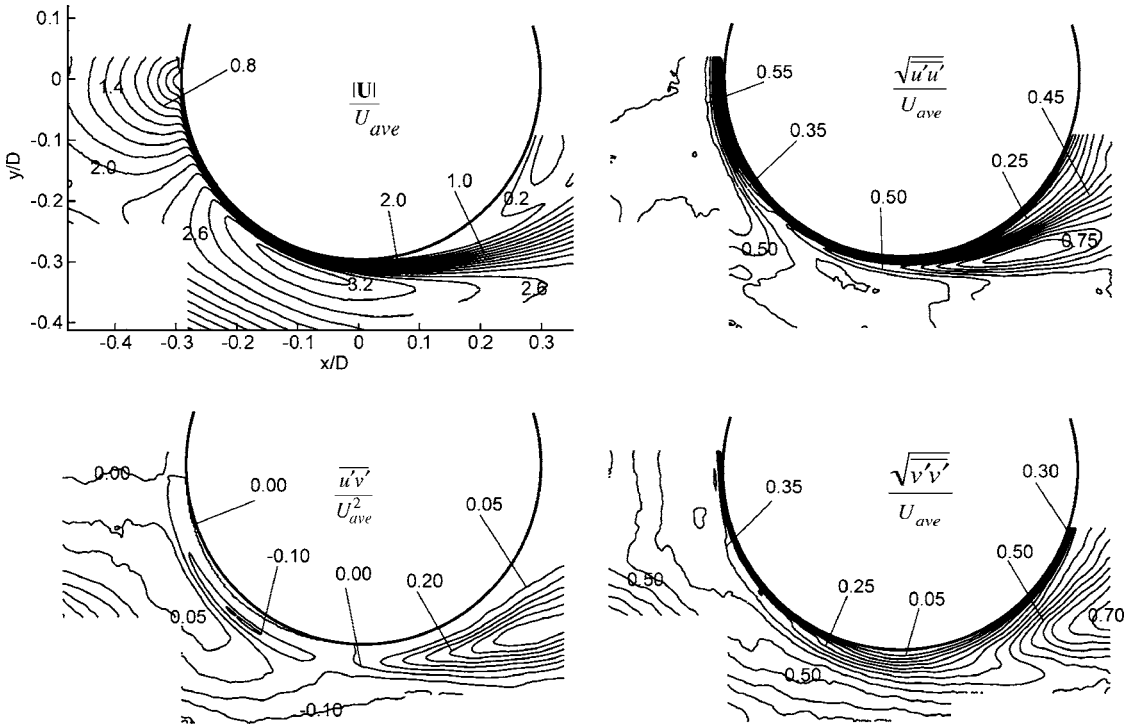

Fig. 21 The time-averaged contours of velocity magnitude (top left, increment is 0.2), Reynolds shear stress $\overline{u'v'}/U_{ave}^2$ (bottom left, increment is 0.05), relative streamwise rms level u_{rms}/U_{ave} (top right, increment is 0.05) and relative cross-stream rms level v_{rms}/U_{ave} (bottom right, increment is 0.05) for Re=2621.

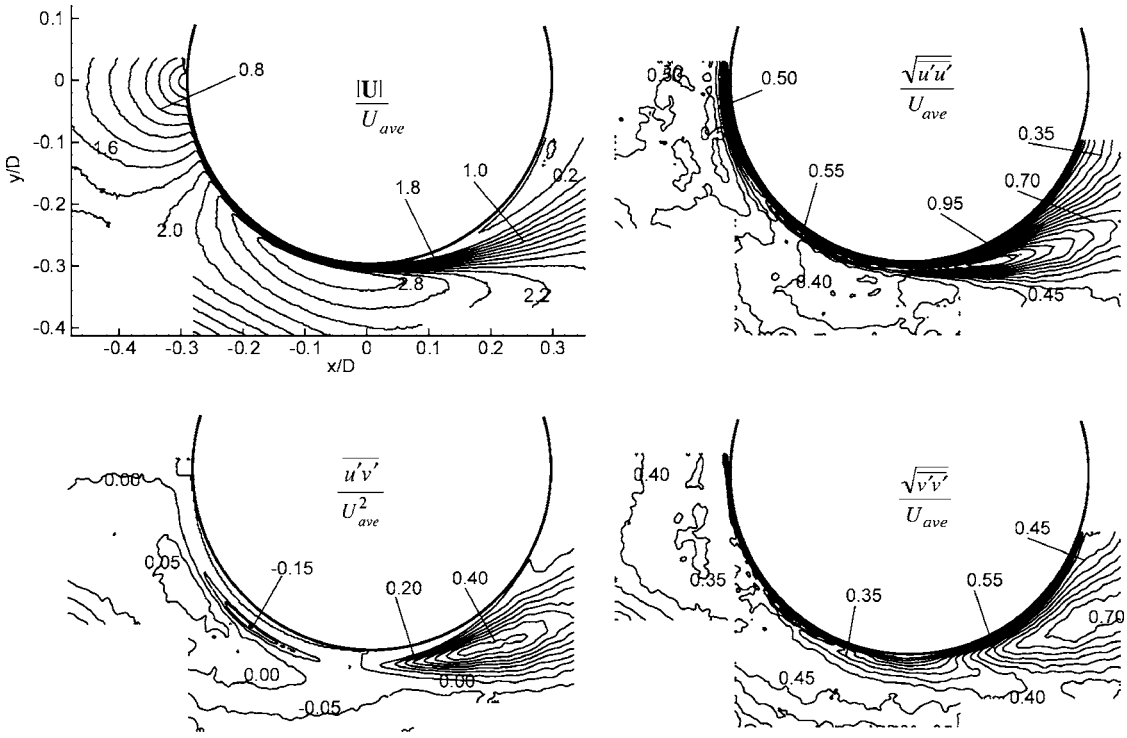

Fig. 22 The time-averaged contours of velocity magnitude (top left, increment is 0.2), Reynolds shear stress $\overline{u'v'}/U_{ave}^2$ (bottom left, increment is 0.05), relative streamwise rms level u_{rms}/U_{ave} (top right, increment is 0.05), and relative cross-stream rms level v_{rms}/U_{ave} (bottom right, increment is 0.05) for Re=15,075

the maximum velocity) is the order of 30 or less in wall coordinates, so the use of wall functions in the turbulence model would be inappropriate. Code users should be further cautioned that the PIV software does not discriminate between periodic fluctuations and turbulence when calculating mean statistics; therefore, the root-mean-square quantities reported differ in definition from

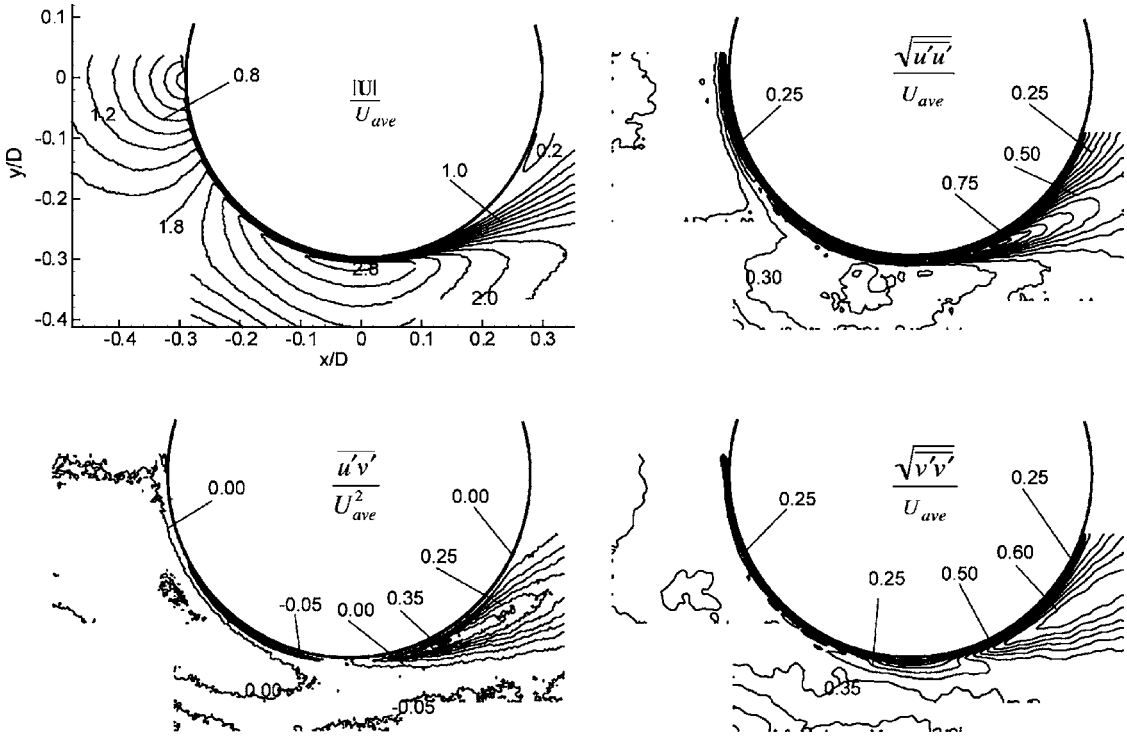

Fig. 23 The time-averaged contours of velocity magnitude (top left, increment is 0.2), Reynolds shear stress $\overline{u'v'}/U_{ave}^2$ (bottom left, increment is 0.05), relative streamwise rms level u_{rms}/U_{ave} (top right, increment is 0.05), and relative cross-stream rms level v_{rms}/U_{ave} (bottom right, increment is 0.05) for Re=55,920

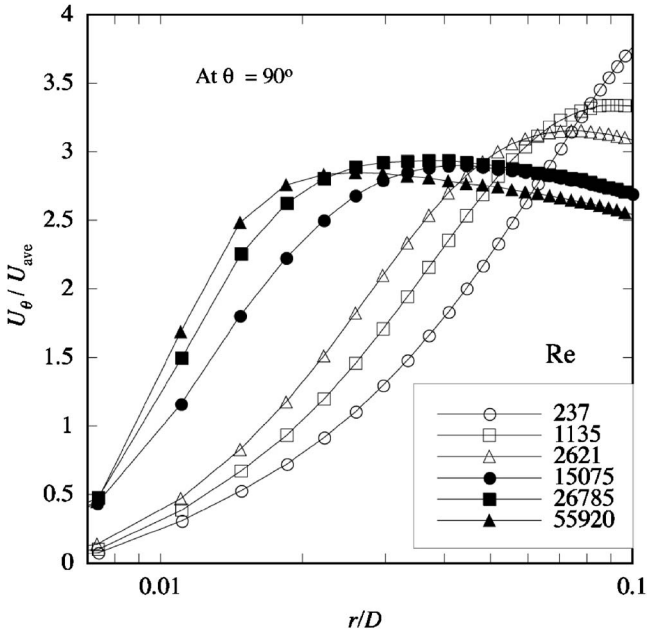

Fig. 24 Radial profiles of U_θ at θ=90 deg for several values of Re above (closed symbols) and below (open symbols) the apparent boundary layer transition to turbulence

those employed in computer turbulence models. We recommend using LESs (or at least unsteady Reynolds-averaged Navier-Stokes (RANS) codes) when attempting to predict these measurements.

Acknowledgment

This work was partly supported by the U.S. Department of Energy, Office of Nuclear Energy, Science and Technology (NE), under Award No. DE-FC07-05ID14670, and DoE-NE Idaho Operations Office Contract No. DE-AC07-05ID14517. The authors would also like to acknowledge the students who built the experiment, acquired, and processed the data: Jake Keller, Matthew Bettridge, and Eric Thorson.

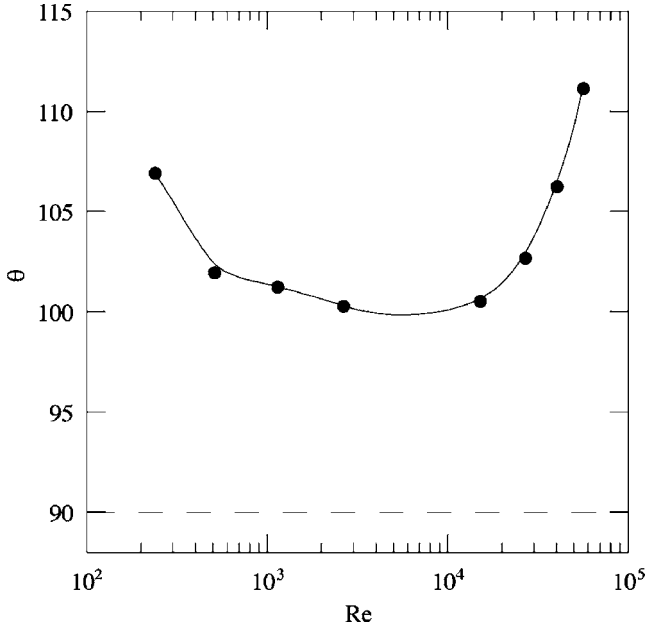

Fig. 25 The angle at which the time-averaged boundary layer separates. The fitted curve is used to provide separation points for wide-angle cases.

References

[1] Schultz, R. R., 2006, "Workshop on Computational Tools for Advanced Reactors," *ASME Fluids Engineering Division Meeting*.
[2] Schultz, R. R., McIlroy, H. M., McCreery, G. E., Johnson, R. W., and McEligot, D. M., 2006, "Specifying Standard Problems for Validating Advanced Reactor Computational Fluid Dynamics Analysis Tools," *ANS Winter Meeting*, Nov.
[3] Stoots, C., Becker, S., Condie, K., Durst, F., and McEligot, D., 2001, "A Large-Scale Matched Index of Refraction Flow Facility for LDA Studies Around Complex Geometries," Exp. Fluids, **30**(4), pp. 391–398.
[4] Condie, K. G., McCreery, G. E., McIlroy, H. M., and McEligot, D. M., 2005, "Development of an Experiment for Measuring Flow Phenomena Occurring in a Lower Plenum for VHTR CFD Assessment," INL, Technical Report No. INL/EXT-05-00603.
[5] Žukauskas, A., 1975, "Heat Transfer From Tubes in Crossflow," Adv. Heat Transfer, **8**, pp. 93–160.
[6] Schultz, R. R., Ball, S. J., and King, J., 2004, "Catalogue of Validation Data for Gas-Cooled Reactor Operational and Accident Scenarios," INEEL, Technical Report No. INEEL/EXT-04-02294.
[7] Zhang, H. Q., Fey, U., Noack, B. R., Konig, M., and Eckelmann, H., 1995, "On the Transition of the Cylinder Wake," Phys. Fluids, **7**(4), pp. 779–794.
[8] Kim, W., Sung, J., Yoo, J. Y., and Lee, M. H., 2004, "High-Definition PIV Analysis on Vortex Shedding in the Cylinder Wake," J. Visualization, **7**(1), pp. 17–24.
[9] Wang, Z. J., and Zhou, Y., 2005, "Vortex Interactions in a Two Side-By-Side Cylinder Near-Wake," Int. J. Heat Fluid Flow, **26**(3), pp. 362–377.
[10] Chilton, T. H., and Genereaux, R. P., 1933, "Pressure Drop Across Tube Banks," , **29**, pp. 161–173.
[11] Grimison, E. D., 1937, "Correlation and Utilization of New Data on Flow Resistance and Heat Transfer for Cross Flow of Gases Over Tube Banks," Trans. ASME, **59**, pp. 583–594.
[12] Bergelin, O. P., Brown, G. A., and Doberstein, S. C., 1952, "Heat Transfer and Fluid Friction During Flow Across Banks of Tubes IV: A Study of the Transition Zone Between Viscous and Turbulent Flow," Trans. ASME, **74**, pp. 953–960.
[13] Kays, W. M., and London, A. L., 1964, *Compact Heat Exchangers*, McGraw-Hill, New York.
[14] Achenbach, E., 1989, "Heat-Transfer From a Staggered Tube Bundle in Cross-Flow at High Reynolds-Numbers," Int. J. Heat Mass Transfer, **32**(2), pp. 271–280.
[15] Velichko, V. I., Pronin, V. A., and Yassin, N., 1993, "Heat Transfer, Hydrodynamics and Energy Efficiency in Closely Packed Tube Bundles in Cross Flow," Heat Transfer Research, **25**, pp. 629–633.
[16] Poskas, P. S., and Survila, V. J., 1983, "Fluctuations of Velocity of Cross Flow of Air in the Space Between Tubes in Bundles," Heat Transfer-Sov. Res., **15**(1), pp. 75–86.
[17] Katinas, V. I., Bakas, R. V., Perednis, E. E., and Svedoscius, V. A., 1990, "Effect of Turbulence of the Incident Flow on Flow-Induced Vibrations of Tube Bundles Operating in Crossflow," Fluid Mech.-Sov. Res., **19**(5), pp. 9–17.
[18] Scholten, J. W., and Murray, D. B., 1998, "Heat Transfer and Velocity Fluctuations in a Staggered Tube Array," Int. J. Heat Fluid Flow, **19**(3), pp. 233–244.
[19] Iwaki, C., Cheong, K. H., Monji, H., and Matsui, G., 2004, "PIV Measurement of the Vertical Cross-Flow Structure Over Tube Bundles," Exp. Fluids, **37**(3), pp. 350–363.
[20] Stanescu, G., Fowler, A., and Bejan, A. J., 1996, "The Optimal Spacing of Cylinders in Free-Stream Cross-Flow Forced Convection," Int. J. Heat Mass Transfer, **39**(2), pp. 311–317.
[21] Beale, S. B., and Spalding, D. B., 1998, "Numerical Study of Fluid Flow and Heat Transfer in Tube Banks With Streamwise-Periodic Boundary Conditions," Trans. Can. Soc. Mech. Eng., **22**, pp. 397–416.
[22] Watterson, J. K., Dawes, W. N., Savill, A. M., and White, A. J., 1999, "Predicting Turbulent Flow in a Staggered Tube Bundle," Int. J. Heat Fluid Flow, **20**(6), pp. 581–591.
[23] Wilson, M. K., and Bassiouny, A. S., 2000, "Modeling of Heat Transfer for Flow Across Tube Banks," Chem. Eng. Process., **39**(1), pp. 1–14.
[24] Benhamadouche, S., Laurence, D., Jarrin, N., Afgan, I., and Moulinec, C., 2005, "Large Eddy Simulation of Flow Across In-Line Tube Bundles," *11th International Topical Meeting on Nuclear Reactor Thermal Hydraulics*, Avignon, France, Paper No. 405.
[25] Perkins, H. C., and Leppert, G., 1964, "Local Heat-Transfer Coefficients on a Uniformly Heated Cylinder," Int. J. Heat Mass Transfer, **7**(2), pp. 143–158.
[26] Žukauskas, A., Daujotas, P. M., and Ilgarubis, V. S., 1982, "Effect of Flow Turbulence and Channel Blockage on the Flow Pattern Over a Cylinder in Crossflow of Water at Critical Re," Fluid Mech.-Sov. Res., **11**, pp. 38–47.
[27] Ames, F. E., Dvorak, L. A., and Morrow, M. J., 2005, "Turbulent Augmentation of Internal Convection Over Pins in Staggered-Pin Fin Arrays," ASME J. Turbomach., **127**(1), pp. 183–190.

[28] Armstrong, J., and Winstanley, D., 1988, "A Review of Staggered Array Pin Fin Heat-Transfer for Turbine Cooling Applications," ASME J. Turbomach., **110**(1), pp. 94–103.
[29] Ames, F. E., and Dvorak, L. A., 2006, "Turbulent Transport in Pin Fin Arrays: Experimental Data and Predictions," ASME J. Turbomach., **128**(1), pp. 71–81.
[30] Moulinec, C., Hunt, J. C. R., and Nieuwstadt, F. T. M., 2004, "Disappearing Wakes and Dispersion in Numerically Simulated Flows Through Tube Bundles," Flow, Turbul. Combust., **73**, pp. 95–116.
[31] Westerweel, J., 1997, "Fundamentals of Digital Particle Image Velocimetry," Meas. Sci. Technol., **8**, pp. 1379–1392.
[32] Westerweel, J., 2000, "Theoretical Analysis of the Measurement Precision in Particle Image Velocimetry," Exp. Fluids, **29**, pp. S3–S12.
[33] Raffel, M., Willert, C., and Kompenhans, J., 1998, *Particle Image Velocimetry*, Springer-Verlag, Berlin.
[34] Beckwith, T. G., Marangoni, R. D., and Lienhard, J. H., 1993, *Mechanical Measurements*, 5th ed., Addison-Wesley, Reading, MA.
[35] Fried, E., and Idelchik, I. E., 1989, *Flow Resistance: A Design Guide for Engineers*, Hemisphere, New York.
[36] Smith, B. L., 2007, "Experimental Fluid Dynamics Laboratory Website," http://www.efdl.usu.edu
[37] Balachandar, S., Mittal, R., and Najjar, F. M., 1997, "Properties of the Mean Recirculation Region in the Wakes of Two-Dimensional Bluff Bodies," J. Fluid Mech., **351**, pp. 167–199.

On the Use of High-Order Accurate Solutions of PNS Schemes as Basic Flows for Stability Analysis of Hypersonic Axisymmetric Flows

Kazem Hejranfar
Assistant Professor
Aerospace Engineering Department,
Sharif University of Technology,
11365-8639, Tehran, Iran
e-mail: khejran@sharif.edu

Vahid Esfahanian
Professor
e-mail: evahid@ut.ac.ir

Hossein Mahmoodi Darian
Ph.D. Candidate

Mechanical Engineering Department,
University of Tehran,
11365-4563, Tehran, Iran
e-mail: hmahmoodi@ut.ac.ir

High-order accurate solutions of parabolized Navier–Stokes (PNS) schemes are used as basic flow models for stability analysis of hypersonic axisymmetric flows over blunt and sharp cones at Mach 8. Both the PNS and the globally iterated PNS (IPNS) schemes are utilized. The IPNS scheme can provide the basic flow field and stability results comparable with those of the thin-layer Navier–Stokes (TLNS) scheme. As a result, using the fourth-order compact IPNS scheme, a high-order accurate basic flow model suitable for stability analysis and transition prediction can be efficiently provided. The numerical solution of the PNS equations is based on an implicit algorithm with a shock fitting procedure in which the basic flow variables and their first and second derivatives required for the stability calculations are automatically obtained with the fourth-order accuracy. In addition, consistent with the solution of the basic flow, a fourth-order compact finite-difference scheme, which does not need higher derivatives of the basic flow, is efficiently implemented to solve the parallel-flow linear stability equations in intrinsic orthogonal coordinates. A sensitivity analysis is also conducted to evaluate the effects of numerical dissipation and grid size and also accuracy of computing the basic flow derivatives on the stability results. The present results demonstrate the efficiency and accuracy of using high-order compact solutions of the PNS schemes as basic flow models for stability and transition prediction in hypersonic flows. Moreover, indications are that high-order compact methods used for basic-flow computations are sensitive to the grid size and especially the numerical dissipation terms, and therefore, more careful attention must be kept to obtain an accurate solution of the stability and transition results. [DOI: 10.1115/1.2776962]

1 Introduction

The prediction of stability and transition of hypersonic flows over blunt bodies is of great importance for the accurate determinations of aerodynamic loads and heating rates for high-speed vehicles. The stability analysis of the flow over blunt slender bodies at high Mach numbers faces three major problems: (1) the computation of the basic flow field and the derivatives of the flow variables with sufficient accuracy, (2) the formulation of the stability problem with proper account for the flow physics, and (3) the accurate solution of the stability equations. Many theoretical efforts have been put to solve these difficulties and improve the results of stability and transition in hypersonic flows over blunt bodies [1–7]. There are two main aspects of the current work: use of high-order accurate solutions of parabolized Navier–Stokes (PNS) schemes as basic-flow models for the stability analysis and transition prediction of hypersonic laminar flows and efficient implementation of a fourth-order compact finite-difference scheme for the solution of stability equations.

An appropriate scheme for efficient computation and stability analysis of high-speed flows over slender-body geometries is to use the PNS equations [6,7]. The PNS equations are paraboliclike with respect to the streamwise direction, hence the PNS schemes can realize appreciable decreases in both computational time and memory requirements relative to Navier–Stokes (NS) or thin-layer NS (TLNS) solutions. The study has been shown that the stability results are very sensitive to the grid size, and therefore, the accuracy of numerical methods used for basic-flow computations [6,7]. Up to now, all the basic-flow models required for the stability analysis and transition prediction of hypersonic axisymmetric flows are based on usual finite-difference or finite-volume methods [1–7]. The main objective of the present work is to use high-order accurate solutions of the PNS schemes [8–11] as efficient basic-flow models for stability and transition prediction of hypersonic axisymmetric flows over blunt and sharp slender bodies and identifying sensitivities that should be considered if adequate stability and transition results are to be obtained.

An accurate numerical method for the computation of the stability equations is the fourth-order compact Euler–Maclaurin scheme [12,13]. The fourth-order Euler–Maclaurin method has smaller truncation error than the fourth-order compact Hermitian formula. However, in applying the Euler–Maclaurin scheme, due to the differentiation of the governing equations, the higher derivatives of the basic-flow variables are required. It was found that in general the higher derivatives obtained from the basic flow for the stability analysis of hypersonic flow are less accurate [6,7]. In the present study, consistent with the solution of the basic flow, the fourth-order Hermitian formula, which does not need the higher derivatives of the basic-flow profiles, is efficiently implemented for the solution of the parallel-flow linear stability equations in the intrinsic orthogonal curvilinear coordinates.

To demonstrate the accuracy and efficiency of using high-order compact solutions of the PNS schemes for use as basic flows, the stability analysis is performed for hypersonic laminar flow over

Contributed by the Fluids Engineering Division of ASME for publication in the JOURNAL OF FLUIDS ENGINEERING. Manuscript received February 20, 2006; final manuscript received May 15, 2007. Review conducted by Subrata Roy.

blunt and sharp cones at Mach 8 for the conditions of the experiment of Stetson et al. [14,15] (the Stetson–Thompson–Donaldson–Siler (STDS) blunt- and sharp-cone cases). Both the PNS and the globally iterated PNS (IPNS) schemes are used. The IPNS scheme employs the full pressure gradient term in the subsonic region of the boundary layer and it can provide the basic-flow field and stability results comparable with those of the TLNS scheme [6,7]. As a result, using the fourth-order compact IPNS scheme, a high-order accurate basic-flow model suitable for stability analysis and transition prediction of hypersonic axisymmetric flows can be efficiently provided. The numerical solution of the PNS equations is based on an implicit algorithm with a shock fitting procedure, similar to the Beam and Warming method [6,7,16], in which the basic-flow variables and their first and second derivatives required for the stability calculations are automatically obtained with the fourth-order accuracy [8–11]. The stability and transition results using high-order accurate basic flows based on the PNS and IPNS schemes are compared with those of the second-order solutions. A sensitivity analysis is also performed to study the effects of grid size and numerical dissipation used and also accuracy of computing the basic-flow derivatives on the stability results. In addition, the transition results for the STDS blunt-cone case are discussed.

2 Benchmark Cases

The most available theoretical stability results of hypersonic axisymmetric flows [1–7,17] have been performed for the conditions of the experiment of Stetson et al. [14,15]. Therefore, the geometry and the freestream conditions are adapted to these wind-tunnel cone experiments. Here, both sharp and blunt cones are considered. For the STDS blunt-cone case, the flow conditions are a freestream Mach number of $M_\infty=8$, a freestream unit Reynolds number of $Re_\infty/m=8.2021\times10^6$, and a freestream temperature of $T_\infty^*=54.3$ K. For the STDS sharp-cone case, the freestream Mach number is set to $M_\infty=8$, the freestream unit Reynolds number to $Re_\infty/m=3.2808\times10^6$, and the freestream temperature to $T_\infty^*=52.75$ K. Both sharp and blunt cones have a half-angle of $\theta_c=7$ deg, and the study is performed at zero angle of attack. The blunt cone has a spherical nose radius of $R_N=3.81$ mm, and the freestream Reynolds number based on this length is $Re_\infty=31{,}250$. The maximum arc length along the body of the sharp cone is set to be $S_{\max}^*=1.9888$ m, which corresponds to the freestream Reynolds number of $Re_\infty=6.525\times10^6$.

3 Basic-Flow Models

3.1 Parabolized Navier–Stokes Equations. The PNS equations are obtained by dropping the unsteady term in the TLNS equations and modifying the streamwise pressure gradient in the streamwise momentum equation to permit stable marching. The PNS equations for axisymmetric compressible flow can be written in dimensionless and conservation form in the generalized coordinate system (ξ,η) as follows:

$$\frac{\partial\bar{F}}{\partial\xi}+\frac{\partial\bar{G}}{\partial\eta}+\bar{H}=0$$

$$\bar{F}=\bar{F}_i \quad \bar{G}=\bar{G}_i-\bar{G}_v \quad \bar{H}=\bar{H}_i-\bar{H}_v \tag{1}$$

where the solution vector is

$$\bar{U}=J^{-1}\tilde{U}=J^{-1}[\rho,\rho u,\rho v,E]^T$$

The PNS equations are a mixed set of hyperbolic-parabolic equations in the marching direction, provided that the inviscid flow is supersonic, the streamwise velocity component is everywhere positive, and the streamwise pressure gradient term is either dropped in the subsonic region or the "departure behavior" is suppressed using a suitable technique [18–20]. For this study, the technique of Vigneron et al. [19] is implemented to prevent departure solutions.

In the approximation of Vigneron et al., the streamwise pressure gradient in the momentum equations is split into an implicit contribution and an explicit contribution

$$\frac{\partial p}{\partial\xi}=\left[\bar{\omega}\frac{\partial p}{\partial\xi}\right]_{\text{implicit}}+\left[(1-\bar{\omega})\frac{\partial p}{\partial\xi}\right]_{\text{explicit}} \tag{2}$$

The weighting function $\bar{\omega}$ is determined as

$$\bar{\omega}=\min\left[1,\frac{\sigma\gamma M_\xi^2}{1+(\gamma-1)M_\xi^2}\right] \tag{3}$$

where M_ξ is the local streamwise Mach number and σ is a safety factor to account for nonlinearities in the analysis. To introduce the technique of Vigneron et al. into the PNS equations, a new vector $\bar{F}^*$ is defined as

$$\bar{F}^*=\bar{F}-P \tag{4}$$

Thus, the new form of the PNS equations appears as

$$\frac{\partial\bar{F}^*}{\partial\xi}+\frac{\partial P}{\partial\xi}+\frac{\partial\bar{G}}{\partial\eta}+\bar{H}=0 \tag{5}$$

where the inviscid vectors $\bar{F}^*$ and P are

$$\bar{F}^*=J^{-1}\begin{bmatrix}\rho U_c\\ \rho u U_c+\bar{\omega}\xi_x p\\ \rho v U_c+\bar{\omega}\xi_y p\\ (E+p)U_c\end{bmatrix} \quad P=J^{-1}\begin{bmatrix}0\\ \xi_x(1-\bar{\omega})p\\ \xi_y(1-\bar{\omega})p\\ 0\end{bmatrix}$$

In this study, the ratio of specific heats is assumed constant, $\gamma=1.4$, the molecular viscosity μ is determined by the Sutherland law, and the coefficient of thermal conductivity is calculated by assuming a constant Prandtl number, $Pr=0.72$. Finally, the system of PNS equations is closed by employing the perfect-gas equations of state. The preceding equations have been nondimensionalized using the reference length L (R_N or $S_{\max}^*$) and freestream conditions.

In the present PNS solver, the "elliptic" part of the streamwise pressure gradient term $(\partial P/\partial\xi)$ responsible for upstream disturbance propagation is omitted to permit the space-marching procedure to be stable.

3.2 Iterative Parabolized Navier–Stokes Equations. For the computation and stability analysis of hypersonic axisymmetric flow fields, the dropping of the explicit part of the streamwise pressure gradient term affects the accuracy of basic-flow variables and their derivatives and also stability and transition results. The globally IPNS equations, called reduced Navier–Stokes equations, employ the full pressure gradient term in the subsonic region of the boundary layer and it can provide the basic-flow field and stability results comparable with those of the TLNS scheme [6,7]. The IPNS scheme is computationally more efficient than the TLNS scheme, and therefore, using the fourth-order compact IPNS scheme [8–11], a high-order accurate basic-flow model suitable for stability analysis and transition prediction can be efficiently provided.

The IPNS model used herein is based on the method proposed by Barnett and Davis [20]. This IPNS scheme utilizes an alternating direction explicit (ADE) procedure which is in the form of a two-step calculation procedure for each global iteration. In the ADE method, the streamwise pressure gradient is split using the technique of Vigneron et al. and a fictitious unsteady term is appended to the elliptic part as follows:

$$\frac{\partial p}{\partial\xi}=\bar{\omega}\frac{\partial p}{\partial\xi}+(1-\bar{\omega})\left[\frac{\partial p}{\partial\xi}-\frac{\partial p}{\partial t}\right] \tag{6}$$

to permit the upstream propagation of information through the subsonic region in a hyperbolic manner.

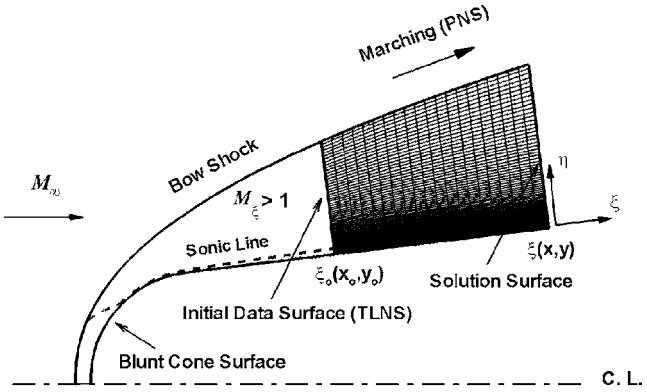

Fig. 1 Marching procedure and initial condition for starting the PNS solution over a blunt cone

4 Grid Generation and Marching Step Size

An algebraic grid scheme is utilized to compute flow field, as shown in Fig. 1. The lines of constant ξ are distributed uniformly along the body surface and are orthogonal to the body. To ensure that the viscous regions are adequately resolved, the lines of constant η are clustered near the body surface according to [18]

$$\frac{x-x_w}{x_s-x_w}=\bar{a} \quad \frac{y-y_w}{y_s-y_w}=\bar{a} \tag{7}$$

where

$$\bar{a}=1+\bar{\beta}\left[\frac{1-\tilde{a}^{(1-\eta/\eta_{\max})}}{1+\tilde{a}^{(1-\eta/\eta_{\max})}}\right] \quad \tilde{a}=\frac{\bar{\beta}+1}{\bar{\beta}-1}$$

in which the clustering parameter $\bar{\beta}$ is assigned to be 1.01 for all calculations presented herein.

The step sizes employed in the downstream marching procedure are $\Delta\xi=2\times10^{-4}$ and 0.05 for the STDS sharp and blunt cones, respectively.

5 Boundary Conditions and Initial Data Plane

The boundary conditions at the wall consist of no-slip conditions for velocity components, a specified wall temperature or an adiabatic wall, and zero pressure gradient approximation normal to the wall. The wall for the cases studied here is assumed to be adiabatic. At the upper boundary, the bow shock is fitted using a shock fitting technique to obtain an accurate solution of the PNS equations near the shock.

The starting data of the PNS equations are provided by the solution of the TLNS equations for the blunt-cone case. Figure 1 shows the initial condition and the marching procedure for the PNS equations. The starting solution on an initial data surface where the inviscid flow is supersonic is obtained from the solution of the TLNS model. The PNS equations are self-starting for the sharp-cone case, and the initial data for the space-marching procedure are provided by the conical solution of the PNS equations.

6 Numerical Method

The numerical solution of the PNS and IPNS schemes is obtained by using an implicit finite-difference method in the wall-normal direction η, similar to the Beam and Warming method [6,7,16], in which the basic-flow variables and their first and second derivatives required for the stability calculations are automatically obtained with the fourth-order accuracy [8–11]. The numerical algorithm of the PNS equations for a marching step $\Delta\xi$ using the first-order backward Euler implicit scheme can be written in delta form as

$$\Delta\bar{F}^{*i}+\Delta\xi\left[\frac{\partial\Delta\bar{G}}{\partial\eta}+\Delta\bar{H}\right]^i=-\Delta\xi\left[\frac{\partial\bar{G}}{\partial\eta}+\bar{H}\right]^i-\Delta P^i \tag{8}$$

After linearization, the equations are reduced to the following nonconservative form:

$$\mathbf{C_0}\Delta\bar{U}^i+\mathbf{C_1}\Delta\bar{U}^i_\eta+\mathbf{C_2}\Delta\bar{U}^i_{\eta\eta}=C_R \tag{9}$$

where $\Delta\bar{U}^i=\bar{U}^{i+1}-\bar{U}^i$ and $(\,)_\eta=d/d\eta$. The following fourth-order compact relations for the first and second derivatives are used ($f'=\Delta\bar{U}_\eta$, $f''=\Delta\bar{U}_{\eta\eta}$)

$$\frac{f'_{j+1}+4f'_j+f'_{j-1}}{6}=\frac{f_{j+1}-f_{j-1}}{2\Delta\eta}+O(\Delta\eta)^4$$

$$\frac{f''_{j+1}+10f''_j+f''_{j-1}}{12}=\frac{f_{j+1}-2f_j+f_{j-1}}{(\Delta\eta)^2}+O(\Delta\eta)^4 \tag{10}$$

to complete the system of equations for computing the basic flow and their derivatives. The preceding system of equations along with the appropriate third-order accurate boundary conditions

$$f_j-f_{j+1}+(\Delta\eta)f'_j+\frac{(\Delta\eta)^2}{6}(2f''_j+f''_{j+1})+O(\Delta\eta)^4=0$$

$$f_j-f_{j+1}+(\Delta\eta)f'_{j+1}-\frac{(\Delta\eta)^2}{6}(f''_j+2f''_{j+1})+O(\Delta\eta)^4=0$$

at the wall and the shock gives a block-tridiagonal system of equations for $[\Delta\bar{U}^i,\Delta\bar{U}^i_\eta,\Delta\bar{U}^i_{\eta\eta}]^T$ with a block size of 12×12. A block-tridiagonal solver is used to calculate the incremental solution vector $[\Delta\bar{U}^i,\Delta\bar{U}^i_\eta,\Delta\bar{U}^i_{\eta\eta}]^T$, and then the flow variables and the first and second derivatives are automatically determined as follows:

$$\bar{U}^{i+1}=\bar{U}^i+\Delta\bar{U}^i$$

$$\bar{U}^{i+1}_\eta=\bar{U}^i_\eta+\Delta\bar{U}^i_\eta$$

$$\bar{U}^{i+1}_{\eta\eta}=\bar{U}^i_{\eta\eta}+\Delta\bar{U}^i_{\eta\eta} \tag{11}$$

At each station, the shock slope is iteratively corrected in an explicit manner. The iterative process is repeated at the shock until the solution converges, and then the solution marches on the next solution plane.

A sixth-order dissipation term is used to stabilize the numerical instability of the method associated with central differencing in the η-direction:

$$D_e=\varepsilon_e\left[\frac{\partial\bar{F}^*}{\partial\bar{U}}\right]^i(\nabla_\eta\Delta_\eta)^3\bar{U}^i \tag{12}$$

The stability analysis of the numerical algorithm has indicated the method is stable for $0\leqslant\varepsilon_e\leqslant1/32$. Details of the numerical algorithm, the boundary conditions implementation and also dissipation term used have been reported in [8–11].

The present study indicates that the stability and transition results based on high-order compact basic-flow models are sensitive to the numerical dissipation used in computing the basic flows, especially for a lower number of grid points (see Sec. 8).

7 Linear Stability Analysis

7.1 Linear Stability Equations. The parallel-flow linear stability analysis is employed for stability analysis and transition prediction of hypersonic flow over axisymmetric bodies. The hydrodynamic stability theory is useful in indicating the major dominant effects which hasten or delay transition in a relative sense. Moreover, the transition location can be approximately predicted

using a semi-empirical correlation such as the e^N method.

The stability calculations of the flow over axisymmetric bodies require the derivation of the disturbance equations in curvilinear coordinates. The disturbance equations are derived from the tensor-analytical form of the NS equations using the body intrinsic curvilinear coordinate system. For the cone frustum, the curvature of the body is zero, and the radius of the body changes linearly with x. Therefore, the scale factors in this orthogonal curvilinear coordinate system (ξ, η, ϕ) are

$$h_1 = 1 \quad h_2 = 1 \quad h_3 = r(\xi) + \eta \cos\theta_c \tag{13}$$

where $r(\xi)$ is the body radius and (ξ, η) denote the actual distances along and normal to the body, respectively. The linear stability equations are obtained in the traditional way, that is, the basic flow is perturbed by fluctuations in the flow; therefore, the flow-field vector Q can be decomposed into a steady laminar axisymmetric mean value (basic flow) $Q_b = (\rho_b, U_b, V_b, 0, T_b)^T$ and an unsteady three-dimensional perturbation quantity $Q' = (\rho', U', V', W', T')^T$ as follows:

$$Q(\xi, \eta, \phi, t) = Q_b(\xi, \eta) + Q'(\xi, \eta, \phi, t) \tag{14}$$

Then, by substituting these equations into the NS equations and subtracting from the governing equations corresponding to the steady basic flow, one can obtain the governing equations for the disturbances Q'. All terms including those arising from longitudinal and transverse curvatures are considered. The streamwise variation of the basic flow is neglected under parallel-flow assumption, that is,

$$U_b = U_b(\eta) \quad V_b = 0 \quad \rho_b = \rho_b(\eta) \quad p_b = p_b(\eta) \quad T_b = T_b(\eta) \tag{15}$$

Since the disturbances are assumed small, the disturbance equations can be linearized; that is, the terms quadratic or higher in the disturbances and their derivatives may be neglected. When it is assumed that the disturbance vector Q' for an instability wave can be expressed as

$$Q'(\xi, \eta, \phi, t) = \hat{Q}(\eta)\exp[i(\alpha\xi + \beta\phi - \omega t)] \tag{16}$$

the linearized disturbance equations are reduced to the following system of ordinary differential equations:

$$\mathbf{A}\frac{d^2\hat{Q}}{d\eta^2} + \mathbf{B}\frac{d\hat{Q}}{d\eta} + \mathbf{C}\hat{Q} = 0 \tag{17}$$

where $\hat{Q} = (\hat{\rho}, \hat{U}, \hat{V}, \hat{W}, \hat{T})^T$ and $\mathbf{A}$, $\mathbf{B}$, and $\mathbf{C}$ are 5×5 matrices. These linearized equations with the homogeneous boundary conditions constitute an eigenvalue problem as follows:

$$\alpha = \alpha(\omega, \beta) \tag{18}$$

which can be solved by standard eigenvalue techniques. All quantities are scaled with freestream conditions and the length $l_\infty = \sqrt{\nu_\infty^* s^* / U_\infty^*}$. Therefore, the nondimensional forms of the wave numbers and the frequency appear as

$$\alpha = \alpha^* l_\infty \quad \beta = \beta^* l_\infty \quad \omega = 2\pi f^* l_\infty / U_\infty \tag{19}$$

The stability analysis considered here is based on the spatial theory where ω is real and α and β are complex. The real and imaginary parts of α give the wave number and the disturbance growth rate, respectively, and unstable disturbance is expected for $-\alpha_i > 0$. Details of the above formulation can be found in Refs. 2 and 7.

7.2 Numerical Solution of Stability Equations. An accurate numerical method for the solution of the stability equations is the two-point fourth-order compact Euler–Maclaurin scheme [12,13]. However, in applying the Euler–Maclaurin scheme, due to the differentiation of the governing equations, the higher derivatives of the basic-flow variables are required. It was shown that in general the higher derivatives obtained from the basic flow for the stability analysis of hypersonic flow are less accurate [6,7]. Here, consistent with the solution of the basic flow, the fourth-order Hermitian formula, which does not need the higher derivatives of basic-flow profiles, is efficiently implemented for the solution of the parallel-flow linear stability equations in the intrinsic orthogonal coordinates. The fourth-order Hermitian formulation for solving the stability equations (17) requires a coordinate transformation to employ the compact relations (10) in a uniform grid distribution in the wall-normal direction $(\bar{\eta})$

$$\bar{\mathbf{A}}\frac{d^2\hat{Q}}{d\bar{\eta}^2} + \bar{\mathbf{B}}\frac{d\hat{Q}}{d\bar{\eta}} + \bar{\mathbf{C}}\hat{Q} = 0 \tag{20}$$

where

$$\bar{\mathbf{A}} = \mathbf{A}\left(\frac{d\bar{\eta}}{d\eta}\right)^2 \quad \bar{\mathbf{B}} = \mathbf{A}\frac{d^2\bar{\eta}}{d\eta^2} + \mathbf{B}\frac{d\bar{\eta}}{d\eta} \quad \bar{\mathbf{C}} = \mathbf{C}$$

Equation (20) and the compact relations for the first and second derivatives (10) along with appropriate boundary conditions constitute a block-tridiagonal system of equations for $[\hat{Q}, \hat{Q}_\eta, \hat{Q}_{\eta\eta}]^T$ with a block size of 14×14. Note that the continuity equation does not need the second derivative of the disturbance relation $\hat{\rho}_{\eta\eta}$. The above formulation can be set into a reduced form by substituting the second derivatives of the disturbance variables $\hat{F} = (\hat{U}_{\eta\eta}, \hat{V}_{\eta\eta}, \hat{W}_{\eta\eta}, \hat{T}_{\eta\eta})^T$ from Eq. (20)

$$\hat{F} = -(\bar{\mathbf{B}}'\hat{Q}_\eta + \bar{\mathbf{C}}'\hat{Q})$$

$$\bar{\mathbf{B}}' = \bar{\mathbf{A}}^{-1}\bar{\mathbf{B}} \quad \bar{\mathbf{C}}' = \bar{\mathbf{A}}^{-1}\bar{\mathbf{C}} \tag{21}$$

into the compact relations for the second derivatives (10), which yields

$$h^2(\bar{\mathbf{B}}'\hat{Q}_\eta)_{j-1} + 10h^2(\bar{\mathbf{B}}'\hat{Q}_\eta)_j + h^2(\bar{\mathbf{B}}'\hat{Q}_\eta)_{j+1} + (12\mathbf{I}' + h^2\bar{\mathbf{C}}'_{j-1})\hat{Q}_{j-1} + (-24\mathbf{I}' + 10h^2\bar{\mathbf{C}}'_j)\hat{Q}_j + (12\mathbf{I}' + h^2\bar{\mathbf{C}}'_{j+1})\hat{Q}_{j+1} = 0 \tag{22}$$

where $h = \Delta\bar{\eta}$, $\mathbf{I}'$ is the unit matrix with a block size of 4×5, and $\bar{\mathbf{B}}'$ and $\bar{\mathbf{C}}'$ are 4×5 matrices. Equation (22) together with the continuity relation for the disturbance equation and the compact relations for the first derivatives (10) along with appropriate boundary conditions give a block-tridiagonal system of equations with a block size of 10×10. The Euler–Maclaurin would require the solution of 7×7 block-tridiagonal system. The present calculations have indicated that the computational times for these two numerical methods for the solution of the stability equations are approximately the same. The present formulation for solving the stability equations is consistent with the solution of the basic flow and it does not require the higher derivatives of basic-flow profiles, which in general are less accurate. Details of the above formulation can be found in Ref. 7.

8 Results and Discussion

The stability analysis of hypersonic laminar flow over blunt and sharp cones at Mach 8 is studied by using high-order accurate solutions of PNS schemes as basic flows. A sensitivity analysis is also performed to investigate the effects of grid size and numerical dissipation and also accuracy of computing the basic-flow derivatives on the stability results. In addition, the transition results for the STDS blunt-cone case are discussed.

For hypersonic flows, the experiments by Stetson et al. [14,15] and also the prediction by Mack [21] clearly indicate the emergence of second-mode instability. It is also found that second-mode waves are most amplified when they are axisymmetric ($\beta = 0$). Therefore, the stability and transition results presented herein are based on the two-dimensional second-mode computations.

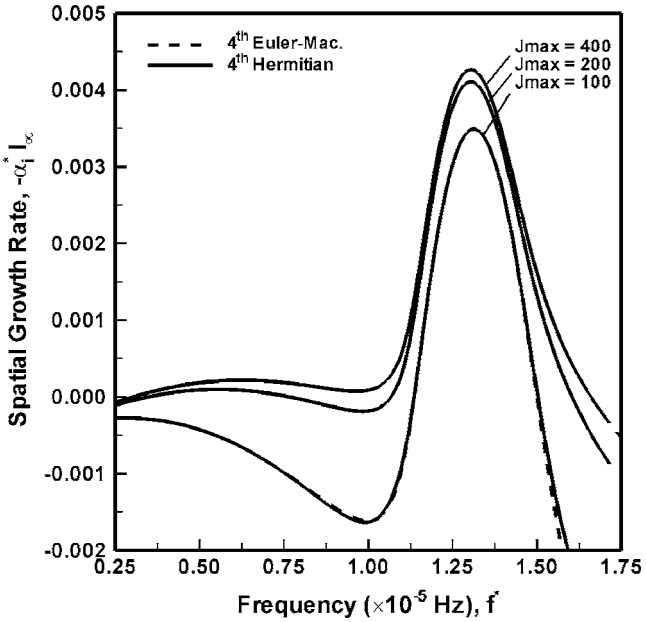

Fig. 2 Comparison of spatial growth rates by solution of stability equations using Hermitian and Euler–Maclaurin methods for the STDS blunt-cone case, $M_\infty=8$ and $Re_\infty=31{,}250$ at $S=175$

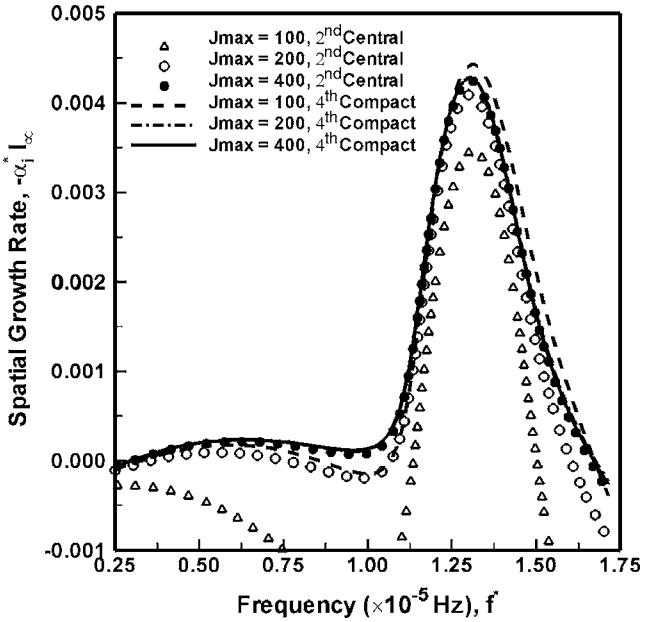

Fig. 3 Comparison of spatial growth rates for second-order central and fourth-order compact PNS solutions for the STDS blunt-cone case, $M_\infty=8$ and $Re_\infty=31{,}250$ at $S=175$

8.1 Stability Results

8.1.1 Stetson–Thompson–Donaldson–Siler Blunt-Cone Case. The accuracy of the present formulation for the fourth-order Hermitian method for the solution of stability equations is tested by comparison with the results of the Euler–Maclaurin method for the STDS blunt-cone case. Figure 2 compares the second-mode spatial growth rates obtained by the solution of the linear stability equations using the Hermitian and Euler–Maclaurin methods at the desired station, $S^*/R_N=175$, by employing the second-order solution of the PNS model [6,7] as basic flow. The stability results are presented for different grid sizes. It is clear that the stability results based on two methods are the same for all the grid points used in computing the basic flow. The figure also indicates the sensitivity of the stability results to the grid size, and therefore, the accuracy of basic-flow computation. The following stability results are based on the fourth-order Hermitian formula implemented to the linear stability equations.

Figure 3 demonstrates a comparison of the spatial growth rates for the second-order central and fourth-order compact solutions of the PNS model at Station 175. Note that the fourth-order and sixth-order dissipation terms are used for the second-order central and fourth-order compact methods, respectively. It is found that the stability results based on the fourth-order compact solution of the PNS equations using $J_{\max}=200$ are comparable with those of the second-order solution using $J_{\max}=400$. It is obvious that the converged solution of the stability results for the fourth-order compact PNS solution at Station 175 is obtained using $J_{\max}=200$, which is much lower than that of the second-order PNS solution, $J_{\max}=400$. It is clear that the fourth-order compact PNS solution with $J_{\max}=100$ gives accurate stability results except near the right region of the second mode.

To clarify this problem, a comparison of the generalized inflection profiles G for the second-order central and fourth-order compact solutions of the IPNS model at Station 175 is performed, as shown in Fig. 4. In fact, the generalized inflection profile G is a good indicator for obtaining the accurate stability results [6,7]. It can be seen that by increasing the number of grid points near the high gradient region of the G profile from $J_{\max}=100$ to $J_{\max}=140$, accurate solution of the G profile can be obtained and oscillations near the critical layer are removed. This is due to the effect of the sixth-order numerical dissipation in this high gradient region, and by using a smaller dissipation value $\varepsilon_e=0.0002$ even with a lower number of grid points, i.e., $J_{\max}=100$, more accurate solution can be achieved. A similar behavior was observed for the higher derivatives of the basic-flow profiles obtained by implementing the fourth-order compact method to the PNS equations [8–11]. Figure 5 verifies this result. It is found that with decreasing value of numerical dissipation in calculating the basic flow using the PNS equations, the stability results computed by $J_{\max}$

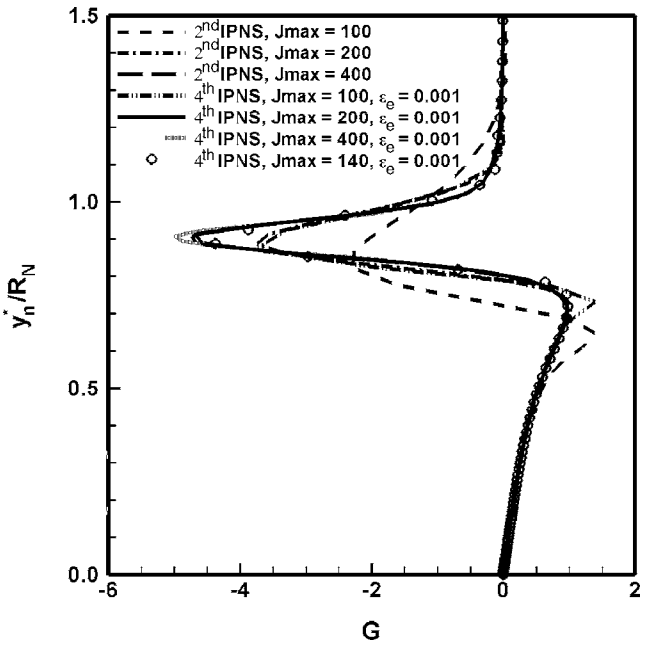

Fig. 4 Comparison of the generalized inflection profiles G for second-order central and fourth-order compact IPNS solutions for the STDS blunt-cone case, $M_\infty=8$ and $Re_\infty=31250$ at $S=175$

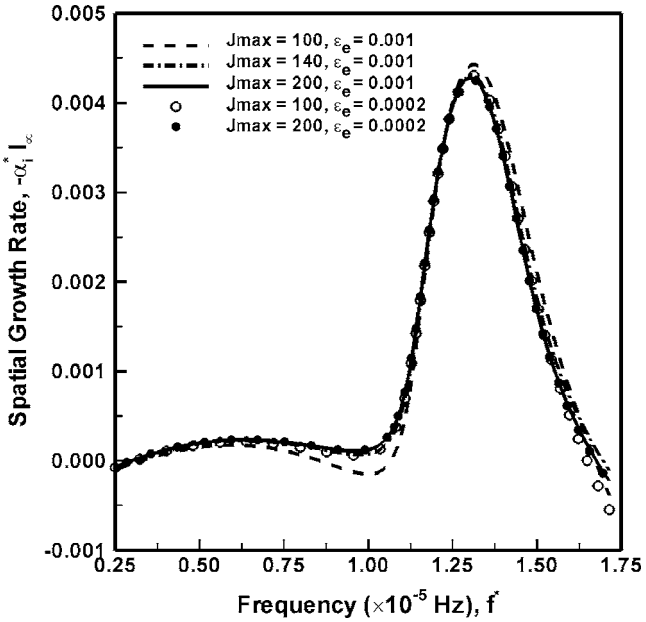

Fig. 5 Effect of grid size and numerical dissipation value on spatial growth rates in the fourth-order compact PNS solution for the STDS blunt-cone case, $M_\infty = 8$ and $Re_\infty = 31{,}250$ at $S = 175$

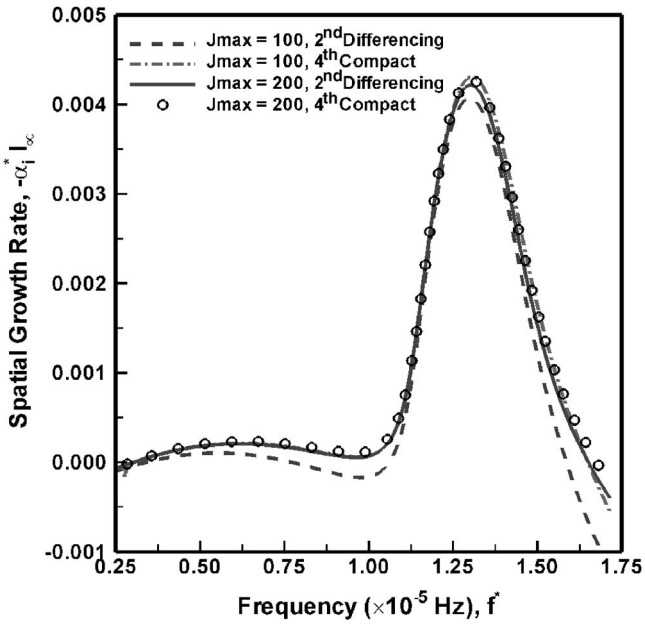

Fig. 6 Effect of accuracy of computing basic-flow derivatives on spatial growth rates in the fourth-order compact PNS solution for the STDS blunt-cone case, $M_\infty = 8$ and $Re_\infty = 31{,}250$ at $S = 175$

$= 100$ converge to the solution of $J_{\max} = 200$. For a higher number of grid points, i.e., $J_{\max} = 200$, the stability results become less sensitive to the numerical dissipation value used in computing the basic flow using the fourth-order compact method.

Besides the global accuracy, the main advantage of the fourth-order compact finite-difference method for the solution of the flow field is that the derivatives of basic flow required for stability computations are automatically computed with the same accuracy of the basic flow and no intermediate computation of the derivatives, which usually produces wiggles in these profiles, is needed [8–11]. Figure 6 gives the effects of accuracy of computing the basic-flow derivatives in the fourth-order solution of the PNS model using $\varepsilon_e = 0.0002$ on the stability results at Station 175. Although the basic-flow field is obtained by the fourth-order compact solution, it is evident that computing the derivatives of the basic flow using the fourth-order compact solution, especially for a lower number of grid points, i.e., $J_{\max} = 100$, produces more accurate stability results compared to those of the second-order differencing of the compact solution. However, as the number of grid points increases, the accuracy of the stability results becomes independent of the way of computing the derivatives, as shown in Fig. 6.

Figure 7 indicates a comparison of the spatial growth rates for the fourth-order compact solution of the PNS and IPNS models with those of the second-order solution of the TLNS model at Station 175. The stability results based on the fourth-order compact solution of the IPNS model using $J_{\max} = 100$ and $\varepsilon_e = 0.0002$ are comparable with those of the TLNS model using $J_{\max} = 200$ for the most amplified region of second mode, and more accurate solution using the fourth-order IPNS model is obtained near the first-mode region and the right branch of second mode than those of the TLNS model. Using the fourth-order compact IPNS scheme, a high-order accurate basic-flow model suitable for stability analysis and transition prediction of hypersonic axisymmetric flows can be efficiently provided.

The CPU time comparison of the various solutions for the STDS blunt-cone case is performed to show the efficiency of using the high-order compact PNS schemes. The present calculations using the PNS and IPNS schemes are performed on a 3.2 GHz Pentium IV computer. The solutions for both the second-order central and fourth-order compact IPNS models are obtained for the global region $4 \leqslant S \leqslant 250$, which includes approximately 5000 marching steps ($\Delta\xi = 0.05$) for each global iteration. The computations are considered to be converged when the root mean square (rms) of the relative change in pressure is less than 1×10^{-6}. Based on the second-order central and fourth-order compact IPNS models using $J_{\max} = 200$, the computation times are about 9 min and 105 min (about 6 s and 70 s for those of the PNS models), respectively. The CPU time of the second-order TLNS

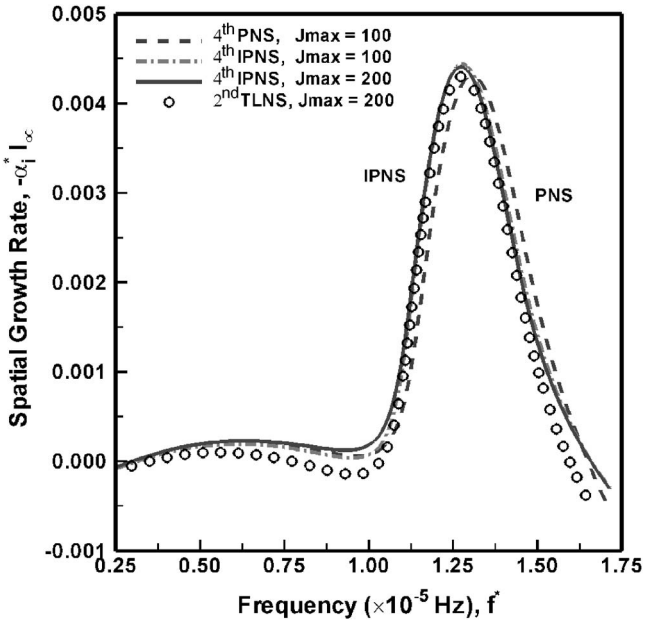

Fig. 7 Comparison of spatial growth rates for fourth-order compact PNS and IPNS solutions with second-order TLNS solution for the STDS blunt-cone case, $M_\infty = 8$ and $Re_\infty = 31{,}250$ at $S = 175$

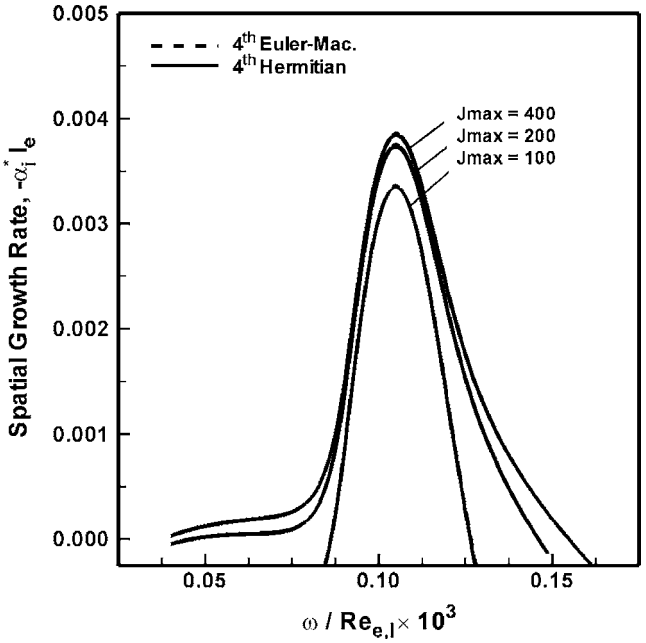

Fig. 8 Comparison of spatial growth rates by solution of stability equations using Hermitian and Euler–Maclaurin methods for the STDS sharp-cone case, $M_\infty=8$ and $Re_\infty=6.525\times10^6$ at $Re_{e,l}=1.73\times10^3$

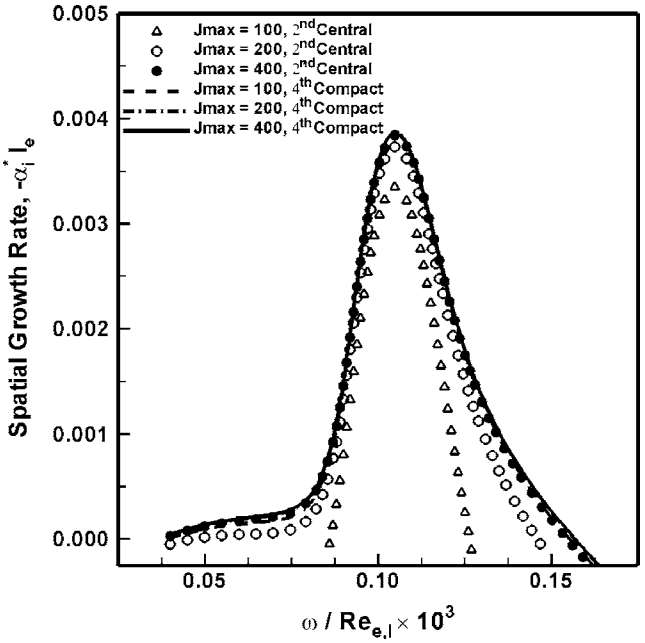

Fig. 9 Comparison of spatial growth rates for second-order central and fourth-order compact PNS solutions for the STDS sharp-cone case, $M_\infty=8$ and $Re_\infty=6.525\times10^6$ at $Re_{e,l}=1.73\times10^3$

solution in the nose region using (80×200) grid points is about 2 h, which must be added to the times of the PNS and IPNS solutions. The CPU time of the second-order TLNS solution for the region $S\leqslant250$ using (1300×200) grid points was about 260 h on a Cray Y-MP for fully vectorized code [2]. It should be noted that the convergence rate of the TLNS solution is slow especially for large values of S, because the shock shape is not known prior to the computation, requiring that the shock location is computed as a part of the solution. This statement can be confirmed by comparing the computational time of the TLNS solution for the whole flowfield and that of the TLNS solution in the nose region. It is clear that both the fourth-order PNS and IPNS schemes significantly reduce the computational time (and memory) required to obtain basic flows in comparison with the TLNS scheme.

8.1.2 Stetson–Thompson–Donaldson–Siler Sharp-Cone Case. The stability analysis of the STDS sharp-cone case is also presented to show the robustness and accuracy of the high-order compact PNS schemes for use as basic flows in predicting the stability characteristics of high-speed flows over sharp bodies. The stability results are compared with the theoretical stability results by Mack [17]. For the STDS sharp-cone case, the stability results are presented at the marching location, $S^*/S^*_{\max}=0.326$, which approximately corresponds to the local Reynolds number based on boundary-layer edge conditions, $Re_{e,l}=U^*_e l_e/\nu^*_e=\sqrt{U^*_e S^*/\nu^*_e}=1730$.

The accuracy of the fourth-order Hermitian method for the solution of the stability equations is also demonstrated by comparison with the results of the Euler–Maclaurin method for the STDS sharp-cone case. Figure 8 shows a comparison of the second-mode spatial growth rates obtained by the solution of the linear stability equations using the Hermitian and Euler–Maclaurin methods at the desired station, $Re_{e,l}=1730$, by employing the second-order solution of the PNS model [6,7] as basic flow for various number of grid points in the wall-normal direction. It is evident that two methods give the same stability results for all the grid points used in calculating the basic flow. The sensitivity of the stability results to the grid size and therefore the accuracy of basic-flow computation is clearly revealed.

Figure 9 compares the spatial growth rates for the second-order central and fourth-order compact solutions of the PNS model at station $Re_{e,l}=1730$. Based on the study of the STDS blunt-cone case, the numerical dissipation value for the solutions of compact PNS schemes is set to be $\varepsilon_e=0.0002$. It can be seen that the fourth-order compact PNS solution using only $J_{\max}=100$ can accurately predict the spatial growth rates of the second mode.

For the STDS sharp-cone case, the present computations based on the fourth-order IPNS model using $J_{\max}=100$ are compared with the results of Mack at the desired station, $Re_{e,l}=1730$, as shown in Fig. 10. The stability results based on the fourth-order IPNS model using $J_{\max}=100$ are nearly the same as Mack's results. The differences between the present calculations and Mack's results are caused by both different basic flows and different stability codes [6,7]. Mack used locally planar flow and neglected all $1/h_3$ terms (curvature terms). He calculated the basic flow using the boundary-layer equations by ignoring the inviscid-viscous interaction. The differences between the present stability results for the left region of the neutral curve are due to the effect of curvature terms. It can be seen that the present stability results based on the fourth-order IPNS model without curvature terms are in good agreement with those of the planar stability study by Mack except for the right branch of second mode. This difference is caused by the inviscid-viscous interaction, which was neglected in Mack's study [6,7]. It should be noted that the PNS equations are valid in both the viscous and inviscid portions of the flow field and therefore, high-order accurate PNS models are more preferable than the boundary-layer equations for computing these flow fields.

8.2 Transition Results. To determine the location of the transition onset, the classical linear stability theory in conjunction with the e^N method is employed. The N factor is defined by the envelope of the total amplification curves as follows:

$$N=\max_f\left[\ln\left(\frac{A}{A_0}\right)\right]=\max_f\left[-\int_{\xi^o}^{\xi}\alpha_i d\xi\right] \tag{23}$$

in which $A=A(\xi)$ denotes the disturbance amplitude and A^o refers to the streamwise position ξ^o where the disturbance becomes am-

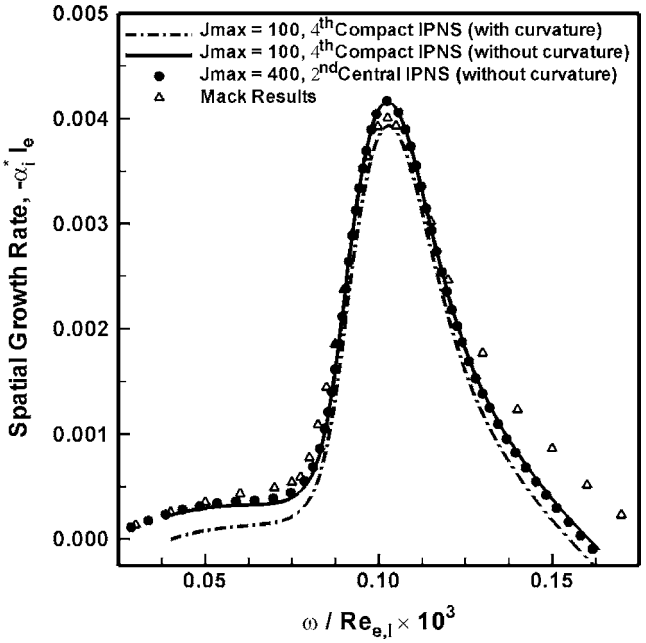

Fig. 10 Comparison of spatial growth rates for the STDS sharp-cone case, $M_\infty=8$ and $Re_\infty=6.525\times10^6$ at $Re_{e,l}=1.73\times10^3$

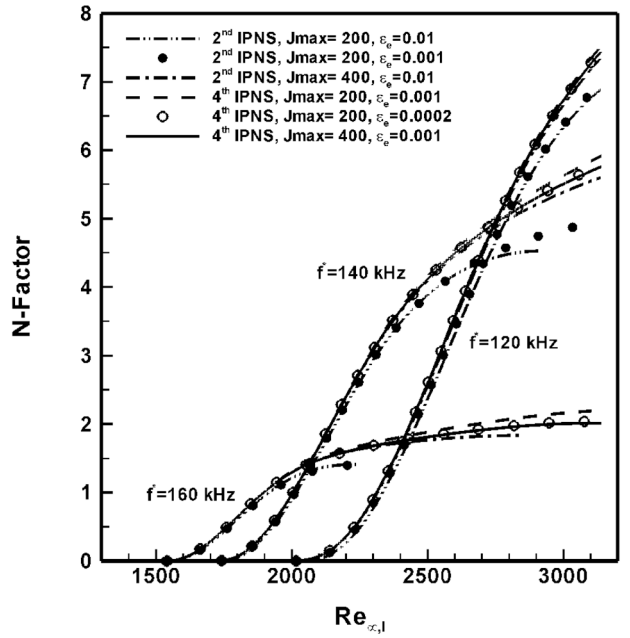

Fig. 12 Comparison of computed second-mode *N*-factor for second-order central and fourth-order compact IPNS models for the STDS blunt-cone case, $M_\infty=8$ and $Re_\infty=31{,}250$

plified. The STDS blunt-cone case is considered herein.

Figure 11 compares the curves of second-mode spatial growth rate for the second-order central and fourth-order compact methods as basic flows. Along each curve, frequency f is held constant. Curves for three frequencies, namely, 120 kHz, 140 kHz, and 160 kHz are shown. Recall that the fourth-order and sixth-order dissipation terms are used for the second-order central and fourth-order compact methods, respectively. All the stability and transition results are presented for $\Delta\xi=0.05$. The curves of the second-order method with $J_{\max}=200$ in the left branch differ slightly from the other curves and at higher Reynolds numbers completely deviate and their second-mode spatial growth rates vanish rapidly, which shows that the second-order method with $J_{\max}=200$ is not much accurate for the stability and transition analysis. However, the curves of the second-order method with $J_{\max}=400$ and the fourth-order compact method with $J_{\max}=200$ and $\varepsilon_e=0.001$ have a little difference with the curves of the fourth-order compact method with $J_{\max}=200$ and $\varepsilon_e=0.0002$, and with $J_{\max}=400$ and $\varepsilon_e=0.001$. These last two curves are almost identical, and comparing with the other curves shows the sensitivity of the stability results to the numerical dissipation even for the high-order compact basic-flow models used. This figure also ensures the convergence of the curves toward the fourth-order compact method with $J_{\max}=400$ and $\varepsilon_e=0.001$.

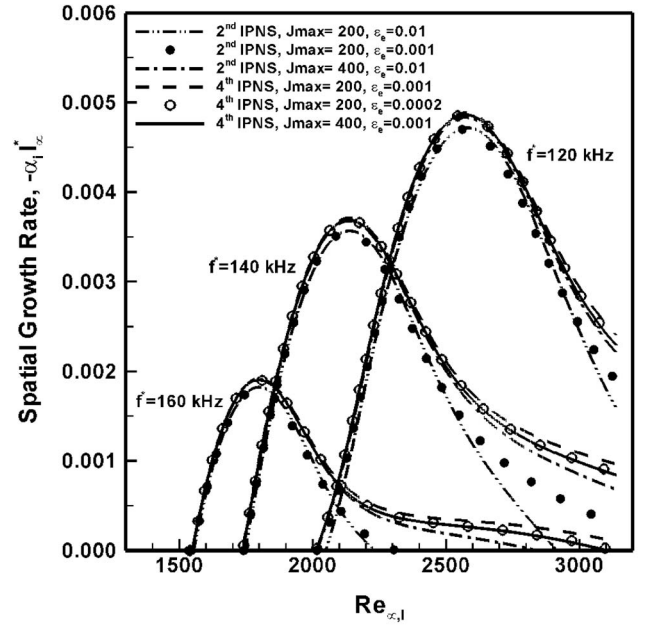

Fig. 11 Comparison of f=const curves of spatial growth rates for second-order central and fourth-order compact IPNS models for the STDS blunt-cone case, $M_\infty=8$ and $Re_\infty=31{,}250$

Figure 12 shows the second-mode N-factor calculations for the STDS blunt-cone case. Three frequencies, namely, 120 kHz, 140 kHz, and 160 kHz, are shown for different number of grid points and for both the second-order central and fourth-order compact IPNS models as basic flows. Considering the fourth-order compact basic-flow model with $J_{\max}=400$ as the most accurate curve, the curves of the second-order method underestimate the N-factor in the most region and other curves of the fourth-order compact method overestimate the N factor. The effect of numerical dissipation value on the transition results is also investigated. The N-factor curves of the fourth-order compact method with $J_{\max}=200$ and $\varepsilon_e=0.0002$, and with $J_{\max}=400$ and $\varepsilon_e=0.001$ are almost the same. Comparing these curves with that of $J_{\max}=200$ and $\varepsilon_e=0.001$ indicates that reducing the amount of numerical dissipation in calculating the basic flow using the high-order compact method is crucial for preserving the accuracy of the stability and transition results. It should be noted that the stability and transition results based on both the second-order central and fourth-order compact methods using $J_{\max}=400$ are not very sensitive to the amount of numerical dissipation used (not shown in Figs. 11 and 12). The results also indicate that since the distance between grids increases with S, the effect of numerical dissipation becomes more important on the flow stability and transition. In addition, the study shows that while the fourth-order numerical dissipation term in the solution of the second-order PNS schemes

Table 1 Prediction of transition location for the STDS blunt-cone case based on the PNS model

Method	Grid	$Re_{\infty,l}$	S	ε_e
Fourth-order compact	400	2790	249.2	0.001
	200	2789	248.9	0.0002
	200	2786	248.3	0.001
Second-order central	400	2801	251.1	0.01
	200	2858	261.3	0.001
	200	2864	262.5	0.01

has a stabilizing influence on the most regions of second-mode spatial growth rate curves, the sixth-order dissipation term in the solution of the fourth-order compact PNS schemes has a destabilizing effect (see Figs. 11 and 12 and also Tables 1 and 2).

Figures 13 and 14 illustrate the curves of second-mode spatial growth rates and the N-factor computation based on the fourth-order compact PNS and IPNS models over $Re_{\infty,l}$, respectively. As shown in Fig. 13, the spatial growth rates for different frequencies are shifted to the right for the PNS solution with respect to the IPNS solution as basic flow with higher maximum growth rate but shifted into the envelope of spatial growth rate curves. As a result, the predicted transition location by the PNS model is expected to be higher than that of the IPNS model for the STDS blunt cone (see Tables 1 and 2). This is due to omitting part of unfavorable streamwise pressure gradient term in the PNS model, which delays the transition location. Therefore, the accurate transition prediction can be obtained by the IPNS solution (equivalent to the TLNS solution) and someone should be careful for the use of PNS scheme as a basic flow to predict transition.

Table 2 Prediction of transition location for the STDS blunt-cone case based on the IPNS model

Method	Grid	$Re_{\infty,l}$	S	ε_e
Fourth-order compact	400	2750	242.0	0.001
	200	2748	241.7	0.0002
	200	2740	240.3	0.001
Second-order central	400	2760	243.7	0.01
	200	2810	252.7	0.001
	200	2815	253.5	0.01

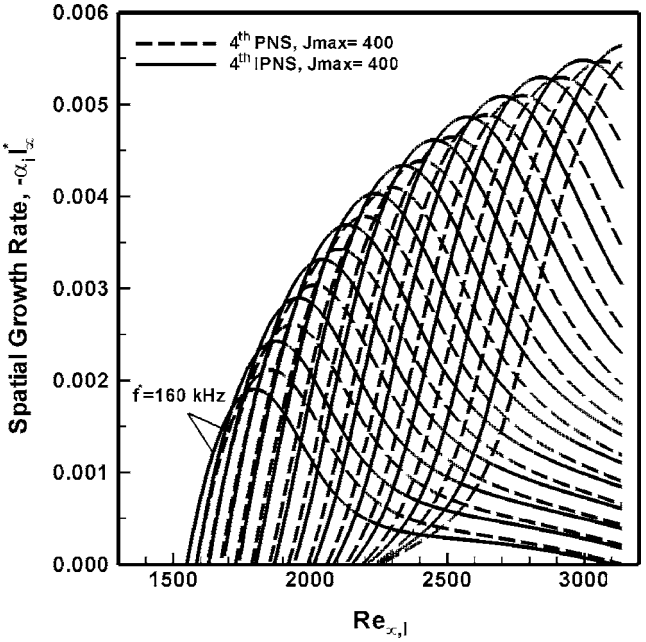

Fig. 13 f=const curves of spatial growth rates for fourth-order compact PNS and IPNS models for the STDS blunt-cone case, M_∞=8 and Re_∞=31,250 (Δf^*=5 kHz)

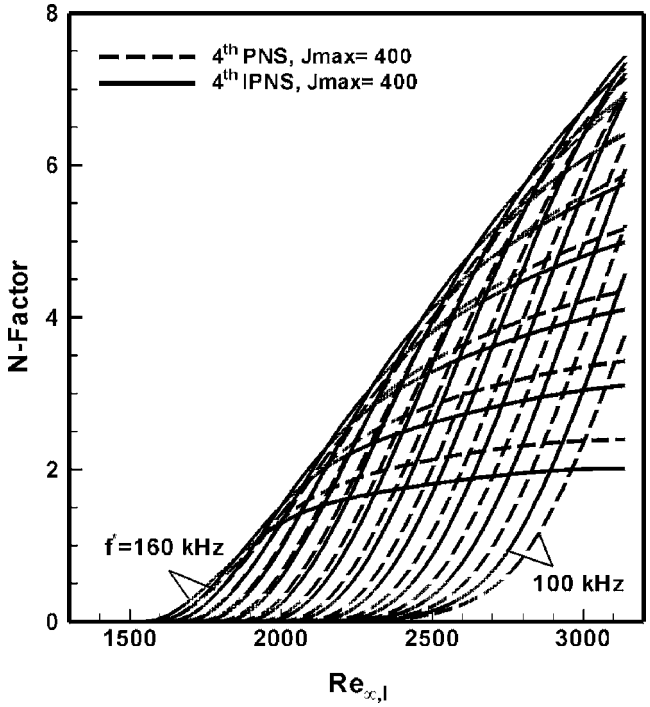

Fig. 14 Second-mode N-factor computation for fourth-order compact PNS and IPNS models for the STDS blunt-cone case, M_∞=8 and Re_∞=31,250 (Δf^*=5 kHz)

N=5.5 is assumed for prediction of the transition location [1,5–7]. Tables 1 and 2 summarize the transition location for the PNS and IPNS models. Using the second-order central and fourth-order compact methods with different number of grid points and different numerical dissipation values, the results indicate that transition Reynolds number for the PNS model is higher by 40–50 units. Furthermore, as it is obvious from Figs. 11 and 12, the stability and transition results of the fourth-order compact method with $J_{\max}$=200 and ε_e=0.0002 and with $J_{\max}$=400 and ε_e=0.001 are nearly the same. Based on the fourth-order compact PNS and IPNS models using $J_{\max}$=400, transition takes place at $Re_{\infty,l}$=2790 and $Re_{\infty,l}$=2750, respectively, which is lower than those predicted by the second-order PNS and IPNS models ($Re_{\infty,l}$=2801 and $Re_{\infty,l}$=2760) and also Malik et al. [1] and Stilla [5] ($Re_{\infty,l}$=2800). The present results demonstrate that transition location is sensitive to the accuracy of the basic flow, grid resolution, and the amount of numerical dissipation used in computing basic flows using the PNS schemes.

9 Concluding Remarks

In the present study, high-order accurate solutions of PNS schemes are used as basic-flow models for stability analysis of hypersonic axisymmetric flows over blunt and sharp cones at Mach 8. Some conclusions regarding the stability and transition computations of hypersonic axisymmetric flows based on high-order compact PNS schemes as basic-flow models are as follows.

(1) It is found that the stability and transition results based on high-order accurate basic flows are sensitive to the grid size and especially the numerical dissipation terms used in computing the basic flows, and therefore, more careful attention must be kept to obtain an accurate solution of the stability and transition results.
(2) Although the stability results based on the IPNS and TLNS

models are almost identical, the IPNS basic-flow model is computationally more efficient than the TLNS model. Therefore, using the fourth-order compact IPNS model, a high-order accurate and efficient basic-flow model appropriate for stability analysis and transition prediction can be provided.

(3) Besides the global accuracy, the main advantage of the fourth-order compact finite-difference method used for computation of the flow field is that the basic-flow variables and their derivatives required for stability computations are automatically calculated with the fourth-order accuracy. The study shows that the stability results are sensitive to the accuracy of computing the derivatives of basic-flow profiles for a lower number of grid points. For a higher number of grid points, the accuracy of the stability results becomes independent of the way of computing the derivatives.

(4) The present compact Hermitian formulation for solving the stability equations is consistent with the solution of the basic flow and does not require the higher derivatives of the basic-flow profiles, which in general are less accurate.

(5) The present study demonstrates the efficiency and accuracy of using high-order compact solutions of the PNS schemes for use as basic flows for the stability and transition prediction of hypersonic axisymmetric flows.

Acknowledgment

The authors would like to thank Sharif University of Technology and University of Tehran for financial support of this research.

Nomenclature

D_e = explicit dissipation terms
E = total energy per unit volume
f = frequency
h_1, h_2, h_3 = scale factors in ξ, η, ϕ direction
$\bar{F}, \bar{G}, \bar{H}, \bar{F}^*, P$ = transformed flux vectors
J = Jacobian, $J = \xi_x \eta_y - \xi_y \eta_x$
G = generalized inflection profile, $G = d/dy_n(\rho dU/dy_n) - \kappa_2 \rho dU/dy_n$
l_e = Blasius length based on boundary-layer edge conditions, $l_e = \sqrt{\nu_e^* S^*/U_e^*}$
l_∞ = Blasius length based on freestream conditions, $l_\infty = \sqrt{\nu_\infty^* S^*/U_\infty^*}$
L = reference length, R_N for blunt cone and $S^*_{\max}$ for sharp cone
N = N factor
p = pressure
Q = flow-field vector, $Q = (\rho, U, V, W, T)^T$
r = body radius
R_N = dimensional nose radius
Re_∞ = Reynolds number based on freestream conditions and L, $Re_\infty = U_\infty^* L/\nu_\infty^*$
$Re_{e,l}$ = Reynolds number based on freestream conditions and l_e, $Re_{e,l} = U_e^* l_e/\nu_e^* = \sqrt{U_e^* S^*/\nu_e^*}$
$Re_{\infty,l}$ = Reynolds number based on freestream conditions and l_∞, $Re_{\infty,l} = U_\infty^* l_\infty/\nu_\infty^* = \sqrt{U_\infty^* S^*/\nu_\infty^*}$
S = arc length along the body
t = time
T = temperature
u, v = velocity components in x, y direction
U, V, W = velocity components in ξ, η, ϕ direction
$\bar{U}$ = solution vector, $\bar{U} = J^{-1}(\rho, \rho u, \rho v, E)^T$
U_c = contravariant velocity in ξ direction, $U_c = \xi_x u + \xi_y v$
x, y = Cartesian coordinates
α, β = wave numbers in ξ, ϕ direction
$-\alpha_i$ = spatial growth rate
$\bar{\beta}$ = clustering parameter
γ = ratio of specific heats
κ_2 = curvature term, $\kappa_2 = (\partial h_3/\partial y_n)/h_3 = \cos\theta_c/h_3$
θ_c = cone half-angle
ν = kinematic viscosity
ξ, η = computational coordinates
ξ, η, ϕ = intrinsic curvilinear coordinates
ρ = density
ε_e = explicit dissipation coefficient
ω = circular frequency
$\bar{\omega}$ = weighting function

Subscripts

b = basic flow
e = boundary-layer edge condition
i = inviscid vector or imaginary part
n = normal to the wall
r = real part
s = shock condition
$\mathbf{v}$ = viscous vector
w = wall condition
∞ = freestream condition

Superscripts

* = dimensional quantity
$'$ = disturbance quantity
$\wedge$ = amplitude quantity
i = marching index

References

[1] Malik, M. R., Spall, R. E., and Chang, C. L., 1990, "Effect of Nose Bluntness on Boundary Layer Stability and Transition," AIAA Paper No. 90-0112.

[2] Esfahanian, V., 1991, "Computation and Stability Analysis of Laminar Flow Over a Blunted Cone in Hypersonic Flow," Ph.D. thesis, Ohio State University, Columbus.

[3] Herbert, T., and Esfahanian, V., 1992, "Stability of Hypersonic Flow Over a Blunt Body," AGARD-CP-514, Italy.

[4] Kufner, E., Dallmann, U., and Stilla, J., 1993, "Instability of Hypersonic Flow Past Blunt Cones-Effects of Mean Flow Variations," AIAA Paper No. 93-2983.

[5] Stilla, J., 1994, "Engineering Transition Prediction for a Hypersonic Axisymmetric Boundary Layer," J. Aircr., **31**(6), pp. 1358–1364.

[6] Esfahanian, V., and Hejranfar, K., 2002, "Accuracy of Parabolized Navier–Stokes Schemes for Stability Analysis of Hypersonic Axisymmetric Flows," AIAA J., **40**(7), pp. 1311–1322.

[7] Hejranfar, K., 2002, "Computation and Stability Analysis of Hypersonic Axisymmetric Flows Using Parabolized Schemes," Ph.D. thesis, University of Tehran, Tehran.

[8] Esfahanian, V., Hejranfar, K., and Mahmoodi Darian H., 2005, "Implementation of Compact Finite-Difference Method to Parabolized Navier–Stokes Equations," *The 13th Annual Conference of the Computational Fluid Dynamics Society of Canada, CFD 2005*, Newfoundland, Canada.

[9] Esfahanian, V., Hejranfar, K., and Mahmoodi Darian, H., 2006, "Implementation of Compact Finite-Difference Method to Iterative Parabolized Navier–Stokes Equations," *The 25th Congress of International Council of the Aeronautical Sciences (ICAS)*, Hamburg, Germany.

[10] Hejranfar, K., Esfahanian, V., and Mahmoodi Darian, H., 2006, "Implementation of High-Order Compact Finite-Difference Method to Parabolized Navier–Stokes Schemes," Int. J. Numer. Methods Fluids (submitted).

[11] Mahmoodi, H., 2004, "Computation of Parabolized Navier–Stokes Equations Using Compact Finite-Difference Method," MS thesis, University of Tehran, Tehran.

[12] Malik, M. R., 1990, "Numerical Methods for Hypersonic Boundary Layer Stability," J. Comput. Phys., **86**(2), pp. 376–413.

[13] Esfahanian, V., Hejranfar, K., and Sabetghadam, F., 2001, "Linear and Nonlinear PSE for Stability Analysis of the Blasius Boundary Layer Using Compact Scheme," ASME J. Fluids Eng., **123**, pp. 545–550.

[14] Stetson, K. F., Thompson, E. R., Donaldson, J. C., and Siler, L. G., 1983, "Laminar Boundary Layer Stability Experiments on a Cone at Mach 8, Part 1: Sharp Cone," AIAA Paper No. 83-1761.

[15] Stetson, K. F., Thompson, E. R., Donaldson, J. C., and Siler, L. G., 1984, "Laminar Boundary Layer Stability Experiments on a Cone at Mach 8, Part 2: Blunt Cone," AIAA Paper No. 84-0006.

[16] Beam, R. M., and Warming, R. F., 1978, "An Implicit Factored Scheme for the Compressible Navier–Stokes Equation," AIAA J., **16**(4), pp. 393–402.
[17] Mack, L. M., 1987, "Stability of Axisymmetric Boundary Layers on Sharp Cones at Hypersonic Mach Numbers," AIAA Paper No. 87-1413.
[18] Tannehill, J. C., Anderson, D. A., and Pletcher, R. H., 1997, *Computational Fluid Mechanics and Heat Transfer*, 2nd ed., Taylor and Francis, Washington, DC.
[19] Vigneron, Y. C., Rakich, J. V., and Tannehill, J. C., 1978, "Calculation of Supersonic Viscous Flow Over Delta Wings With Sharp Subsonic Leading Edges," AIAA Paper No. 78-1137.
[20] Schiff, L. B., and Steger, J. L., 1980, "Numerical Simulation of Steady Supersonic Viscous Flow," AIAA J., **18**(12), pp 1421–1430.
[21] Barnett, M., and Davis, R. T., 1986, "Calculation of Supersonic Flows With Strong Viscous-Inviscid Interaction," AIAA J., **24**(12), pp. 1949–1455.

Design, Fabrication, and Characterization of a Micro Vapor-Jet Vacuum Pump

Marco Doms
e-mail: m.doms@tuhh.de

Jörg Müller
e-mail: mueller@tuhh.de

Institute of Microsystems Technology,
Hamburg-Harburg University of Technology,
Hamburg 21073, Germany

A microelectromechanical system (MEMS) vapor-jet pump for vacuum generation in miniaturized analytical systems, e.g., micro-mass-spectrometers (Wapelhorst, E., Hauschild, J., and Mueller, J., 2005, "A Fully Integrated Micro Mass Spectrometer," in Fifth Workshop on Harsh-Environment Mass Spectrometry; Hauschild, J., Wapelhorst, E., and Mueller, J., 2005, "A Fully Integrated Plasma Electron Source for Micro Mass Spectrometers," in Ninth International Conference on Miniaturized Systems for Chemistry and Life Sciences (μTAS), pp. 476–478), is presented. A high velocity nitrogen or water vapor jet is used for vacuum generation. Starting from atmospheric pressure, a high throughput of more than 23 ml/min *and an ultimate pressure of* 495 mbars *were obtained with this new type of micropump. An approach for the full integration of all components of the pump is presented and validated by experimental results. The pump is fabricated from silicon and glass substrates using standard MEMS fabrication techniques including deep reactive ion etching, trichlorosilane molecular vapor deposition, and metal-assisted chemical etching for porous silicon fabrication. Micromachined pressure sensors based on the Pirani principle have been developed and integrated into the pump for monitoring.* [DOI: 10.1115/1.2776968]

Introduction

Micropumps are an essential component of many microsystems for chemical and biomedical analyses. Countless approaches to realize miniaturized pumps have been pursued [1–4]. None of them is capable of generating a vacuum that meets the demands of miniaturized complex analytical instruments such as micro-mass-spectrometers [5,6]. In this paper, a new approach to micro-vacuum-pumps is presented. Based on macroscopic vapor-jet and diffusion pumps, a miniaturized pump is designed, fabricated, and characterized. The advantages of this pump mechanism and its miniaturization are as follows:

- There are moving parts, i.e., no friction and wear.
- Multiple stages in a stack arrangement can be used to reach the desired vacuum level.
- No valves are required.
- Small geometries lead to a purely laminar flow even at atmospheric pressure, i.e., the pump can be operated without a foreline pump.

The presented approach is based on the well known macroscopic diffusion pump design. The functional principle is very simple (see Fig. 1). A high pressure gas or vapor inside the jet assembly expands through a Laval nozzle, forming a high velocity jet. The gas molecules to be pumped mix with the jet and are accelerated toward the outlet.

A complete system consists of a heater unit to evaporate the working fluid, the jet assembly (high pressure unit) from where the vapor expands through the nozzles, an area where the pumped gas mixes with the vapor jet, cooled sidewalls to condense the vapor, and a mechanism to return the working fluid to the heater unit. In macroscopic diffusion pumps, an additional foreline pump is required (see Fig. 1). The presented micro vapor-jet pump can be operated at atmospheric pressure due to its small dimension.

Contributed by the Fluids Engineering Division of ASME for publication in the JOURNAL OF FLUIDS ENGINEERING. Manuscript received August 23, 2006; final manuscript received May 22, 2007. Review conducted by Kenneth Breuer. Paper presented at the 2006 ASME Fluids Engineering Division Summer Meeting and Exhibition (FEDSM2006), Miami, FL, July 17–20, 2006.

To simplify the approach, the micropump is divided into three subsystems, which are designed and tested separately before merging them into a complete pump system:

1. The pumping unit with an external supply of the working fluid (gas or vapor). It consists of the jet assembly with Laval nozzles and cooled sidewalls.
2. The working fluid loop, which consists of a reservoir for the liquid, a heater to evaporate it, and a mechanism to return the condensed working fluid to the heater. As the condensed working fluid is located in the atmospheric pressure region, it has to be transported to the heater, which is situated inside the high pressure unit. The pressure difference has to be overcome in order to create a closed loop.
3. A pressure sensor, which can be integrated into the micropump to monitor and control its function.

Gas Dynamics of Vapor-Jet Vacuum Pumps

For the design of the nozzle-sidewall geometry (see Fig. 2 for the nomenclature), gas dynamical calculations derived for macroscopic diffusion pumps were used [7,8].

Laval nozzles are used to generate the supersonic jet. The ratio of flow velocity v and sound velocity c is defined as the Mach number Ma:

$$\mathrm{Ma}_a := \frac{v}{c} = \sqrt{\frac{2}{\kappa - 1}\left[\left(\frac{p_a}{p_0}\right)^{(1-\kappa)/\kappa} - 1\right]} \tag{1}$$

where p_a is the pressure at the nozzle exit and κ is the specific heat ratio. The index 0 denotes the passive state ($v_0 = 0$) of the gas inside the high pressure unit.

The area ratio of the outlet port of the nozzle (A_a and the minimum cross section A^* can be calculated for a given Mach number),

$$\frac{A_a}{A^*} = \frac{b_a}{b^*} = \frac{1}{\mathrm{Ma}}\sqrt{\left[1 + \frac{\kappa - 1}{\kappa + 1}(\mathrm{Ma}^2 - 1)\right]^{(\kappa+1)/(\kappa-1)}} \tag{2}$$

The length of the linearly diverging part of the Laval nozzle is then given by

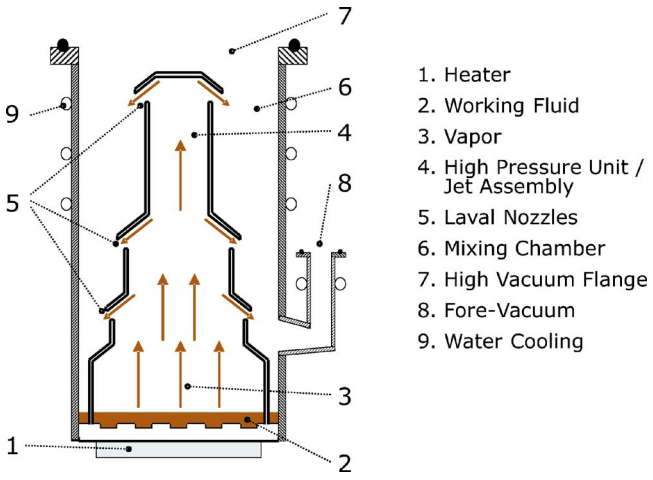

Fig. 1 Schematic diagram of a macroscopic diffusion pump

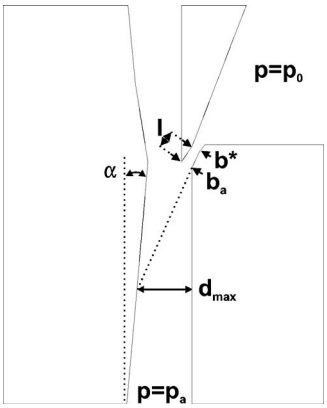

Fig. 2 Schematic drawing of the nozzle-sidewall region of the micropump (top view). See Fig. 4 for the location of this region.

$$l = \frac{b_a - b^*}{2 \tan 5 \text{ deg}} \tag{3}$$

An expansion angle of 5 deg was chosen in order to minimize the risk of turbulence inside the nozzle. The cross-sectional area ratio of the jet is given by

$$\frac{A^*}{A_s} = \frac{b^*}{b_s} = \sqrt{\frac{[(\kappa+1)/2]^{(\kappa+1)/(\kappa-1)}}{(\kappa-1)/2}\left[\left(\frac{p_s}{p_0}\right)^{2/\kappa} - \left(\frac{p_s}{p_0}\right)^{(1+\kappa)/\kappa}\right]} \tag{4}$$

where the index s denotes the position where the jet impinges the sidewall [7,8] (p_s is the pressure inside the jet right before it impinges the wall). Together with the static pressure ratio

$$\frac{p_a}{p_0} = \frac{\kappa+1}{\kappa-1}\left(\frac{p_s}{p_0}\right)^{1/\kappa} \frac{[1-(p_s/p_0)^{(\kappa-1)/\kappa}]^{\kappa/(\kappa-1)}}{[4\kappa/(\kappa+1)^2 - (p_a/p_0)^{(\kappa-1)/\kappa}]^{1/(\kappa-1)}} \tag{5}$$

the maximum allowed distance d_{max} between the nozzle and the sidewall is defined as $d_{max}=A_s/(\text{pump height})$. Equation (5) is solved for p_s/p_0 and the result is inserted into Eq. (4). A^*/A_s now defines the ratio between the minimum jet diameter (inside the nozzle) and the maximum jet diameter (where the jet is supposed to impinge the sidewall). As the solution of Eq. (5) is fairly difficult, both equations are plotted and A^*/A_s is taken from the graph. If the distance between the nozzle and the sidewall is further increased, the jet does not impinge the sidewall and no pumping occurs.

As the jet does not propagate linearly, the position of the impingement is not known. This is why it is not exactly clear where to measure the distance d for slanted sidewalls. As is apparent from Fig. 2, changing the sidewall angle α causes a change in d_{max}. For the design, it was assumed that the impingement occurs in the extension of the nozzle, as shown in Fig. 2.

Design and Fabrication

The design and fabrication of the three micropump subsystems are presented in the following sections. Figure 3 shows a sectional drawing of the complete system. It consists of five anodically bonded substrates.

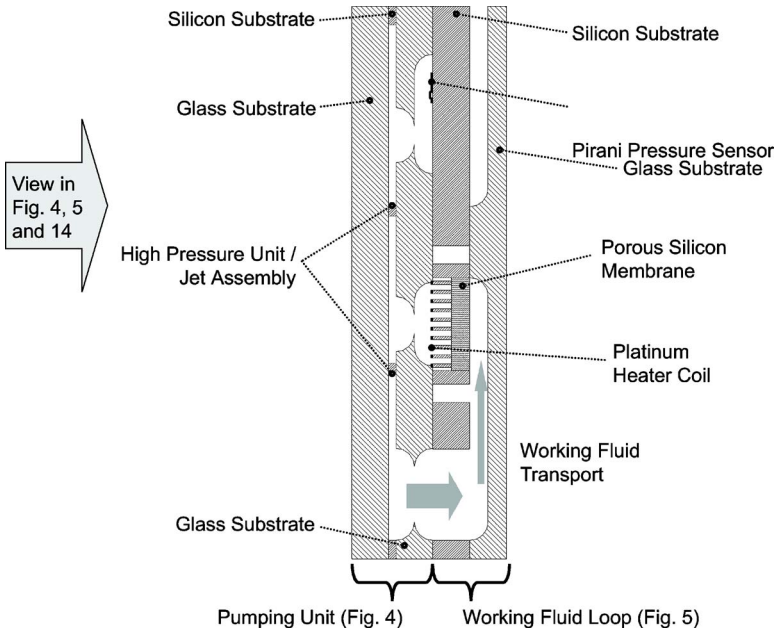

Fig. 3 Sectional drawing of the micro vapor-jet pump (side view)

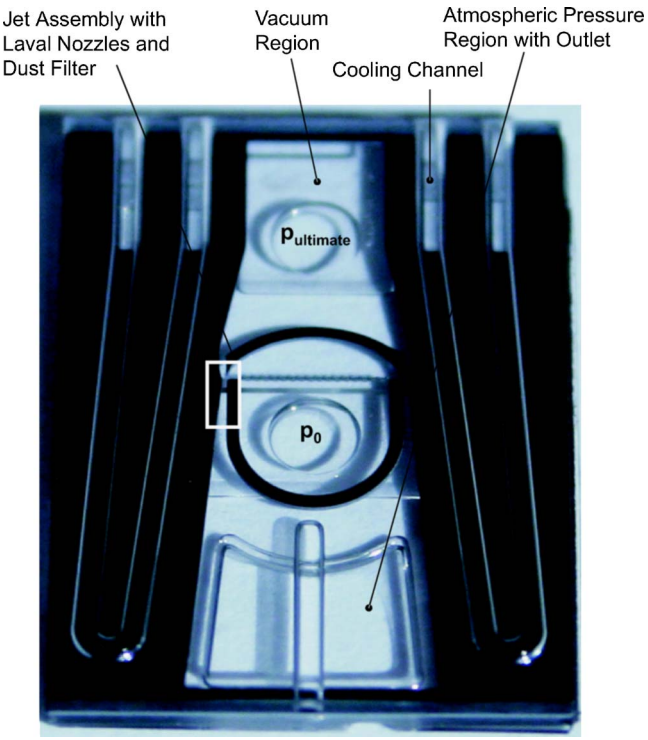

Fig. 4 The pumping unit (top view). The white box indicates the position of the geometry from Fig. 2.

Top views of the micropump subsystems are depicted in Fig. 4 (pumping unit) and Fig. 5 (fluid transport system, heater, and pressure sensor). These two subsystems are anodically bonded to form the complete pump, as drafted in Fig. 3.

Pumping Unit: Nozzles and Sidewall. Using Eqs. (1)–(3), the geometry of the Laval nozzles can be calculated. For a given

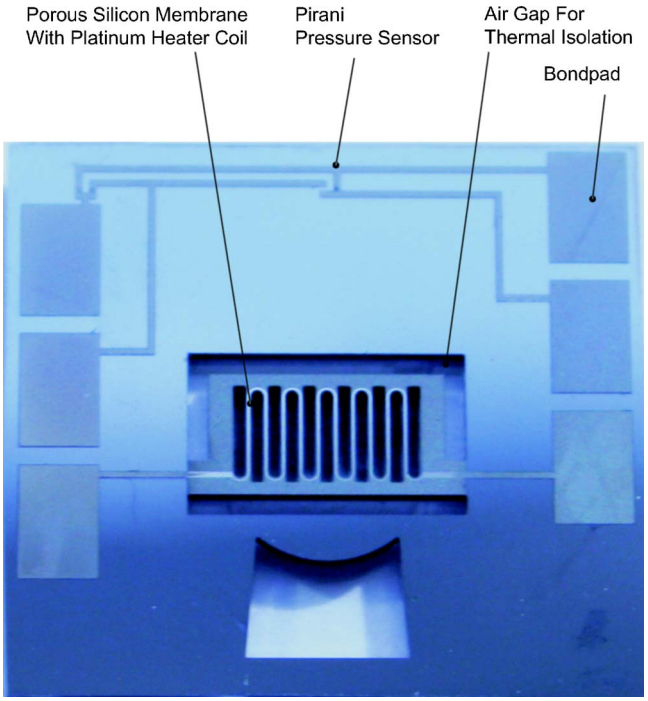

Fig. 5 Working fluid transport system and pirani pressure sensor (top view)

Table 1 Geometry of the Nozzle-Sidewall Region

Ma	p_0 (bar)	b^* (μm)	b_a (μm)	l (μm)	d_{max} (μm)
1.5	3.6	20	24	20	90
1.75	5.3	20	28	44	140

Mach number, the required pressure inside the jet assembly is defined. For a given b^*, which is defined by the fabrication processes, b_a and l can be calculated. Equations (4) and (5) are used to compute the maximum distance between the nozzle and the sidewall. The geometry of the presented system is given in Table 1.

Different angles α of the pump sidewall were investigated as they are expected to influence the backstreaming behavior of the gas or vapor (nitrogen gas or water vapor in this case). A mechanical filter structure is integrated into the high pressure unit to avoid blocking of the nozzles due to dust or residues from dicing the systems.

The pumping unit is fabricated from a 100 μm thick silicon substrate, which is sandwiched between two glass substrates by anodic bonding. The pump structure is created by deep reactive ion etching (DRIE) (ASE™). A molecular vapor deposition [9] (MVD) process with a trichlorosilane (dimethyldichlorosilane (DDMS), heptadecafluoro-1, 1, 2, 2-tetrahydrodecyltrichlorosilane (FDTS), or tridecafluoro-1, 1, 2, 2-tetrahydrooctyltrichlorosilane (FOTS)) as precursor is used to deposit a molecular hydrophobic layer inside the pumping system. The coating guides the condensed fluid from the pumping unit to the hydrophilic channel of the transport system (see Fig. 2). Channels in the top glass substrate can be used to supply water for cooling. Three openings in the bottom glass substrate are used to supply the working fluid, to perform measurements, and to act as an outlet. The same openings are used as interconnects between the pumping unit and the fluid channel, the heater, and the pressure sensor of the fluid transport unit in the closed-loop system.

Working Fluid Loop: Vaporization and Fluid Transport. As described before, the working fluid condenses on the cooled sidewalls of the pump. From the atmospheric pressure region of the micropump, the fluid has to be transported to the heater. This is achieved by locally varying the surface energy of the system. Hydrophobic coatings (MVD deposited trichlorosilanes) define regions where the fluid is repelled, hydrophilic surfaces (glass, oxides) attract the fluid.

The main problem in transporting the fluid to the heater is the high pressure difference between the high pressure heater region and the low pressure region where the working fluid condenses.

A mesoporous silicon membrane [10], fabricated by metal-assisted chemical etching, is used to "absorb" this pressure. Due to the capillary forces inside the porous membrane, the working fluid is conducted toward the heater despite the high counterpressure. The maximum pressure the pores can absorb is given by

$$F_{pore} = 2\pi R_{pore}\gamma\cos\Theta = pA_{pore} = p\pi R_{pore}^2 = F_{pressure} \qquad (6)$$

where R_{pore} is the pore radius, γ is the surface free energy of the porous silicon, and Θ is the contact angle of the working fluid (water) on the walls of the pores (adapted from Ref. [11]). For a contact angle of θ=30 deg of water on a silicon oxide surface (the pore sidewalls will be covered with natural oxide due to the elevated temperature near the heater) and a surface free energy of $\gamma=5.89\times10^{-2}$ N/m, the results are given in Table 2. As the pore radius of the mesoporous silicon membrane is around 300 nm, the expected available pressure inside the jet assembly of the micropump lies in the range of 3 bars.

A platinum heater coil, fabricated on top of the porous membrane, is used to evaporate the working fluid. Around the membrane, an air gap is etched into the silicon substrate to thermally isolate the heater. Figure 5 shows a photograph of this subsystem.

Table 2 Maximum Pore Diameter of the Mesoporous Silicon for Different Pressures Across the Membrane

Pressure (bar)	Pore radius (nm)
5	200
3	340
2	510
1.5	680

The silicon substrate with its mesoporous membrane, the heater, and the supply channel is anodically bonded between two glass substrates with the necessary interconnects.

Pirani Pressure Sensor. A pressure sensor based on the Pirani principle is integrated into the micropump to monitor and control its function [12]. The sensor is fabricated on the same substrate as the working fluid loop and is depicted in Fig. 5.

Pirani sensors use an electrically heated freestanding bridge or wire to measure the pressure dependent thermal conductivity of a gas. The sensor is assembled in a bridge circuit. The reference resistor is positioned close to the sensor to compensate for temperature changes. The thermal conductivity of a gas for a Pirani sensor in a parallel plate configuration is found as (p is the pressure of the surrounding gas, $\bar{c}$ the average velocity, and $\bar{l}$ the mean free path of the gas molecules)

$$\lambda = \frac{\bar{c}}{2}\frac{C_{\text{molar},V}}{RT}_{\lambda_0}\bar{l}p\frac{d}{d+2\bar{l}(2/a_E-1)}_{G_E} \tag{7}$$

where a_E is the accommodation coefficient(a_E=0.77 for nitrogen on clean platinum surfaces [7]), λ_0 is the pressure independent thermal conductivity for the high pressure range ($\bar{l} \ll d[a_E/2(2-a_E)] \Rightarrow G_E=1$), and G_E is a geometry factor. The thermal conductivity (a material property) does not change with pressure, since the pressure dependence of $\bar{l}$ cancels with p ($\bar{l} \sim 1/p$). In a thermal conductivity pressure sensor, the characteristic length of the system limits the allowable mean free path of the gas molecules and the thermal conductivity is proportional to p. Therefore, the characteristic dimension of the sensor (the distance between the wire and the substrate, d) needs to be smaller than $\bar{l}$ within the desired range of operation.

Figure 6 depicts Eq. (7) for three different gap widths d. The measurement range of the device shifts to lower pressure with increasing distance between the wire and the substrate. Beyond an upper pressure limit, the thermal conductivity becomes independent of the gas pressure (continuum regime). On the vacuum side, a low pressure limit exists, where the thermal conductivity of the gas becomes small compared to the heat that is lost to the substrate through the leads. The operating range, where the distance between the heated bridge and the substrate defines the mean free path and the thermal conductivity is pressure dependent (molecular regime), is located between these two pressure independent regimes. Furthermore, transition regions form as the molecular regime approaches the continuum and the vacuum regime, respectively.

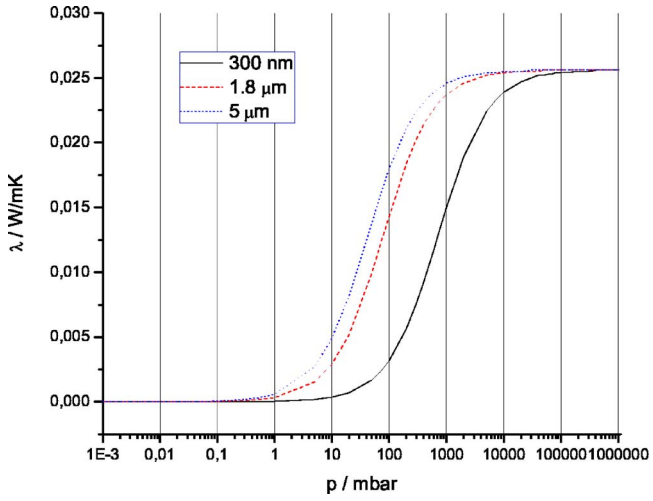

Fig. 6 Theoretical pressure dependent thermal conductivity for different distances between the heated bridge and the substrate

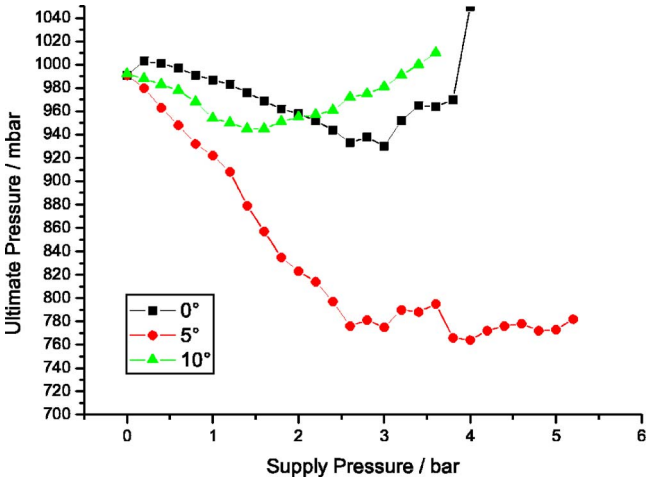

Fig. 7 Ultimate pressure as a function of N_2 supply pressure for different sidewall angles

The Pirani sensors are fabricated on silicon substrates. A ZnO sacrificial layer is sputter deposited on the substrate and structured with diluted HCl. The thickness of the ZnO layer defines the distance between the heated bridge and the substrate. The freestanding bridges are made of platinum. To change the operating range of the Pirani sensor, only the thickness of the ZnO layer has to be varied to obtain the desired gap width between the heated bridge and the substrate.

Results

Experimental results for the three micropump subsystems are presented in the following sections.

Pumping. To characterize the pumping unit of the micro vapor-jet pump, nitrogen gas and water vapor were externally supplied to the high pressure unit and used as working fluids. Calibrated pressure and flow sensors (Greisinger GMH3155/GMSD2BA (accuracy of ±0.6%), Voegtlin red-y smart (accuracy of ±0.5%)) were attached to the system to measure the generated pressure and throughput. All figures presented in this section show the characteristics of a single system measured once. Repeated measurements of the same system gave nearly identical results with a deviation of ±2 mbars. Measurements of different systems with the same design produced results within 15%, which can be explained by the variations in geometry (typically ±10%) caused by inhomogeneous etching. (The etch rate at the wafer edge is 20% higher than that at the wafer center, causing a significant undercut in the systems at the wafer edge.)

Figure 7 depicts the pump characteristics of systems with different sidewall angles. The minimum ultimate pressure is reached for a 5 deg sidewall angle. It is not fully understood why increasing or decreasing the angle seems to impede the pumping.

Figure 8 depicts the ultimate pressure for different distances between the nozzle and the sidewall. The largest distance gives the best results, which indicates that the maximum distance $d_{\max}$

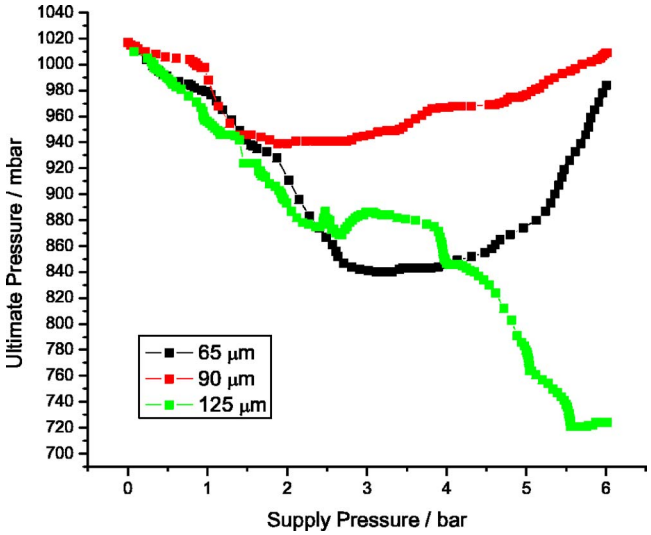

Fig. 8 Ultimate pressure as a function of N_2 supply pressure p_0 for different distances between nozzle and sidewall (5 deg sidewall angle)

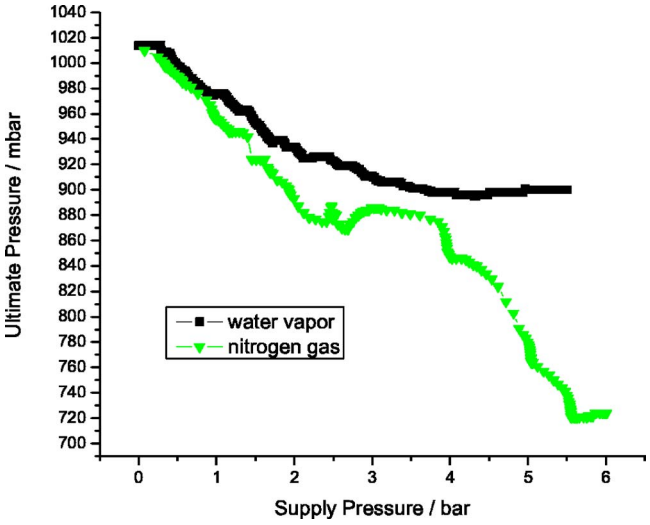

Fig. 10 Ultimate pressure as a function of water vapor and nitrogen gas supply pressures (5 deg sidewall angle, d =125 μm)

has not been exceeded. Larger distances will be investigated in the near future to determine the exact position where to measure the distance given by Eqs. (4) and (5). The minimum pressure that was reached with externally supplied nitrogen is 720 mbars with a 5 deg sidewall angle and a distance between the nozzle and the sidewall of 125 μm.

Figure 9 shows the measured throughput for that system. For this measurement, the pressure sensor (p_{ultimate}) was replaced by a flow sensor. A maximum throughput of 23.1 ml/min was reached with a relatively low supply pressure of around 3 bars. While a higher supply pressure is needed to generate a lower ultimate pressure, it is not needed for a high throughput.

Figure 10 shows the characteristic of the 125 μm system from Fig. 7 with water vapor as a working fluid. Until a supply pressure of about 3 bars is reached, nearly no difference to the experiments with nitrogen as a working fluid is noticeable. At higher pressures, the water accumulates at the outlet of the system and blocks it. The consequential increase of the pressure inside the atmospheric pressure region impedes the pumping and leads to a rise in pressure in the vacuum region of the system.

Several systems with identical nozzle-sidewall geometries but a wider outlet were also tested. These systems reached an ultimate pressure of 495 mbars when water vapor was used as a working fluid. In these systems, the observed accumulation of water, and thus the obstruction of the pumping, was less. Almost all of the systems break during the water vapor measurement due to the high temperature and the high stress resulting from the necessary clamping of the system. Unfortunately, no graph can be shown for the system that showed 495 mbars; only a minimum pressure was recorded.

It is expected that the minimization of the water consumption, and thus the reduction of the amount of water to be removed from the pumping unit, will decrease the ultimate pressure drastically. The minimization will be achieved by the use of smaller nozzles.

Working Fluid Loop. The working fluid transport system (see Fig. 5) including the porous silicon membrane and the platinum heater was characterized by connecting a pressure sensor to the high pressure output and applying electrical power to the heater. Water was supplied to the water inlet port.

Figure 11 shows the generated pressure (which will later serve

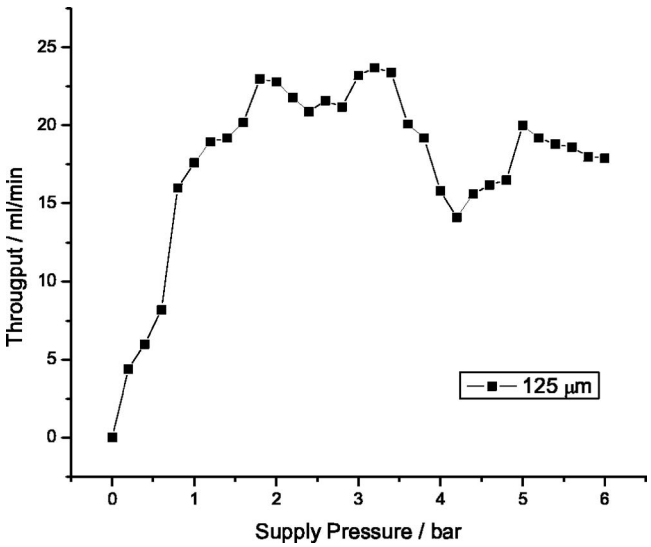

Fig. 9 Throughput as a function of N_2 supply pressure p_0 (5 deg sidewall angle)

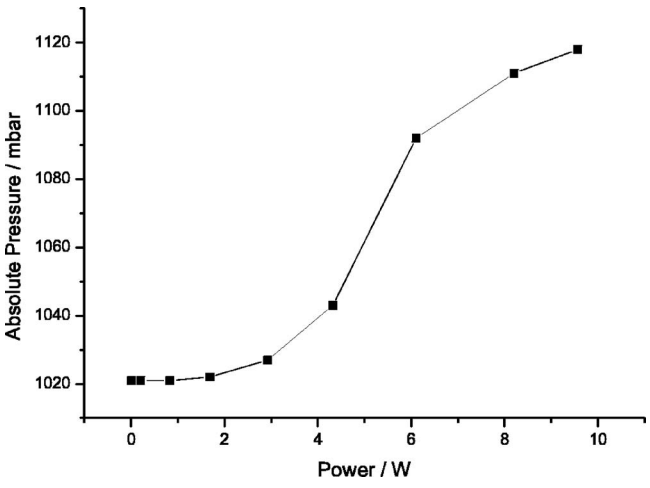

Fig. 11 Pressure generated by the heater from Fig. 5 as a function of supplied electrical power

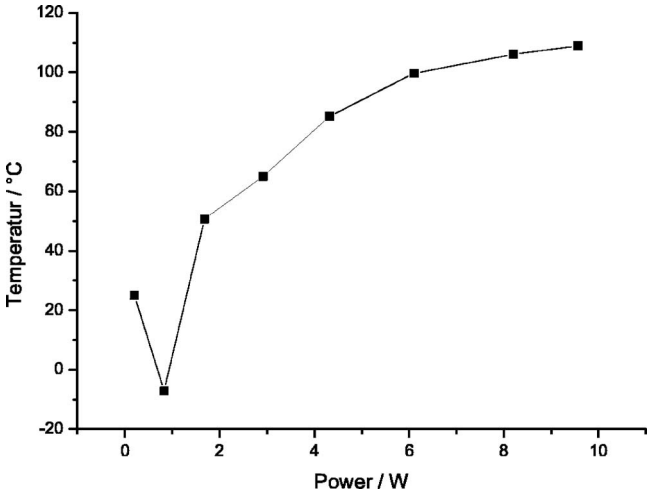

Fig. 12 Temperature of the heater as a function of supplied power

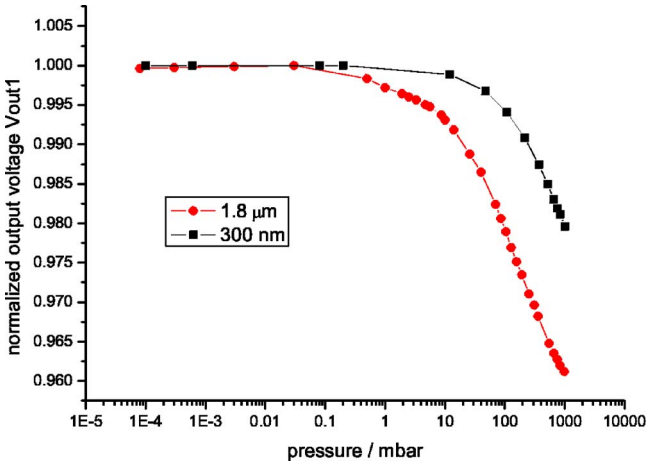

Fig. 13 Voltage-pressure characteristics of two pirani pressure sensors with different gap widths ($V_{inconst}$=5 V, bridge geometry: 8×100 μm^2)

as supply pressure p_0) as a function of supplied electrical power. (The supplied voltage and the supplied current are measured simultaneously with accuracies of 0.001 V and 0.1 mA, respectively.) An overpressure of about 100 mbars was reached at an input power of about 10 W. Other systems generated an overpressure of up to 300 mbars at 10 W input power. The pressure is assumed to be much higher inside the fully integrated pump system than the measured one due to the following reasons:

— During the measurements, the water condenses in the tube connecting the heater system and the pressure sensor.
— Water had to be supplied to the water inlet port regularly to substitute for the evaporated fluid, causing a decrease of temperature and pressure.

Figure 12 depicts the temperature of the heater as a function of supplied electrical power. The temperature is calculated from the change in resistance. (The first order temperature coefficient of the sputtered platinum layer has been measured as α=0.00188.) It is assumed that the 130°C necessary for creating a pressure of 3 bars [13] can be reached with a slightly increased supply power.

The concept of using a porous silicon membrane to absorb the high pressure generated by the heater is proven to be effective. Increased supply power, an optimized heater design, and an improved thermal isolation of the heater will lead to a higher generated pressure, and thus a fully functional pump system.

Pirani Pressure Sensor. A vacuum chamber equipped with a foreline vacuum pump, a turbomolecular pump, and two calibrated pressure sensors (Leybold Inficon Sky ((5×10^{-10})–10 mbars), Greisinger GDH 12 AN (0–1300 mbar absolute, accuracy of ±1 mbar)) were used to characterize the micro-Pirani pressure sensors. A manual valve was used to vent the chamber with nitrogen gas. A constant voltage of 5 V was applied to the bridge circuit. The micro-Piranis were inserted into the test setup, the chamber was evacuated and slowly vented while the bridge voltage was monitored as a function of the chamber pressure.

Figure 13 depicts the measured output voltage of two micro-Piranis with different gap widths. The characteristic of the micro-Pirani with the wider gap shifts toward a lower pressure regime, as predicted by the theory (see Fig. 6). Repeated measurements of the same Pirani gave identical results within a range of less than ±1 mV.

An operating range at even lower pressure could be easily obtained by further increasing the deposition time of the sacrificial layer and with it the distance between the heated bridge and the substrate. As no change of the mask design is necessary to do this adaption, the presented device can serve different applications at low cost.

Complete System

Figure 14 depicts the complete micropump. It is assembled from the two subsystems shown in Figs. 4 and 5.

For the measurements, the reservoir was filled with water, electrical power was applied to the heater, and an external pressure sensor was used to measure the generated pressure.

During the measurements, the evaporated water did not only fill the high pressure unit but the whole micropump due to incomplete bonding between the two subsystems. As the bonded areas are not visible, an inspection is not possible. Thus, the optimization of the bonding process will solve this problem and lead to a working micropump system.

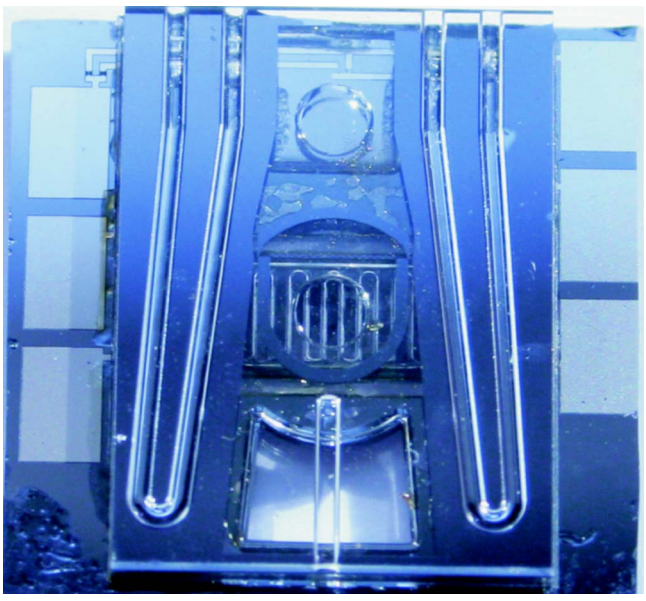

Fig. 14 The complete micropump consisting of the systems from Figs. 4 and 5

Conclusion and Outlook

The first micromachined vapor-jet pump is presented. The pump is divided into three subsystems: the pumping unit, the working fluid transport unit, and a micro-Pirani pressure sensor. The aim is a fully integrated and microfabricated vapor-jet pump that is capable of generating a high throughput and a low pressure in the range of several pascals.

It is proven that the pumping mechanism can be transferred to microsystems. A pump system with an external supply of nitrogen gas and water vapor, respectively, has been designed, fabricated, and characterized. Starting from atmospheric pressure, a maximum throughput of 23 ml/min and an ultimate pressure of 495 mbars were reached with different pump geometries. The performance will be further improved by the use of different working fluids, multiple nozzle stages, and smaller Laval nozzles to decrease the working fluid consumption of the system.

The working fluid transport is based on a mesoporous silicon membrane and regions with locally altered surface energy. A planar platinum coil serves as a heater to evaporate the fluid. Characteristics of the fluid transport subsystem of the micropump have been presented. It is shown that a porous membrane can be used to absorb the high pressure difference, and thus create a closed working fluid loop.

A microfabricated Pirani pressure sensor is integrated into the pump system to monitor and control its function. The sensor gives precise pressure readings and its operating range can easily be altered during the fabrication process.

So far, assembling the complete system from all three subsystems by bonding the systems from Figs. 4 and 5 and failed due to incomplete bonding. The optimization of the bonding process will lead to a fully integrated and working micropump.

References

[1] Nguyen, N., Huang, X., and Chuan, T., 2002, "MEMS-Micropumps: A Review," ASME J. Fluids Eng., **124**, pp. 384–392.

[2] Woias, P., 2001, "Micropumps—Summarizing the First Two Decades," Proc. SPIE, **4560**, pp. 39–52.

[3] Laser, D., and Santiago, J., 2004, "A Review of Micropumps," J. Micromech. Microeng., **14**, pp. R35–R64.

[4] Shoji, S., and Esahi, M., 1994, "Micro Flow Devices," *IEEE Fifth International Symposium on Micro Machine and Human Science*, pp. 89–95.

[5] Wapelhorst, E., Hauschild, J., and Mueller, J., 2005, "A Fully Integrated Micro Mass Spectrometer," in *Fifth Workshop on Harsh-Environment Mass Spectrometry*.

[6] Hauschild, J., Wapelhorst, E., and Mueller, J., 2005, "A Fully Integrated Plasma Electron Source for Micro Mass Spectrometers," in *Ninth International Conference on Miniaturized Systems for Chemistry and Life Sciences* (μTAS), pp. 476–478.

[7] Wutz, M., Adam, H., and Walcher, W., 1992, *Handbuch Vakuumtechnik*, Vieweg, Braunschweig.

[8] Doms, M., and Müller, J., 2005, "A Micromachined Vapor-Jet Pump," Sens. Actuators, A, **119**(2), pp. 462–467.

[9] Ashurst, W., Carraro, C., and Maboudin, R., 2003, "Vapor Phase Anti-Striction Coatings for MEMS," IEEE Trans. Device Mater. Reliab., **3**(4), pp. 173–178.

[10] Cruz, S., Hönig-d'Horville, A., and Mueller, J., 2005, "Fabrication and Optimization of Porous Silicon Substrates for Diffusion Membrane Applications," J. Electrochem. Soc., **152**(6), pp. 418–424.

[11] Munson, B., Young, D., and Okiishi, T., 2006, *Fundamentals of Fluid Mechanics*, Wiley, New York.

[12] Doms, M., Bekesch, A., and Müller, J., 2005, "A Microfabricated Pirani Pressure Sensor Operating Near Atmospheric Pressure," J. Micromech. Microeng., **15**, pp. 1504–1510.

[13] Schmidt, E., 1989, *Properties of Water and Steam in SI-Units*, Springer, Berlin.

Streaming Electric Potential in Pressure-Driven Flows Through Reservoir-Connected Microchannels

S. A. Mirbozorgi
Mechanical Engineering Department,
University of Birjand,
Birjand 97175–376, Iran

H. Niazmand
Mechanical Engineering Department,
Ferdowsi University of Mashhad,
Mashhad 91775–1111, Iran

M. Renksizbulut[1]
Mechanical and Mechatronics Engineering Department,
University of Waterloo,
Waterloo, ON, N2L 3G1, Canada
e-mail: metin@uwaterloo.ca

Electrical power generation employing pressure-driven flows is a fundamental problem in microfluidics. In the present work, analytical and numerical analyses are performed to study the interplaying effects of electrolyte motion with the associated electrical current in a flat microchannel with and without fluid reservoirs. The modified Navier–Stokes equations as well as a Poisson equation for the distribution of electric potential and the Nernst–Planck equations for the distribution of charge densities are solved for the steady flow of a Newtonian liquid. The results show that for a pressure-driven flow, an electric potential is induced due to the motion of charged particles, which increases linearly along the microchannel. This streaming potential generates an opposing conduction current in the core region of the channel as well as in the immediate vicinity of the walls, where the streaming current is negligible. The streaming potential varies in a nonlinear manner with the zeta potential at the walls such that a maximum potential exists at a certain zeta potential. The maximum potential is also observed to increase with both the applied pressure difference and the electric double layer thickness in the range studied. The presence of reservoirs adds significant complexity to this electrokinetic flow. [DOI: 10.1115/1.2776967]

Keywords: electrokinetic flow, zeta potential, microchannel flow, reservoir effects, streaming electric potential

1 Introduction

Interest in electrical power generation by means of electrolyte flows through microchannels has stimulated many fundamental studies on electrokinetic phenomena. Channels with characteristic sizes or diameters measured in microns are called microchannels, which typically have very large surface area to volume ratios, and some physical processes that are not important in macrochannels become prominent. One such process is associated with electrostatic charges that often exist at channel walls. Related studies have mainly focused on either electro-osmotic flows or electrokinetic flows. As a base for micropumps, electro-osmotic flows involve electrolyte solutions driven by externally applied electric fields. As a base for micro-scale power supplies, electrokinetic flows involve electrolytes forced through dielectric microchannels to generate electric potential. In the present work, the generation of electric potential by means of pressure-driven flows through dielectric microchannels is studied, including the effects of connected reservoirs that have been largely ignored in the literature. The primary objectives are to develop a better understanding of the underlying processes and to determine the maximum induced voltage in a given electrokinetic flow.

In a typical macroscale pressure-driven flow, an applied pressure gradient forces the fluid through the duct. However, in a microchannel with an electrolyte solution as the working fluid, the pressure-driven flow is coupled with electrokinetic effects due to the presence of an electric double layer (EDL) in the vicinity of the walls [1]. With the forced motion of the fluid, the mobile ions in the EDL are carried with the flow, thus generating a streaming current and an associated streaming voltage.

In one of the earliest studies, Burgreen and Nakache [2] analytically modeled the effect of surface potential on microflow between parallel plates, with the EDL thickness parameter k in the range of 2–8. They obtained an analytical solution for combined electro-osmotic and pressure-driven flows. An explicit integral relation for the streaming potential was also derived for the pressure-driven flow. Rice and Whitehead [3] repeated this work for a circular capillary, while Levine et al. [4] extended the solution to the higher surface potentials in a circular capillary by using an approximate solution of the Poisson–Boltzmann equation.

Yang and Li [5] and Yang et al. [6] considered pressure-driven liquid flows in the rectangular microchannels. Their analytical solution predicted significant electroviscous effects for different aspect ratios of the channel cross section. In addition, an integral expression for the induced electric potential was derived as a function of Reynolds number for different electrolyte concentrations and zeta potentials. Ren et al. [7,8] also performed an experimental study to describe the EDL effects on the velocity field based on the concept of electroviscous effects.

Yang and Kwok [9,10] presented an in-depth analytical solution of an oscillating microfluid in a parallel-plate microchannel by combining the electrokinetic effect with liquid slip. Considering liquid slip over hydrophobic walls, they derived an analytical solution for both electro-osmotic and pressure-driven flows with EDL effects. Their results showed that liquid slip counteracts the electroviscous effect of EDL, resulting in a larger flow rate, while a higher apparent viscosity would be predicted if slip is neglected.

Chen et al. [11] developed a model to numerically study electrokinetic effects on both hydrodynamically and thermally developing flows in parallel-plate microchannels using the Nernst–Planck equations with variable thermophysical properties. Their results showed that the presence of EDL in the developing flow

[1]Corresponding author.

Contributed by the Fluids Engineering Division of ASME for publication in the JOURNAL OF FLUIDS ENGINEERING. Manuscript received August 28, 2006; final manuscript received May 16, 2007. Review conducted by Ali Beskok.

region decreases the fluid velocities resulting in velocity distributions that deviate from their pure pressure-driven flow counterparts.

All of the above investigations are concerned with the electric potential in order to explain the electroviscous effect in pressure-driven flows. However, another application of this phenomenon is the electrokinetic battery concept proposed by Yang et al. [12], which involves an array of microchannels. Since the streaming current is typically of the order of 1 nA/kPa in a single microchannel, they hypothesized that if many microchannels are assembled in parallel, the streaming currents would be additive and can be significant. Their results based on a transient analytical solution showed that the idea of an electrokinetic microbattery is feasible. Next, Chun et al. [13] presented a detailed analysis of electrokinetic phenomenon in a uniformly charged straight cylindrical microchannel. It is shown that the flow-induced streaming potential increases with increasing zeta potential, decreasing wall conductivity, and increasing microchannel radius. They also observed that a maximum value of streaming potential can be obtained with variations of bulk electrolyte concentration.

Mansouri et al. [14] investigated the transient development of streaming potential for a pressure-driven flow in a finite-length circular microchannel connected to infinitely large reservoirs. Their numerical simulation based on a finite element analysis showed that the streaming potential heavily depends on the geometry, ionic concentration, and surface charge density. They indicated that the origin of streaming potential is charge accumulation in the reservoirs at the entrance and exit of the channel, while no axial charge gradient occurs within the microchannel during transient transport.

This review of the relevant literature shows that even though the fundamental features of electrokinetic flows have been identified and analyzed, the effects of fluid reservoirs on the flow field, the electric field, and the induced electric potential have not been examined in detail. The authors have recently investigated the role of fluid reservoirs in pure electro-osmotic flows through microchannels [15]. Here, attention is focused on electrokinetic pressure-driven flows in large aspect-ratio microchannels modeled as flow between parallel plates. Particular attention is given to the presence of fluid reservoirs and to the application of conservation of electrical current, leading to the development of new boundary conditions for the electric potential field. Furthermore, an analytical solution is provided for a simplified pressure-driven flow in the presence of EDL effects. Closed form expressions are given for the velocity field and streaming and conduction currents, and, more importantly, the induced electric potential is related to the applied pressure difference and other relevant parameters. The governing equations including the Poisson equation for the distribution of EDL potential, the Nernst–Planck equations for the distribution of charge density, the continuity equation, and the modified Navier–Stokes equations are solved for the incompressible and steady flow of a Newtonian fluid. These equations are numerically solved using a finite-volume method in a generalized coordinate system. The ultimate goal is to determine the maximum induced voltage in a given electrokinetic flow.

2 Mathematical Model

Consider a parallel-plate microchannel with height H and length L placed between two identical reservoirs, as shown in Fig. 1. The Cartesian coordinate system used here is anchored at the flow inlet, where $y=0$ corresponds to the elevation of the lower plate. An electrolyte solution (KCl in water) is driven in the positive x direction by means of an applied pressure difference $\Delta P = P_{\text{in}} - P_{\text{out}}$. It is assumed that the channel and the reservoirs are made of different materials such that the reservoir walls are charge free, while the electric potential at the microchannel walls is uniform and equal to ζ.

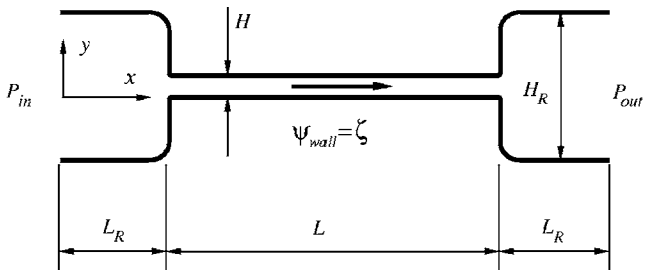

Fig. 1 Flow geometry and coordinates

2.1 Electric Field. It is well known that when an ionized liquid interacts with electrostatic charges on a dielectric surface, a so-called EDL forms in the liquid in the vicinity of the surface. The distribution of electric potential $\Psi(x,y)$ in the fluid is related to the net electric charge density ρ_e via a Poisson equation in the following nondimensional form:

$$\frac{\partial^2\Psi}{\partial x^2} + \frac{\partial^2\Psi}{\partial y^2} = -\frac{1}{2}k^2\rho_e \tag{1}$$

where $k=HK$ is the EDL parameter. Here, $K = (2z^2e^2n_0/\varepsilon_r\varepsilon_0k_bT)^{1/2}$ is a dimensional group referred to as the Debye–Hückel parameter, and its reciprocal represents the characteristic EDL thickness. The net charge density in the fluid is determined by the ionic concentrations, and for a symmetric electrolyte, $\rho_e = n^+ - n^-$ in nondimensional form.

2.2 Ionic Concentrations. The distributions of ionic concentrations n^+ and n^- in the flow field are governed by the following Nernst–Planck equations:

$$\frac{\partial(un^+)}{\partial x} + \frac{\partial(vn^+)}{\partial y} = \frac{1}{\text{ScRe}}\left[\frac{\partial^2 n^+}{\partial x^2} + \frac{\partial^2 n^+}{\partial y^2} + \frac{\partial}{\partial x}\left(n^+\frac{\partial\Psi}{\partial x}\right) + \frac{\partial}{\partial y}\left(n^+\frac{\partial\Psi}{\partial y}\right)\right] \tag{2}$$

$$\frac{\partial(un^-)}{\partial x} + \frac{\partial(vn^-)}{\partial y} = \frac{1}{\text{ScRe}}\left[\frac{\partial^2 n^-}{\partial x^2} + \frac{\partial^2 n^-}{\partial y^2} - \frac{\partial}{\partial x}\left(n^-\frac{\partial\Psi}{\partial x}\right) - \frac{\partial}{\partial y}\left(n^-\frac{\partial\Psi}{\partial y}\right)\right] \tag{3}$$

where $\text{Re} = \rho U_{\text{ref}} H/\mu$ is the Reynolds number. Here, the reference velocity is chosen as the maximum velocity corresponding to the classical Poiseuille flow between parallel plates; that is $U_{\text{ref}} = u^*_{\max} = H^2\Delta P^*/8\mu L^*$. Also, $\text{Sc} = \mu/\rho D$ is the Schmidt number, where D is the diffusion coefficient of the ions. The diffusion coefficients of the positive and negative ions in a KCl-water solution are commonly considered equal and constant. The first two terms on the right hand side of Eqs. (2) and (3) are the familiar diffusion terms due to concentration gradients, while the last two terms are known as the conduction (or migration) terms.

2.3 Modified Navier–Stokes Equations. In the present work, the electrolyte solution is treated as a constant-property Newtonian fluid. For the steady electrokinetic flow under consideration, the continuity and momentum equations in nondimensional form are

$$\frac{\partial u}{\partial x} + \frac{\partial v}{\partial y} = 0 \tag{4}$$

$$\frac{\partial(uu)}{\partial x} + \frac{\partial(vu)}{\partial y} = -\frac{\partial P}{\partial x} + \frac{1}{\text{Re}}\left(\frac{\partial^2 u}{\partial x^2} + \frac{\partial^2 u}{\partial y^2}\right) - B\rho_e\frac{\partial\Psi}{\partial x} \tag{5}$$

$$\frac{\partial(uv)}{\partial x}+\frac{\partial(vv)}{\partial y}=-\frac{\partial P}{\partial y}+\frac{1}{\mathrm{Re}}\left(\frac{\partial^2 v}{\partial x^2}+\frac{\partial^2 v}{\partial y^2}\right)-B\rho_e\frac{\partial\Psi}{\partial y} \quad (6)$$

The last term in the momentum equations above is the body force associated with the induced electric field where $\Psi(x,y)$ includes the combined effects of the zeta potential at the walls and the flow-induced electric potential.

2.4 Boundary Conditions. The boundary conditions for this complex flow require special attention, particularly for the electric potential and the ionic concentration fields. It should be noted that in the present work, the electrokinetic flow in the microchannel is allowed to develop naturally based on the reservoir conditions rather than physically unrealistic boundary conditions often specified at the channel ends in the absence of reservoirs. The boundary conditions associated with the velocity, ionic concentration, and electric potential fields are described in detail below.

2.4.1 Flow Field. The usual no-slip velocity boundary condition ($u=v=0$) is applied at the walls. Consistent with pressure-driven flows, $\partial u/\partial x=0$ and $v=0$ are applied at the entrance of the upstream reservoir and at the exit of the downstream reservoir. In electrokinetic flows, the boundary condition for pressure at the walls is not trivial. However, this can be formally derived by taking the divergence of the momentum equation and employing the fact that the advection terms vanish at the walls. The resulting Poisson equation relates the pressure at the walls to the electric potential such that $\nabla^2 P=-B\rho_e\nabla^2\Psi$, where $\nabla^2\Psi=-k^2\rho_e/2$ from Eq. (1). Thus, taking η as the normal direction, the boundary condition for pressure at the wall becomes

$$\frac{\partial^2 P}{\partial\eta^2}=\frac{1}{2}Bk^2\rho_e^2 \quad (7)$$

Note that $\rho_e=n^+-n^-$ at the walls is known based on the prescribed zeta potential, as will be shown in the next section. In the axial direction, P_{in} is specified at $x=0$, while pressure is set to zero at the flow exit.

2.4.2 Ionic Concentration Field. The ionic concentrations at the microchannel walls are given by the equilibrium Boltzmann distribution at the prevailing zeta potential, while the reservoir walls are assumed to be charge free ($\zeta=0$); that is,

$$n^{\pm}=\begin{cases}1 & \text{reservoir walls}\\ e^{\mp\zeta} & \text{microchannel walls}\end{cases} \quad (8)$$

It is also assumed that the flow entering the upstream reservoir is electroneutral; that is, $n^+=n^-=1$ at $x=0$. At the other end, the downstream reservoir has charge-free walls and is large enough to allow an equal and uniform distribution of ions to be reestablished. Thus, the flow returns once again to an electroneutral state at the exit of the downstream reservoir. Furthermore, $\partial n^{\pm}/\partial x=0$ at both ends, consistent with the uniform distribution of ions at these locations.

2.4.3 Electric Potential Field. The general form of the electric potential boundary conditions can be derived from the corresponding electric current boundary conditions. For this purpose, the current continuity equation is obtained from the Nernst–Planck equations by subtracting Eq. (3) from Eq. (2),

$$\frac{\partial[u(n^+-n^-)]}{\partial x}+\frac{\partial[v(n^+-n^-)]}{\partial y}=\frac{1}{\mathrm{ScRe}}\left\{\frac{\partial^2(n^+-n^-)}{\partial x^2}+\frac{\partial^2(n^+-n^-)}{\partial y^2}+\frac{\partial}{\partial x}\left[(n^++n^-)\frac{\partial\Psi}{\partial x}\right]+\frac{\partial}{\partial y}\left[(n^++n^-)\frac{\partial\Psi}{\partial y}\right]\right\} \quad (9)$$

which can be simply written as $\nabla\cdot\mathbf{I}=0$, where the nondimensional electric current density is

$$\mathbf{I}=(n^+-n^-)\mathbf{V}-[\nabla(n^+-n^-)+(n^++n^-)\nabla\Psi]/(\mathrm{ScRe}) \quad (10)$$

The Cartesian components of the electric current density are

$$I_x=(n^+-n^-)u-\frac{1}{\mathrm{ScRe}}\left[\frac{\partial}{\partial x}(n^+-n^-)+(n^++n^-)\frac{\partial\Psi}{\partial x}\right] \quad (11)$$

$$I_y=(n^+-n^-)v-\frac{1}{\mathrm{ScRe}}\left[\frac{\partial}{\partial y}(n^+-n^-)+(n^++n^-)\frac{\partial\Psi}{\partial y}\right] \quad (12)$$

where the terms on the right hand side are identified as the streaming (I_s), diffusion (I_d), and conduction (I_c) current densities. Considering zero velocity slip at the walls and the fact that $\mathbf{I}\cdot\hat{\boldsymbol{\eta}}=0$ for dielectric surfaces, the electric potential boundary condition becomes

$$\left.\frac{\partial\Psi}{\partial\eta}\right|_{\mathrm{wall}}=-\left.\frac{\partial(n^+-n^-)/\partial\eta}{(n^++n^-)}\right|_{\mathrm{wall}} \quad (13)$$

where η is the wall-normal coordinate. It is important to note that Ψ incorporates the combined effects of the wall zeta potential and the unknown induced electric potential. Consequently, Ψ_{wall} may not be simply set equal to ζ.

In the present work, $\Psi=0$ is prescribed at the entrance of the upstream reservoir, which is consistent with the assumption of charge-free reservoir walls. The appropriate boundary condition at the exit of the downstream reservoir is $\partial\Psi/\partial x=0$, which is obtained from Eq. (11) using $I_x=0$ and recognizing that the electrical charges attain a neutral uniform distribution at the exit. Note that imposing $I_x=0$ is consistent with the present task of searching for the maximum induced voltage in a given electrokinetic flow.

2.5 Input Data. In the present study, it is assumed that the microchannel is made of silicon, with the zeta potential at the wall varying in the range $-300\ \mathrm{mV}\leqslant\zeta^*\leqslant-25\ \mathrm{mV}$. The working fluid is water with KCl in solution, where the bulk molar concentration of each ionic species is specified as $C=10^{-5}$ kmol/m^3. Hence, the bulk ionic number concentration is $n_0=N_aC=6.022\times10^{21}$ ions/m^3. It is further assumed that the temperature of the solution is constant at 298 K, and the mass diffusion coefficients of the K^+ and Cl^- ions are approximately equal such that $D=D^+\cong D^-=2\times10^{-9}$ m^2/s. The fluid density, viscosity, and dielectric constant are specified as $\rho=10^3$ kg/m^3, $\mu=10^{-3}$ N s/m^2, and $\varepsilon_r=78.5$ (Masliyah [16]), respectively. The other required physical constants that are given in the Nomenclature are taken from Weast et al. [17]. With these values, the Schmidt number is $\mathrm{Sc}=\mu/(\rho D)=500$ and the Debye–Hückel parameter becomes $K=1.04\times10^7$ m^{-1}.

In the present work, the microchannel height is not an input parameter; rather, it is calculated using the specified nondimensional EDL thickness parameter k, that is, $H=k/K$. Furthermore, the reference velocity U_{ref} is calculated based on the specified pressure difference via the Poiseuille pressure drop relation $\Delta P^*=8\mu L^*U_{\mathrm{ref}}/H^2$, where U_{ref} corresponds to the maximum velocity. In electrokinetic flows under consideration here, the velocity field is influenced more significantly by the applied pressure difference than the induced electric field; therefore, it is appropriate to base the reference velocity on this pressure drop relation. In nondimensional form, the applied pressure difference is related to the Reynolds number as $\Delta P=8L/\mathrm{Re}$. In the present work, $\Delta P=80$, $\mathrm{Re}=1$, $L=L^*/H=10$, and $k=20$ have been used in all cases, unless otherwise specified, which correspond to a microchannel approximately 2 μm in height and 20 μm in length with an applied pressure difference of about 20 kPa.

3 Numerical Method

The governing equations are solved numerically using the well-known finite-volume method with collocated variables in a body fitted coordinate system. The SIMPLEC [18] scheme handles the linkage between velocity and pressure fields. However, to avoid

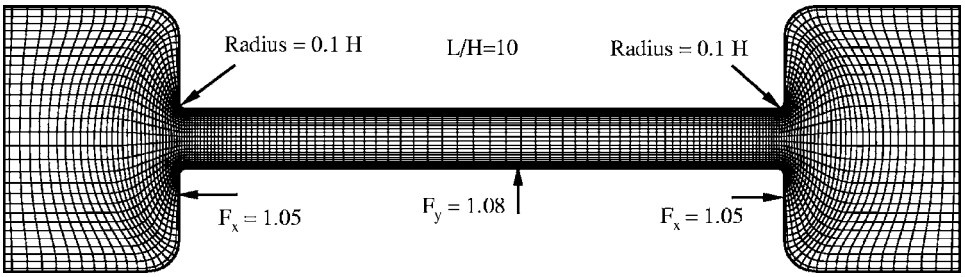

Fig. 2 Typical numerical mesh and grid expansion ratios. For clarity, a coarse grid is shown with smaller reservoirs.

the checker-board effect in the pressure field due to the use of collocated variables, the interpolation scheme of Rhie–Chow [19] is used to calculate the convecting mass flow rates. The diffusive and convective terms at face location are evaluated using a central differencing scheme; thus, the method is second order accurate in space. The resulting algebraic system of equations is then solved in a line-by-line iterative manner using the TDMA (Tri-Diagonal Matrix Algorithm) [20]. This computer code was extensively tested for accuracy as part of a companion study on electro-osmotic flows [15]. However, additional tests were performed for the electrokinetic flow under consideration, as described below and in Sec. 4.

A typical mesh used in this study is shown in Fig. 2, where a coarser grid is displayed for clarity. Near the walls where a thin EDL forms, a high grid concentration is required to resolve the electric potential distribution accurately. A typical transverse grid expansion factor is $F_y=1.08$. However, for a given k (representative of the EDL thickness), the grid density near the walls must be further increased for larger absolute values of the zeta potential. In the axial direction, regions with rapid changes in the geometry require higher grid densities, where a typical expansion factor is $F_x=1.05$.

A grid study involving an electrokinetic flow between parallel plates (no reservoirs) with Re=1, $k=20$, $L=10$, and $\zeta^*=-50$ mV indicates that a grid density of 151×91 points in the flow and transverse directions, respectively, having an expansion ratio of 1.07, produces grid-independent results, as shown in Fig. 3. An electrokinetic flow between parallel plates is considered as a reference because an analytical solution is available for comparison, as will be presented in the next section. For a grid with 51×31 points, the numerically calculated mass flow rate normalized by the corresponding analytical value (see Eq. (28)) is 1.0267. For grids with 101×61 and 151×91 points, the corresponding normalized flow rates are 1.0052 and 1.0001, respectively. Hence, a numerical mesh with 151×91 points leads to grid-independent results. However, the required number of grid points and the associated expansion factors require further refinement with increasing zeta-potential values. For example, in an identical case with $\zeta^*=-75$ mV, a grid density of 151×141 is required with an expansion ratio of 1.05 for grid-independent results.

4 Results and Discussion

Initially, a simplified electrokinetic flow between parallel plates is studied analytically. A matching numerical study is then presented to simulate the same flow conditions in an effort to examine the effects of the Debye–Hückel approximation on the important flow parameters. Comparisons with the analytical solution at very low zeta potentials also serve as a further validation of the numerical scheme. Finally, results are presented for electrokinetic flows in finite-length flat channels connected to fluid reservoirs.

4.1 Analytical Solution. In this section, an explicit closed form solution is presented for a pressure-driven flow in the presence of the EDL effects in a planar microchannel (no reservoirs) with uniform zeta potential along the walls. Steady-state and fully developed conditions are considered throughout the microchannel, that is, $v=0$, $\partial u/\partial x=0$, and $\partial n^{\pm}/\partial x=0$. Since u and $n^{\pm}$ may only be functions of y, it can be inferred from the Nernst–Plank equations that the electrical potential variation in the flow direction may be at most linear. Hence, a solution is sought in the following form:

$$\Psi(x,y)=\psi(y)-E_x x \tag{14}$$

where $E_x\equiv-\partial\Psi/\partial x$ is the strength of the induced electric field in the axial direction. Under the above conditions, the Nernst–Planck equations simplify to the well-known Boltzmann distribution $n^{\pm}=\exp[\mp\psi(y)]$. Using this distribution to determine the net electric charge density $\rho_e=n^+-n^-$ and employing the well-known Debye–Hückel approximation $\sinh(ze\psi/k_bT)\cong ze\psi/k_bT$, Eq. (1) leads to the following Poisson–Boltzmann equation: $d^2\psi/dy^2=k^2\psi$. The solution of this equation in a coordinate system attached to the lower plate is

$$\psi(y)=\zeta\frac{\cosh(ky-k/2)}{\cosh(k/2)} \tag{15}$$

Equation (15) has been obtained using $\psi=\zeta$ at the wall and $d\psi/dy=0$ at the midplane ($y=0.5$). Its accuracy is limited to small zeta potentials due to the Debye–Hückel approximation. It should

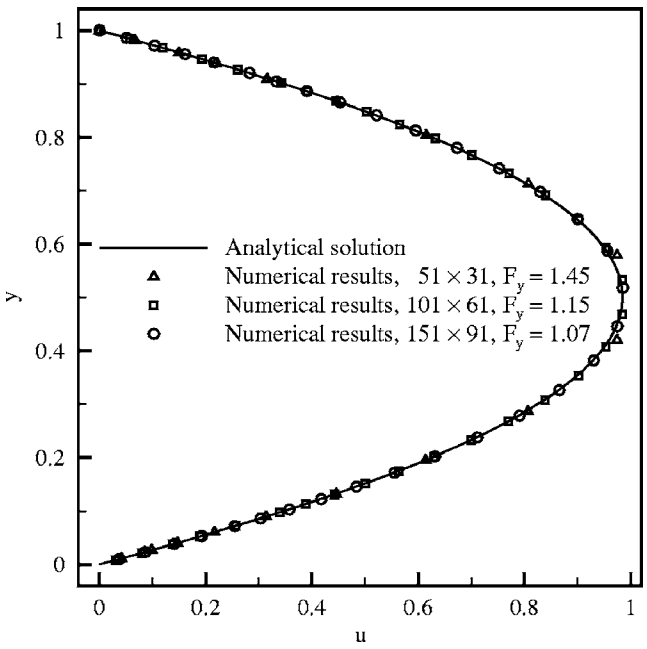

Fig. 3 Velocity profiles at midchannel ($x=L/2$) for different grid sizes and expansion ratios for Re=1, $k=20$, $\zeta^*=-50$ mV, $\Delta P=80$, and $L=10$

be noted that employing $\psi=0$ at the midplane instead of the symmetry condition used here leads to a solution in terms of the hyperbolic-sine function. Strictly speaking, the basic assumption behind the Boltzmann distribution given above is the existence of an infinitely large motionless fluid such that not only does the electric potential approach zero far away from the charged surface, but the ionic concentrations there are also equal to the original bulk ionic concentration. It is obvious that these conditions are not satisfied for very dilute electrolyte solutions flowing in very small microchannels (i.e., small k or relatively thick EDL), which is typical of electrokinetic flows; therefore, $d\psi/dy=0$ is a more appropriate boundary condition for the midplane.

For the problem under consideration, the x-momentum equation reduces to

$$\frac{1}{\mathrm{Re}}\frac{\partial^2 u}{\partial y^2}-\frac{\partial P}{\partial x}+B\rho_e E_x=0 \tag{16}$$

In pressure-driven electrokinetic flows, $\partial P/\partial x$ is a prescribed constant, which is equal to $\partial P/\partial x=-8/\mathrm{Re}$ with the present nondimensionalization scheme On the other hand, E_x is an induced unknown parameter; therefore, additional information is required, which can be obtained by setting the cross-sectional average of the x component of electric current equal to zero in Eq. (11). As indicated before, setting $\bar{I}_x=0$ corresponds to searching for the maximum induced electric potential, which results in

$$\frac{1}{A_c}\int_0^1 (n^+-n^-)u dy-\frac{1}{A_c}\int_0^1 \frac{(n^++n^-)}{\mathrm{ScRe}}\frac{\partial \Psi}{\partial x}dy=0 \tag{17}$$

Identifying the nondimensional electrical conductivity of the fluid as $\sigma_e(y)=n^++n^-$ and recognizing that $-\partial\Psi/\partial x=E_x$ is a constant, the above equation can be rewritten as

$$\frac{1}{A_c}\int_0^1 \rho_e u dy+\frac{\bar{\sigma}_e E_x}{\mathrm{ScRe}}=0 \tag{18}$$

where A_c is the nondimensional cross-sectional area ($A_c=1$) of the channel and $\bar{\sigma}_e=\int_0^1\sigma_e dy/A_c$ is the average electrical conductivity of the fluid. This equation simply states that the streaming current density $\bar{I}_s=\int_0^1\rho_e u dy/A_c$ is balanced by the conduction current density $\bar{I}_c=\bar{\sigma}_e E_x/\mathrm{ScRe}$, that is, $\bar{I}_s+\bar{I}_c=0$. It is worth mentioning that surface electrical conductivity associated with the immobile portion of the EDL is ignored in the present work.

From Eqs. (16) and (18), the nondimensional velocity and electric fields are obtained as follows:

$$u(y)=4\left\{y-y^2-G\left[1-\frac{\cosh(2\beta y-\beta)}{\cosh\beta}\right]\right\} \tag{19}$$

$$E_x=\frac{8G\beta^2}{\mathrm{Re}B\zeta} \tag{20}$$

$$G=\frac{1}{\beta^2}\left[\frac{1-(\tanh\beta)/\beta}{N\beta^2-1+\tanh^2\beta+(\tanh\beta)/\beta}\right] \tag{21}$$

where $\beta=k/2$ and $N=2\bar{\sigma}_e/(\mathrm{Sc}B\mathrm{Re}^2\zeta^2)$. It is important to note that both B and Re are related to ΔP via U_{ref}; therefore, E_x is an implicit function of ΔP. Thus, for a given electrolyte solution and microchannel particulars, the voltage increase across the channel ($\Delta\Psi=\Psi_{\mathrm{out}}-\Psi_{\mathrm{in}}$) is related to the applied ΔP by

$$\left|\frac{\Delta\Psi}{L}\right|=E_x=\frac{2Gk^2}{\mathrm{Re}B\zeta} \tag{22}$$

The net charge density, electrical conductivity, and components of the axial current are given below for completeness:

$$\rho_e=-2\sinh(\psi) \tag{23}$$

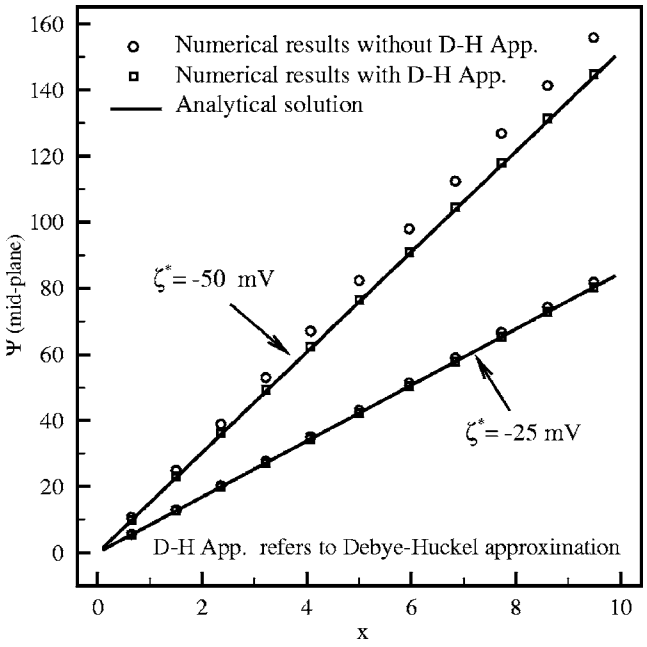

Fig. 4 Distribution of midplane ($y=H/2$) electric potential along the channel for Re=1, $k=20$, $\Delta P=80$, and $L=10$

$$\sigma_e=2\cosh(\psi) \tag{24}$$

$$I_{x,s}=-2u\sinh(\psi) \tag{25}$$

$$I_{x,d}=0 \tag{26}$$

$$I_{x,c}=(2E_x/\mathrm{ReSc})\cosh(\psi) \tag{27}$$

Since $\psi=\psi(y)$ only, it is apparent that ρ_e, σ_e, and the electric current components do not vary in the flow direction. Finally, it is useful to note that the mass flow rate per unit depth of the channel is given by

$$\dot{m}=\frac{2}{3}-4G\left[1-\frac{\tanh(k/2)}{k/2}\right] \tag{28}$$

4.2 Microchannel Without Reservoirs. As shown in the preceding section, electrokinetic flows in channels without reservoirs lend themselves to full analytical solution subject to some simplifying assumptions. In this section, a full numerical solution of the same problem is presented without any simplifications. The capabilities of the numerical scheme make it a suitable tool to evaluate the range of validity of the approximations used in the analytical approach.

In the absence of reservoirs ($L_R=0$), the length of the channel is specified as $L=L^*/H=10$. The applied pressure difference remains fixed at $\Delta P=80$ corresponding to $Re=1$, unless otherwise stated. The boundary conditions for this fully developed flow are the same as those used in the analytical solution with a few additional considerations. In the absence of reservoirs, it is assumed that the ionic concentrations at the entrance of the channel follow the Boltzmann distribution $n^\pm=\exp[\mp\psi]$, while $\partial n^\pm/\partial x=0$ at the exit. The boundary conditions for the electric potential field are based on the requirement that $\bar{I}_x=0$: therefore, using Eq. (18), $\partial\Psi/\partial x=\mathrm{ReSc}\rho_e u/\bar{\sigma}_e$ is applied at both the inlet and the exit.

Figure 4 shows the induced electric potential at the midplane for two different values of zeta potential with $k=20$. It is apparent that the numerical and analytical solutions are in good agreement for $\zeta^*=-25$ mV. As expected, at $\zeta^*=-50$ mV, a significant deviation is observed as the Debye–Hückel approximation begins to deteriorate. In fact, it is seen that the results show an excellent

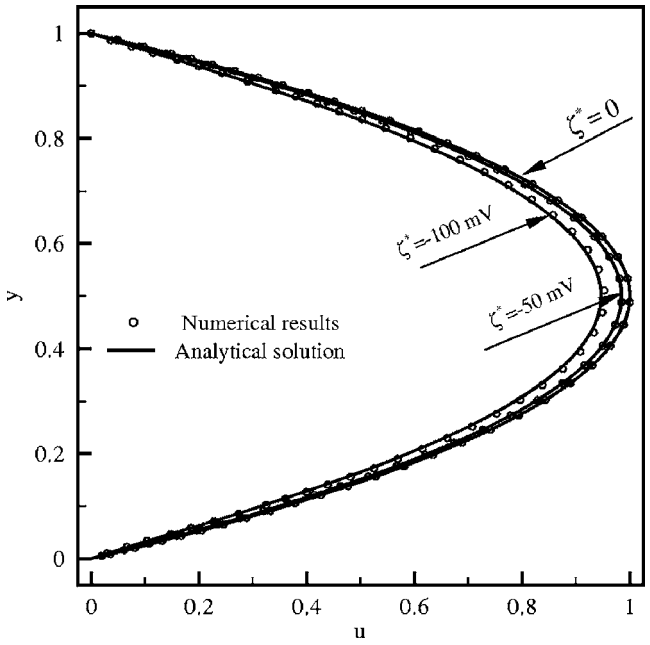

Fig. 5 Velocity profiles at midchannel ($x=L/2$) for Re=1, $k=20$, $\Delta P=80$, $L=10$, and $\zeta^*=0, -50, -100$ mV

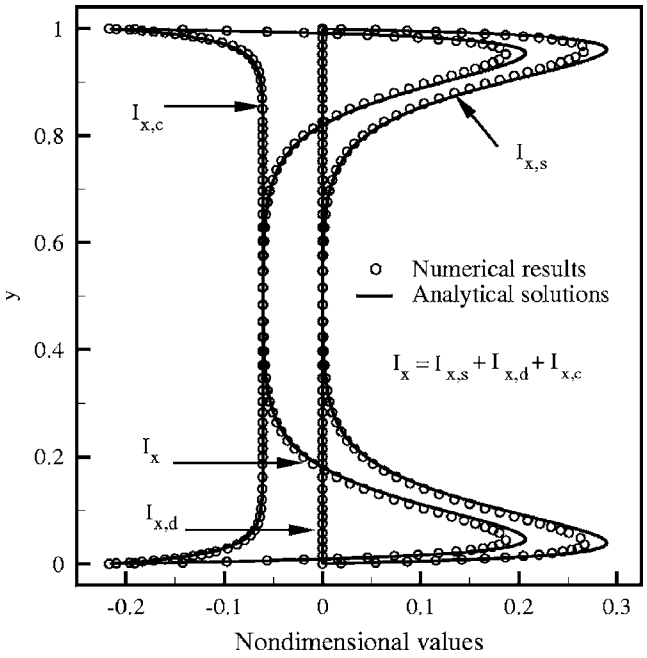

Fig. 6 Cross-sectional variation of electric current components at midchannel ($x=L/2$) for Re=1, $k=20$, $\zeta^*=-50$ mV, $\Delta P=80$, and $L=10$

agreement regardless of the value of the zeta potential if the same approximation is also embedded in the numerical solution, providing further evidence for the accuracy of the numerical code.

Apparently, the velocity profile is less sensitive to the EDL effects, as shown in Fig. 5. This figure compares the numerical velocity profiles with the corresponding analytical solution, indicating a good agreement for zeta potentials as high as 100 mV. It is also apparent that the presence of the EDL affects the flow field in such a way that the mass flow rate is reduced with increasing zeta potential (the so-called electroviscous effect [16]). In this case, the mass flow rate reduction is about 2% and 6% for $\zeta^*=-50$ mV and -100 mV, respectively.

In Fig. 6, the cross-sectional distribution of the axial electric current density and its components are compared with their analytical counterparts at $\zeta^*=-50$ mV. The streaming current density $I_{x,s}$ depends on the values of the net charge density and the flow velocity, as indicated in Eq. (11). In the presence of a negative zeta potential, the net charge density near the wall is positive, and with a positive axial velocity, the axial streaming current density is positive everywhere. Note that zero velocity at the walls leads to $I_{x,s}=0$ despite the maximum charge density there. Also, $I_{x,s} \rightarrow 0$ in the core section of the channel where the net charge density vanishes. Therefore, the maximum streaming current density is encountered very close to the wall, as seen in this figure.

The axial conduction current density $I_{x,c}$ is negative everywhere, balancing the streaming current density. This can also be inferred from the last term in Eq. (11), where both $\partial\Psi/\partial x$ and σ_e are positive everywhere. Moreover, the electrical conductivity is highest at the walls; therefore, the maximum (absolute) conduction current density occurs there. In this fully developed flow, the axial diffusion current density $I_{x,d}$ is equal to zero everywhere because there is no axial variation in the net charge density throughout the channel. The net axial current density I_x shown in Fig. 6 is simply the sum of its components: $I_x=I_{x,s}+I_{x,d}+I_{x,c}$. It is also noted that the cross-sectional average of I_x is zero everywhere along the channel consistent with the "maximum-induced-voltage" problem under consideration.

The present study provides useful information regarding the induced voltage $\Delta\Psi$ for a microchannel of length L, which is central to the concept of a microfluidic battery or power supply. Figure 7 shows the variation of $|E_x|=\Delta\Psi/L=(\Psi_L-\Psi_0)/L$ for different values of the EDL parameter k over a wide range of zeta potential. It is seen that the induced voltage increases with decreasing k, which is due to the fact that lower values of $k=HK$ correspond to smaller channel heights and, therefore, to larger flow velocities, which generate higher streaming currents and potentials. Predictions of the full numerical solution for $k=10$ and 20 are also included in Fig. 7 for comparison. It must be emphasized that unlike the analytical solution, the numerical results are not constrained by the Debye–Hückel approximation. Again, the

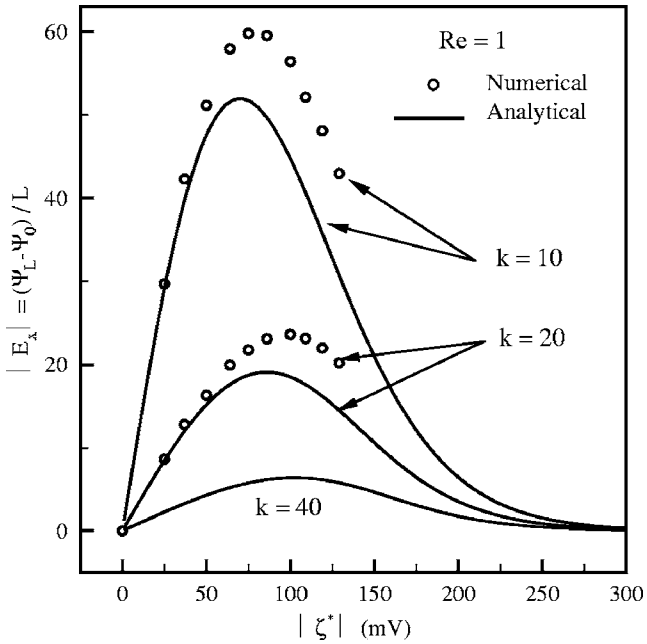

Fig. 7 Nondimensional induced electric field strength as a function of zeta potential for Re=1, $\Delta P=80$, $L=10$, and $k=10,20,40$

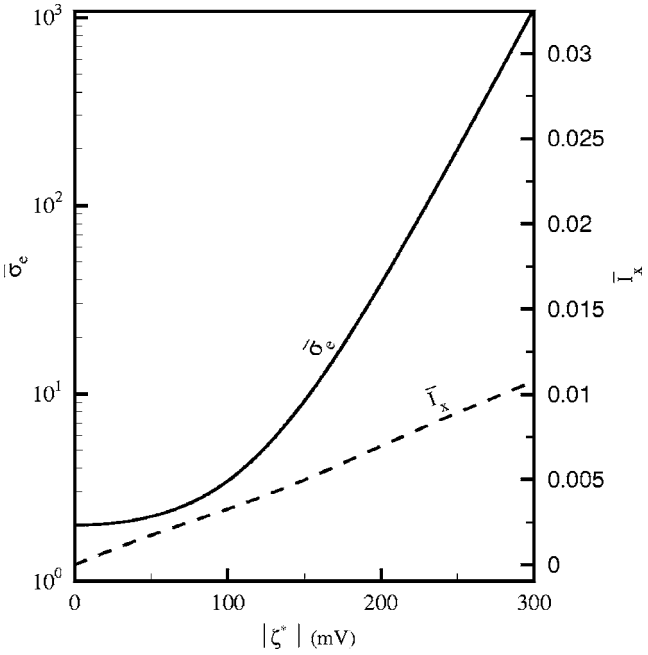

Fig. 8 Cross-section averaged electrical conductivity and streaming current density as a function of zeta potential for Re=1, k=20, ΔP=80, and L=10

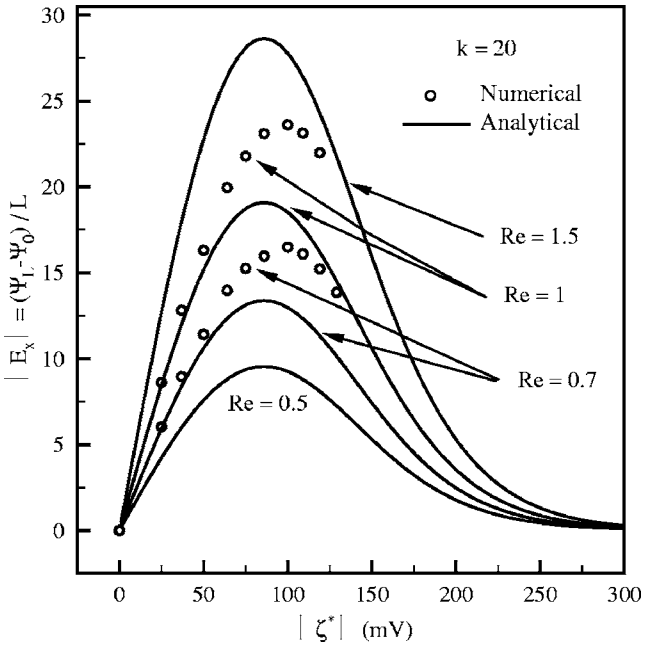

Fig. 9 Induced electric potential as a function of zeta potential for k=20, ΔP=80, L=10, and Re=0.5,0.7,1,1.5

agreement is excellent as long as the Debye–Hückel approximation is valid, and the numerical results depart from the analytical curve at higher values of zeta potential. Numerical results for k =40 are not shown in Fig. 7, but the trend is the same. Since the numerically predicted induced voltages are larger, it can be stated that the analytical solution with the embedded approximations provides a lower limit for $\Delta\Psi$. The numerical calculations become more intensive as the zeta potential increases; therefore, they are not continued beyond $\zeta^*=-130$ mV, which is a reasonable upper limit for practical applications.

Figure 7 also shows that $\Delta\Psi/L$ attains maximum values at zeta potentials less than 100 mV and tends to zero at large ζ^*. This behavior can be explained with the help of Eq. (18) and Fig. 8, where the streaming current density and electrical conductivity are plotted as a function of zeta potential. It is observed that $\bar{\sigma}_e$ is relatively insensitive to ζ^* at first, but then increases exponentially beyond $|\zeta^*|\approx 100$ mV. Such large electrical conductivities at higher ζ^* indicate that only very weak electric potentials can be established for the prevailing streaming currents; hence, $\Delta\Psi\to 0$ for large ζ^*. On the other hand, for small values of ζ^*, the electrical conductivity remains very low and almost constant; therefore, progressively larger electric potentials can be established even at low streaming currents, as seen in Fig. 7.

Although Fig. 8 offers some justification for the common practice of treating electrical conductivity as a constant at low zeta potentials, it is useful to note that $\bar{\sigma}_e$ varies between 2 and 3.4 for $|\zeta^*|\leq 100$ mV, which is a significant variation.

The effects of Reynolds number on the induced voltage potential are shown in Fig. 9. The channel height is fixed for a given k; therefore, increasing Re leads to higher velocities, which in turn increases the streaming current and potential. It is seen that, while following a similar trend, the numerical data show substantial deviations from the analytical results beyond the range of validity of the Debye–Hückel approximation. Again, the analytical results correspond to the lower limit of the induced voltages.

The variation of induced voltage as a function of applied pressure difference is of practical importance for the design of a microfluidic power supply. Figure 10 shows the induced potential calculated using Eq. (22) for a wide range of ΔP at four different zeta potentials. It is seen that the induced potential increases linearly with increasing pressure. Larger zeta potentials also lead to higher induced potentials but only up to a certain point, beyond which an exponential increase in electrical conductivity forces E_x to zero, as explained previously in relation to Fig. 7. An explicit but approximate relation between the applied ΔP and the resulting induced voltage can be obtained in the limit of a very thin EDL simply by linearizing the velocity profile near the wall and ignoring electrical effects on the flow field (i.e., basic Poiseuille flow). This relation is given by Hunter [1] in dimensional form as $\Delta\Psi^*=\varepsilon_r\varepsilon_0\zeta^*\Delta P^*/\mu\bar{\sigma}^*$, which in nondimensional form becomes

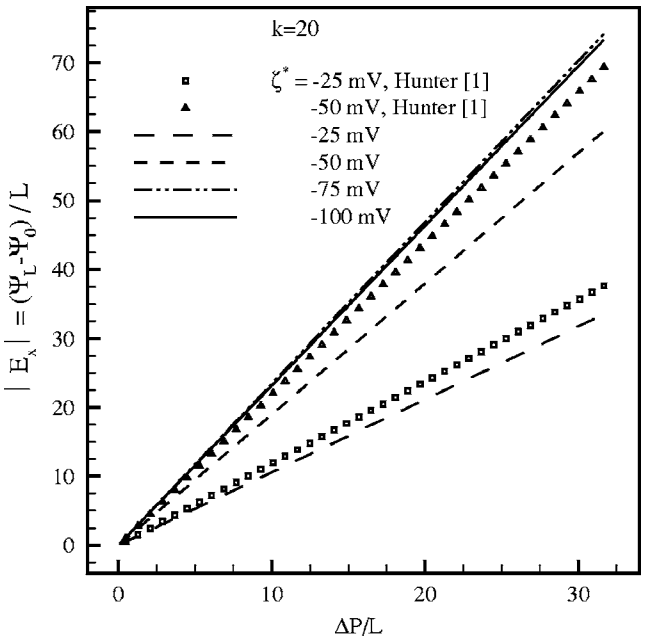

Fig. 10 Induced electric potential as a function of applied pressure difference for k=20, L=10, and ζ^*=−25, −50, −75, −100 mV

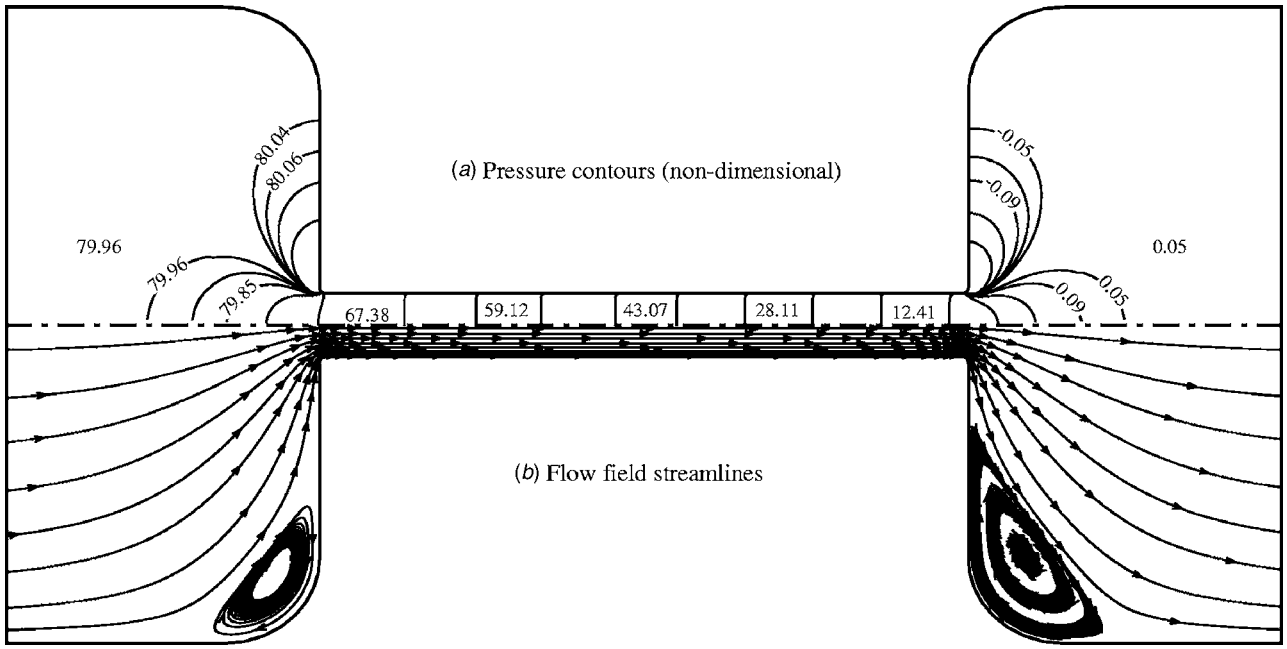

Fig. 11 Numerical results for Re=1, k=20, ζ^*=−50 mV, ΔP=80, and L=10: (*a*) pressure contours and (*b*) streamlines

$$\left|\frac{\Delta\Psi}{L}\right| = E_x = \left(\frac{2\zeta \mathrm{ScRe}^2}{\bar{\sigma}_e k^2}\right)\frac{\Delta P}{L} \tag{29}$$

As expected, the present analytical solution also yields the same equation for large k. Consistent with the underlying assumptions, this equation loses its accuracy rapidly for $k<40$ as the EDL thickens. For example, as shown in Fig. 10, at k=20 with ζ^*=−50 mV, Re=1, and $\Delta P/L$=8, Eq. (29) predicts $\Delta\Psi/L$ =17.5 while Eq. (22) yields $\Delta\Psi/L$=15.4.

4.3 Microchannel With Reservoirs. In proposed applications, such as a microfluidic power supply, the microchannels have finite lengths and communicate with fluid reservoirs. Hence, the flow is forced through regions with abrupt contraction and expansion; therefore, the problem cannot be fully analyzed based on simplified reservoir-free models such as the one presented in the preceding section. In other words, the entrance and exit effects may significantly affect electrokinetic flows, especially in the case of relatively short channels. The geometry of the problem under consideration here is as shown in Fig. 1 with $L=L^*/H=10$ and $L_R=L_R^*/H=5$. As indicated before, it is assumed that the channel and the reservoir walls are made of different materials such that only the channel walls have a finite zeta potential. In this section, numerical results are reported for the case of Re=1, k=20, and ζ^*=−50 mV, unless otherwise stated.

In Fig. 11, pressure contours and flow streamlines are presented for the upper and lower halves of the system, respectively. Obviously, conditions are symmetric with respect to the midplane in this problem. As expected, recirculation zones form in the corner regions of the reservoirs due to the sudden contraction and expansion of the flow. As the pressure contours indicate, the pressure drop within the reservoirs is negligible except near the entrance and exit of the channel. The axial variation of pressure along the midplane is shown in Fig. 12 and compared to its counterparts in two cases without reservoirs: a simple Poiseuille flow between parallel plates and a pressure-driven flow with electrokinetic effects. This figure clearly shows that the EDL effect on the midplane ($y=H/2$) pressure distribution is negligible in the absence of reservoirs. On the other hand, when reservoirs are present, well-known hydrodynamic effects associated with the sudden contraction and expansion of the flow cause a pressure drop in the entrance region and a pressure rise at the exit, which explains the relatively weaker pressure gradient seen in Fig. 12.

Figure 13 shows the midchannel ($x=L/2$) velocity profiles corresponding to the same cases described above in relation to Fig. 12. In comparison to a basic pressure-driven flow, it is observed that the EDL effects alone have a weak influence on the flow field. The associated mass flow rate is reduced by less than 2% in the present case. It is also observed that the presence of reservoirs alters the velocity field inside the microchannel significantly, such

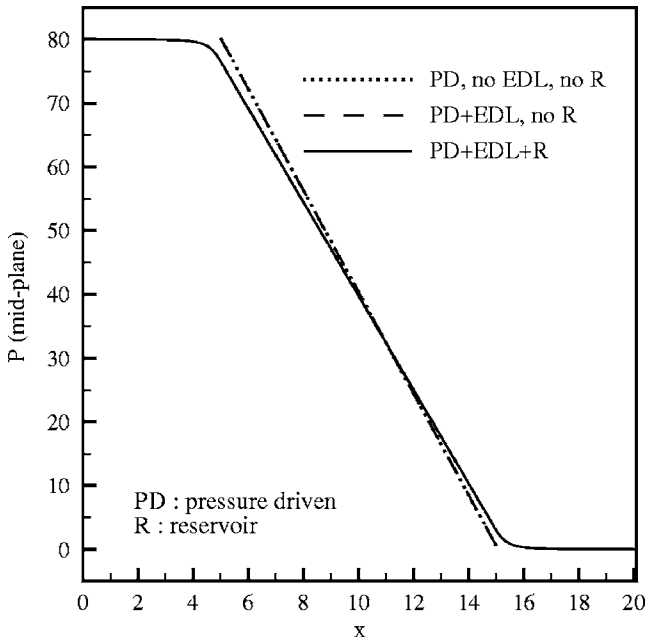

Fig. 12 Comparison of midplane ($y=H/2$) pressure distributions along the channel for Re=1, k=20, ζ^*=−50 mV, ΔP=80, and L=10

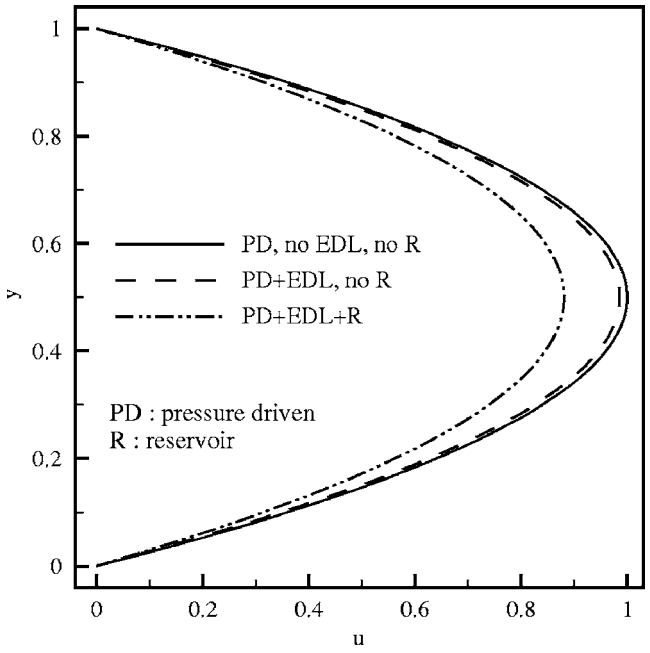

Fig. 13 Comparison of axial velocity profiles at midchannel ($x=L/2$) for Re=1, $k=20$, $\zeta=-50$ mV, $\Delta P=80$, and $L=10$

that the mass flow rate is now 11% less than the corresponding Poiseuille flow. Clearly, any reduction in liquid velocities directly affects the ionic fields, resulting in lower induced electric potentials.

The flow rate reduction due to EDL effects is also referred to as the electroviscous effect in the literature (e.g., Ref. [16]). Briefly, the streaming current in the flow direction builds up a streaming potential, which, in turn, generates an electric current in the opposite direction to the flow. When ions move in a liquid, the liquid molecules are dragged with them; therefore, this countercurrent produces a retardation effect on the liquid velocities. Consequently, the flow behaves as if the liquid viscosity is higher.

The detailed numerical solutions of the equations governing charge transport and electric potential obtained in the present work provide further insight to the nature of electrical current flow and induced voltage. The electric current lines as well as the electric potential contours for the problem under consideration are presented in Fig. 14. This figure shows that under the applied hydrostatic pressure, the charges in the EDL are carried toward the downstream reservoir, establishing a streaming current, and a streaming potential is built up along the channel due to the accumulation of charges in the exit reservoir. As indicated before, this induced potential field establishes a conduction current in the opposite direction to the flow. For the maximum-induced-voltage case considered here, the net axial current flow is zero; therefore, the streaming current must be balanced by the conduction current, which is clearly seen in Fig. 14 as current flows toward the upstream reservoir.

Magnified views of the wall region at the channel inlet and exit are also given in Fig. 14, which show the presence of conduction currents in the immediate vicinity of the wall as well. This can also be inferred from the double counter-loop pattern of the current lines in the exit reservoir. Recall that the streaming current density is almost zero in the vicinity of the walls where the flow velocity is very small and in the core region of the channel where the fluid is essentially electroneutral. Therefore, these are regions where the conduction current density is dominant. In the middle of the microchannel where the entrance and exit effects are negligible, the behavior of the current density components is well represented by Fig. 6.

Figure 14(*b*) indicates a fairly linear distribution of induced voltage inside the channel. Consistent with the electric current patterns discussed above, two regions of high electric potential are observed in the downstream reservoir. However, the variation of induced potential inside the reservoirs (assumed to have charge-free walls) is negligible as compared to changes along the microchannel. This fact is clearer in Fig. 15 where the axial distributions of the electric potential at the wall and on midplane are shown for three different values of zeta potential. It is seen that the maximum induced potential increases very substantially with

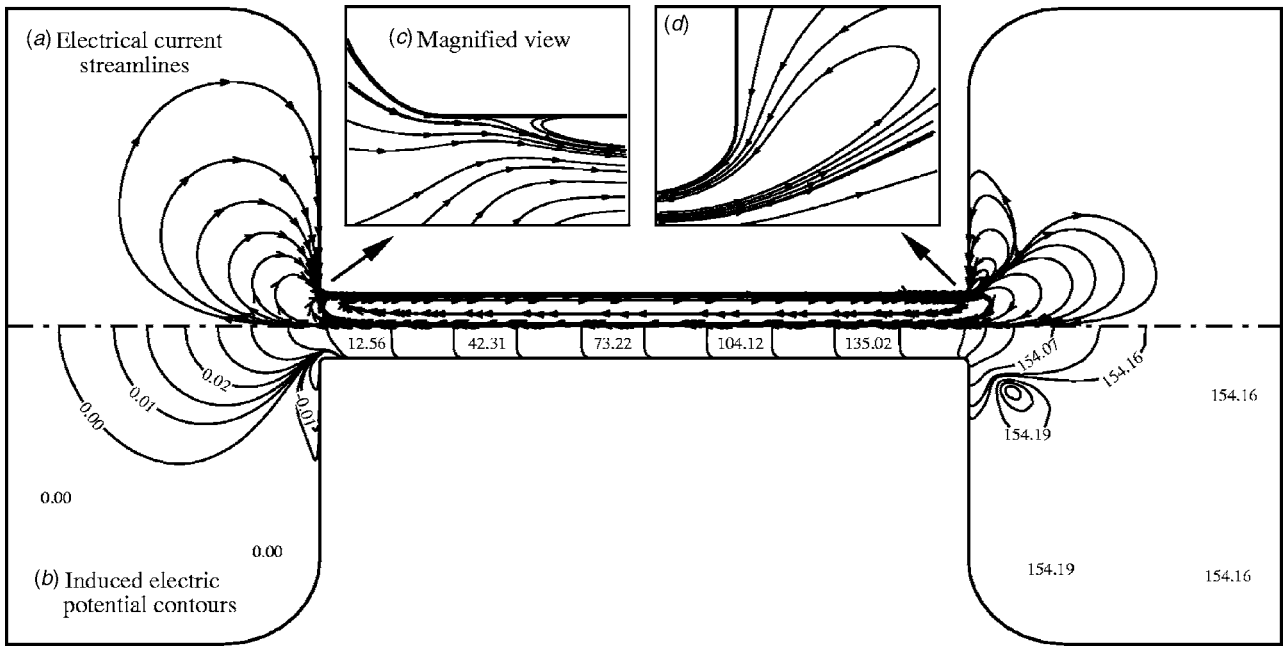

Fig. 14 Numerical results for Re=1, $k=20$, $\zeta=-50$ mV, $\Delta P=80$, and $L=10$: (*a*) electric current lines, (*b*) induced electric potential contours, (*c*) magnified view of current lines at the channel inlet region, and (*d*) magnified view of current lines at the channel outlet region

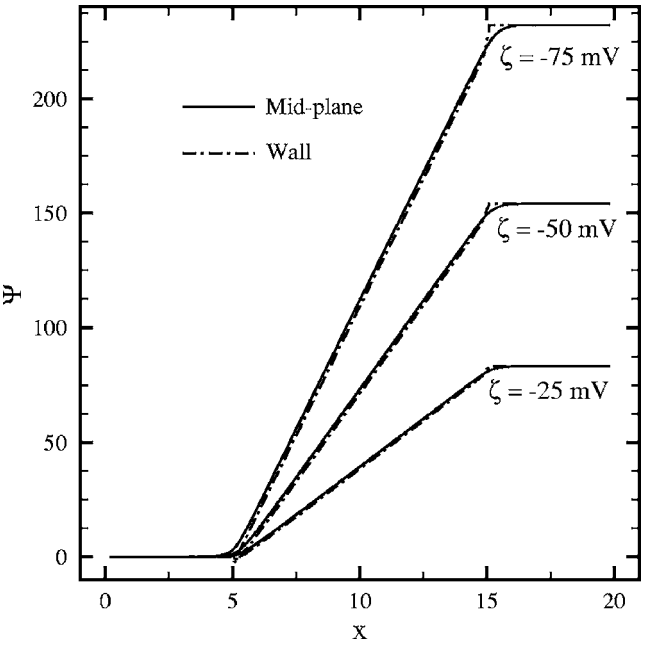

Fig. 15 Axial variation of midplane ($y=H/2$) and wall electric potentials for Re=1, $k=20$, $\zeta^*=-25$, -50, -75 mV, $\Delta P=80$, and $L=10$

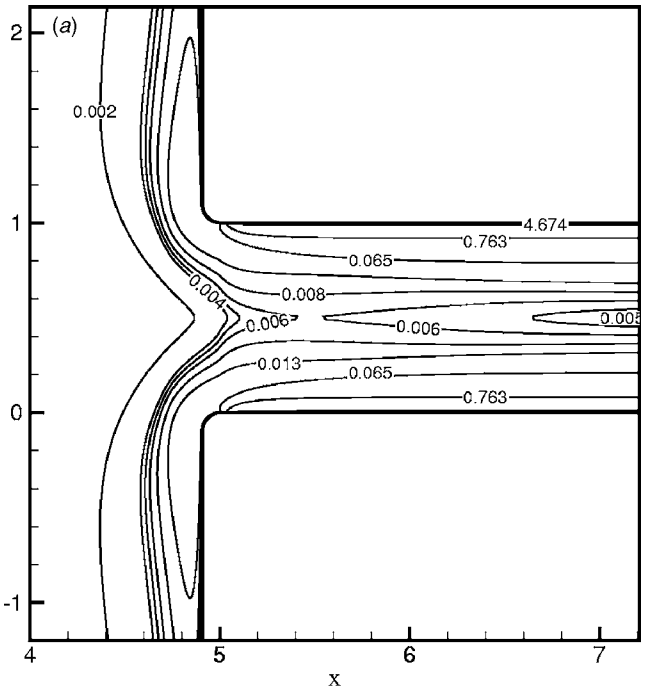

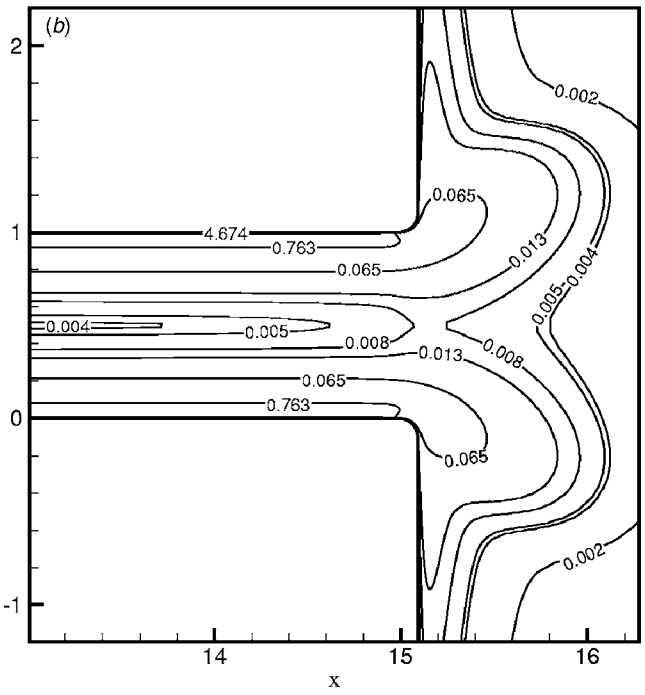

Fig. 16 Net charge density counters at the channel (*a*) inlet and (*b*) outlet for Re=1, $k=20$, $\zeta^*=-50$ mV, $\Delta P=80$, and $L=10$

increasing zeta potential, which is consistent with the simplified analytical model presented earlier (see Fig. 4) for a microchannel without reservoirs. A comparison of the data in Figs. 4 and 16 indicates that the induced voltages are lower when reservoirs are taken into account (e.g., $\Psi_{\max}=154$ versus 163 at $\zeta^*=-50$ mV). As mentioned earlier, a channel with reservoirs experiences a smaller mass flow rate for the same applied ΔP, which, in turn, reduces the streaming current and the induced potential. Note that Fig. 13 indicates about 11% reduction in mass flow due to the presence of reservoirs, while the maximum voltage reduction is about 5% due to the fact that the streaming current is also influenced by the net charge distribution. It is also apparent from Fig. 15 that Ψ at the wall is dictated by the induced potential rather than the zeta potential.

The induced electric potential is governed by a Poisson equation, which is strongly influenced by the geometry as being of elliptic type. Therefore, the size of the reservoirs can be an issue, and was investigated in the present study. The results showed that increasing the length of the reservoirs beyond the chosen size ($L_R=L_R^*/H=5$) does not affect the maximum induced voltage since the electric potential distribution is almost uniform inside the reservoirs. The height of the reservoir (or the H_R/H ratio) must also be large enough so that its upper and lower walls do not affect the flow patterns at the channel inlet and outlet. In the present case, it is found that the reservoir height should be about ten times larger than the channel height to meet this requirement, which is consistent with the observations of Mansouri et al. [14] in cylindrical geometry. They observed that the radius of the reservoir should be about five times larger than the radius of the microtube for satisfactory results.

As mentioned earlier, Mansouri et al. [14] studied the transient development of induced voltage in a capillary connected to infinite reservoirs at both ends. They found that at early stages, advection of the ions leads to local disturbances in the charge distribution in the stagnant fluid at the inlet and outlet of the capillary in such a way that a potential difference begins to build up. The migration and diffusion transport mechanisms are then formed under the influence of the resulting electric field. They also observed that during this transient process, no axial variations of the charges are formed inside the capillary beyond the inlet and exit regions. However, no information is provided regarding the steady-state distribution of the net charge density along the capillary. In Fig. 16, the net charge distributions at steady state are presented at the inlet and outlet regions of the microchannel for the case under consideration. As compared to the inlet, the larger total amount of net charge in the exit region is responsible for the formation of a high potential zone there. Figure 17 shows the net charge density along the midplane, where very large gradients are observed at the inlet and exit regions while $\partial\rho_e/\partial x\approx 0$ over the rest of the microchannel. Clearly, the electric potential field is very complex in the inlet and exit zones due to the presence of

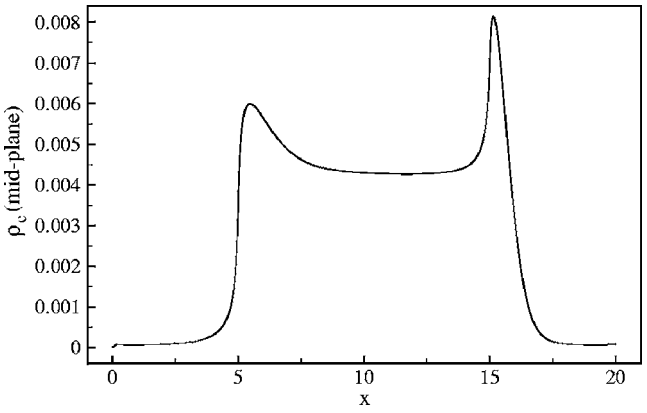

Fig. 17 Axial variation of midplane ($y=H/2$) net charge density for Re=1, $k=20$, $\zeta^*=-50$ mV, $\Delta P=80$, and $L=10$

reservoirs.

In Fig. 18, cross-section averaged components of the electric current density are shown along the channel. Zero current flow at the system boundaries along with charge-free walls and essentially uniform electric potential variations are the reasons for the observed component profiles inside the reservoirs. In the microchannel, the dominant components are the streaming and conduction current densities, which are in balance such that $\bar{I}_x=0$ everywhere. It is also seen that the diffusion component of the electric current density is noticeable only at the entrance and exit of the channel where the zeta potential changes in a stepwise manner, which explains the small spikes observed there.

5 Conclusions

In the present work, both analytical and numerical analyses were performed to study pressure-driven electrokinetic flows in flat microchannels with and without attached reservoirs. The main objectives were to develop a better understanding of the underlying physical processes and to determine the maximum induced voltage in a given electrokinetic flow, the latter being associated with the concept of a microfluidic power supply or battery.

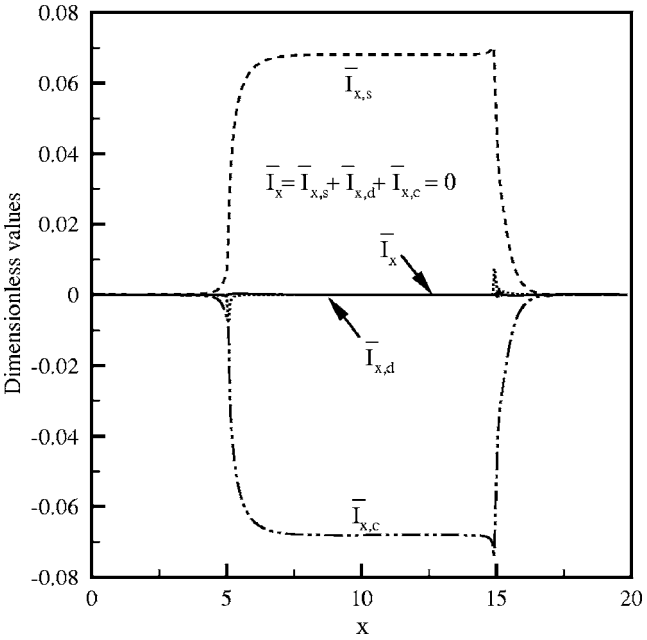

Fig. 18 Axial variation of cross-section averaged electric current density components for Re=1, $k=20$, $\zeta^*=-50$ mV, $\Delta P=80$, and $L=10$

The results show that the pressure-driven electrolyte flow creates a streaming current that leads to an electric potential that increases linearly along the microchannel. This induced potential field, in turn, creates conduction currents in the opposite direction to the flow. Conduction currents are high adjacent to the walls and in the core region of the channel where the streaming currents are negligible. The diffusion currents due to ionic concentration gradients have been found to be negligible in all cases studied here. For the condition of maximum induced voltage, the net current flow at any location along the channel is zero. Both the induced potential and the electrical conductivity of the flow are highly nonlinear functions of the wall zeta potential such that the maximum voltage occurs at $|\zeta^*|\approx 100$ mV. This maximum increases with the applied pressure difference as well as the EDL thickness in the range of parameters considered in the present work.

The results also show that the presence of reservoirs creates complex electrokinetic conditions in the entrance and exit regions of the microchannel, leading to very large charge density gradients there, which affect the entire flow field particularly for shorter channels.

Acknowledgment

Financial support of the Ministry of Science, Research and Technology of Iran and the Natural Sciences and Engineering Research Council of Canada are greatly appreciated.

Nomenclature

B = ratio of ionic pressure to dynamic pressure, $B=n_0k_bT/\rho U_{\text{ref}}^2$

D = diffusion coefficient (m^2/s)

e = elementary charge, $e=1.602\times10^{-19}$ C

E_x = axial electrical field, $E_x=E_x^*/(\Psi_{\text{ref}}/H)$

H = microchannel height (m)

H_R = reservoir height (m)

I = electrical current density, $I=I^*/I_{\text{ref}}$

I_{ref} = reference current density, $I_{\text{ref}}=\rho_{e,\text{ref}}U_{\text{ref}}$ ($C/s\ m^2$)

I_s, I_d, I_c = streaming, diffusion, and conduction current densities

K = Debye–Hückel parameter, $K=(2z^2e^2n_0/\varepsilon_r\varepsilon_0k_bT)^{1/2}$ (1/m)

k = EDL thickness parameter, $k=KH$

k_b = Boltzmann constant, $k_b=1.381\times10^{-23}$ J/K

L = nondimensional microchannel length, $L=L^*/H$

L_R = reservoir length, $L_R=L_R^*/H$

$\dot{m}$ = mass flow rate per unit depth of channel, $\dot{m}=\dot{m}^*/\rho U_{\text{ref}}H$

N_a = Avogadro's number, $N_a=6.022\times10^{23}$ mol^{-1}

n^+, n^- = positive and negative ion concentrations, $n^\pm=n^{\pm *}/n_0$

n_0 = bulk ionic concentration ($ions/m^3$)

P = pressure, $P=P^*/\rho U_{\text{ref}}^2$

Re = Reynolds number, $\text{Re}=\rho U_{\text{ref}}H/\mu$

Sc = Schmidt number, $\text{Sc}=\mu/\rho D$

u, v = Cartesian velocity components, $u=u^*/U_{\text{ref}}$, $v=v^*/U_{\text{ref}}$

U_{ref} = reference velocity, $U_{\text{ref}}=u_{\max}^*=H^2\Delta P^*/8\mu L^*$ (m/s)

x, y = Cartesian coordinates, $x=x^*/H$, $y=y^*/H$

z = valence number of ions for a symmetric electrolyte, $z=z^+=z^-$

Greek symbols

ε_0 = permittivity of vacuum, $\varepsilon_0=8.854\times10^{-12}$ C/V m

ε_r = dielectric constant of the electrolyte
ζ = zeta potential, $\zeta=\zeta^*/\Psi_{\text{ref}}$
η = surface-normal coordinate
μ = dynamic viscosity (N s/m^2)
ρ = fluid density (kg/m^3)
ρ_e = net electric charge density, $\rho_e=\rho_e^*/\rho_{e,\text{ref}}$
$\rho_{e,\text{ref}}$ = reference charge density, $\rho_{e,\text{ref}}=zen_0$ (C/m^3)
σ_e = electrical conductivity, $\sigma_e=\sigma_e^*/\sigma_{e,\text{ref}}$
$\sigma_{e,\text{ref}}$ = reference conductivity, $\sigma_{e,\text{ref}}=Dz^2e^2n_0/k_bT$ ($1/\Omega\,\text{m}$)
Ψ = electrical potential, $\Psi=\Psi^*/\Psi_{\text{ref}}$
Ψ_{ref} = reference electrical potential, $\Psi_{\text{ref}}=k_bT/ze$ (V)

Superscript

* = dimensional variable
$\bar{}$ = cross-sectional average
$\hat{}$ = unit vector

References

[1] Hunter, R. J., 1981, *Zeta-Potential in Colloid Science: Principles and Applications*, Academic, London.
[2] Burgreen, D., and Nakache, F. R., 1964, "Electrokinetic Flow in Ultra Fine Capillary Slits," J. Phys. Chem., **68**, pp. 1084–1091.
[3] Rice, C. L., and Whitehead, R., 1965, "Electrokinetic Flow in a Narrow Cylindrical Capillary," J. Phys. Chem., **69**, pp. 4017–4023.
[4] Levine, S., Marriott, J. R., Neale, G., and Epstein, N., 1975, "Theory of Electrokinetic Flow in Fine Cylindrical Capillaries at High Zeta-Potential," J. Colloid Interface Sci., **52**, pp. 136–149.
[5] Yang, C., and Li, D., 1997, "Electrokinetic Effects on Pressure-Driven Liquid Flows in Rectangular Microchannels," J. Colloid Interface Sci., **194**, pp. 95–107.
[6] Yang, C., Li, D., and Masliyah, J. H., 1998, "Modeling Forced Liquid Convection in Rectangular Microchannels With Electrokinetic Effects," Int. J. Heat Mass Transfer, **41**, pp. 4229–4249.
[7] Ren, L., Qu, W., and Li, D., 2001, "Interfacial Electrokinetic Effects on Liquid Flow in Microchannels," Int. J. Heat Mass Transfer, **44**, pp. 3125–3134.
[8] Ren, L., Li, D., and Qu, W., 2001, "Electro-Viscous Effects on Liquid Flow in Microchannels," J. Colloid Interface Sci., **233**, pp. 12–22.
[9] Yang, J., and Kwok, D. Y., 2003, "Effect of Liquid Slip in Electrokinetic Parallel-Plate Microchannel Flow," J. Colloid Interface Sci., **260**, pp. 225–233.
[10] Yang, J., and Kwok, D. Y., 2004, "Analytical Treatment of Electrokinetic Microfluidics in Hydrophobic Microchannel," Anal. Chim. Acta, **507**, pp. 39–53.
[11] Chen, X. Y., Toh, K. C., Yang, C., and Chai, J. C., 2004, "Numerical Computation of Hydrodynamically and Thermally Developing Liquid Flow in Microchannels With Electrokinetics Effects," ASME J. Eng. Gas Turbines Power, **126**, pp. 70–75.
[12] Yang, J., Lu, F., Kostiuk, L. W., and Kwok, D. Y., 2003, "Electrokinetic Microchannel Battery by Means of Electrokinetic and Microfluidic Phenomena," J. Micromech. Microeng., **13**, pp. 963–970.
[13] Chun, M. S., Lee, T. S., and Choi, W., 2005, "Microfluidic Analysis of Electrokinetic Streaming Potential Induced by Microflows of Monovalent Electrolyte Solution," J. Micromech. Microeng., **15**, pp. 710–719.
[14] Mansouri, A., Scheuerman, C., Bhattacharjee, S., Kwok, D. Y., and Kostiuk, L. W., 2005, "Influence of Entrance and Exit Conditions on the Transient Evolution of Streaming Potential in a Finite Length Microchannel," *Third International Conference on Microchannels and Minichannels*, Toronto, Canada, Paper No. ICMM2005-75176.
[15] Mirbozorgi, S. A., Niazmand, H., and Renksizbulut, M., 2006, "Electro-Osmotic Flow in Reservoir-Connected Flat Micro-Channels With Non-Uniform Zeta Potential," ASME J. Fluids Eng., **128**, pp. 1133–1143.
[16] Masliyah, J. H., 1994, *Electrokinetic Transport Phenomena*, Alberta Oil Sands Technology and Research Authority, Alberta, Canada.
[17] Weast, R., Astle, M. J., and Beyer, W. H., 1986, *CRC Handbook of Chemistry and Physics*, CRC, Boca Raton, FL.
[18] Van Doormaal, J. P., and Raithby, G. D., 1984, "Enhancement of the SIMPLE Method for Predicting Incompressible Fluid Flows," Numer. Heat Transfer, **7**, pp. 147–163.
[19] Rhie, C. M., and Chow, W. L., 1983, "Numerical Study of the Turbulent Flow Past an Airfoil With Trailing Edge Separation," AIAA J., **21**, pp. 1525–1532.
[20] Patankar, S. V., 1980, *Numerical Heat Transfer and Fluid Flow*, McGraw-Hill, New York.